Compositional Diversity and Structural Dynamics of Perovskite Solar Cells (Alternative format thesis).

Niemann, Ralf

Award date:
2017

Awarding institution:
University of Bath

Compositional Diversity and Structural Dynamics of Perovskite Solar Cells

by

Ralf Gregor Niemann

B.Sc. Chemistry, University of Duisburg-Essen (2010)
M.Sc. Chemistry, University of Duisburg-Essen (2013)

submitted to the Department of Chemistry
in partial fulfillment of the requirements for the degree of

Doctor of Philosophy

at the

University of Bath

February 2017

Contents

List of Figures

List of Tables

Acknowledgments

First and foremost I would like to thank the Petra Cameron Group for over three years of support which made this thesis possible. This goes especially for Petra and group members that were there from day one and gave me support and patience when I started (Kat, Adam and Wentao), but also every single past and present group member who adds their contribution to the group.

The whole DESTINY ITN network (grant agreement 316494) gave me an invaluable amount of feedback, training and eventually job opportunities (as turned out recently). Alison as the coordinator deserves special thanks for making DESTINY come true and supporting every single fellow. During my placements I was warmly welcomed by the Zaban Group (and well trained by Laxman), learned a lot about spectroscopy from the Falaras Group (with a lot of help from Thanassis and Harry) and finally got to experience the industrial side at Dyesol UK (with helpful guidance from Zaka) and 3GSolar (with Jiangang showing us around the labs).

The University of Bath provided a great environment for research, leisure and sports. Lunch has always been fun with international groups from all over Italy and Spain and also Europe and the rest of the world (especially Federico as the glue to many of those). Thanks to the microscopy and analysis suite for providing plenty of equipment and keeping it running (Ursula and John).

Finally special thanks goes to everyone else who helped me out with a wise word, nice gesture or hands-on help: House mates (thanks Andy *et al.*) and sports clubs (Velo Club Walcot, Bath University Boat Club). I also can not underestimate the support from friends for making long days with tedious research somehow enjoyable in the end after a run, a chat or a beer (I am not going to start listing names, because I would not know where to stop). Last but not least I would like to thank my whole family including Niemänner, Willmse, Brandewinder and most of all Rissels (Karen, Peter, Olivia and Zoe): without your constant support from abroad I could not have managed this thesis.

Declaration of work done in conjunction with others

This thesis includes publications, which are based on collaborative work. Detailed contributions are listed before each publication in context.

Publications

1. Casaluci, S., Cina, L., Pockett, A., Kubiak, P. S., **Niemann, R. G.**, Reale, A., Di Carlo, A., and Cameron, P. J. A Simple Approach for the Fabrication of Perovskite Solar Cells in Air. *Journal of Power Sources* 297 (2015), 504-510.

2. **Niemann, R. G.**, Kontos, A. G., Palles, D., Kamitsos, E. I., Kaltzoglou, A., Brivio, F., Falaras, P., and Cameron, P. J. Halogen Effects on Ordering and Bonding of CH3NH3+ in CH3NH3PbX3 (X = Cl, Br, I) Hybrid Perovskites: A vibrational spectroscopic study. *Journal of Physical Chemistry C* 120, 5 (2016), 2509-2519.

3. Richardson, G., O'Kane, S. E. J., **Niemann, R. G.**, Peltola, T. A., Foster, J. M., Cameron, P. J., and B.Walker, A. Can slow-moving ions explain hysteresis in the current-voltage curves of perovskite solar cells? *Energy & Environmental Science* 9 (2016), 1476-1485.

4. **Niemann, R. G.**, Gouda, L., Hu, J., Tirosh, S., Gottesman, R., Cameron, P. J., and Zaban, A. Cs+ incorporation into CH3NH3PbI3 perovskite: Substitution limit and stability enhancement. *Journal of Materials Chemistry A* 4 (2016), 17819-17827.

5. Pering, S. R., Deng, W., Troughton, J. R., **Niemann, R. G.**, Brivio, F., Kubiak, P. S., Jeffrey, F. E., Watson, T. M., Raithby, P. R., Johnson, A. L., Lewis, S. E., and Cameron, P. J. Azetidinium as a Stable Organic Cation for Perovskite Solar Cells, (2017) under review.

Abstract

This thesis deals with perovskite materials for photovoltaic applications. Specifically the methylammonium lead iodide perovskite ($MAPbI_3$) has experienced a recent surge of research interest, due to its promising performance as a photovoltaic absorber and its potential to provide cheap and abundant energy. The downside remains an insufficient stability as well as a poor understanding of the relationship between structure, property and photovoltaic performance. The aim of this thesis is to improve both shortcomings, stability and fundamental understanding, by optimising the fabrication process and an in-depth analysis of different $MAPbI_3$ derivatives.

For the optimisation of the fabrication process, the substrate treatment protocol was optimised regarding its influence on the adjacent TiO_2 compact layer and its electrochemical response. Secondly, the cell layout and measurement protocol was optimised. Finally, two new fabrication routes were introduced. One that allows a crystallisation of the perovskite thin-film at a lower temperature (about 84 °C) by using a high air-flow rate; the other fabrication technique uses a vacuum assisted vapour conversion of PbI_2, which allows for a controlled conversion process without environmental exposure and without the necessity of a glovebox.

New perovskite materials were synthesised, which show an enhanced stability towards water, by replacing the organic A-site cation methylammonium (MA^+). Firstly, cation mixtures with Cs^+ ($Cs_xMA_{1-x}PbI_3$) show structural limitations with an estimated substitution limit of $x > 0.13$, that is not solely caused by steric factors, as expected, but indicates chemical bonding contributions. Secondly, the organic cation azetidinium (Az^+) was employed, which does not form a perovskite structure on its own (δ-$AzPbI_3$), like the δ-$CsPbI_3$. However, solid-state solutions $Az_xMA_{1-x}PbI_3$ formed for small Az-ratios ($x \leq 0.05$) and showed an enhanced photovoltaic performance and reduced hysteresis. Notably, both systems, Cs^+- and Az^+-containing, improved the water-resistance of the resulting perovskite. An initial assessment of the instability of the $AzPbI_3$ was undertaken with Raman spectroscopy and indicates a strong interaction between the amine group and the inorganic part, which could offer an alternative bonding scheme to the three-dimensional $[PbX_6]^{4-}$ octahedra network and therefore result in the formation of a two-dimensional structure.

Finally, different halide derivatives $MAPbX_3$ (X = Cl, Br, I) were analysed regarding their structural dynamics, by measuring the spectroscopic response in resonance and off-resonance conditions. It was shown that the low-frequency modes are mainly caused by the inorganic lattice and matched the model of an harmonic oscillator, thus having negligible influence from the organic cation. Internal MA^+ vibrations showed an continuous red-shift for smaller halide derivatives, which shows an increasing interaction with the inorganic scaffold. Temperature dependent measurements for the $MAPbBr_3$ between 100 K and RT indicate an order-disorder transition with an activation energy of about $E_a = 7.5 \pm 1.0$ kJ for the reorientation motion. The measurement of all $MAPbX_3$ species at 100 K indicates long-range order between the MA^+ cations in the orthorhombic phase.

List of Acronyms

AC	Alternating Current
AFM	Atomic Force Microscopy
AM	Air Mass Coefficient
AMBER	Assisted Model Building with Energy Refinement
CB	Conduction Band
CV	Cyclic Voltammetry
CVD	Chemical Vapour Deposition
DC	Direct Current
DMSO	Dimethyl sulfoxide
EDX	Energy Dispersive Xray Spectroscopy
EIS	Electrochemical Impedance Spectroscopy
EPBT	Energy Payback Time
ETM	Electron Transporting Material
FWHM	Full Width Half Maximum
HOIP	Hybrid Organic-Inorganic Perovskite
HTM	Hole Transporting Material
IR	Infrared
Kapton	Poly(4,4'-oxydiphenylene-pyromellitimide)
MA^+	Methylammonium cation ($CH_3NH_3^+$)

MAPX	Methylammonium lead halide perovskite
MAX	Methylammonium halide
mp	Mesoporous
OCVD	Open-Circuit Voltage Decay
PCE	Power Conversion Efficiency
PL	Photoluminescence
PSC	Perovskite based Solar Cell
PV	Photovoltaics
RMS	Root Mean Square
RT	Room Temperature
SC	Spin-coating
SEM	Scanning Electron Microscopy
SP	Spray Pyrolysis
spiro	Spiro-OMeTAD
sq	Square
ss	Solid-State
tBP	4-tert-Butylpyridine
TFSI	bis-(Trifluoromethylsulfonyl)imide
UV	Ultraviolet
V-VASP	Vacuum Vapour Assisted Solution Processing
VASP	Vapour Assisted Solution Processing
VB	Valence Band
Vis	Visible
XRD	X-ray Diffraction
Yrs	Years

Chapter 1

Introduction

Untersuchungen über photoelektrische Eigenschaften stehen noch aus.
Studies on photoelectric properties are outstanding.

Detlev Weber, *$CH_3NH_3PbX_3$, a Pb(II)-System with Cubic Perovskite Structure*, Zeitschrift für Naturforschung, 1978, 33b, 1443-1445.[1]

Light plays a major role from the very beginning of the universe, where the early dynamics were mostly set by photons and neutrinos, being the highest energetic particles during the radiation-dominated era (first $47,000$ yrs of the universe).[2] Even after the end of this era, when the energy density of matter became dominant and was later succeeded by dark energy[2] and throughout the following 13.8 billion years[3, 4] until present, light remained essential for life, as being the driving force for photosynthesis in plants and therefore one of our most fundamental energy sources. Without it the earth would be nothing but a frozen ice block at 3 K.

In fact, solar power is the underlying driving force behind almost all human energy sources: wind energy is based on a mass movement of air, caused by pressure differences in the atmosphere which are in turn caused by buoyancy forces that are triggered by solar heating. Hydro-power is based on the kinetic energy of fast-running water, which in turn is gained by an evaporation process, fuelled by solar power. Fossil fuels are ancient sources of carbohydrates, synthesised from carbon dioxide, water and solar energy.[5] Even nuclear energy is fuelled by solar power, when looking at its very origin: The only reason why heavy elements (including radioactive elements such as uranium) exist is the so called stellar nucleosynthesis;[6] this process exclusively happens under extremely harsh conditions which can only be found in stars, such as our sun.

1.1 Powering the planet

Nowadays, a growing population, of currently almost 7.5 billion people (February 2017),[7] tied to an increasing industrialisation in most parts of the world, causes a continuous growth of the world's energy demand; this brings up an energy problem on the terawatt scale.[8] More precisely, the estimated energy consumption in 2013 was 3.9×10^{20} J or 9.3×10^{9} MT (mega-tonne) of oil equivalent,[9] which corresponds to an average power output of 12.3 TW. Currently, most of our energy needs are covered by limited fossil fuel based energy sources.[10] In order to secure a steady energy supply for the future, it seems perspicuous to decouple emissions and economical growth by utilising renewable energy sources in the future to follow the '*irreversible momentum of clean energy*',[11] as it has been recently called by Obama *et al.*

When comparing different types of renewable energy sources, solar power is the most abundant resource on earth and therefore forms by far the largest part of the terrestrial energy budget. Solar radiation of 172 PW (full spectrum) accounts for 99.97 % of the incoming energy,[12] while internal, tidal and waste heat constitute the rest.[13] The currently most used energy sources are oil, coal and gas with known reserves of 1750 PW · h, 1400 PW · h and 5500 PW · h, respectively.[14] Thus a few days of solar radiation contain as much energy as the entire known fossil fuel reserves. Or from a different point of view, our energy demands (12.3 TW) could easily be covered from the sunlight that reaches the earth (172 PW), if only 0.072 ‰ could be used. In order to cover the world's energy needs with a 20 % efficient solar cell (SC), one would have to cover an area of $183,600$ km^2 (neglecting night time), which is less than Great Britain (counting $209,331$ km^2) and only about 2 % of the Sahara desert (counting over $9,000,000$ km^2). Even though this sounds like a small area, it would still come with a big price tag. The costs of photovoltaic (PV) modules tumbled recently to less than 1 \$/W, but are still considerably higher for complete PV systems, including soft costs, *e.g.* labour.[15] With an assumed price of 1.4 \$/W for a finished PV system, an investment of about 17.2 trillion USD would be necessary to produce enough energy to cover the above mentioned 12.3 TW. That is about as much as the current GDP of the United States or the European Union.

This shows that solar energy is the most reasonable approach when it comes to powering the planet, but it also comes with a disproportional price tag. The reason for this lies in the high costs of PV systems, more than half of which is made up from module costs.[15] The reason for the relatively high costs of current modules lies in the elaborate and energy-intensive fabrication procedure for current silicon PV modules, which will be explained in the next section.

1.2 Solar cell materials: Gold, silicon and perovskites

The French physicist Alexandre-Edmond Becquerel was the first to discover that sunlight can be converted into electricity in 1839.[16] He used wires of gold and platinum in an electrolyte and observed an electric current when the plates were exposed to solar radiation *'in an uneven way'*. The first solid-state PV cell was built in 1883 by Charles Fritts, who used selenium that was coated with two thin layers of gold to form the junctions. The cell had a relatively low power conversion efficiency (PCE) of about 1 %.[17] Further progress was not made before the 20^{th} century, when a better theoretical understanding was combined with the design of more efficient cells. Albert Einstein published his *'heuristic viewpoint concerning the production and transformation of light'* in 1905, which described the photoelectric effect and underpinned the quantum revolution.[18] The importance of this work earned him the Nobel Price for physics in 1921. The first silicon SC was patented in 1941 by Ohl, which made him not only the inventor of the silicon SC but also the first person to implant ions into silicon and to discover the p-n junction.[19] However, efficiencies of his devices were below 1 %. The first *practical* example of a SC was shown in 1954 by Pearson, Chapin, and Fuller in the Bell Laboratories.[20] While working on alternative off-grid solutions for power generation they managed to efficiently dope silicon pieces through diffused junctions and thereby produced efficiencies of around 6 %.[20] This was the first SC to be efficient enough to power large-scale devices, *e.g.* a radio transmitter during the Bell Laboratories press conference, when this efficient SC was presented for the first time. The discovery sparked a large public interest and ignited further research into silicon PV, which is up to day the most commonly used PV technology. After almost three more decades of research, another milestone was reached in the early 80s, when silicon cells surpassed 20 % PCE. Nowadays single-crystal silicon cells reach 25.6 % PCE,[21] which is not far from the theoretical limit of around 30 % for the given bandgap of silicon,[22] and a proposed practical limit of about 26 %.[23]

The reason for the popularity of silicon PV lies not only in their good PCE performance, but also their stability. Moreover, it is one of the most abundant elements on earth, that can be found almost anywhere in its oxidised form SiO_2. The purification of silicon has become a major industrial process, as micro-electronics have been developed. Nevertheless, for both PV and electronic applications, a very high purity level of silicon is needed. Impurities in form of dopants would give rise to recombination processes and decrease the efficiency of the SC. But the purification process of silicon is very energy intense and requires multiple processing steps, aggressive chemicals and very high temperatures. A schematic of the widely used Siemens process for silicon purification is

depicted below; it was developed by the company Siemens in the 60s.

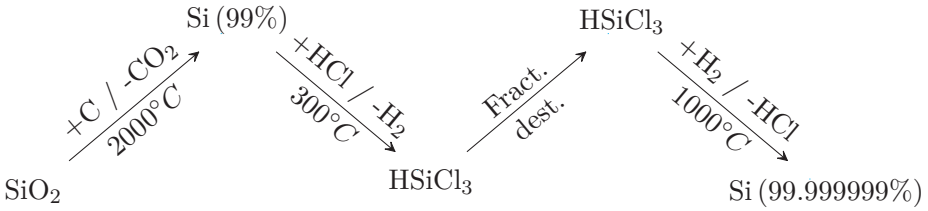

Figure 1-1: Schematic of the Siemens process to purify silica into silicon, in its pure elemental state.

The next step after obtaining pure silicon pellets is to form large single crystals. Therefore, the pellets need to be melted and crystals slowly grown from a seed crystal just above their melting point of 1414 °C. This is known as the Czochralski Process.[24]

It becomes clear that silicon is a questionable candidate for delivering a majority of the global energy demand, despite its favourable bandgap and stability. The energetic and financial investment during the production is relatively high. Because of its indirect bandgap, a material thickness of about 200 μm is needed. This is only slightly thicker than a human hair, but still a lot when thinking about covering huge areas, *e.g.* 183,600 km^2 as discussed above. Modern research on next-generation SC focuses on novel PV materials that are processable at low temperatures and have a high absorption coefficient, to decrease the required thickness of active material.

This brings us back to the year 1839, where this section started. Not only did A.E. Becquerel demonstrate the photovoltaic effect in Paris for the first time in this year, but Gustav Rose also discovered a new material, $CaTiO_3$ (see fig. 1-2b), in the Ural mountains of Russia.[25] It was later named perovskite after Lev Aleksevich von Perovski (see fig. 1-2a). It has the general structure ABX_3 and can consist of ternary oxides, nitrides, halides and other compositions with the same crystal structure. Another prerequisite for the perovskite structure, besides the ABX_3 stoichiometry is corner sharing octahedral units, *e.g.* the AB_3. For a metal oxide perovskite (X representing oxygen), the valence of the metals A and B must sum to six in order to achieve charge neutrality, *e.g.* I-V-VI_3, II-IV-VI_3 and III-III-VI_3. If X is formed by an halide (as in this thesis), the valence of the two cations must sum to three, leaving only one possible valence: I-II-VII_3. The B-site is then occupied by a metal, *e.g.* Pb, which is surrounded by six halides and forms a corner-shared $[PbX_6]^{4-}$ octahedral structure. The A-site cation is located in the voids between the octahedra (*e.g.* see fig. 1.1c).

The first reported synthesis of a perovskite material was done in 1893 by Wells,[26]

and a crystallographic characterisation followed in 1958 by Moller.[27] One candidate in the class of perovskites which is of special interest for PV applications as a high-performance semiconductor (details in section 1.3) is the methylammonium ($CH_3NH_3^+$ = MA^+) lead iodide $MAPbI_3$ (see fig. 1-2c). It was first synthesised in 1978;[1] in this very first report about the now so popular perovskite, Weber synthesises different methylammonium lead halides $MAPbX_3$ and presents their complete structural characterisation.[1] He also mentions that *'studies on photoelectric properties are outstanding'*; little did he know that this inconspicuous gap in his study would later on engage thousands of researchers.

Before perovskites were finally discovered for PV applications, they drew attention for their electronic properties. Mitzi *et al.* conducted several studies in the mid-90s and 2000s for electronic and optical applications.[29, 30, 31, 32, 33, 34, 35] Intriguing features of these materials are high carrier mobility, tunable electronic properties and an easy and low-cost solution deposition. There are now multiple reports on the exciting physical properties of different perovskite materials, like colossal magnetoresistance, [36] ferroelectricity, [37] superconductivity, [38] thermoelectric properties [39] and thermochemical catalysis.[40] Perovskites were finally introduced to PV in 2009 by Kojima *et al.* with an initial PCE of 3.8 %.[41] This relatively low initial efficiency would soon become the fastest rising PV technology in history. This rapid evolution of perovskite based solar cells (PSC) is explained in more detail in section 1.4.

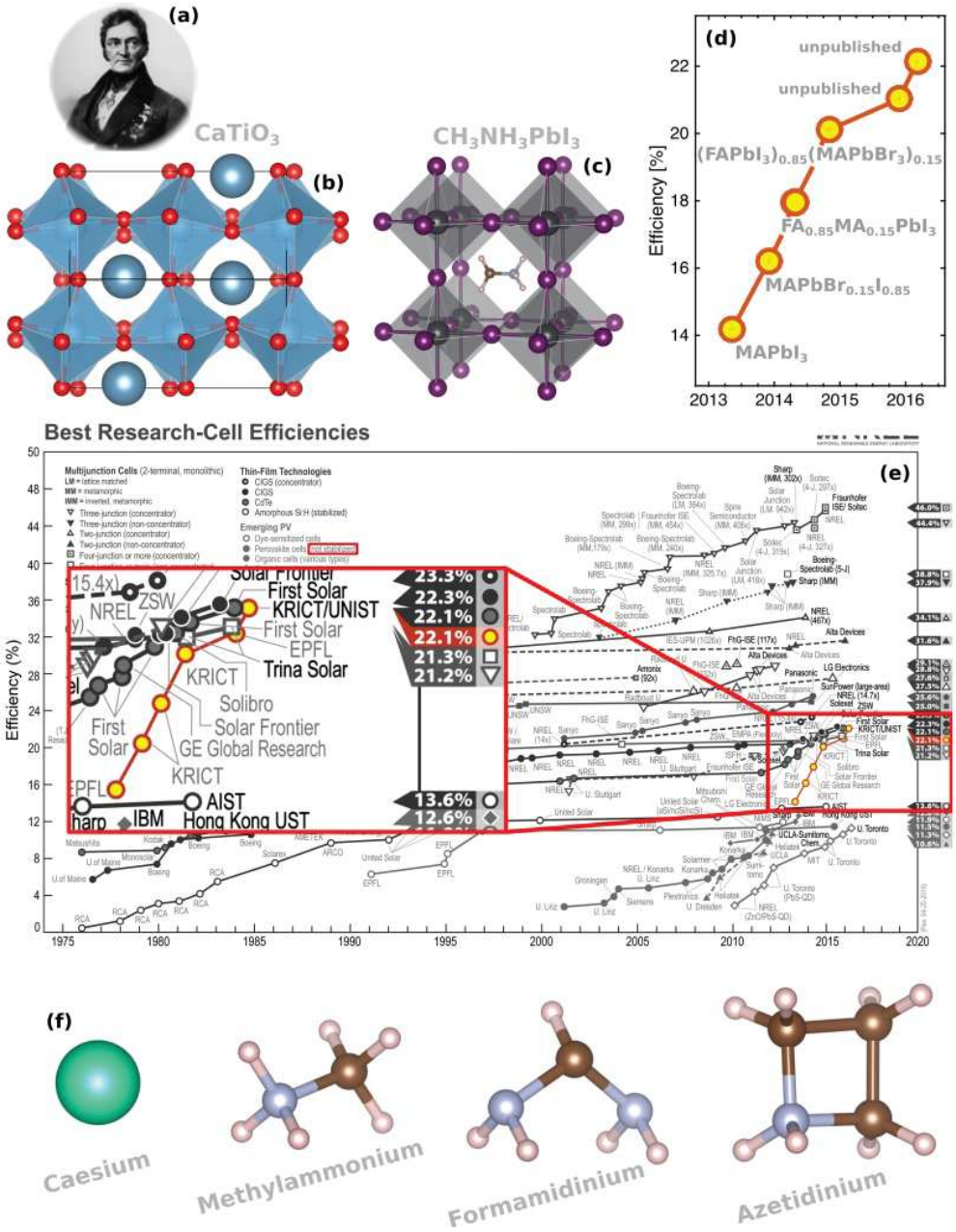

Figure 1-2: (a) Portrait of Lev Perovskite, name patron of the perovskite structure (picture taken from wikipedia; CC in public domain).[28] (b) Crystallographic structure of the first discovered perovskite $CaTiO_3$. (c) Crystallographic structure of the $MAPbI_3$ perovskite. (d) Extract from the NREL chart, focussing on perovskite reports and their compositions. (e) NREL chart with perovskite solar cells colour coded and zoomed in the inset.[21] (f) Different cations that can serve as an A-site substitution in $APbI_3$ perovskites and are further discussed in this work.

1.3 Hybrid perovskites as low-cost and high-performance semiconductors

The outstanding performance of HOIP as a semiconductor is based on a variety of effects. This interplay of optical properties, charge-transport behaviour and electronic response can be partially explained by classical models but also includes important relativistic contributions.

The optical response of HOIP shows a direct absorption across an indirect bandgap, which is attributed to a Dresselhaus spin-orbit coupling that causes k-dependent splitting of the conduction band minimum.[42, 43] The bandgap can be continuously tuned by substituting either position of the ABX_3 structure (details in section 1.7). A high photoluminescence efficiency and a sharp absorption makes its performance comparable to other state-of-the-art semiconductors like GaAs,[42] which is currently the best performing single junction PV material (certified 27.5 % PCE, see fig. 1-2e). This is at least partially due to the low defect density of $\sim 10^{10}$ cm^{-3}, which makes this material practically defect-free.[44] Even though many oxidic perovskites can be n-doped up to a point of metallic behaviour, this effect can not be seen for halide perovskites, which seem to be always intrinsic.[45]

The bandgap of HOIP is direct for all halide-based species and solely influenced by the metal and halide. The valence band is contributed by the p^6 orbital of the halide and the s^2 orbital of the metal. The conduction band consists of the p^0 orbital of the metal. Orbitals from the A-site cation are not contributing.[46] An important contribution to the band structure is given by spin-orbit coupling, which causes an effect known as Dresselhaus splitting;[42] thus the conduction band splits, which is one of the contributions underpinning the large mobility (~ 164 $cm^2V^{-1}s^{-1}$), allowing a carrier diffusion length of 175 μm.[44] Other effects that possibly contribute to the optoelectronic response are too manifold to be addressed at this point, but include band filling,[47] dual excited state,[48] bimolecular recombination,[49] photon recycling[50] and self-trapped excitons.[51]

1.4 The surge of perovskite solar cells

In order to produce a high-efficiency solar cell, it is not enough to simply have the right material. A good example is the silicon solar cell: it took about six decades to get efficiency levels from less than 1 % in 1941[19] to over 25 % today.[52] A comprehensive understanding of the material's photo-physics as well as several milestones in the processing of the cell were needed to reach this point. The first surge in efficiencies was set off after Chapin, Fuller and Pearson introduced diffused junctions in 1954,[20] that kick-started the development of silicon cells with the report of 6 % PCE. During the next decade further improvements in the diffusion technique alongside the development of the Siemens process (see above) resulted in a further rise to about 16 %.[53, 52] Another series of improvements came along with advancement in the microelectronics industry, which brought efficiencies up to 25 %,[52] by using closely spaced metal lines, lithography techniques and anti-reflection coatings.

For perovskites, a similar trend can be seen in their early development. The first two reports of perovskites in SC came from Kojima *et al.* in 2009 (3.8 %) and Im *et al.* in 2011 (6.5 %). Both reports passed almost unnoticed and used $MAPbI_3$ only as a nano-crystalline absorber in conjunction with a liquid electrolyte that decomposes the material,[41, 54] therefore underestimating the novelty of this new absorber. Two individual PSC studies in 2012 by Lee *et al.* and Kim *et al.* employed the $MAPbI_3$ as a photoactive thin-film material and showed that it was possible to achieve efficiencies around 10 %. From that point on PSC started to gain significant interest. Sensationally, PSC were in the same efficiency-league as other third-generation PV technologies, just after their first report as a solid-state absorber. Now, they competed with dye-sensitised solar cells and organic photovoltaics, which at that time used to be praised as the most promising material to produce cheap and abundant solar energy with a short energy payback time.[55] This already impressive efficiency was soon to be turned over by a succession of improvements that lead to the current record performance of 22.1 %.[21]

First improvements focused on different deposition techniques and processing parameters. An example of this is the introduction of a sequential conversion technique by Burschka *et al.* in 2013.[56] In this approach a plain PbI_2 layer is deposited first, which is then converted to $MAPbI_3$, by dipping the film into a MAI solution. This significantly improved film morphology, gave a certified 14.1 % efficiency and now marks the first entry of PSC in the NREL chart.[56, 21] The development of PSC record cells on the NREL chart can be seen in figure 1-2d with details listed in table 1.1. Shortly after, another deposition technique was reported where the precursors salts PbI_2 and MAI were simultaneously sublimed onto the substrate.[57, 58] This deposition

technique gave perfectly smooth cells with an efficiency around 15 %. Even though the process of vapour deposition is opposed to the idea of a cheap and mass producible technology (not easily up-scalable), it allowed the creation of smooth films with a controlled thickness, which was important for spectroscopic studies and to elaborate on elemental device properties.[51, 49, 59, 60, 61, 62, 63] Further studies investigated a dazzling array of processing parameters *e.g.* precursor compositions,[64, 65, 66, 67, 61, 68] different solvents,[69] deposition temperatures,[70, 71] atmospheric influences,[72, 73] humidity,[74, 75, 76, 73, 77] alternative precursor salts,[78] pre-treatments,[79, 80] solvent dripping[81] and dipping[56] just to name a few. A more detailed discussion of parameters affecting thin-film morphology is given below (section 1.5).

The next step that lead from efficiencies of around 15 % to current record cells focussed on chemical optimisation to tune the intrinsic material properties. $MAPbI_3$ might be an excellent photovoltaic material but it has up to now failed to reach efficiencies of 20 %,[84] a benchmark that its derivatives had already reached in 2014.[83] In order to further improve the PSC performance a judicious design of the material composition was necessary. First studies focused on the utilisation of Br-derivatives to increase the V_{OC} and it was found that the stability of the perovskite towards moisture also improved.[85] The next NREL record cell was made from a $MAPb(Br_{0.15}I_{0.85})_3$ mixture, achieving 16.2 %.[81] However, the inclusion of the smaller Br halide blue-shifts the bandgap into a less favourable region, away from the optimum 1.34 eV.[22] A general problem is that the empirical Goldschmidt factor dictates that for a further decrease of the bandgap towards the optimum 1.32 eV, the size of the cation or halide needs to increase.[86] But halide derivatives larger than iodine are radioactive and cations larger than MA are mostly not within in the frame of the Goldschmidt factor and lead to a transformation into a yellow non-perovskite δ-phase at room temperature. A more detailed discussion of the Goldschmidt factor can be found below (section 1.7). It gives an empirical estimation for the stability of perovskites based on their ionic radii. Therefore, cations that are larger than MA^+ and on the upper end of the allowed cation size need an

Table 1.1: Overview of perovskite record cells as reported in the NREL table, which time, performance, chemical composition and publication data, if available.

Year	Efficiency [%]	Perovskite	Journal	Ref.
2013	14.1	$MAPbI_3$	Nature	[56]
2013	16.2	$MAPb(Br_{0.15}I_{0.83})_3$	Nature Materials	[81]
2014	17.9	$FA_{0.85}MA_{0.15}PbI_3$	Nature	[82]
2014	20.1	$(FAPbI_3)_{0.85}(MAPbBr_3)_{0.15}$	Science	[83]
2015	21.0	unpublished		
2016	22.1	unpublished		

entropic stabilisation, which can be achieved by mixing several types of cations in one material (solid-state solutions). This marks the next NREL record cell in 2014 by Jeon *et al.* with 17.9 %.[82] From there on PSC employed progressively more ions. Jang *et al.* were able to pass an important milestone by producing a 20.1 % cell in 2014 with a $(FAPbI_3)_{0.85}(MAPbBr_3)_{0.15}$ perovskite (with FA^+ = formamidinium, $HC(NH_2)_2$, see fig. 1-2f).[83] The next two NREL entries lie at 21.0 % and 22.1 %, but are not published in literature yet (stand: February 2017). However, from published literature that achieves similar performances it can be seen that the usage of an increasing number of ions decreases the amount of impurities and gives more stable device with a higher photovoltage and reproducibility. This was impressively shown by Saliba *et al.* with the ternary cation system CsFAMA ($Cs_x(FA_{0.87}MA_{0.13})_{1-x}PbBr_{0.17}I_{0.87}$) and more recently the quadruple RbCsFAMA perovskite, achieving a stabilised efficiency of 21.1 % and 21.6 %, respectively.[87, 88] A more detailed discussion of compositional and structural engineering of perovskites is given below (section 1.7).

1.5 Thin-film formation and device fabrication

The control of morphological parameters might seem trivial from a scientific point of view, but is of paramount importance for cell performance, as has been discussed above. Small changes in the process, that often go unnoticed, can give a vastly different response of the perovskite. Therefore, a major difficulty during device fabrication is the reproducibility of the process. A vast array of parameters influence the thin-film formation and crystallisation of the perovskite layer. This is partially caused by the sensitivity and meta-stability of this class of HOIP.[89, 90, 91] Zhang *et al.* showed recently that, at least from a first-principle perspective, $MAPbI_3$ as a material is unstable.[92] This results in a variety of factors that can have an impact on film formation, resulting in a variety of different fabrication protocols. [61, 64, 65, 66, 67, 68, 69, 70, 71, 72, 73, 74, 75, 76, 77] The result is that the most widely used deposition process (spin-coating) is influenced by the ambient atmosphere, which varies from day to day and can even be influenced during a deposition process in a glovebox by solvent concentrations that stem from the solvent evaporation during the spin-coating. For example Pockett *et al.* reported that cells which were prepared under nominally identical conditions fell into two distinctive groups.[93] Several processes were developed to better control the perovskite fabrication. The earlier mentioned dual-source sublimation of both precursors PbI_2 and MAI is one approach,[57, 58] but requires a full evaporation setup. Chen *et al.* introduced another approach, where the PbI_2 layer was spin coated and only the MAI was evaporated, which can be done on a hotplate. This method was called vapour assisted solution processing (VASP).[94] This process was further developed in a study that is included later in this work, in order to minimise environmental effects.[95] The MAI vapour conversion process was transferred into a low-vacuum environment by using a desiccator lid and a vacuum pump.

In 2013 the wakening interest in PSC was accompanied with an uncertainty regarding long-term impact. Only a few laboratories were able to produce high performing cells, but PSC already drew considerable attention with 14.1 % efficient cells published in several major scientific journals, *e.g.* Science and Nature.[96, 56] Under these peripherals, Snaith and Hoke announced at the 2013 MRS fall meeting an anomalous hysteresis (further referred to as simply hysteresis) during the IV measurement, that makes the obtained IV curve highly dependent on scan speed and direction.[97] This caused scepticism for virtually all reported IV curves, a measurement method that was hitherto considered to be unambiguous. Even though hysteresis is normal at extremely high scan speeds for every type of solar cell and can be explained by capacitive effects, the extent and type of hysteresis in PSC were more severe and indicated a more fundamental

problem.[98] Snaith *et al.* proposed three possible origins for this effect, namely: surface trap states, ferroelectric domains and ion diffusion.[97]

Initially, several studies pointed towards surface trap states and ferroelectric domains as the main reason for hysteresis, with both experimental and computational support.[99, 100, 101, 102] Later work however gave increasing support to the idea of vacancy mediated ion diffusion. Even though the formation of ferroelectic domains by alignment of MA^+ dipoles is still considered possible in PSC, the degree of freedom at room temperature (RT) is too high and the activation energy is too low to contribute to IV scan measurements.[103, 104] A further discussion about implications of MA^+ dynamics is given in the next paragraphs.

Even though vacancy mediated halide diffusion had already been reported more than three decades ago,[106] the exact nature and extent remained uncertain until it became a popular explanation for the anomalous hysteresis phenomenon. Xiao *et al.* showed that the intrinsic electric field can be flipped in a symmetric architecture by applying a bias to the material,[107] which was the first evidence for an electric field induced change of the $MAPbI_3$ morphology and an indirect proof for ion motion. Later studies then emphasised the contribution of ion motion to the IV hysteresis by more detailed studies at different scan speeds and temperatures.[108, 109, 110, 98] A quantitative approach was given later on by Eames *et al.* from first principles; he derived activation energies for different ionic species, *e.g.* 0.6 eV for iodide.[111] This approximation was later supported in several studies, for example Pockett *et al.* (*via* Arrhenius activation energy for low frequency processes in IMVS and EIS measurements) and Richardson *et al.* (employing these values in a drift-diffusion model that predicts IV curves).[112, 105, 113] A possible explanation for the deviation of reported values for ion transport could be that the transport is photo-induced or at least photo-assisted, as could be shown by a visual imaging of photo-brightening, caused by a net migration of iodide.[114]

These iodide vacancies form charges in the device, that can move in a similar way as electrons and holes, driven by the electric potential, only more slowly (higher activation energy). The build-in electric field, that is caused by the different Fermi-levels of the p- and n-type contacts, drives these mobile charges towards the contacts at short-circuit conditions. The positively charged vacancies therefore accumulate at the p-type contact and are opposed by a negatively charged region, caused by the depletion of vacancies at the n-type contact.[105] These accumulated charges form a diffuse double layer at the interface, that is labelled *Debye layer* throughout this work (see fig. 1-3), even though different names can be given (*e.g.* Helmholtz, Stern, Gouy-Chapman), depending on the assumed underlying mechanism. An applied positive voltage can oppose the build-in potential and decrease the amount of charges in the Debye layer. This has a direct

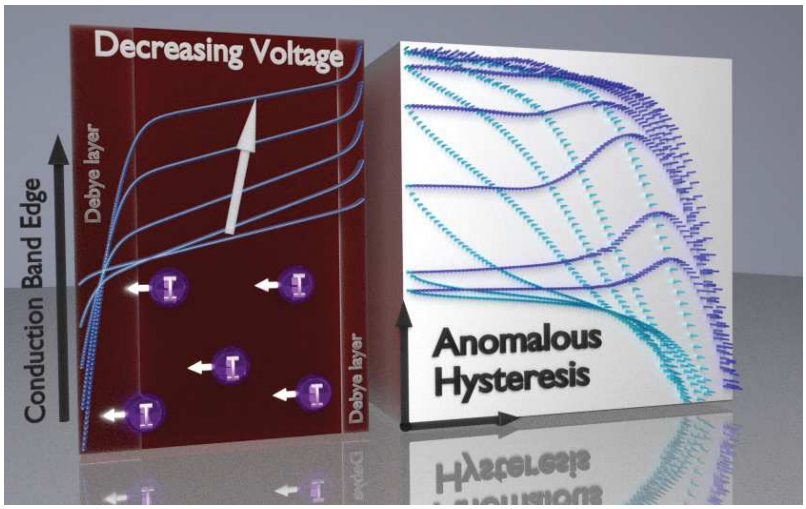

Figure 1-3: (left) Schematic of conduction band evolution while decreasing the voltage and build-up of Debye layers at the interfaces. (right) Resulting anomalous hysteresis in an IV scan. Data from Richardson *et al.*[105] Creative Commons Attribution 3.0 Unported License.

contribution to the measured IV-curve, where the applied voltage is constantly changed together with the distribution of mobile charges throughout the device.[105]

From a structural point of view the reason for the impact of hysteresis is twofold. On one hand the rotational freedom of the organic cation facilitate the movement of ionic species through the material,[115, 103] which is reflected in a low defect diffusion barrier ΔE_b. On the other hand, the relatively soft inorganic lattice and strong lattice polarisation, caused by relativistic effects, result in a low defect formation energy ΔH during crystal formation. The latter gives rise to a high fraction of defects N_0, while the former allows their free movement under an applied electrical field. In a readily formed crystal, ΔE_b is generally large, while the fraction of defect sides is comparably small. This allows the expression of the ionic conductivity σ_{ion} with the following equation:[116, 117]

$$\sigma_{ion} = A \cdot \exp\left(\frac{-\Delta H - \Delta E_b}{kT}\right) = A \cdot N_0 \cdot \exp\left(\frac{-\Delta E_b}{kT}\right) \tag{1.1}$$

$$\text{with} \quad A = \frac{n_0(Ze)^2 \cdot \alpha \cdot d^2 \cdot \nu_0^2}{k \cdot T}$$

σ_{ion}	Ionic conductivity	α	Geometrical factor
ΔH	Defect formation energy	d	Jump distance
ΔE_b	Defect diffusion barrier	ν_0	Vibrational frequency
N_0	Fraction of defects n/n_0		
$n_0(Ze)$	Charge carrier concentration		

In this context, k is the Boltzmann constant and T refers to the temperature. Equation 1.1 possess two parameters (besides temperature), that can be tuned in order to reduce the ionic conductivity and hence hysteretic effects.

Firstly, one could aim to increase ΔE_d, which could be done by changing the mobility or polarity of the organic cation. This would reduce the orientational disorder and lattice deformation that assist the diffusion process.[118] Therefore, one would have to employ different cations to chemically engineer the bonding schemes. Several options for compositional derivatives will be discussed below (section 1.7) and practical examples are given in chapter 4.

The other aspect of hysteresis that has to be thought of is the level of defect concentration $[D]$, which can be controlled during device fabrication. In a comprehensive structural study about different AMI_3 perovskites Stoumpos *et al.* said that *'It needs to be mentioned that not only the material composition but also the level of impurities and therefore synthesis conditions have a significant influence on the final physical and chemical properties and thereby influences the performance of the solar cell.'*[119] Even though the study was conducted on single crystal materials, his statement holds true for thin-films and solar cells as well. Up to now, a variety of factors in the fabrication process were shown to influence the hysteresis of the device, *e.g.* purity and concentration of the precursor solution,[120, 61] grain size,[121] humidity,[74] or temperature.[122]

A critical link between the amount of defects that support ion migration and observed hysteresis is the device's interface. Barnes *et al.* showed recently that, while ion migration is most likely the underlying mechanism for hysteresis, high interfacial recombination rate is necessary to trigger it.[123] This explains why high-performing cells usually experience less hysteresis compared to poorer-performing or degraded cells. A practical example of fabrication parameters that influence defect density and hysteresis will be given in this work (chapter 3).

1.6 Structural dynamics of hybrid organic-inorganic perovskites

Since the discovery of $MAPbX_3$ perovskites in 1978, their structure has been extensively analysed.[1, 124] Initial reports focused on X-ray diffraction, which however fails to resolve the positions of lighter elements, namely the organic cation, which are clouded by the presence of the heavier lead and halide atoms. Initial reports on the position, orientation and dynamics of the MA^+ were done by NMR and millimetre-wave spectroscopy.[125, 124, 126] An extremely fast reorientation of the MA^+ was found,[125] which corresponds to a dynamic disorder processes on the pico-second time scale.[124] In the low-temperature orthorhombic phase this reorientation process becomes restricted.[125] These studies in themselves already allow for far-reaching assumptions about the behaviour of this type of material. A set of complimentary studies about the physiochemical properties of $CH_3NH_3MX_3$ (M = Pb, Sn and X = Cl, Br, I) by Onoda-Yamamuro *et al.* allowed for a further refinement through calorimetric and spectroscopic methods.[127, 128, 129, 130] Early work of Mitzi *et al.* in the 90s mainly focused on electronic properties of this new field of '*organic-inorganic electronics*'.[29, 30, 31, 32, 33, 34, 35] Since the use of perovskites as a PV material, considerable effort has been put into the investigation of MA^+ dynamics, including neutron scattering and DFT methods, described in more detail in the next few paragraphs.[115, 103, 131, 132, 133, 134, 135, 136]

A key property that has to be considered in order to understand the structure and dynamics of this type of perovskite is its organic-inorganic character. But nevertheless, it should be noted that perovskites are not organometallic, following the IUPAC definition, because there is no bond between the metal and carbon.[137] The dynamics of the perovskite structure have important implications on the operation of perovskite solar cells, *e.g.* to assist charge separation,[138] tune the band gap[139, 140] and to improve open-circuit voltage.[133, 122] The description of the MA^+ dynamics is complex and influenced by a variety of factors. Hydrogen bonding offers coupling between the amine group and the halide network and seems to be a key motive to understand bonding.[141, 142] It induces a strong orientational disorder and lattice deformations that perturb the electronic landscape within the $[PbX_3]^-_n$ cage and assists ionic transport.[143] The structural dynamics of the MA^+ can be thought of as a plastic crystal,[144] with strong bonding motives that induce tilting and distortion of the octahedral network, which affects the structure and optoelectronic response of the system as a whole.[142] This network can be influenced through the application of an external electrical field, which aligns the MA^+ dipoles and shifts photo-luminescence (PL) and Raman signals,

as measured through the sensitive torsional mode.[145] Recently, the development of a phonon model by Brivio *et al.* for $MAPbI_3$ (and later $MAPbX_3$, X = Cl, Br, I) allowed for an in-depth discussion of the underlying bonding schemes for each vibrational mode.[146, 147] The study showed that even though the low-frequency modes of the inorganic $[PbX_3]_n^-$ framework are energetically separated from the high-frequency MA^+ internal modes (*e.g.* stretching and rocking in fig. 1-4a), significant coupling is found to the cation for those,[146] *e.g.* for the torsional mode (see fig. 1-4a). This emphasises the interaction between the inorganic cage and organic cation as well as common bonding motives.[142]

The measurement and modelling of MA^+ dynamics in the $MAPbX_3$ has seen a surge within recent years. Two individual studies by Leguy *et al.* and Weller *et al.* both used neutron scattering to investigate the structural influence of the organic cation.[103, 115] They found that the MA^+ increases its disorder with increasing temperature, as has been stated before,[125, 124] and that the cation directs towards the faces of the $[PbI_3]_n^-$ framework in the tetragonal phase,[115] reorienting on a time scale of about 14 fs.[103] Vibronic analysis of the $MAPbI_3$ dynamics gave useful information and distinguished mainly two regimes which are related to internal MA^+ vibrations in the high-frequency region > 800 cm^{-1} (see fig. 1-4a) and internal $[PbI_3]_n^-$ cage modes (< 120 cm^{-1}),[153, 127] while some studies also refer to libration modes at $140-180$ cm^{-1} that refer to the constraint of the MA^+ movement.[154] A real-time observation of the reorientation dynamics with 2D IR spectroscopy distinguished between fast 'wobbling in a cone' (~ 300 fs) and a slower reorientation process (~ 3 ps),[155] which proves the assumption from first principle, that MA^+ aligns in certain orientations.[100, 99] These structural fluctuations can cause a variation of the electronic properties (bandgap) of $\pm 0.1 - 0.2$ eV,[131] which shows their influence on optoelectronic performance. However, the vibronic analysis of $MAPbI_3$ focused mainly on IR spectroscopy because of intrinsic difficulties that arose during measurements with most Raman setups. The problem lies in the fact that the most commonly used excitation sources are 315, 515 and 785 nm, which is in the resonant regime of $MAPbI_3$ and can cause a variety of unwanted side effects. First of all, resonant absorption of HOIP materials is known to change the structure and optical properties of the perovskite and therefore also the Raman spectrum during excitation.[156] Secondly, many recent Raman studies are controversial because the measured modes might have been caused by the degradation product PbI_2,[148] *e.g.* a strong signal around 120 cm^{-1} that is caused by PbI_2 'quantum-wells',[157] which occur during the degradation of $MAPbI_3$. These ambiguities can be seen when comparing different reported Raman spectra, as can be seen in figure 1-4b. Gottesman *et al.* reported on a 'dark spectrum' (fig. 1-4),[149] that gradually changes to a spectrum

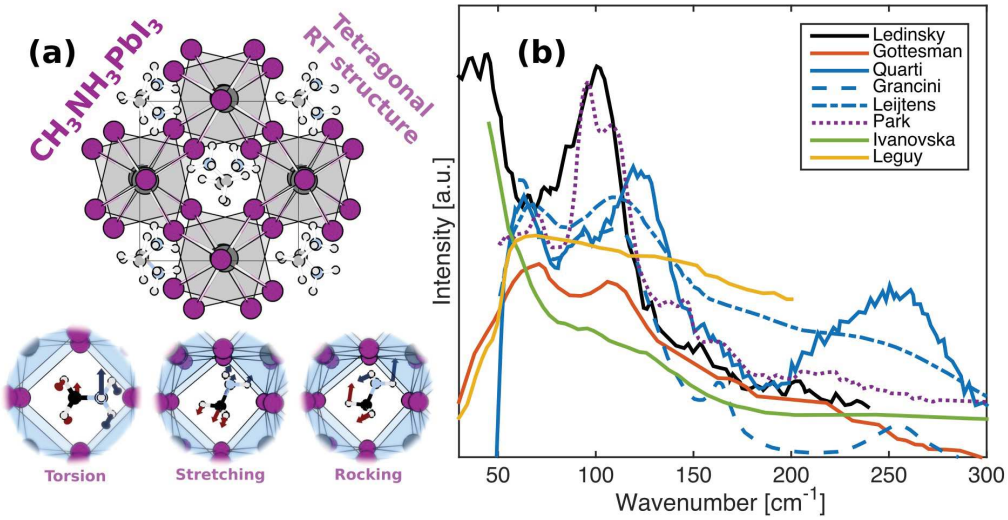

Figure 1-4: (a) Tetragonal $MAPbI_3$ structure at room temperature with three important vibrational modes below. (b) Comparison of different reported Raman spectra of $MAPbI_3$ from literature,[148, 149, 132, 150, 151, 152, 135, 147] focussing on the low-frequency region.

that resembles the one measured by Park *et al.* and Ledinsky *et al.* upon prolonged light exposure.[152, 148] Spectra that were measured by the same research group are plotted in the same colour and show a similar behaviour. However, comparison to spectra measured in different laboratories can show completely different spectra. The degradation feature mentioned above can be quite commonly seen. One also has to notice that especially the measurement of low-frequency modes is difficult because of a high photoluminescent (PL) background when measuring in resonant conditions and the sensitivity of these modes towards photo-induced changes and degradation.

The spectroscopic Raman study, which forms part of this thesis (chapter 4), followed from a number of contradicting measurements that reported different spectra for $MAPbI_3$ which appeared to be dependent on measurement intensity,[132, 158, 148] material architecture,[150] electric field,[151] or measurement time.[149] The presented study employed multiple excitation sources, including the first off-resonant measurement of $MAPbX_3$ perovskites, and can therefore be seen as the first 'true' and unambiguous Raman spectra of this material.[159] Similar studies using neutron scattering followed up after our off-resonance Raman study, with similar results for the correlation time ranging from 5 ps to 14 ps,[160, 103] which also agrees with previously reported values by NMR,[125, 126] millimeter-wave spectroscopy[124] and *ab-initio* calculations.[131, 161]

1.7 Beyond $MAPbI_3$: Compositional derivatives

Due to the strength of chemical bonding effects in HOIP, the atomic radii of substituting elements play a critical role.[162] This can be predicted by the Kupustinskii equation for binary compounds or the more recent Glasser generalisation for more complex systems.[163] They are crucial to help predict the formation of any perovskite structure and can be used for an empirical estimation of the obtained phase. For perovskite systems, the Goldschmidt tolerance factor t was introduced in 1927 as a criterion for the formation of a perovskite structure and for an easier and empirical classification of the system. The equation predicts structural variety of the perovskite class by correlating the ionic radii of the constituents to the underlying structure.

$$\text{Goldschmidt tolerance factor} \qquad t = \frac{r_A + r_X}{\sqrt{2} \cdot (r_B + r_X)} \tag{1.2}$$

r_A, r_B and r_X are the respective radii of the anions in A, B and X position in the perovskite ABX_3. From a structural perspective, the equation gives an estimation of how much of a mismatch the perovskite lattice can compensate before transforming to a different structure. As long as the tolerance factor is within the regime $0.75 < t < 1.00$, the formability of a perovskite structure is empirically probable at RT. Hybrid organic-inorganic halide perovskites tend to form an orthorhombic structure for $t < 0.8$, a cubic structure for $0.8 < t < 1$ and a hexagonal structure for $t > 1$.

It is important to note that the Goldschmidt model is based upon the hard sphere model, which does not accommodate temperature-size dependence.[164] However, perovskites show a variety of phase transitions upon changing the temperature. The highest degree of symmetry is obtained in the cubic structure, usually formed at high temperatures, also labelled α-phase in the context of this study, in accordance with previous work.[165, 166] For lower temperatures many perovskite structures induce a tilting of the metal-halide octahedra, which brakes the symmetry (*e.g.* transfer from cubic into tetragonal phase) and hence lowers the energy of the system.[119] Certain perovskite structures (*e.g.* $FAPbI_3$) break down the 3D-network when lowering the temperature and form a 1D-array of octahedra, which, by definition, does not classify as perovskite structure and is denoted as the δ-phase in this work. Another decisive factor is that organic cations are often disordered, as opposed to hard spheres. This gives rise to fascinating properties such as ferroelectric domains, but also causes deviations from the Goldschmidt model. With increasing temperature, the effective radius of organic cations increases, which has a direct influence on the geometry of the lattice. At lower temperatures, directional inhomogeneity occurs, which is caused by specific bonding motives (*e.g.* hydrogen bonding). This hinders the free rotation of the cation and causes

an alignment along specific directions.[103] As a result the Goldschmidt model is only valid for RT structures, with both inorganic (spherical) and organic cations.

Another parameter that was introduced by Li *et al.* in 2008 is the octahedral factor μ. It adds a further refinement with perovskite structures usually laying in the range of $0.414 \leq \mu \leq 0.723$.[167]

$$\text{Octahedral factor} \qquad \mu = \frac{r_B}{r_X} \tag{1.3}$$

It addressed an issue that some halide perovskites ABX_3 failed to be correctly predicted. This modified structural window correctly predicts 96 % of halide perovskites ABX_3.[167] Both, the tolerance and octahedral factor, are necessary but not sufficient conditions for ABX_3 perovskite formation but combined they give a strong empirical model that allows to build a structural map of different perovskite compositions.[167]

This refined compositional window offers access to a large amount of perovskite compounds. For example a simple but impressive study that screened 13 different organic cations, 21 metals and 8 anions, reported the tolerance factors of 2352 possible combinations.[168] However, the window for materials that have good PV properties is a lot narrower. Because of the instability of the $+II$ oxidation state in Sn compounds (and lighter group IV elements),[169] the most promising metal cation remains Pb, which is relatively stable in its $+II$ oxidation state because of spin-orbit coupling effects. Mixtures of Pb-Sn were shown to form a stable perovskite,[170, 171, 172] which indicates an entropic stabilisation effect. The relatively large metal cation needs to be matched with a large halide, in order to keep the bandgap energy low. The largest constituent that is not radioactive is I^-. This narrows the only viable structural choices to the choice of the A-site cation. Here again, the motto is '*bigger is better*' in order to match the large metal cation size and minimise the optical bandgap. The widely used MA^+ has a tolerance factor of $t_{MA^+} = 0.91$ (see tab. 1.2). Larger cations, *e.g.* FA^+, tend to transform into a lower dimensional non-perovskite phase (δ-phase), by isolating the $[PbI_6]^{4-}$ octahedra.[173, 174, 175] An increasingly popular strategy is the entropic stabilisation, by using mixtures of large and small A-site cations, that average to a desirable value. This trend can be followed when comparing the compositions of record cells over time, as done above (section 1.4). Increasing the number of ions in the perovskite can be a successful strategy to increase stability, for example in order to avoid the yellow polymorph only the $(FAPbI_3)_{1-x}(MAPbBr_3)_x$ fully avoids a structural transformation.[173]

It is difficult to determine the influence of the mixing on the properties of the resulting solid-state solution. It could be shown that for binary mixtures the expansion of the lattice parameter and bandgap follow the stoichiometric composition in a nearly linear fashion, with only a small parabolic contribution.[173] But for more complex mixtures

Table 1.2: Listed values of ionic radii R_{ion} and tolerance factors t as well as dipole moment μ_{dp} (DFT calculation) of all perovskite A-site cations used in this work. The octahedral factor for all ABI_3 compound listed below is $\mu = 0.54$.

Ion	r_{ion} [pm]	Source	t ($APbI_3$)	μ_{dp} [D]
Pb^{2+}	119	[176]	-	-
I^-	220	[176]	-	-
MA^+	217	[177]	0.91	2.176
FA^+	253	[177]	0.99	0.605
Cs^+	167	[176]	0.81	0.0
Az^+	250	[168]	0.98	2.519

such as the currently used multi-halide and multi-cation mixtures, it is challanging to predict their properties. However, a common motive that occurs when increasing the number of constituents is that the stability and reproducibility improve, alongside the J_{SC} and FF, which often show a large statistical spread.[87, 88]

Generally speaking, the stability and thermal decomposition threshold for hybrid perovskites with organic cations is considerably lower than conventional inorganic semiconductors with $\sim$ 300 °C in bulk and $\sim$ 150 °C in thin films, and is further decreased under photo-excitation.[178] An approach to improve stability of HOIP is to (partially) replace the weakest link in the chain. Regarding the $MAPbI_3$ the weak link in the stability chain is the MA^+,[138, 179] which has a relatively high vapour pressure.[91] Its sublimation, either as CH_3NH_2 or CH_3I and NH_3,[179] is therefore a major driving force in the decomposition process. Mixing with other ionic species is likely to entropically stabilise the perovskite, in the same way that salt lowers the boiling temperature of water. However, the replacement with an inorganic cation would increase stability more dramatically. For example, the $CsPbI_3$ perovskite remains stable up to its melting point at 460 °C.[180, 88] However, similar to the $FAPbI_3$, it transforms into the δ-phase at room temperature and therefore is not an eligible PV material in its pure form.[181] Ionic mixtures are a common motive to stabilise the perovskite phase as a solid-state solution, *e.g.* the CsFA ($Cs_xFA_{1-x}PbI_3$).[182, 183, 184, 185] However, the CsMA ($Cs_xMA_{1-x}PbI_3$) does not form such solid-state solutions (as discussed later in this work),[186] even thought the triple and quadruple solutions CsFAMA and RbCsFAMA are stable.[87, 88] Considering the range of publications across a wide range of Cs^+-containing HOIP compositions, it seems surprising that only one publication deals with the Cs-MA mixture. Therefore, the Cs-MA mixture will be covered in more depth in this work (chapter 4).

1.8 Objectives of research

Despite the rapid development of PSC, it still has to overcome some shortcomings in terms of stability and a possible environmental toxicity (*e.g.* Pb^{2+} leakage), before it can be commercialised as a widely available PV product.[187, 188] The latter will not be addressed in this thesis, but the former forms the focus of this thesis: The improvement of the stability of PSC and the understanding of the underlying mechanisms influencing stability. The ultimate aim is to facilitate a rapid commercialisation of HOIPs as a photovoltaic material that can provide cheap and abundant energy, as outlined by the underlying funding body (DESTINY ITN, FP7). Most commercial technologies, *e.g.* cadmium telluride CdTe, copper indium gallium diselenide CIGS, amorphous Si (a:Si), polycrystalline Si (poly-Si) and monocrystalline silicon (mono-Si), have an energy payback time (EPBT) of about one to four years (see tab. 1.3).[189] This means that they need to operate for this time until they become truly renewable. Dye-sensitised solar cells (DSSC) however have an approximate EPBT of 0.8 years, which makes them a promising and cheap alternative to conventional PV systems.[190]

In 2013, when the DESTINY ITN (underlying funding body to this thesis) started, PSC arose as a new technology, which would quickly outperform DSSC in terms of efficiency and commercial interest. The EPBT of PSC is estimated to be around $0.2-0.3$ yrs,[191] which is a fraction of the estimated DSSC's EPBT. Moreover, the surge of efficiencies awoke a momentous research interest in this technology. The resulting amount of publications rose from only two in 2012[96, 192] (excluding two further papers about $CsSnI_3$[193, 194], one about $MAPbI_3$[195] and one about $(CH_3CH_2NH_3)PbI_3$[196] because they do not use the pattern '*perovskite solar*' in their title) to 25 in 2013 and reached 2083 publications in 2016 (source: *SciFinder*, accessed 27^{th} of December, 2016, see fig. 1-5 right y axis). Alongside, the interest in 'perovskite solar cell' on the web search engine *Google* rose sharply. Unfortunately no absolute numbers are available,

Table 1.3: Energy payback time (EPBT) for different PV technologies. The listed efficiency values refer to the average lifetime efficiency. If the source evaluates several types of the same PV technology, the average is taken.

Material	Efficiency [%]	EPBT	Source
mono-Si	13.00	4.6 ± 2.3	[189]
poly-Si	12.30	3.3 ± 1.4	[189]
a:Si	6.30	2.5 ± 1.0	[189]
CdTe	10.90	1.3 ± 0.8	[189]
CIGS	11.50	2.0 ± 0.9	[189]
DSSC	8.00	0.8	[190]
PSC	10.05	0.23 ± 0.05	[191]

only relative search interest of two or more key words, which is displayed in figure 1-5 left y axis. Until 2011 almost no web search interest was existent. In 2012 a slight interest awoke as the baseline rose to about 5 % of the current web search interest. Only in mid-2013 the interest started to rise sharply, which is probably caused by one of the major conferences in the field of hybrid and organic PV happening in May that year (HOPV13) and the announcement of a new record efficiency in the NREL chart, which was at that time attributed to a '*perovskite pigment*' as part of a DSSC,[21] and was only later on labelled separately on the NREL chart. Simultaneously the the web search popularity of 'dye solar cell' dropped and was surpassed by PSC in late-2013. In general, the chart shows that the web search interest preceded the trend in publications, most likely because publications take significantly longer to process. The former seems to start levelling off in 2016, which suggests that the amount of publications might stop growing for the following years and that PSC are finally settling within their technology hype cycle.

In order to fulfil the aim of this PhD research and improve the stability of hybrid perovskite materials, different chemical modifications are tested in order to improve water-resistance, which is a major cause of degradation for this material.[197, 187] Furthermore, perovskites represent a relatively new and under-explored class of photovoltaic material, which makes it necessary to investigate its fundamental structural properties in order to understand their macroscopic response and factors that influence stability. Finally, the novelty of HOIPs as a PV material makes it necessary to develop a fabrication routine for perovskite solar cells and investigate processing parameters that influence the cell performance. In summary the objectives of this thesis can be itemised as following:

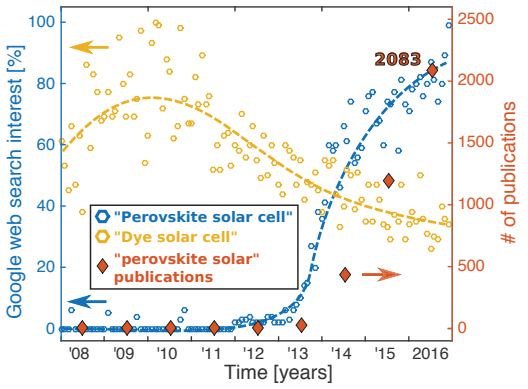

Figure 1-5: Development of the popularity of perovskite solar cells: The blue and yellow data show Google web search interest for 'perovskite solar cell' and 'dye solar cell', respectively (left y axis, source *Google Trends*). Red diamonds show number of publications for 'perovskite solar' per year (right y axis, source *SciFinder*, accessed 27^{th} of December, 2016).

(a) Optimisation of processing parameters that influence the perovskite thin-film formation regarding the development of a solar cells fabrication routine

(b) Development of new perovskite materials with an enhanced stability, specifically against water-induced degradation

(c) Analysis of underlying structural motives of organic-inorganic hybrid perovskites regarding their macroscopic response and stability

1.9 Bibliography

[1] D. Weber, "CH3NH3PbX3, a Pb(II)-System with Cubic Perovskite Structure," *Zeitschrift für Naturforschung*, vol. 33b, pp. 1443–1445, 1978.

[2] B. S. Ryden, *Introduction to cosmology*. Addison-Wesley, 2003.

[3] C. L. Bennett, D. Larson, J. L. Weiland, N. Jarosik, G. Hinshaw, N. Odegard, R. S. Hill, B. Gold, M. Halpern, E. Komatsu, M. R. Nolta, L. Page, N. Spergel, E. Wollack, J. Dunkley, A. Kogut, M. Limon, S. S. Meyer, E. L. Wright, K. M. Smith, D. N. Spergel, and G. S. Tucker, "Nine-year Wilkinson Microwave Anisotropy Probe (WMAP) observations: final maps and results," *The Astrophysical Journal Supplement Series*, vol. 208, pp. 1 – 177, 2012.

[4] P. Ade, N. Aghanim, M. Arnaud, M. Ashdown, J. Aumont, P. Bielewicz, D. Harrison, and G. Helou, "Planck 2013 results. I. Overview of products and scientific results," *Astronomy & Astrophysics manuscript*, 2013.

[5] G. Boyle and O. University, *Renewable Energy*. Oxford University Press, 2004.

[6] D. D. Clayton, *Principles of Stellar Evolution and Nucleosynthesis*. University of Chicago Press, 1968.

[7] U.S. Census Bureau, "World POPClock Projection." http://www.census.gov/popclock/ [Online; accessed: 10-Feb-2017], 2016.

[8] N. S. Lewis and D. G. Nocera, "Powering the planet: Chemical challenges in solar energy utilization," *PNAS*, vol. 104, no. 42, pp. 15729–15735, 2006.

[9] International Energy Agency, "Key World Energy Statistics," tech. rep., 2016.

[10] B. plc, "Statistical review of world energy." http://www.bp.com/statisticalreview/ [Online; accessed: 14-September-2016], 2015.

[11] B. Obama, "The irreversible momentum of clean energy," *Science*, vol. 355, no. 6321, pp. 126 – 129, 2017.

[12] Institute of Marine and Coastal Science, "Earth Radiation Budget." http://marine.rutgers.edu/cool/education/class/yuri/erb.html [Online; accessed: 14-Aug-2014], 2014.

[13] NASA Earth Observatory, "Climate and Earth's Energy Budget." http://earthobservatory.nasa.gov/Features/EnergyBalance/ [Online; accessed: 01-February-2015], 2009.

[14] T. C. Sum and N. Mathews, "Advancements in Perovskite Solar Cells: Photophysics behind the Photovoltaics," *Energy & Environmental Science*, vol. 7, pp. 2518 – 2534, 2014.

[15] R. Fu, D. Chung, T. Lowder, D. Feldman, K. Ardani, and R. Margolis, "U.S. Solar Photovoltaic System Cost Benchmark: Q1 2016," Tech. Rep. September, 2016.

[16] E. Becquerel, "Memoire sur les effets electriques produits sous le influence des rayons solaires," *Comptes Rendus*, vol. 9, pp. 561–567, 1839.

[17] C. E. Fritts, "On a New Form of Selenium Photocell," *American Journal of Science*, vol. 26, p. 465, 1883.

[18] A. Einstein, "On a Heuristic Viewpoint Concerning the Production and Transformation of Light," *Annalen der Physik*, vol. 17, no. 6, pp. 132–148, 1905.

[19] R. S. Ohl, "Light-Sensitive Electric Device," *U.S. Patent*, vol. 2, pp. 402,602, 1941.

[20] D. M. Chapin, C. S. Fuller, and G. L. Pearson, "A new silicon p-n junction photocell for converting solar radiation into electrical power [3]," *Journal of Applied Physics*, vol. 25, no. 5, pp. 676–677, 1954.

[21] NREL, "Research Cell Efficiency Records." http://www.nrel.gov/ncpv/ [Online; accessed: 17-December-2016], 2016.

[22] W. Shockley and H. J. Queisser, "Detailed balance limit of efficiency of p-n junction solar cells," *Journal of Applied Physics*, vol. 32, no. 3, pp. 510–519, 1961.

[23] I. C. Smith, E. T. Hoke, D. Solis-ibarra, M. D. Mcgehee, and H. I. Karunadasa, "A Layered Hybrid Perovskite Solar-Cell Absorber with Enhanced Moisture Stability," *Angewandte Chemie International Edition*, vol. 53, pp. 11232–11235, 2014.

[24] J. Czochralski, "Ein neues Verfahren zur Messung der Kristallisationsgeschwindigheit der Metalle," *Zeitschrift Fur Physikalische Chemie*, vol. 92, pp. 219–221, 1918.

[25] H. R. Wenk and A. Bulakh, *Minerals: Their Constitution and Origin*. Cambridge University Press, 2004.

[26] H. L. Wells, "Uber die Caesium- und Kalium-Bleihalogenide," *Zeitschrift fur anorganische Chemie*, vol. 3, no. 1, pp. 195–210, 1893.

[27] C. K. Moller, "Crystal Structure and Photoconductivity of Caesium Plumbohalides," *Nature*, vol. 182, p. 1436, 1958.

[28] Wikipedia, "Lev Perovski." https://en.wikipedia.org/wiki/Lev_Perovski [Online; accessed: 27-December-2016], 2016.

[29] D. B. Mitzi, C. Feild, W. Harrison, and A. Guloy, "Conducting tin halides with a layered organic-based perovskite structure," *Letters to Nature*, vol. 369, no. 9, pp. 467–469, 1994.

[30] D. B. Mitzi, S. Wang, C. A. Feild, C. A. Chess, and A. M. Guloy, "Conducting Layered Organic-inorganic Halides Containing 110-Oriented Perovskite Sheets.," *Science*, vol. 267, no. 5203, pp. 1473–1476, 1995.

[31] D. B. Mitzi and C. Feild, "Transport, Optical and Magnetic Properties of the Conducting Halide Perovskite CH3NH3SnI3," *Journal of Solid State Chemistry*, vol. 114, pp. 159–163, 1995.

[32] K. Liang, D. B. Mitzi, and M. Prikas, "Synthesis and Characterization of Organic - Inorganic Perovskite Thin Films Prepared Using a Versatile Two-Step Dipping Technique," *Chemistry of materials*, vol. 4756, no. 8, pp. 403–411, 1998.

[33] D. B. Mitzi, "Templating and structural engineering in organic-inorganic perovskites," *Journal of the Chemical Society, Dalton Transactions*, vol. 1, pp. 1–12, 2001.

[34] D. B. Mitzi, K. Chondroudis, and C. R. Kagan, "Organic-inorganic electronics," *IBM Journal of Research and Development*, vol. 45, no. 1, pp. 29–45, 2001.

[35] D. B. Mitzi, "Solution-processed inorganic semiconductors," *Journal of Materials Chemistry*, vol. 14, pp. 2355–2365, 2004.

[36] A. P. Ramirez, "Colossal magnetoresistance," *Journal of Physics: Condensed Matter*, vol. 9, no. 39, p. 8171, 1997.

[37] R. Cohen, "Origin of ferroelectricity in perovskite oxides," *Letters to Nature*, vol. 358, pp. 136–138, 1992.

[38] M. Antonietta Loi and J. C. Hummelen, "Hybrid solar cells: Perovskites under the Sun.," *Nature Materials*, vol. 12, no. 12, pp. 1087–1089, 2013.

[39] Y. He and G. Galli, "Perovskites for Solar Thermoelectric Applications: A First Principle Study of CH3NH3AI3 (A = Pb and Sn)," *Chemistry of materials*, vol. 26, pp. 5394–5400, 2014.

[40] A. McDaniel, A. Ambrosini, E. Coker, J. Miller, W. Chueh, R. O'Hayre, and J. Tong, "Nonstoichiometric Perovskite Oxides for Solar Thermochemical H2 and CO Production," *Energy Procedia*, vol. 49, pp. 2009–2018, 2014.

[41] A. Kojima, K. Teshima, Y. Shirai, and T. Miyasaka, "Organometal halide perovskites as visible-light sensitizers for photovoltaic cells.," *Journal of the American Chemical Society*, vol. 131, pp. 6050–6051, may 2009.

[42] F. Brivio, K. T. Butler, A. Walsh, and M. van Schilfgaarde, "Relativistic quasiparticle self-consistent electronic structure of hybrid halide perovskite photovoltaic absorbers," *Physical Review B*, vol. 89, no. 15, p. 155204, 2014.

[43] J. Even, "Pedestrian Guide to Symmetry Properties of the Reference Cubic Structure of 3D All-Inorganic and Hybrid Perovskites," *Journal of Physical Chemistry Letters*, vol. 6, no. 12, pp. 2238–2242, 2015.

[44] Q. Dong, Y. Fang, Y. Shao, P. Mulligan, J. Qiu, L. Cao, and J. Huang, "Electron-hole diffusion lengths >175 um in solution-grown CH3NH3PbI3 single crystals," *Science*, vol. 347, no. 6225, pp. 967–970, 2015.

[45] F. Hao, C. C. Stoumpos, Z. Liu, R. P. H. Chang, and M. G. Kanatzidis, "Hole Conductor-Free Solar Cells with Steady Power Conversion," *Journal of the American Chemical Society*, vol. 136, pp. 16411–16419, 2014.

[46] L.-y. Huang and W. R. L. Lambrecht, "Electronic band structure, phonons, and exciton binding energies of halide perovskites CsSnCl3, CsSnBr3, and CsSnI3," *Physical Review B*, vol. 88, no. 16, p. 165203, 2013.

[47] J. S. Manser and P. V. Kamat, "Band filling with free charge carriers in organometal halide perovskites," *Nature Photonics*, vol. 8, no. 9, pp. 737–743, 2014.

[48] K. G. Stamplecoskie, S. Manser, and P. V. Kamat, "Dual nature of the excited state in organic - inorganic lead halide perovskites," *Energy & Environmental Science*, vol. 8, pp. 208–215, 2015.

[49] C. Wehrenfennig, M. Liu, H. J. Snaith, M. B. Johnston, and L. M. Herz, "Charge-carrier dynamics in vapour-deposited films of the organolead halide perovskite CH3NH3PbI3-xClx," *Energy & Environmental Science*, vol. 7, no. 7, p. 2269, 2014.

[50] L. M. Pazos-Outon, M. Szumilo, R. Lamboll, J. M. Richter, M. Crespo-Quesada, M. Abdi-Jalebi, H. J. Beeson, M. Vru ini, M. Alsari, H. J. Snaith, B. Ehrler, R. H. Friend, and F. Deschler, "Photon recycling in lead iodide perovskite solar cells," *Science*, vol. 351, no. 6280, pp. 1430–1433, 2016.

[51] C. Wehrenfennig, M. Liu, H. J. Snaith, M. B. Johnston, and L. M. Herz, "Homogeneous Emission Line Broadening in the Organo Lead Halide Perovskite CH3NH3Pb3-xClx," *The Journal of Physical Chemistry Letters*, vol. 5, pp. 1300–1306, 2014.

[52] M. Green, "The Path to 25% Silicon Solar Cell Efficiency: History of Silicon Cell Evolution," *Progress in Photovoltaics: Research and Applications*, vol. 17, pp. 183–189, 2009.

[53] J. Mandelkorn, C. McAfee, J. Kesperis, L. Schwartz, and W. Pharo, "Fabrication and Characteristics of Phosphorous-Diffused Silicon Solar Cells," *Journal of the Electrochemical Society*, vol. 109, no. 4, p. 313, 1962.

[54] J.-H. Im, C.-R. Lee, J.-W. Lee, S.-W. Park, and N.-G. Park, "6.5% Efficient Perovskite Quantum-Dot-Sensitized Solar Cell.," *Nanoscale*, vol. 3, no. 10, pp. 4088–4093, 2011.

[55] P. V. Kamat, "Evolution of Perovskite Photovoltaics and Decrease in Energy Payback Time," *The Journal of Physical Chemistry Letters*, vol. 4, no. 21, pp. 3733–3734, 2013.

[56] J. Burschka, N. Pellet, S.-J. Moon, R. Humphry-Baker, P. Gao, M. K. Nazeeruddin, and M. Grätzel, "Sequential deposition as a route to high-performance perovskite-sensitized solar cells.," *Nature*, vol. 499, no. 7458, pp. 316–320, 2013.

[57] M. Liu, M. B. Johnston, and H. J. Snaith, "Efficient planar heterojunction perovskite solar cells by vapour deposition.," *Nature*, vol. 501, no. 7467, pp. 395–398, 2013.

[58] M. Era, T. Hattori, T. Taira, and T. Tsutsui, "Self-organized growth of PbI-based layered perovskite quantum well by dual-source vapor deposition," *Chemistry of Materials*, vol. 4756, no. 16, pp. 8–10, 1997.

[59] C. Wehrenfennig, M. Liu, H. J. Snaith, M. B. Johnston, and L. M. Herz, "Charge carrier recombination channels in the low-temperature phase of organic-inorganic lead halide perovskite thin films," *APL Materials*, vol. 2, p. 081513, 2014.

[60] V. Gonzalez-Pedro, E. J. Juarez-Perez, W.-S. Arsyad, E. M. Barea, F. Fabregat-Santiago, I. Mora-Sero, and J. Bisquert, "General Working Principles of CH3NH3PbX3 Perovskite Solar Cells.," *Nano Letters*, vol. 14, no. 2, pp. 888–893, 2014.

[61] J. Teuscher, A. Ulianov, O. Muntener, M. Gratzel, and N. Tetreault, "Control and Study of the Stoichiometry in Evaporated Perovskite Solar Cells," *ChemSusChem*, vol. 8, no. 22, pp. 3847–3852, 2015.

[62] A. M. Soufiani, F. Huang, P. Reece, R. Sheng, A. Ho-Baillie, and M. A. Green, "Polaronic exciton binding energy in iodide and bromide organic-inorganic lead halide perovskites," *Applied Physics Letters*, vol. 107, p. 231902, 2015.

[63] P. Pistor, J. Borchert, W. Franzel, R. Csuk, and R. Scheer, "Monitoring the phase formation of coevaporated lead halide perovskite thin films by in situ x-ray diffraction," *Journal of Physical Chemistry Letters*, vol. 5, no. 19, pp. 3308–3312, 2014.

[64] D. H. Cao, C. C. Stoumpos, C. D. Malliakas, M. J. Katz, O. K. Farha, J. T. Hupp, and M. G. Kanatzidis, "Remnant PbI2, an unforeseen necessity in high-efficiency hybrid perovskite-based solar cells?," *APL Materials*, vol. 2, no. 9, p. 091101, 2014.

[65] Y. C. Kim, N. J. Jeon, J. H. Noh, W. S. Yang, J. Seo, J. S. Yun, A. Ho-Baillie, S. Huang, M. A. Green, J. Seidel, T. K. Ahn, and S. I. Seok, "Beneficial Effects of PbI2 Incorporated in Organo-Lead Halide Perovskite Solar Cells," *Advanced Energy Materials*, vol. 6, p. 1502104, 2016.

[66] T. J. Jacobsson, J.-P. Correa-Baena, E. Halvani Anaraki, B. Philippe, S. D. Stranks, M. E. F. Bouduban, W. Tress, K. Schenk, J. Teuscher, J.-E. Moser, H. Rensmo, and A. Hagfeldt, "Unreacted PbI2 as a Double-Edged Sword for Enhancing the Performance of Perovskite Solar Cells," *Journal of the American Chemical Society*, vol. 138, no. 32, pp. 10331–10343, 2016.

[67] C. Roldan Carmona, P. Gratia, I. Zimmermann, G. Grancini, P. Gao, M. Gratzel, and N. Mohammad K., "High efficiency methylammonium lead triiodide perovskite solar cells: the relevance of non-stoichiometric precursors," *Energy & Environmental Science*, vol. 8, pp. 3550–3556, 2015.

[68] S. Wang, W. Dong, X. Fang, Q. Zhang, S. Zhou, Z. Deng, R. Tao, J. Shao, R. Xia, C. Song, L. Hu, and J. Zhu, "The credible evidence for passivation effect of remnant PbI2 in CH3NH3PbI3 films for improving the performance of perovskite solar cells," *Nanoscale*, vol. 8, pp. 6600–6608, 2016.

[69] D. Shen, X. Yu, X. Cai, M. Peng, Y. Ma, X. Su, L. Xiao, and D. Zou, "Understanding the solvent-assisted crystallization mechanism inherent in efficient organic-inorganic halide perovskite solar cells," *Journal of Materials Chemistry A*, vol. 2, pp. 20454–20461, 2014.

[70] G. E. Eperon, V. M. Burlakov, P. Docampo, A. Goriely, and H. J. Snaith, "Morphological Control for High Performance, Solution-Processed Planar Heterojunction Perovskite Solar Cells," *Advanced Functional Materials*, pp. 151–157, 2013.

[71] Q. Chen, H. Zhou, T.-B. Song, S. Luo, Z. Hong, H.-S. Duan, L. Dou, Y. Liu, and Y. Yang, "Controllable self-induced passivation of hybrid lead iodide perovskites toward high performance solar cells.," *Nano Letters*, vol. 14, no. 7, pp. 4158–4163, 2014.

[72] S. Pathak, A. Sepe, A. Sadhanala, F. Deschler, A. Haghighirad, N. Sakai, K. C. Goedel, S. D. Stranks, N. Noel, M. Price, S. Hu, N. A. Hawkins, R. H. Friend, U. Steiner, and H. J. Snaith, "Atmospheric Influence upon Crystallization and Electronic Disorder and Its Impact on the Photophysical Properties of Organic-Inorganic Perovskite Solar Cells," *ACS Nano*, vol. 9, no. 3, pp. 2311–2320, 2015.

[73] C. Muller, T. Glaser, M. Plogmeyer, M. Sendner, S. Doring, A. A. Bakulin, C. Brzuska, R. Scheer, M. S. Pshenichnikov, W. Kowalsky, A. Pucci, and R. Lovrincic, "Water Infiltration in Methylammonium Lead Iodide Perovskite: Fast and Inconspicuous," *Chemistry of Materials*, vol. 27, no. 22, pp. 7835–7841, 2015.

[74] G. E. Eperon, S. N. Habisreutinger, T. Leijtens, B. J. Bruijnaers, J. J. van Franeker, D. W. DeQuilettes, S. Pathak, R. J. Sutton, G. Grancini, D. S. Ginger, R. A. J. Janssen, A. Petrozza, and H. J. Snaith, "The Importance of Moisture in Hybrid Lead Halide Perovskite Thin Film Fabrication," *ACS Nano*, vol. 9, no. 9, pp. 9380–9393, 2015.

[75] A. M. A. Leguy, Y. Hu, M. Campoy-Quiles, M. I. Alonso, O. J. Weber, P. Azarhoosh, M. van Schilfgaarde, M. T. Weller, T. Bein, J. Nelson, P. Docampo, and P. R. F. Barnes, "Reversible Hydration of CH3NH3PbI3 in Films, Single Crystals, and Solar Cells," *Chemistry of Materials*, vol. 27, no. 9, pp. 3397–3407, 2015.

[76] D. Li, S. A. Bretschneider, V. W. Bergmann, I. M. Hermes, J. Mars, A. Klasen, H. Lu, W. Tremel, M. Mezger, H.-J. Butt, S. A. L. Weber, and R. Berger,

"Humidity-Induced Grain Boundaries in MAPbI3 Perovskite Films," *The Journal of Physical Chemistry C*, vol. 120, no. 12, pp. 6363–6368, 2016.

[77] M. K. Gangishetty, R. W. J. Scott, and T. L. Kelly, "Effect of Relative Humidity on Crystal Growth, Device Performance and Hysteresis in Planar Heterojunction Perovskite Solar Cells," *Nanoscale*, vol. 8, pp. 6300–6307, 2016.

[78] W. Zhang, M. Saliba, D. T. Moore, S. K. Pathak, M. T. Hörantner, T. Stergiopoulos, S. D. Stranks, G. E. Eperon, J. A. Alexander-Webber, A. Abate, A. Sadhanala, S. Yao, Y. Chen, R. H. Friend, L. A. Estroff, U. Wiesner, and H. J. Snaith, "Ultrasmooth organic-inorganic perovskite thin-film formation and crystallization for efficient planar heterojunction solar cells," *Nature Communications*, vol. 6, p. 6142, 2015.

[79] Z. Zhou, Z. Wang, Y. Zhou, S. Pang, D. Wang, H. Xu, Z. Liu, N. P. Padture, and G. Cui, "Methylamine-Gas Induced Defect-Healing Behavior of CH3NH3PbI3 Thin Films for Perovskite Solar Cells," *Angewandte Chemie International Edition*, vol. 54, no. 33, pp. 9705–9709, 2015.

[80] L. Gouda, R. Gottesman, S. Tirosh, E. Haltzi, J. Hu, A. Ginsburg, D. A. Keller, Y. Bouhadana, and A. Zaban, "Vapor and Healing Treatment for CH3NH3PbI3-xClx Films toward Large-Area Perovskite Solar cells," *Nanoscale*, vol. 8, pp. 6386–6392, 2016.

[81] N. Jeon, J. Noh, Y. Kim, W. Yang, S. Ryu, and S. Seok, "Solvent engineering for high-performance inorganic-organic hybrid perovskite solar cells," *Nature Materials*, vol. 13, pp. 897–903, 2014.

[82] N. J. Jeon, J. H. Noh, W. S. Yang, Y. C. Kim, S. Ryu, J. Seo, and S. I. Seok, "Compositional engineering of perovskite materials for high-performance solar cells," *Nature*, vol. 517, no. 7535, pp. 476–480, 2015.

[83] W. S. Yang, J. H. Noh, N. J. Jeon, Y. C. Kim, S. Ryu, J. Seo, and S. I. Seok, "High-performance photovoltaic perovskite layers fabricated through intramolecular exchange," *Science*, vol. 348, pp. 1234–1237, may 2015.

[84] N. Ahn, D.-Y. Son, I.-H. Jang, S. M. Kang, M. Choi, and N.-G. Park, "Highly Reproducible Perovskite Solar Cells with Average Efficiency of 18.3% and Best Efficiency of 19.7% Fabricated via Lewis Base Adduct of Lead(II) Iodide," *Journal of the American Chemical Society*, vol. 137, no. 27, pp. 8696–8699, 2015.

[85] J. H. Noh, S. H. Im, J. H. Heo, T. N. Mandal, and S. I. Seok, "Chemical management for colorful, efficient, and stable inorganic-organic hybrid nanostructured solar cells.," *Nano Letters*, vol. 13, no. 4, pp. 1764–1769, 2013.

[86] V. M. Goldschmidt, "Krystallbau und chemische Zusammensetzung," *Berichte der Deutschen Chemischen Gesellschaft*, vol. 60, no. 5, pp. 1263–1296, 1927.

[87] M. Saliba, T. Matsui, J.-Y. Seo, K. Domanski, J.-P. Correa-Baena, N. Mohammad K., S. M. Zakeeruddin, W. Tress, A. Abate, A. Hagfeldt, and M. Grätzel, "Cesium-containing Triple Cation Perovskite Solar Cells: Improved Stability, Reproducibility and High Efficiency," *Energy & Environmental Science*, vol. 9, pp. 1989–1997, 2016.

[88] M. Saliba, T. Matsui, K. Domanski, J.-Y. Seo, A. Ummadisingu, S. M. Zakeeruddin, J.-P. Correa-Baena, W. R. Tress, A. Abate, A. Hagfeldt, and M. Grätzel, "Incorporation of rubidium cations into perovskite solar cells improves photovoltaic performance," *Science*, vol. 354, no. 6309, pp. 206–209, 2016.

[89] J. Schoonman, "Organic-inorganic lead halide perovskite solar cell materials: A possible stability problem," *Chemical Physics Letters*, vol. 619, pp. 193–195, 2015.

[90] P. Gratia, G. Grancini, J.-N. Audinot, X. Jeanbourquin, E. Mosconi, I. Zimmermann, D. Dowsett, Y. Lee, M. Grätzel, F. De Angelis, K. Sivula, T. Wirtz, and M. K. Nazeeruddin, "Intrinsic Halide Segregation at Nanometer Scale Determines the High-Efficiency of mixed cation/mixed halide Perovskite Solar Cells.," *Journal of the American Chemical Society*, vol. 138, no. 49, pp. 15821–15824, 2016.

[91] B. Conings, J. Drijkoningen, N. Gauquelin, A. Babayigit, J. D'Haen, L. D'Olieslaeger, A. Ethirajan, J. Verbeeck, J. Manca, E. Mosconi, F. D. Angelis, and H.-G. Boyen, "Intrinsic Thermal Instability of Methylammonium Lead Trihalide Perovskite," *Advanced Energy Materials*, p. 1500477, 2015.

[92] Y.-Y. Zhang, S. Chen, P. Xu, H. Xiang, X.-G. Gong, A. Walsh, and S.-H. Wei, "Intrinsic Instability of the Hybrid Halide Perovskite Semiconductor CH3NH3PbI3," *arXiv preprint*, p. 1506.01301, 2015.

[93] A. Pockett, G. E. Eperon, T. Peltola, H. J. Snaith, A. Walker, L. M. Peter, and P. J. Cameron, "Characterization of Planar Lead Halide Perovskite Solar Cells by Impedance Spectroscopy, Open-Circuit Photovoltage Decay, and Intensity-Modulated Photovoltage/Photocurrent Spectroscopy," *Journal of Physical Chemistry C*, vol. 119, pp. 3456–3465, 2015.

[94] Q. Chen, H. Zhou, Z. Hong, S. Luo, H.-S. Duan, H.-H. Wang, Y. Liu, G. Li, and Y. Yang, "Planar heterojunction perovskite solar cells via vapor-assisted solution process.," *Journal of the American Chemical Society*, vol. 136, no. 2, pp. 622–625, 2014.

[95] S. Casaluci, L. Cina, A. Pockett, P. S. Kubiak, R. G. Niemann, A. Reale, A. Di Carlo, and P. J. Cameron, "A Simple Approach for the Fabrication of Perovskite Solar Cells in Air," *Journal of Power Sources*, vol. 297, pp. 504–510, 2015.

[96] M. M. Lee, J. Teuscher, T. Miyasaka, T. N. Murakami, and H. J. Snaith, "Efficient hybrid solar cells based on meso-superstructured organometal halide perovskites," *Science*, vol. 338, no. 6107, pp. 643–647, 2012.

[97] H. Snaith, A. Abate, and J. Ball, "Anomalous Hysteresis in Perovskite Solar Cells," *Journal of Physical Chemistry Letters*, vol. 5, pp. 1511–1515, 2014.

[98] B. C. O'Regan, P. R. F. Barnes, X. Li, C. Law, E. Palomares, and J. M. Marin-Beloqui, "Optoelectronic studies of methylammonium lead iodide perovskite solar cells with mesoporous TiO2: Separation of electronic and chemical charge storage, understanding two recombination lifetimes, and the evolution of band offsets during J - V hy," *Journal of the American Chemical Society*, vol. 137, no. 15, pp. 5087–5099, 2015.

[99] Y. Kutes, L. Ye, Y. Zhou, and S. Pang, "Direct Observation of Ferroelectric Domains in Solution-Processed CH3NH3PbI3 Perovskite Thin Films," *The Journal of Physical Chemistry Letters*, vol. 5, pp. 3335–3339, 2014.

[100] J. M. Frost, K. T. Butler, and A. Walsh, "Molecular ferroelectric contributions to anomalous hysteresis in hybrid perovskite solar cells," *APL Materials*, vol. 2, no. 8, p. 081506, 2014.

[101] E. T. Hoke, D. J. Slotcavage, E. R. Dohner, A. R. Bowring, H. I. Karunadasa, and M. D. McGehee, "Reversible photo-induced trap formation in mixed-halide hybrid perovskites for photovoltaics," *Chemical Science*, vol. 6, pp. 613–617, 2015.

[102] H.-S. Kim, S. K. Kim, B. J. Kim, K.-S. Shin, M. K. Gupta, H. S. Jung, S.-W. Kim, and N.-G. Park, "Ferroelectric Polarization in CH3NH3PbI3 Perovskite," *Journal of Physical Chemistry Letters*, vol. 6, pp. 1729–1735, 2015.

[103] A. M. A. Leguy, J. M. Frost, A. P. McMahon, V. G. Sakai, W. Kochelmann, C. Law, X. Li, F. Foglia, A. Walsh, B. C. O'Regan, J. Nelson, J. T. Cabral, and P. R. F. Barnes, "The dynamics of methylammonium ions in hybrid organic-inorganic perovskite solar cells," *Nature Communications*, vol. 6, p. 7124, may 2015.

[104] Y. Yuan and J. Huang, "Ion Migration in Organometal Trihalide Perovskite and Its Impact on Photovoltaic Efficiency and Stability," *Accounts of Chemical Research*, vol. 49, no. 2, pp. 286–293, 2016.

[105] G. Richardson, S. E. J. O'Kane, R. G. Niemann, T. A. Peltola, J. M. Foster, P. J. Cameron, and A. B.Walker, "Can slow-moving ions explain hysteresis in the current-voltage curves of perovskite solar cells?," *Energy & Environmental Science*, vol. 9, pp. 1476–1485, 2016.

[106] J. MIZUSAKI, K. ARAI, and K. FUEKI, "Ionic Conduction of the Perovskite-type halides," *Solid State Ionics*, vol. 11, pp. 203–211, 1983.

[107] Z. Xiao, Y. Yuan, Y. Shao, Q. Wang, Q. Dong, C. Bi, P. Sharma, A. Gruverman, and J. Huang, "Giant switchable photovoltaic effect in organometal trihalide perovskite devices," *Nature materials*, vol. 14, pp. 193–8, 2015.

[108] I. Levine, P. K. Nayak, J. Tse, W. Wang, N. Sakai, S. Van Reenen, T. M. Brenner, S. Mukhopadhyay, H. J. Snaith, G. Hodes, D. Cahen, and S. V. Reenen, "Interface-Dependent Ion Migration/Accumulation Controls Hysteresis in MAPbI 3 Solar Cells," *Journal of Physical Chemistry C*, vol. 120, no. 30, pp. 16399–16411, 2016.

[109] D. Bryant, S. Wheeler, B. C. O'Regan, T. Watson, P. R. Barnes, D. a. Worsley, and J. Durrant, "Observable Hysteresis at Low Temperature in Hysteresis Free Organic-Inorganic Lead Halide Perovskite Solar Cells," *The Journal of Physical Chemistry Letters*, p. 150721102758007, 2015.

[110] W. Tress, N. Marinova, T. Moehl, S. M. Zakeeruddin, M. K. Nazeeruddin, and M. Grätzel, "Understanding the rate-dependent J-V hysteresis, slow time component, and aging in CH3NH3PbI3 perovskite solar cells: the role of a compensated electric field," *Energy & Environmental Science*, vol. 8, no. 3, pp. 995–1004, 2015.

[111] C. Eames, J. M. Frost, P. R. F. Barnes, B. C. O'Regan, A. Walsh, and M. S. Islam, "Ionic transport in hybrid lead iodide perovskite solar cells," *Nature Communications*, vol. 6, p. 7497, 2015.

[112] A. Pockett, G. Eperon, N. Sakai, H. Snaith, L. M. Peter, and P. J. Cameron, "Microseconds, milliseconds and seconds: deconvoluting the dynamic behaviour of planar perovskite solar cells," *Phys. Chem. Chem. Phys.*, vol. 19, pp. 5959 – 5970, 2017.

[113] S. O'Kane, G. Richardson, A. Pockett, R. G. Niemann, J. M. Cave, N. Sakai, G. E. Eperon, H. Snaith, J. M. Foster, P. J. Cameron, and A. Walker, "Measurement and modelling of dark current decay transients in perovskite solar cells," *J. Mater. Chem. C*, vol. 5, pp. 452–462, 2016.

[114] D. W. DeQuiletttes, W. Zhang, V. M. Burlakov, D. J. Graham, T. Leijtens, A. Osherov, H. J. Snaith, D. S. Ginger, and S. D. Stranks, "Photo-induced halide redistribution in organic - inorganic perovskite films," *Nature Communications*, vol. 7, p. 11683, 2016.

[115] M. T. Weller, O. J. Weber, P. F. Henry, A. M. D. Pumpo, and T. C. Hansen, "Complete structure and cation orientation in the perovskite photovoltaic methylammonium lead iodide between 100 and 352 K," *Chemical Communications*, vol. 51, pp. 4180–4183, 2015.

[116] H. Tuller, D. Button, and D. Uhlmann, "Fast ion transport in oxide glasses," *Journal of Non-Crystalline Solids*, vol. 40, no. 1, pp. 93–118, 1980.

[117] D. Yang, W. Ming, H. Shi, L. Zhang, and M. Du, "Fast diffusion of native defects and impurities in perovskite solar cell material," *Chemistry of Materials*, vol. 28, no. 12, pp. 4349–4357, 2016.

[118] E. Mosconi and F. De Angelis, "Mobile Ions in Organohalide Perovskites: Interplay of Electronic Structure and Dynamics," *ACS Energy Letters*, vol. 1, no. 1, pp. 182–188, 2016.

[119] C. C. Stoumpos, C. D. Malliakas, and M. G. Kanatzidis, "Semiconducting tin and lead iodide perovskites with organic cations: phase transitions, high mobilities, and near-infrared photoluminescent properties.," *Inorganic Chemistry*, vol. 52, no. 15, pp. 9019–9038, 2013.

[120] H. D. Kim, H. Ohkita, H. Benten, and S. Ito, "Photovoltaic Performance of Perovskite Solar Cells with Different Grain Sizes," *Advanced Materials*, vol. 28, no. 5, pp. 1521–4095, 2016.

[121] H. Kim and N. Park, "Parameters Affecting I-V Hysteresis of CH3NH3PbI3 Perovskite Solar Cells: Effects of Perovskite Crystal Size and Mesoporous TiO2 Layer," *Journal of Physical Chemistry Letters*, vol. 5, no. 17, pp. 2927–2934, 2014.

[122] H. Zhang, X. Qiao, Y. Shen, T. Moehl, S. M. Zakeeruddin, M. Grätzel, and M. Wang, "Photovoltaic behaviour of lead methylammonium triiodide perovskite solar cells down to 80 K," *Journal of Materials Chemistry A*, pp. 11762–11767, 2015.

[123] P. Calado, A. M. Telford, D. Bryant, X. Li, J. Nelson, C. Brian, O. Regan, and P. R. F. Barnes, "Evidence for ion migration in hybrid perovskite solar cells with minimal hysteresis," *Nature Communications*, vol. 7, p. 13831, 2016.

[124] A. Poglitsch and D. Weber, "Dynamic disorder in methylammoniumtrihalogenoplumbates (II) observed by millimeter-wave spectroscopy," *The Journal of Chemical Physics*, vol. 87, no. ii, p. 6373, 1987.

[125] R. Wasylishen, O. Knop, and J. Macdonald, "Cation rotation in methylammonium lead halides," *Solid State Communications*, vol. 56, no. 7, pp. 581–582, 1985.

[126] O. Knop, R. E. Wasylishen, M. A. White, T. S. Cameron, and M. J. M. V. Oort, "(X = Cl, Br, I) perovskites: cuboctahedral halide cages with isotropic cation reorientation," *Canadian Journal of Chemistry*, vol. 68, no. 3, pp. 412–422, 1990.

[127] N. Onoda-Yamamuro, T. Matsuo, and H. Suga, "Calorimetric and IR Spectroscopic Studies of Phase Transitions in Methylammonium Trihalogenoplumbates," *Journal of Physics and Chemistry of Solids*, vol. 51, no. 12, pp. 1383–1395, 1990.

[128] N. Onoda-Yamamuro, "Dielectric Study of CH3NH3PbX3 (X = Cl, Br, I)," *Journal of Physics and Chemistry of Solids*, vol. 53, no. 7, p. 935, 1992.

[129] N. Onoda-yamamuro, O. Yamamuro, T. Matsuo, and H. Suga, "p-T Phase Relations of CH3NH3PbX3 (X=Cl, Br, I) Crystals," *Journal of Physics and Chemistry of Solids*, vol. 53, no. 2, pp. 277–281, 1992.

[130] N. Onoda-Yamamuro, *Physico-chemical Study of Some Perovskite-type Methylammonium Trihalogenometallates*. PhD thesis, Osaka University, 1992.

[131] E. Mosconi, C. Quarti, T. Ivanovska, G. Ruani, and F. De Angelis, "Structural and electronic properties of organo-halide lead perovskites: a combined IR-spectroscopy

and ab initio molecular dynamics investigation.," *Physical Chemistry Chemical Physics*, vol. 16, pp. 16137–16144, 2014.

[132] C. Quarti, G. Grancini, E. Mosconi, P. Bruno, J. M. Ball, M. M. Lee, H. J. Snaith, A. Petrozza, and F. D. Angelis, "The Raman Spectrum of the CH3NH3PbI3 Hybrid Perovskite: Interplay of Theory and Experiment," *Journal of Physical Chemistry Letters*, vol. 5, pp. 279–284, 2014.

[133] C. Quarti, E. Mosconi, and F. De Angelis, "Interplay of Orientational Order and Electronic Structure in Methylammonium Lead Iodide: Implications for Solar Cells Operation," *Chemistry of Materials*, vol. 26, no. 22, pp. 6557–6569, 2014.

[134] E. Mosconi, J. M. Azpiroz, and F. De Angelis, "Ab Initio Molecular Dynamics Simulations of Methylammonium Lead Iodide Perovskite Degradation by Water," *Chemistry of Materials*, p. 4885, 2015.

[135] T. Ivanovska, C. Quarti, G. Grancini, A. Petrozza, F. De Angelis, A. Milani, and G. Ruani, "Vibrational Response of Methylammonium Lead Iodide: From Cation Dynamics to Phonon-Phonon Interactions," *ChemSusChem*, vol. 9, pp. 2994–3004, 2016.

[136] C. Quarti, E. Mosconi, J. M. Ball, V. D'Innocenzo, C. Tao, S. Pathak, H. J. Snaith, A. Petrozza, and F. De Angelis, "Structural and optical properties of methylammonium lead iodide across the tetragonal to cubic phase transition: implications for perovskite solar cells," *Energy & Environmental Science*, vol. 9, pp. 155–163, 2016.

[137] A. Walsh, "Principles of Chemical Bonding and Band Gap Engineering in Hybrid Organic-Inorganic Halide Perovskites," *Journal of Physical Chemistry C*, vol. 119, pp. 5755–5760, 2015.

[138] J. Frost, K. Butler, and F. Brivio, "Atomistic origins of high-performance in hybrid halide perovskite solar cells," *Nano Letters*, vol. 14, pp. 2584–2590, may 2014.

[139] S. Liu, F. Zheng, N. Z. Koocher, H. Takenaka, F. Wang, and A. M. Rappe, "Ferroelectric Domain Wall Induced Band Gap Reduction and Charge Separation in Organometal Halide Perovskites," *Journal of Physical Chemistry Letters*, vol. 6, pp. 693–699, 2015.

[140] A. Leguy, P. Azarhoosh, M. I. Alonso, M. Campoy-Quiles, O. J. Weber, J. Yao, D. Bryant, M. T. Weller, J. Nelson, A. Walsh, M. van Schilfgaarde, and P. R. F. Barnes, "Experimental and theoretical optical properties of methylammonium lead halide perovskites," *Nanoscale*, vol. 8, pp. 6317–6327, 2016.

[141] N. E. Schumaker and C. W. Garland, "Infrared Investigation of Structural and Ordering Changes in Ammonium Chloride and Bromide," *The Journal of Chemical Physics*, vol. 53, no. 1, p. 392, 1970.

[142] R. Ohmann, L. K. Ono, H.-S. Kim, H. Lin, M. V. Lee, Y. Li, N.-G. Park, and Y. Qi, "Real-space imaging of the atomic structure of organic-inorganic perovskite," *Journal of the American Chemical Society*, vol. 137, no. 51, pp. 16049–16054, 2015.

[143] A. Amat, E. Mosconi, E. Ronca, C. Quarti, P. Umari, M. K. Nazeeruddin, M. Grätzel, and F. De Angelis, "Cation-induced band-gap tuning in organohalide perovskites: Interplay of spin-orbit coupling and octahedra tilting," *Nano Letters*, vol. 14, no. 6, pp. 3608–3616, 2014.

[144] J. Even, M. Carignano, and C. Katan, "Molecular disorder and translation/rotation coupling in the plastic crystal phase of hybrid perovskites," *Nanoscale*, vol. 8, pp. 6222–6236, 2016.

[145] T. Leijtens, A. R. Srimath Kandada, G. Eperon, G. Grancini, V. D'Innocenzo, J. M. Ball, S. D. Stranks, H. J. Snaith, and A. Petrozza, "Modulating the Electron - Hole Interaction in a Hybrid Lead Halide Perovskite with an Electric Field.," *Journal of the American Chemical Society*, vol. 137, no. 9, pp. 15451–15459, 2015.

[146] F. Brivio, J. M. Frost, J. M. Skelton, A. J. Jackson, O. J. Weber, M. T. Weller, A. Walsh, A. R. Goni, A. M. A. Leguy, and P. R. Barnes, "Lattice dynamics and vibrational spectra of the orthorhombic, tetragonal and cubic phases of methylammonium lead iodide," *Physical Review B*, vol. 92, p. 144308, 2015.

[147] A. M. A. Leguy, A. R. Goni, J. M. Frost, J. Skelton, F. Brivio, X. Rodriguez-Martínez, O. J. Weber, A. Pallipurath, M. I. Alonso, M. Campoy-Quiles, M. T. Weller, J. Nelson, A. Walsh, and P. R. F. Barnes, "Dynamic disorder, phonon lifetimes, and the assignment of modes to the vibrational spectra of methylammonium lead halide perovskites," *Physical Chemistry Chemical Physics*, vol. 18, pp. 27051–27066, 2016.

[148] M. Ledinsky, P. Löper, B. Niesen, J. Holovsky, J.-h. Yum, S. D. Wolf, A. Fejfar, and C. Ballif, "Raman Spectroscopy of Organic-Inorganic Halide Perovskites," *Journal of Physical Chemistry Letters*, vol. 6, pp. 401–406, 2015.

[149] R. Gottesman, L. Gouda, B. S. Kalanoor, E. Haltzi, S. Tirosh, E. Rosh-Hodesh, Y. Tischler, A. Zaban, C. Quarti, E. Mosconi, and F. De Angelis, "Photoinduced Reversible Structural Transformations in Free-Standing CH3NH3PbI3 Perovskite Films," *Journal of Physical Chemistry Letters*, pp. 2332–2338, 2015.

[150] G. Grancini, S. Marras, M. Prato, C. Giannini, C. Quarti, F. D. Angelis, M. D. Bastiani, G. E. Eperon, H. J. Snaith, L. Manna, and A. Petrozza, "The Impact of the Crystallization Processes on the Structural and Optical Properties of Hybrid Perovskite Films for Photovoltaics," *Journal of Physical Chemistry Letters*, vol. 5, no. 21, pp. 3836–3842, 2014.

[151] T. Leijtens, E. T. Hoke, G. Grancini, D. J. Slotcavage, G. E. Eperon, J. M. Ball, M. De Bastiani, A. R. Bowring, N. Martino, K. Wojciechowski, M. D. McGehee,

H. J. Snaith, and A. Petrozza, "Mapping Electric Field-Induced Switchable Poling and Structural Degradation in Hybrid Lead Halide Perovskite Thin Films," *Advanced Energy Materials*, vol. 5, p. 1500962, 2015.

[152] B.-W. Park, S. M. Jain, X. Zhang, A. Hagfeldt, G. Boschloo, and P. E. T. Al, "Resonance Raman and Excitation Energy Dependent Charge Transfer Mechanism in Halide-Substituted Hybrid Perovskite Solar Cells," *ACS Nano*, vol. 9, no. 2, pp. 2088–2101, 2015.

[153] A. Theoret and C. Sandorfy, "The infrared spectra of solid methylammonium halides-II," *Spectrochimica Acta*, vol. 23A, pp. 519–542, 1967.

[154] M. A. Perez Osorio, R. L. Milot, M. R. Filip, J. B. Patel, L. M. Herz, M. B. Johnston, and F. Giustino, "Vibrational Properties of the Organic-Inorganic Halide Perovskite CH3NH3PbI3 from Theory and Experiment: Factor Group Analysis, First-Principles Calculations, and Low-Temperature Infrared Spectra," *The Journal of Physical Chemistry C*, vol. 119, no. 46, pp. 25703–25718, 2015.

[155] A. A. Bakulin, O. Selig, H. J. Bakker, Y. L. A. Rezus, C. Müller, T. Glaser, R. Lovrincic, Z. Sun, Z. Chen, A. Walsh, J. M. Frost, and T. L. C. Jansen, "Real-Time Observation of Organic Cation Reorientation in Methylammonium Lead Iodide Perovskites," *The Journal of Physical Chemistry Letters*, vol. 6, pp. 3663–3669, 2015.

[156] R. Gottesman, E. Haltzi, L. Gouda, S. Tirosh, Y. Bouhadana, A. Zaban, E. Mosconi, and F. D. Angelis, "Extremely Slow Photoconductivity Response of CH3NH3PbI3 Perovskites Suggesting Structural Changes under Working Conditions," *Journal of Physical Chemistry Letters*, vol. 5, pp. 2662–2669, 2014.

[157] I. Baltog, M. Baibarac, and S. Lefrant, "Quantum well effect in bulk PbI(2) crystals revealed by the anisotropy of photoluminescence and Raman spectra.," *Journal of physics. Condensed matter*, vol. 21, p. 025507, 2009.

[158] M. Antoniadou, E. Siranidi, N. Vaenas, A. G. Kontos, E. Stathatos, and P. Falaras, "Photovoltaic Performance and Stability of CH3NH3PbI3-xClx Perovskites," *Journal of Surfaces and Interfaces of Materials*, vol. 2, no. 4, pp. 323–327, 2014.

[159] R. G. Niemann, A. G. Kontos, D. Palles, E. I. Kamitsos, A. Kaltzoglou, F. Brivio, P. Falaras, and P. J. Cameron, "Halogen Effects on Ordering and Bonding of CH3NH3+ in CH3NH3PbX3 (X = Cl, Br, I) Hybrid Perovskites: A vibrational spectroscopic study," *The Journal of Physical Chemistry C*, vol. 120, no. 5, pp. 2509–2519, 2016.

[160] T. Chen, B. J. Foley, B. Ipek, M. Tyagi, J. R. D. Copley, C. M. Brown, J. J. Choi, and S. H. Lee, "Rotational Dynamics of Organic Cations in CH3NH3PbI3 Perovskite," *Physical Chemistry Chemical Physics*, vol. 17, pp. 31278–31286, 2015.

[161] A. Mattoni, A. Filippetti, M. I. Saba, and P. Delugas, "Methylammonium Rotational Dynamics in Lead Halide Perovskite by Classical Molecular Dynamics: The

Role of Temperature," *Journal of Physical Chemistry Letters*, vol. 119, no. 30, pp. 17421–17428, 2015.

[162] H. D. B. Jenkins and K. P. Thakur, "Reappraisal of Thermochemical Radii for Complex Ions," *Journal of Chemical Education*, vol. 56, no. 9, pp. 576–577, 1979.

[163] H. K. Roobottom, H. D. B. Jenkins, J. Passmore, and L. Glasser, "Thermochemical Radii of Complex Ions," *Journal of Chemical Education*, vol. 76, no. 11, pp. 1570–1573, 1999.

[164] R. D. Shannon, "Revised effective ionic radii and systematic studies of interatomic distances in halides and chalcogenides," *Acta Crystallographica Section A*, vol. 32, no. 5, pp. 751–767, 1976.

[165] K. Yamada, T. Tsuritani, T. Okuda, and S. Ichiba, "Structure and Bonding of Two Modifications of CsSnI3 by Means of Powder X-Ray Diffraction, 127NQR and DTA," *Chemistry Letters*, vol. 18, no. 8, pp. 1325–1328, 1989.

[166] K. Yamada, S. Funabiki, H. Horimoto, T. Matsui, T. Okuda, and S. Ichiba, "Structural Phase Transitions of the Polymorphs of CsSnI3 by Means of Rietveld Analysis of the X-Ray Diffraction," *Chemistry Letters*, vol. 20, pp. 801–804, may 1991.

[167] C. Li, X. Lu, W. Ding, L. Feng, Y. Gao, and Z. Guo, "Formability of ABX3 (X = F, Cl, Br, I) halide perovskites," *Acta Crystallographica Section B Structural Science*, vol. 64, no. 6, pp. 702–707, 2008.

[168] G. Kieslich, S. Sun, and T. Cheetham, "An Extended Tolerance Factor Approach for Organic-Inorganic Perovskites," *Chemical Science*, vol. 6, pp. 3430–3433, 2015.

[169] A. Kaltzoglou, M. Antoniadou, A. G. Kontos, C. C. Stoumpos, D. Perganti, E. Siranidi, V. Raptis, K. N. Trohidou, V. Psycharis, M. G. Kanatzidis, and P. Falaras, "Optical-Vibrational Properties of the Cs2SnX6 (X = Cl, Br, I) Defect Perovskites and Hole-Transport Efficiency in Dye-Sensitized Solar Cells," *The Journal of Physical Chemistry C*, vol. 120, pp. 11777–11785, may 2016.

[170] F. Giustino and H. J. Snaith, "Towards Lead-free Perovskite Solar Cells," *ACS Energy Letters*, vol. 1, no. 6, pp. 1233–1240, 2016.

[171] Z. Yang, A. Rajagopal, S. B. Jo, C.-C. Chueh, S. T. Williams, C.-C. Huang, J. K. Katahara, H. W. Hillhouse, and A. K. Y. Jen, "Stabilized wide bandgap perovskite solar cells by Tin substitution," *Nano Letters*, vol. 16, no. 12, pp. 7739–7747, 2016.

[172] G. E. Eperon, T. Leijtens, K. A. Bush, T. Green, J. T.-W. Wang, D. P. McMeekin, G. Volonakis, R. L. Milot, D. J. Slotcavage, R. Belisle, J. B. Patel, E. S. Parrott, R. J. Sutton, W. Ma, F. Moghadam, B. Conings, A. Babayigit, H.-g. Boyen, F. Giustino, L. M. Herz, M. B. Johnston, M. D. McGehee, and H. J. Snaith, "Perovskite-perovskite tandem photovoltaics with optimised bandgaps," *Science*, vol. 354, no. 6314, pp. 861–865, 2016.

[173] J. Seo, J. H. Noh, and S. I. Seok, "Rational Strategies for Efficient Perovskite Solar Cells," *Accounts of Chemical Research*, vol. 49, no. 3, pp. 562–572, 2016.

[174] D. P. McMeekin, G. Sadoughi, W. Rehman, G. E. Eperon, M. Saliba, M. T. Hörantner, A. Haghighirad, N. Sakai, L. Korte, B. Rech, M. B. Johnston, L. M. Herz, and H. J. Snaith, "A mixed-cation lead mixed-halide perovskite absorber for tandem solar cells," *Science*, vol. 351, no. 6269, pp. 151–155, 2016.

[175] O. J. Weber, B. Charlesa, and M. T. Weller, "Phase Behaviour and Composition in the Formamidinium- Methylammonium Hybrid Lead Iodide Perovskite Solid Solution," *Journal of Materials Chemistry A*, vol. 4, pp. 15375–15382, 2016.

[176] R. D. Shannon, "Revised effective ionic radii and systematic studies of interatomic distances in halides and chalcogenides," *Acta Crystallographica Section A*, vol. 32, no. 5, pp. 751–767, 1976.

[177] G. Kieslich, S. Sun, and A. K. Cheetham, "Solid-state principles applied to organic-inorganic perovskites: new tricks for an old dog," *Chemical Science*, vol. 5, pp. 4712–4715, 2014.

[178] R. K. Misra, S. Aharon, B. Li, D. Mogilyansky, I. Visoly-Fisher, L. Etgar, and E. A. Katz, "Temperature- and Component-Dependent Degradation of Perovskite Photovoltaic Materials under Concentrated Sunlight," *The Journal of Physical Chemistry Letters*, vol. 6, pp. 326–330, 2015.

[179] E. J. Juarez-Perez, Z. Hawash, S. R. Raga, L. K. Ono, and Y. Qi, "Thermal degradation of CH3NH3PbI3 perovskite into NH3 and CH3I gases observed by coupled thermogravimetry-mass spectrometry analysis," *Energy & Environmental Science*, vol. 9, pp. 3406–3410, 2016.

[180] D. M. Trots and S. V. Myagkota, "High-temperature structural evolution of caesium and rubidium triiodoplumbates," *Journal of Physics and Chemistry of Solids*, vol. 69, pp. 2520–2526, 2008.

[181] S. Kondo, A. Masaki, T. Saito, and H. Asada, "Fundamental optical absorption of CsPbI3 and Cs4PbI6," *Solid State Communications*, vol. 124, no. 5-6, pp. 211–214, 2002.

[182] C. Yi, J. Luo, S. Meloni, A. Boziki, N. Ashari-Astani, C. Grätzel, S. M. Zakeeruddin, U. Röthlisberger, and M. Grätzel, "Entropic stabilization of mixed A-cation ABX3 metal halide perovskites for high performance perovskite solar cells," *Energy & Environmental Science*, vol. 9, pp. 656–662, 2015.

[183] X. Xia, W. Wu, H. Li, B. Zheng, Y. Xue, J. Xu, D. Zhang, C. Gao, and X. Liu, "Spray Reaction Prepared FA1-xCsxPbI3 Solid Solution as Light Harvester for Perovskite Solar Cells with Improved Humidity Stability," *RSC Adv.*, vol. 6, pp. 14792–14798, 2016.

[184] J.-W. Lee, D.-H. Kim, H.-S. Kim, S.-W. Seo, S. M. Cho, and N.-G. Park, "Formamidinium and Cesium Hybridization for Photo- and Moisture-Stable Perovskite Solar Cell," *Advanced Energy Materials*, vol. 5, no. 20, pp. 1614–6840, 2015.

[185] Z. Li, M. Yang, J.-S. Park, S.-H. Wei, J. Berry, and K. Zhu, "Stabilizing Perovskite Structures by Tuning Tolerance Factor: Formation of Formamidinium and Cesium Lead Iodide Solid-State Alloys," *Chemistry of Materials*, vol. 28, pp. 284 – 292, 2016.

[186] R. G. Niemann, L. Gouda, J. Hu, S. Tirosh, R. Gottesman, P. J. Cameron, and A. Zaban, "Cs+ incorporation into CH3NH3PbI3 perovskite: Substitution limit and stability enhancement," *Journal of Materials Chemistry A*, vol. 4, pp. 17819–17827, 2016.

[187] T. Leijtens, G. E. Eperon, N. K. Noel, S. N. Habisreutinger, A. Petrozza, and H. J. Snaith, "Stability of Metal Halide Perovskite Solar Cells," *Advanced Energy Materials*, vol. 5, no. 20, pp. 1614–6840, 2015.

[188] A. Babayigit, A. Ethirajan, M. Muller, and B. Conings, "Toxicity of organometal halide perovskite solar cells," *Nature Materials*, vol. 15, no. 3, pp. 247–251, 2016.

[189] K. P. Bhandari, J. M. Collier, R. J. Ellingson, and D. S. Apul, "Energy payback time (EPBT) and energy return on energy invested (EROI) of solar photovoltaic systems: A systematic review and meta-analysis," *Renewable and Sustainable Energy Reviews*, vol. 47, pp. 133–141, 2015.

[190] M. de Wild-Scholten and A. Veltkamp, "Environmental life cycle analysis of large area dye sensitized solar modules; status and outlook," *Presented at: 22nd European Photovoltaic Solar Energy Conference and Exhibition*, vol. 3, pp. 1–7, 2007.

[191] J. Gong, S. B. Darling, and F. You, "Perovskite photovoltaics: life-cycle assessment of energy and environmental impacts," *Energy & Environmental Science*, vol. 8, pp. 1953–1968, 2015.

[192] H.-S. Kim, C.-R. Lee, J.-H. Im, K.-B. Lee, T. Moehl, A. Marchioro, S.-J. Moon, R. Humphry-Baker, J.-H. Yum, J. E. Moser, M. Grätzel, and N.-G. Park, "Lead iodide perovskite sensitized all-solid-state submicron thin film mesoscopic solar cell with efficiency exceeding 9%.," *Scientific Reports*, vol. 2, p. 591, 2012.

[193] I. Chung, B. Lee, J. He, R. P. H. Chang, and M. G. Kanatzidis, "All-solid-state dye-sensitized solar cells with high efficiency," *Nature*, vol. 485, pp. 486–489, may 2012.

[194] U. Bach and T. Daeneke, "A solid advancement for dye-sensitized solar cells," *Angewandte Chemie - International Edition*, vol. 51, no. 42, pp. 10451–10452, 2012.

[195] L. Etgar, P. Gao, Z. Xue, Q. Peng, A. K. Chandiran, and B. Liu, "Mesoscopic CH3NH3PbI3/TiO2 Heterojunction Solar Cells," *Journal of the American Chemical Society*, vol. 134, pp. 17396 – 17399, 2012.

[196] J.-H. Im, J. Chung, S.-J. Kim, and N.-G. Park, "Synthesis, structure, and photovoltaic property of a nanocrystalline 2H perovskite-type novel sensitizer (CH3CH2NH3)PbI3," *Nanoscale Research Letters*, vol. 7, no. 1, p. 353, 2012.

[197] J. A. Christians, P. A. Miranda Herrera, and P. V. Kamat, "Transformation of the excited state and photovoltaic efficiency of CH3NH3PbI3 perovskite upon controlled exposure to humidified air," *Journal of the American Chemical Society*, vol. 137, no. 4, pp. 1530–1538, 2015.

Chapter 2

Methodology

If your experiment needs statistics, you ought to have done a better experiment.

Ernest Rutherford
1871 - 1937

This chapter gives an explanation of the techniques used throughout this thesis and their basic working principles. This includes electrochemical characterization, as it underpins much of the research, as well as optical methods, which allow a fast and straightforward characterization of materials and thin-films. Standard PV characterisation methods were included as well.

2.1 Solar cell analysis

The sun can be approximated as a black body radiator with an effective temperature of $\sim$ 5800 K.[1] This results in a maximum emission in the yellow-green part of the visible spectrum, according to Stefan-Boltzmann's black body radiation rule.[2] Solar radiation intensity from the sun on an object in space is determined by its distance from the sun. For the earth with a distance of $1.5 \cdot 10^{11}$ m this results in a radiation of about 1366.1 mW/cm^2. This solar spectrum is also denoted as AM0, where AM is the *air mass coefficient*. Upon entering the earth's atmosphere, certain wavelengths get absorbed and reflected by the atmosphere and the radiation intensity decreases (see fig. 2-1). The standard solar radiation spectrum used to characterise solar cells for terrestrial applications is the AM1.5 spectrum, where 1.5 denotes the relative path length in relation to the atmosphere's zenith path length. For example, AM1.0 refers to solar radiation at the equator and AM1.5 is about the solar radiation that reaches the surface in most European countries.

In order to characterise solar cells under working conditions, typically a light bias of AM1.5 is applied while different measurements are performed. One way to measure the cell is to determine its steady-state output in terms of current and voltage to estimate the solar cell performance. Another approach is based on decay or perturbation measurements, that aim at understanding the response and thereby the working mechanism of the solar cell. Several of the techniques that are used in this thesis will be briefly described in the following sections.

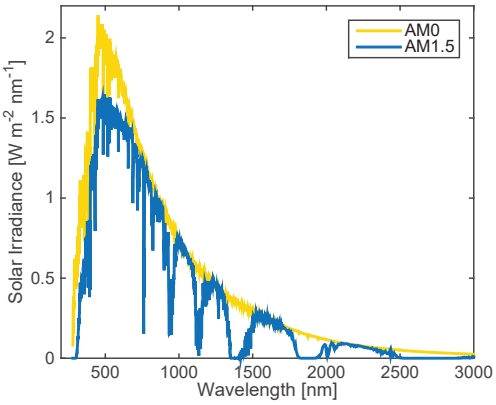

Figure 2-1: Comparison of extraterrestrial sun illumination (AM0, imitating black body radiation), and the terrestrial (AM1.5) spectrum.

2.1.1 Current-voltage curves

Current-voltage (IV) curves are one of the most fundamental characterization techniques for solar cells. IV curves are usually measured with source-measurement units which allow the potential to be set and the current to be measured at any point in the fourth quadrant. This offers a fast and (mostly) straight-forward measurement of the most important performance parameters of solar cells: **The short-circuit current, I_{SC},** is the maximum current that the cell can produce when current travels along a path with neglectable resistance. It can be extracted from the IV curve as the value of the ordinate when the abscissa is zero. It correlates to the amount of photons absorbed minus the losses by recombination processes. **The open-circuit voltage, V_{OC},** is the maximum voltage that the cell produces upon illumination with a defined light source and can be extracted as intersection with the abscissa. **The maximum power point, P_{max},** is a point in the IV curve where the most power ($P = I \cdot V$) can be extracted; in practical applications it is the ideal operating point of a cell. **The fill factor, FF,** defines the shape of the IV curve between short- and open-circuit. For a perfect solar cell, one would like to extract a high current (close to I_{SC}) at the highest possible voltage (close to V_{OC}), which would in turn yield a high power output of the cell. The FF is therefore defined as the ratio of the theoretically attainable power to the attainable P_{max}. It can also be seen as the squareness of the curve. Besides those straight-forward attainable parameters one can extract much more information from an

IV curve, when approximating it with a diode equation.[3]

$$\text{Diode equation} \qquad I = I_0 \left(\exp(\frac{q \cdot V}{n \cdot k_B \cdot T}) - 1 \right) \tag{2.1}$$

$$\Rightarrow \qquad \frac{\delta V_{OC}}{\delta ln(I_0)} = \frac{n \cdot k_B \cdot T}{q} \tag{2.2}$$

Where I is the current output, I_0 is the reverse saturation current, n is the ideality factor and is determined by the order of the recombination mechanism (*e.g.* Hall Shockley Read, Sah Noyce Shockley, Auger).[4] Fitting the diode equation to an IV curves allows for the extraction of shunt- and series resistance of the cell from the slopes at I_{SC} and V_{OC}, respectively.

Despite the relatively easy acquisition of an IV measurement, this measurement protocol can be flawed due to hysteretic effects that are described in the next chapter. This can undermine the reported performance of PSC and makes it useful to combine IV scans with other methods, such as chronoamperometry, maximum power point tracking or incident photon to charge-carrier efficiency, as described in the next section.

2.1.2 Open-circuit voltage decay (OCVD)

Open-circuit voltage decay (OCVD) is a large amplitude transient measurement. The cell is illuminated at open-circuit until it reaches equilibrium conditions and then the light is switched off and the voltage decay is monitored. The voltage decay can be converted to an electron lifetime, as was shown by Zaban *et al.* in 2003 for dye-sensitised solar cells.[5] However, for perovskite cells the decay kinetics depend as well on relaxation effects and can not be fully correlated to a lifetime.[6] In fact, differentiating between relaxation effects and charge-carrier decay is difficult and can not be done unambiguously. It can be assumed that ion motion dominates the response in the slow (μs and s) time regime,[7] which in turn depends on the starting conditions. Most of the charge-carrier decay happens on a nanosecond time scale,[8, 9] which is too fast to be detected by normal OCVD setups.[10] This leaves the sub-μs regime as an intermediate region that can be accessed with OCVD, but needs to be treated carefully because the system's response can stem from cooperative effects, *e.g.* reciprocal interaction between electronic effects and a material relaxation.[6] Therefore, one needs to be aware of the just mentioned cooperative effects in PSC when applying the following equation for the (pseudo-)lifetime τ_n:

$$\tau_n = - \left(\frac{kT}{q} \cdot \frac{dV}{dt} \right)^{-1} \tag{2.3}$$

2.2 Electrochemical analysis

The electrochemical analysis in this study deals with small perturbation measurements (EIS, IMVS, IMPS), as well as current voltage sweeping techniques, such as CV.

The electrochemical reaction happens at the electrode, which usually consists of a metal or semiconductor. An electron tunnels across this interface either through the external application of electromotive force to trigger a chemical reaction or from a spontaneous reaction to power an external supply. An empirical description of charge transport processes at electrode interfaces was brought forward in 1905 by *Juilius Tafel* and could be shown to have a theoretical justification later on, as it can be deduced from the Butler-Volmer equation.[11] It is the most fundamental equation about electrochemical kinetics. It describes the behaviour of an electron at an interface and whether it can tunnel the electrode's surface:

$$\text{Butler-Volmer equation} \qquad I = j_0 \cdot A \cdot \left\{ \exp\left[\frac{\alpha_a n F \eta}{RT}\right] - \exp\left[-\frac{\alpha_c n F \eta}{RT}\right] \right\} \tag{2.4}$$

I	Current	F	Faraday constant
j_o	Exchange current density	α_c	Cathodic charge transfer coefficient
A	Electrode surface area	α_a	Anodic charge transfer coefficient
T	Temperature	η	Activation overpotential ($E - E_{eq}$)
n	Number of electrons		
R	Universal gas constant		

This equation basically states that a cathodic and an anodic current exist which sum up to the net current. Both currents have opposite signs. At equilibrium, the net current is zero, even though the forward and reverse current are not necessarily zero, *e.g.* there is a dynamic equilibrium. For a net current to flow, the potential needs to be moved away from its equilibrium state E_{eq}. Charge-transfer can be hampered by kinetic effects, which are described by the charge transfer coefficients α_a and α_c. The Butler-Volmer equation gives a basic and straightforward description of electrochemical reactions but it can only be used where the reaction at the electrode is dominating the electron transfer kinetics. For processes that are controlled by diffusion or chemical kinetics, the Butler-Volmer equation can not be used. It forms the foundation for most electrochemical reactions and supports the cyclic voltammetry results in this work (chapter 3).

2.2.1 Cyclic voltammetry

Cyclic voltammetry moves the system away from its equilibrium state, by applying a linear potential increase until a certain potential is reached and the potential ramp is reversed. The resulting potential waveform profile is therefore zig-zag shaped. Variation of the scan speed allows for the analysis of not only static properties (e.g. redox potential), but also for dynamic processes (e.g. diffusion, reaction kinetics). The changing potential at the electrode induces a change in the equilibrium concentration, as predicted by the

$$\text{Nernst equation} \qquad E = E_0 - \frac{RT}{zF} \ln \frac{c_{Red}}{c_{Ox}} \tag{2.5}$$

E	Equilibrium redox potential	z	Electrons transferred
E_0	Standard redox potential	F	Faraday constant
R	Universal gas constant	$c_{Red/Ox}$	Concentration
T	Absolute temperature		

During the reaction, species at the electrode are converted and a concentration gradient builds up. Assuming a stagnant solution and presence of a background electrolyte, mass transport of the reactant to the electrode depends on the diffusional flux, which is defined by *Fick's laws of diffusion*. This results in the typical shape of a CV, where the reaction starts with a steep concentration gradient, resulting in fast diffusion to the electrode (*Fick's first law*) and therefore a high current. While the reactants are being used up, a peak current I_p is reached. As the reaction continues, species need to diffuse from further away and the concentration gradient decreases, until a stationary level is reached.

$$\text{Fick's first law:} \qquad J = -D\frac{\partial \phi}{\partial x} \tag{2.6}$$

$$\text{Fick's second law:} \qquad \frac{\partial \phi}{\partial t} = D\frac{\partial^2 \phi}{\partial x^2} \tag{2.7}$$

J	Diffusion flux	x	Position
D	Diffusion coefficient	t	Time
ϕ	Concentration		

Increasing the scan speed will, according to Fick's first law, increase the concentration gradient and therefore the peak current. Another important factor to consider is the peak separation E_{pp}, which increases with high scan rates, as the system becomes irreversible. In this case '*reversible*' refers to an electrochemical context, meaning that

the Nernst equation is maintained at any point of the sweep and therefore electron transfer is much faster than mass transport. The intrinsic peak to peak separation at room temperature for a reversible redox reaction is about 57 mV (assuming an intermediate transition state). Further increase of E_{pp} can appear as other factors come into play, e.g. activation overpotential η. However, an increasing peak offset with increasing scan rate n indicates that the reaction is moving away from being reversible.

Fick's laws of diffusion can also be applied to perovskites, where ions can move across the cell through a vacancy-mediated mechanism. Later on in this work, measured IV curves will be compared to a model that takes this ion movement into account and is based on two contributions: drift and diffusion. The latter can be also be ascribed with the above equations.

2.3 Optical spectroscopy

Optical spectroscopy, *i.e.* the interaction between light and matter, is used throughout this study in a variety of ways. Basic optical analysis is done with UV-Vis, a detailed vibronic study is undertaken with Raman. An explanation of their basic working principle is given in the following sections.

2.3.1 UV-Vis spectroscopy

UV-Vis spectroscopy is used to determine the basic absorption characteristics of thin-film samples. The transmission T and diffuse reflectance R are measured, which give the absorptance $A = 1 - T - R$; it is plotted on a logarithmic scale for a normal absorption UV-Vis spectrum. In order to determine the bandgap of a semiconductor, a Tauc plot can be used. Therefore, the abscissa is plotted as $(\alpha \cdot h \cdot \nu)^2$ against photon energy in eV (with absorption coefficient α). The exponent depends on the type of excitation and 2 (as used above) corresponds to a direct and allowed transition.[12] An alternative determination can be done with the Kubelka-Munk function with $(F(R) \cdot h \cdot \nu)^2$. This however is only valid for flat and thin samples with negligible scattering.

$$\text{Kubelka-Munk function} \qquad F(R) = \frac{(1-R)^2}{2R} \tag{2.8}$$

Caution needs to be taken because a Tauc plot has no theoretical basis in the presence of excitonic features.[13] The exciton binding energy and contribution of excitons to the optical properties and charge transport are still uncertain in perovskites, with most studies suggesting values between 5 and 20 meV,[13, 14, 15] which is below the thermal energy at RT (25.7 meV).

A peculiarity for $MAPbI_3$ and other HOIPs is the broad range of reported absorption onsets. While theoretical studies and single crystalline materials show a bandgap of 1.57 eV,[13, 16] many studies on thin-films (as well as this study) show blue-shifted bandgaps. This effect has been attributed to water intercalation into the perovskite structure,[17] crystallite size,[18] or a lattice expansion and electron-phonon interactions according to

$$\text{Bandgap} \qquad E_g(T) = E_g(0\ \text{K}) + \frac{dE_g}{dT} \times T \tag{2.9}$$

Therefore the measured bandgaps are usually higher than reported bandgaps, but agree with other reports when the above mentioned corrections are taken into account.[19]

2.3.2 Vibrational spectroscopy

In 1908 Gustav Mie formulated a fundamental description of the behaviour of light that he derived from the scattering of a colloidal gold dispersion.[20] This elastic scattering on ideal spheres gives rise to different effects, *e.g.* the blue sky, red sunsets and grey colour clouds. It can be solved by the Rayleigh approximation for particles that are much smaller than the wavelength of light.

$$\text{Rayleigh approximation} \qquad I = I_0 \left(\frac{1 + \cos^2 \theta}{2R^2} \right) \left(\frac{2\pi}{\lambda} \right)^4 \left(\frac{n^2 - 1}{n^2 + 2} \right)^2 \left(\frac{d}{2} \right)^6 \tag{2.10}$$

I_0	Incident light	λ	Wavelength
I	Scattered light	n	Refractive index
θ	Scattering angle	d	Particle diameter
R	Distance to observer		

It becomes clear that the wavelength λ contributes with an exponent of four. The so called '*inverse fourth power law*' is responsible for the different colours of the sky mentioned above. Solving the Mie equations for particles that are about the size of the wavelength of light however is more complicated.[20] The light that scatters elastically off a particle contains valuable information about the size and relative refractive index of the particle, in relation to its medium. That information can be extracted when measuring the scattering over time for the further (*e.g.* dynamic light scattering) or the scattering intensity over wavelength for the latter (*e.g.* plasmonic spectroscopy). However, the scattered light does not interact with the material and hence does not change the energy of the photon (see fig. 2-2, Rayleigh scattering). Even more information can be gathered from light that scatters inelastically: During light scattering, the photon excites an electron into an imaginary state for a very short time before the energy is re-emitted. In the case of inelastic scattering the light interacts with the sample and hence changes its energy. When the emitted light gains energy during the scattering, it is called a Stokes shift; when the scattering results in an energy loss, it is called anti-Stokes shift (compare fig. 2-2). The magnitude of the shift can give information about vibrational relaxations (or dissipation processes). Correlating this shift to vibrational processes was done by Sir Chandrasekhara Venkata Raman, a discovery that earned him the Nobel Price in physics in 1930.

Besides the so called normal modes, where the light frequency matches a molecular oscillation, overtone bands and combination modes also contribute to the vibrational spectrum of perovskites. The former refer to doubly excited vibrational states that occur at about double the frequency of the respective normal mode. The latter consists

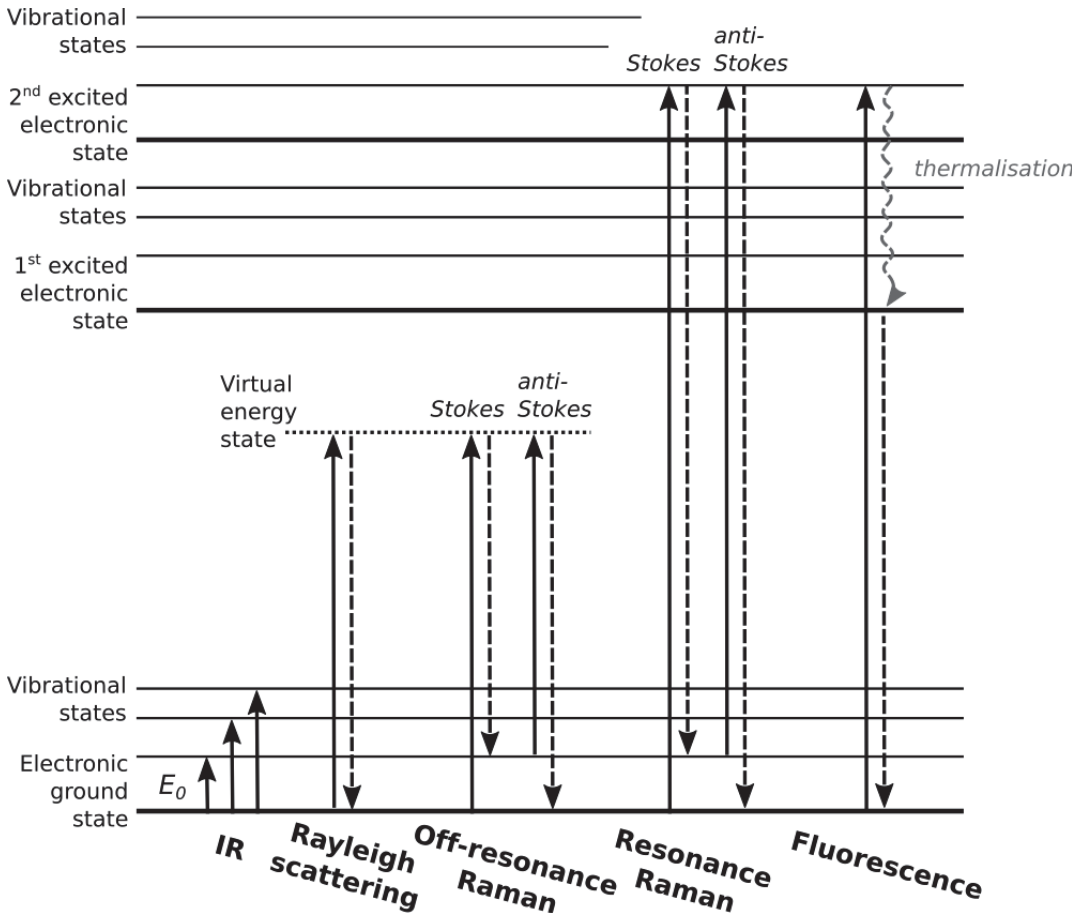

Figure 2-2: Electronic and vibrational (vibronic) energy levels and different types of electronic excitation and relaxation processes, which are of importance in this study.

of combinations of normal modes at different frequencies. Derivative changes in a molecule can be approximated with Hooke's law. This is usually applied to isotopes, which change in mass, while the bond strength remains almost unchanged. The easiest approximation for a changing oscillation frequency is the harmonic oscillator:

$$\text{Harmonic oscillator} \quad \nu = \frac{1}{2\pi}\sqrt{k/\mu} \quad \text{with} \tag{2.11}$$

$$\text{Reduced mass} \quad \mu^{-1} = m_1^{-1} + m_2^{-1} \tag{2.12}$$

ν	Frequency	$m_{1,2}$	Atomic mass of element 1 / 2
k	Bond strength		
μ	Reduced mass		

Measurement of the Raman spectrum can be principally done under two conditions, resonant and off-resonant. In the former case, the probe beam can be absorbed by the material and the intermediate excited state matches an electronic excitation. This gives rise to a high selectivity because the probe is matched to the sample, but it also induces electronic excitations in the sample, and can potentially alter or damage the sample. Another problem with resonant excitation is PL, which is similar to Raman scattering but an unwanted side reaction that can decrease the signal-to-noise ratio. For PL, the electrons are also excited but then thermalised and given back from a relaxed state without any information about vibrational processes. PL processes can be $\times 10^8$ stronger than Raman-shifts for high-performance semiconductors, which also imposes problems for the measurement of $MAPbI_3$.

Another option is to use wavelengths above the bandgap energy of the material. The Raman shift is therefore measured in the absence of any electronic excitation and associated degradation of the perovskite. But it also lowers the scattering sensitivity and selectivity, because the excited state is now virtual and not electronic. Moreover, the inverse fourth power law dependence decreases the scattering for a given material if the wavelength is increased. But because of the decreased interaction with the sample, higher probe beam intensities are usually applied and the absence of PL effects improves the signal to noise ratio.

To interpret the measured spectra at various temperatures, a correction according to the Bose-Einstein distribution is necessary. An even more precise correction for the perovskite systems studied was obtained by using the reduced Intensity relationship,

that was employed recently for glasses and viscoelastic materials.[21, 22]

$$\text{Reduced Intensity} \qquad I_{red}(\omega) = \frac{I(\omega)}{n(\omega,T)+1} \quad \text{with} \tag{2.13}$$

$$\text{Bose-Einstein Factor} \qquad n(\omega,T) = (\exp(k_B \cdot T - 1)^{-1} \approx \exp(\frac{1.44\omega}{T} - 1)^{-1} \tag{2.14}$$

The measured line-width can then be related to structural dynamics in the material. For example, bands due to the rocking vibrations can be related to corresponding correlation times, which is the average time it takes the molecule to move one radian.[23, 24]

$$\text{Correlation time} \qquad \tau_c = \frac{1}{2\pi \cdot c \cdot FWHM}$$

The FWHM hereby refers to an assumed homogeneous line-shape that resembles the probe beam and is expressed by a Lorentzian shape. In some materials (like in this study) the measured peaks show a different peak shape *e.g.* mixed Lorentzian-Gaussian. The reason for this is an inhomogeneous behaviour of different scatterers, which causes a splitting of homogeneous peaks below the resolution limit of the measurement. Hence, no individual peaks can be seen, instead the line-shape becomes inhomogeneous. In order to correct a measured inhomogeneous line-width, one needs to calculate the true inhomogeneous line-width $\Delta\nu_{calc}$ by correcting the measured linewidth $\Delta\nu_{meas}$ with the finite width of the spectrometer $\Delta\nu_0$:[25]

$$\Delta\nu_{calc}^2 = \Delta\nu_{meas}^2 - \Delta\nu_0^2$$

In cases of small values $\Delta\nu_0$ ($\approx$ 2 cm^{-1}, as in this study), this correction does not significantly contribute.

Besides the excitation of molecular vibrations *via* a Stokes shift caused by high energy visible light, one can also directly excite the vibration with infrared (IR) light that matches the vibration frequency. Both techniques are complimentary, while the mutual exclusion principle dictates that each vibration is either Raman active (if it changes its polarisability) or IR active (if it changes its dipole moment). Therefore, the former gives an indication of the covalent character of a bond, while the latter measures the ionic character.[26] Because IR is based on a direct excitation of vibrations, the excitation energy is much lower than for Raman and less damaging on the sample, *e.g.* between 10 cm^{-1} (1 mm) and 3000 cm^{-1} (2 μm).

2.4 Structural and compositional analysis

2.4.1 X-ray diffraction

X-ray diffraction is based on the resonant interaction of electromagnetic radiation with lattice atoms of crystalline materials. These (mostly) periodic crystals interact with light of a given wavelength and undergo constructive interference at certain diffraction angles:

$$\text{Bragg equation} \qquad n \cdot \lambda = 2d \cdot \sin(\theta) \tag{2.15}$$

n	Positive integer	θ	Diffraction angle
λ	Wavelength		
d	Interstitial spacing		

Equation 2.15 forms the very foundation of X-ray diffraction and allows the correlation of angular shifts 2θ to a structural d-spacing. For example, as will be shown later in chapter 5, the introduction of smaller cations into the perovskite lattice shrinks the unit cell and, according to the Bragg equation, shifts all reflections to larger values of 2θ.

The experimental setup for powder-XRD (as opposed to single crystal XRD) consists of a radiation source with a wavelength that is similar to the lattice spacing (*e.g.* $\lambda = 1.5406$ Å for CuKα1 radiation). The beam is collimated towards the sample at various angles. The recorded intensities of the scattered radiation are plotted as a function of scattering angle 2θ form the X-ray diffractogram. Each reflection corresponds to a certain interstitial lattice spacing (d-spacing) that can be calculated *via* the Bragg equation 2.15. In this study however, XRD is used solely on known structures, so that peak assignment *via* d-spacing value is not essential. However, information about the nature of the sample can be taken from a variety of parameters, that indicate structural changes within the material, *e.g.* the peak shape and shift. The full width at half maximum (FWHM) relates to crystallinity and grain size, as defined by the Scherrer formula.[27] It states that large crystals give sharper, more narrow reflections:

$$\text{Scherrer equation} \qquad \tau = \frac{K \cdot \lambda}{\Delta \cdot \cos \cdot \theta} \tag{2.16}$$

τ	Crystalline size	Δ	FWHM
K	Shape factor	θ	Diffraction angle
λ	Wavelength		

The relative intensity of the peaks in a diffraction pattern in powder XRD depends,

amongst other factors as occupancy, on the distribution of crystalline orientations. These can be described by a relatively simple model, called March function, that correlates a single pole-density function $P_H(\phi)$ to the crystalline orientation that is described by the March coefficient R.[28]

$$\text{March function} \qquad P_H(\phi) = \left(R^2 \cdot \cos(\phi)^2 \cdot R^{-1} \cdot \sin(\phi)^2\right)^{-3/2} \tag{2.17}$$

$P_H(\phi)$	Pole density function
R	March coefficient
ϕ	Angle with symmetry axis

An easy way to evaluate the impact of these factors on a sample with a known crystal structure is to simulate the diffraction pattern from structural parameters (reported in literature in form of a .cif file). Several programs employ this functionality; in this study the program CrystalDiffract (CrystalMaker Software Ltd., Oxford, UK) was used.

2.4.2 Energy-dispersive X-ray spectroscopy (EDX)

Energy-dispersive X-ray spectroscopy (EDX) was used for the purpose of compositional analysis and to monitor the chemical exchange of perovskite cation derivatives. Measurements were carried out inside the vacuum chamber of a SEM setup, where the high energy electron beam was focused on the sample to excite and eject electrons around the atomic nuclei and thereby creating a vacancy that can be filled with electrons from outer shells (higher in energy). The differential energy that is emitted during the relaxation process in form of X-rays is characteristic for the energy difference between the electronic states and the respective element. The emitted radiation is then detected with an energy dispersive sensor. The resulting spectrum shows all emitted lines and peak fitting and comparison to literature can correlate each peak to an elemental transition.

2.5 Bibliography

[1] R. M. Goody and Y. L. Yung, *Atmospheric Radiation: Theoretical Basis*. OUP USA, 1996.

[2] M. Planck and M. Masius, *The Theory of Heat Radiation*. Blakiston, 1914.

[3] M. A. Green, *Solar Cells: Operating Principles, Technology and System Applications*. University of New South Wales, 1992.

[4] P. Landsberg, *Recombination in semiconductors*. Cambridge New York: Cambridge University Press, 1991.

[5] A. Zaban, M. Greenshtein, and J. Bisquert, "Determination of the Electron Lifetime in Nanocrystalline Dye Solar Cells by Open-Circuit Voltage Decay Measurements," *ChemPhysChem*, vol. 4, pp. 859–864, 2003.

[6] L. Bertoluzzi, I. Herraiz-Cardona, R. Gottesman, A. Zaban, and J. Bisquert, "Relaxation of electron carriers in the density of states of nanocrystalline TiO2," *Journal of Physical Chemistry Letters*, vol. 5, no. 4, pp. 689–694, 2014.

[7] a. Baumann, K. Tvingstedt, M. C. Heiber, S. Väth, C. Momblona, H. J. Bolink, and V. Dyakonov, "Persistent photovoltage in methylammonium lead iodide perovskite solar cells," *APL Materials*, vol. 2, no. 8, p. 081501, 2014.

[8] S. D. Stranks, V. M. Burlakov, T. Leijtens, J. M. Ball, A. Goriely, and H. J. Snaith, "Recombination Kinetics in Organic-Inorganic Perovskites: Excitons, Free Charge, and Subgap States," *Physical Review Applied*, vol. 2, no. 3, p. 034007, 2014.

[9] Y. Yamada, T. Nakamura, M. Endo, A. Wakamiya, and Y. Kanemitsu, "Photocarrier Recombination Dynamics in Photocarrier Recombination Dynamics in Perovskite CH3NH3PbI3 for Solar Cell Applications," *Journal of American Chemical Society*, vol. 136, pp. 11610–11613, 2014.

[10] A. Pockett, G. E. Eperon, T. Peltola, H. J. Snaith, A. Walker, L. M. Peter, and P. J. Cameron, "Characterization of Planar Lead Halide Perovskite Solar Cells by Impedance Spectroscopy, Open-Circuit Photovoltage Decay, and Intensity-Modulated Photovoltage/Photocurrent Spectroscopy," *Journal of Physical Chemistry C*, vol. 119, pp. 3456–3465, 2015.

[11] J. Tafel, "Uber die Polarisation bei kathodischer Wasserstoffentwicklung," *Zeitschrift Fur Physikalische Chemie, Stochiometrie und Verwandtschaftslehre*, vol. 50, p. 1712, 1905.

[12] E. A. Davis and N. F. Mott, "Conduction in non-crystalline systems V. Conductivity, optical absorption and photoconductivity in amorphous semiconductors," *Philosophical Magazine*, vol. 22, no. 179, pp. 903–922, 1970.

[13] M. A. Green, Y. Jiang, A. Mahboubi Soufiani, and A. W.-Y. Ho-Baillie, "Optical Properties of Photovoltaic Organic-Inorganic Lead Halide Perovskites," *The Journal of Physical Chemistry Letters*, vol. 6, pp. 4774–4785, 2015.

[14] K. Galkowski, A. Mitioglu, A. Miyata, P. Plochocka, O. Portugall, G. E. Eperon, J. T.-W. Wang, T. Stergiopoulos, S. D. Stranks, H. Snaith, and R. J. Nicholas, "Determination of the exciton binding energy and effective masses for methylammonium and formamidinium lead tri-halide perovskite semiconductors," *Energy & Environmental Science*, vol. 9, pp. 962–970, 2016.

[15] A. M. Soufiani, F. Huang, P. Reece, R. Sheng, A. Ho-Baillie, and M. A. Green, "Polaronic exciton binding energy in iodide and bromide organic-inorganic lead halide perovskites," *Applied Physics Letters*, vol. 107, p. 231902, 2015.

[16] A. Leguy, P. Azarhoosh, M. I. Alonso, M. Campoy-Quiles, O. J. Weber, J. Yao, D. Bryant, M. T. Weller, J. Nelson, A. Walsh, M. van Schilfgaarde, and P. R. F. Barnes, "Experimental and theoretical optical properties of methylammonium lead halide perovskites," *Nanoscale*, vol. 8, pp. 6317–6327, 2016.

[17] G. Grancini, V. D'Innocenzo, E. R. Dohner, N. Martino, A. R. Srimath Kandada, E. Mosconi, F. De Angelis, H. I. Karunadasa, E. T. Hoke, and A. Petrozza, "CH3NH3PbI3 Perovskite Single Crystals: Surface Photophysics and its Interaction with the Environment," *Chemical Science*, vol. 6, pp. 7305–7310, 2015.

[18] V. D'Innocenzo, A. R. Srimath Kandada, M. De Bastiani, M. Gandini, and A. Petrozza, "Tuning the light emission properties by band gap engineering in hybrid lead-halide perovskite.," *Journal of the American Chemical Society*, vol. 136, no. 51, pp. 17730–17733, 2014.

[19] C. Quarti, E. Mosconi, J. M. Ball, V. D'Innocenzo, C. Tao, S. Pathak, H. J. Snaith, A. Petrozza, and F. De Angelis, "Structural and optical properties of methylammonium lead iodide across the tetragonal to cubic phase transition: implications for perovskite solar cells," *Energy & Environmental Science*, vol. 9, pp. 155–163, 2016.

[20] G. Mie, "Beiträge zur Optik trüber Medien, speziell kolloidaler Metallösungen," *Annalen der Physik*, vol. 4, no. 25, pp. 377 – 445, 1908.

[21] G. E. Walrafen, M. S. Hokmabadi, P. N. Krishnan, S. Guha, and R. G. Munro, "Low-frequency Raman scattering from vitreous and molten B2O3," *The Journal of Chemical Physics*, vol. 79, no. 8, pp. 3609–3620, 1983.

[22] E. I. Kamitsos, J. A. Kapoutsis, H. Jain, and C. H. Hsieh, "Vibrational study of the role of trivalent ions in sodium trisilicate glass," *Journal of Non-Crystalline Solids*, vol. 171, no. 1, pp. 31–45, 1994.

[23] N. Onoda-Yamamuro, T. Matsuo, and H. Suga, "Calorimetric and IR Spectroscopic Studies of Phase Transitions in Methylammonium Trihalogenoplumbates," *Journal of Physics and Chemistry of Solids*, vol. 51, no. 12, pp. 1383–1395, 1990.

[24] W. G. Rothschild, *Dynamics of Molecular Liquids*. Wiley-Interscience publication, John Wiley & Sons, 1984.

[25] V. C. Stergiou, A. G. Kontos, and Y. S. Raptis, "Anharmonic effects and Faust-Henry coefficient of CdTe in the vicinity of the energy gap," *Physical Review B - Condensed Matter and Materials Physics*, vol. 77, no. 23, pp. 1–8, 2008.

[26] E. Smith and G. Dent, *Modern Raman Spectroscopy: A Practical Approach*. Wiley, 2005.

[27] A. L. Patterson, "The Scherrer Formula for X-Ray Particle Size Determination," *Physical Review*, vol. 56, no. 10, pp. 978–982, 1939.

[28] C. J. Howard and E. H. Kisi, "Preferred orientation in Debye-Scherrer geometry: Interpretation of the March coefficient," *Journal of Applied Crystallography*, vol. 33, no. 6, pp. 1434–1435, 2000.

Chapter 3

Development of different fabrication routes for perovskite solar cells

Progress is made by trial and failure;
the failures are generally a hundred times more numerous than the successes;
yet they are usually left unchronicled.

Sir W. Ramsay
'Radium and its Products', 1904 [1]

MANY different variations of fabrication techniques were reported since perovskites entered the solar cell race in 2009.[2] Even though the processing can be done with equipment that can be found in most scientific laboratories, experience shows that a thorough control and judicious adjustment of every parameter involved in the fabrication process needs to be done. This is opposed to their promise of being a cheap and easily processable photovoltaic material. Studied fabrication parameters include simple things such as processing temperature,[3] and almost esoteric studies that report enhanced efficiencies when playing pop rather than classical music during fabrication.[4] This chapter will shed further light on the importance of the substrate cleaning procedure and presents different fabrication approaches to obtain $MAPbI_3$ thin films with favourable properties for PV applications. The effects of temperature, air flow and humidity during the deposition process are highlighted. Furthermore, an easy technique to fabricate efficient perovskite cells in ambient air is presented. Modification of the processing parameters of this new technique gave high-hysteresis cells, that were used as a model to quantify ion motion in perovskite cells. This is of particular interest

as part of an ongoing discussion in the perovskite community about the underlying mechanism of the observed hysteresis during current-voltage scans.

3.1 Experimental methods

A brief description of the cleaning procedure is given here, while a more detailed account is given in the appendix. FTO-covered glass (TEC7 with 7 Ω/sq sheet resistance, Pilkington) was cut to device size of (25×25 mm^2) and cleaned with Hellmanex solution, then rinsed with deionised water, ethanol and finally 2-propanol (IPA for isopropyl alcohol). Organic residuals were removed *via* oxygen plasma treatment for 30 min.

Spin-coated blocking layers were deposited at a spinning speed of 2000 rpm for 60 s from a sightly acidic titanium isopropoxide (TTIP) solution, which was dried at 150 °C for 30 min and subsequently annealed at 500 °C for 30 min to form a blocking layer of TiO_2. Spray pyrolysis blocking layers were deposited from a hand-held atomiser with a solution of titanium diisopropoxy bis(acetylacetonate) (0.2 M). The substrate was preheated to 450 °C and left to equilibrate for 30 min before spraying the solution in intervals of 10 s for 2.5 min. The substrate was further annealed for 5 min and then allowed to cool down to room temperature.

Perovskite thin-film deposition was carried out in three different ways. For the morphological study a precursor solution was spin-coated and the resulting thin-film annealed with a heat gun to evaporate the solvent and crystallise the perovskite.

For the so called simple fabrication approach, PbI_2 thin-films were spin-coated and then converted into a perovskite layer by vacuum-vapour assisted solution processing (V-VASP). For the high hysteresis cell a modified V-VASP process was used with different parameters and cells deposited in a planar architecture, rather than onto a mp-TiO_2 scaffold. All deposition methods are described in detail further down in this paragraph.

For the high air-flow processing of the perovskite, a 3:1 wt/wt ratio of MAI:$PbCl_2$ was dissolved in dimethylformamide (DMF). The precursor solution was spin-coated at 2000 rpm for 45 s and immediately afterwards taken onto a home-build stage, that fixed the substrate into its position and had the heat gun (Steinel HL 2020 E) above at a distance of 15 cm. The stage had a build-in window below the cell that allowed for an attachment of a reflection probe that was attached to an optical spectrometer (Ocean Optics USB2000+) and light source (DT-MINI-2-GS) to measure the reflectance signal during the perovskite formation. Different temperatures were used for the annealing, which are described in the text below (for calibration see Appendix A, fig. A-2a). The annealing duration was dependent on temperature (see Appendix A, fig. A-2b).

This was necessary because low temperatures required longer annealing times to fully evaporate the solvent and crystallise the perovskite. Using the same annealing time at higher temperatures would have decomposed the perovskite. For the simple fabrication approach, a mp-TiO_2 layer was first deposited from a paste (Dyesol 18NR-T) and annealed at 500 °C for 30 min. The PbI_2 layer was deposited by spin-coating a hot solution of PbI_2 in DMSO. The thin-film was annealed at 120 °C for 60 min. The substrate was placed onto a preheated hotplate, surrounded by MAI powder and the desiccator lid was placed on top with a rubber ring to seal the vacuum that was created with an attached rotary pump. For the conversion process, the substrates and MAI powder were put under a low vacuum and the timer was started after the pressure equilibrated (annealing time mentioned in context). The process was carried out under static vacuum. For the high-hysteresis cells, the V-VASP fabrication was used as described above but in a planar architecture, rather than onto a mp-layer. The PbI_2 film was spun at a slower speed (details in appendix) to compensate for the absence of the mp-scaffold and the PbI_2 annealing time was shortened to 10 min. The perovskite conversion temperature was decreased from 150 °C to 120 °C and the time was set to 30 min, which is also shorter than the standard V-VASP process.

For the deposition of the hole transport material (HTM), a solution of Spiro-OMeTAD (spiro) was dissolved in chlorobenzene and doped with bis(trifluoromethane)sulfonimide lithium salt solution. The HTM was spin-coated at 4000 rpm for 45 s. The substrates were left overnight for oxygen doping before the gold back contacts were evaporated with a thickness of about 80 nm and an active area of 0.1 cm^2.

For the sample analysis different characterisation techniques were used. Contact angle measurements were performed according to the *Sessile drop technique*. The bl-TiO_2 blocking behaviour with cyclic voltammetry (AUTOLAB PGSTAT30). The area of the electrode was 1 cm^2 and was measured against a Ag/AgCl (3 M KCl) reference with a Pt wire as counter electrode. The electrodes were immersed into a 100 mM solution of Fe^{+II}/Fe^{+III} (equimolar amounts of $K_3Fe(CN)_6$ and $K_4Fe(CN)_6$) with background electrolyte (10 mM KCl). Scans went from −1 V to 1.2 V at different scan rates, which are mentioned in context. For the morphological analysis of the perovskite thin-films, an AFM (Nanosurf FlexAFM) was used in tapping mode (Budget Sensors AFM Probes TAP190-G). Powder X-ray diffraction (XRD) analysis was performed with a BRUKER D8-Advance. Device performance was evaluated using a Class AAA solar simulator at AM1.5G and 100 mW/cm^2 connected to a source-meter (Keithley 2601A) that was driven by a home-built program written in LabView (see fig. 3-8). For the measurements, the samples were covered with a shadow mask with an opening area of 0.1 cm^2. Measurements were performed by holding the cell at a voltage slightly above

V_{OC} (1 - 1.2 V, depending on cell) for 5 s to equilibrate the cell. The measurement was then performed by sweeping the voltage to short-circuit and then back up to the equilibration potential. The sweeping speed was usually 100 mV/s, if not stated otherwise in the text.

For the estimation of the size of the ferro-cyanide anion, an Assisted Model Building with Energy Refinement (AMBER) force field was used, as part of the Avogadro software package.[5]

3.2 Results and discussion

3.2.1 Substrate cleaning optimisation

The preparation of the glass/FTO substrate before deposition of the blocking layer can be elaborate and there is no standard procedure, as every laboratory uses a slightly different approach. However, the basic steps are similar: etching the transparent conducting oxide (TCO) to prevent short-circuiting in the final cell and cutting the substrate into device size pieces (first step in fig. 3-1). Then cleaning the substrate with surfactants (*e.g.* Hellmanex) and organic solvents and in most cases an additional step of oxygen plasma (or ozone) cleaning in order to remove organic monolayers that are left over from the cleaning procedure earlier on (second row in fig. 3-1). Afterwards the deposition of pin- or nip-type solar cell layers can proceed onto the clean substrate surface.

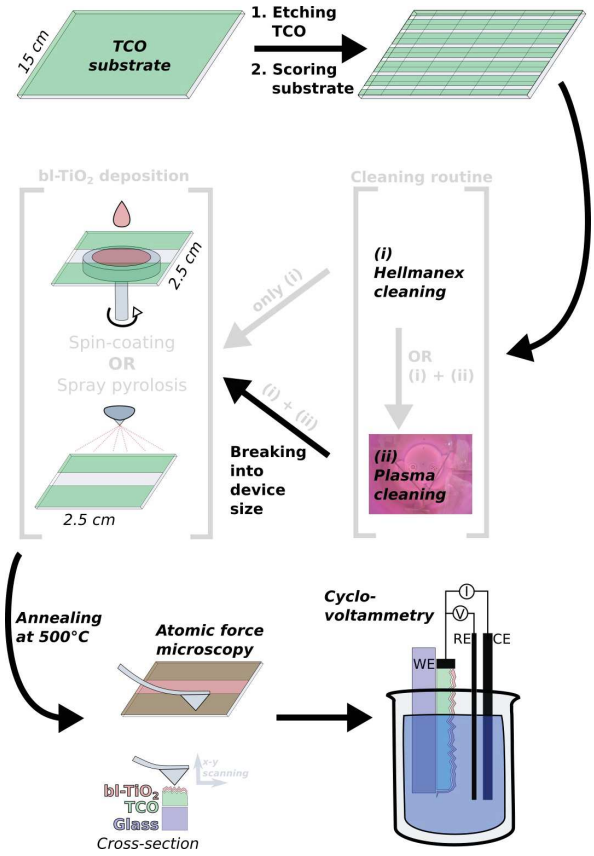

Figure 3-1: Schematic of the substrate preparation procedure and evaluation *via* AFM and cyclovoltammetry

Reports on the exact cleaning procedure of the substrate can differ and show that in some cases the cleaning with surfactants and solvents is combined with a sonication step.[6, 7, 8, 9, 10] However, this treatment is time-intense and mostly applied during the fabrication of dye cells. For perovskite cells an increasing amount of literature shows that the substrates are solely cleaned through solvent rinsing and without sonication.[11, 12, 13, 14, 15, 16, 17] High efficiencies can be obtained nevertheless and considering that the additional sonication steps in multiple solvents takes several hours, this step was left out in order to rationalise the process.

Additional cleaning after solvent treatment of the substrate is mostly done with ozone treatment or plasma etching. The effect of surface pre-treatment was analysed

with contact angle measurement, AFM and cyclic voltrammetry of differently prepared substrates. The cleaning procedure consisted of scrubbing the samples with a 2 wt% Hellmanex solution and then rinsing with milliQ water, acetone and IPA. Oxygen plasma cleaning was done after the normal cleaning procedure. The effect of the cleaning procedure on the substrate was measured *via* contact angle (see fig. 3-2a-c). Measurements on the bare FTO surface were taken directly after cleaning and in certain time intervals after the plasma cleaning in order to test the reversibility of the treatment (see figure 3-2d). A significant decrease of the contact angle upon plasma treatment was seen from around 20 ° for an untreated surface to complete spreading ($\Theta \approx 0$ °) immediately after the plasma treatment. The surface wetting slowly decreases again until it almost reached its initial value after about 2 days. The correlation between time and contact angle does not follow a strict linear regression, as a data point after 28 h decreases its value, instead of increasing. The reason for that is probably that a fresh (and different part) of the substrate was measured each time, which could have experienced a slightly different pre-treatment during the pulsed laser deposition of the FTO layer, the soap or solvent cleaning. During measurements it can also be seen that the contact angle is not always consistent at every point throughout the substrate area (2.5×2.5 cm^2), which is why five measurements were taken for each data point and the mean average and standard deviation were calculated.

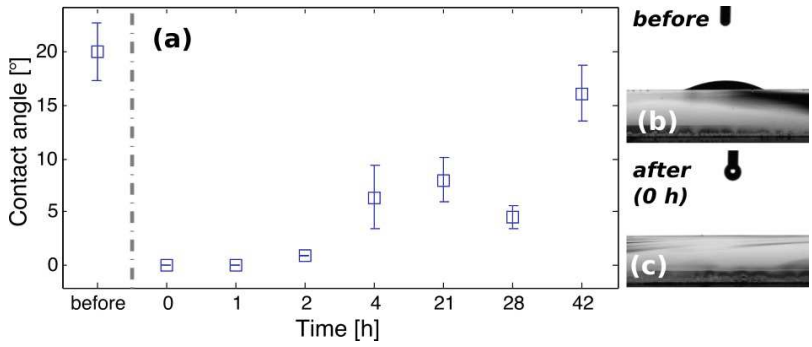

Figure 3-2: Plasma cleaning of TCO substrates causes an almost complete wetting directly after the treatment. This effect decreases over time if the substrates are left in dry air, so that substrates return to almost their initial surface wetting properties about 2 days after treatment (a). All measurements were taken 5 times to determine average and standard deviation. Optical images taken before (b) and immediately after (c) the plasma cleaning.

Clearly, the quality of the deposited TiO_2 thin-film is influenced by the surface cleaning procedure, as figure 3-2 shows that it has a significant effect on surface wetting and thin-film formation. This is of special importance during the spin-coating and crystallisation of the TiO_2 film. The surface oxidation of the FTO also influences its work function as a degenerate semiconductor, which in turn determines electron transport in the working cell.[18] Besides the direct measurement of the bare FTO surface with contact angle measurements, the quality of the spin-coated TiO_2 film was analysed with cyclic voltammetry with a Fe^{+II}/Fe^{+III} redox couple as described in the experimental section. A blank FTO substrate and a bl-TiO_2 (blocking layer) that was deposited with spray-pyrolysis were measured as references. The samples were spin-coated solutions of TTIP, spun at 2000 rpm onto FTO substrates after different cleaning procedures. The results showed that the bare FTO electrode has the fastest electron transfer kinetics. This can be seen by the separation of the anodic and cathodic peak potentials (see fig. 3-3a). The measured peak separation is greater than the expected 57 mV for a reversible system. This can be explained by the FTO, which is a non-ideal electrode and is likely to induce an activation overpotential (see equation 2.4) and also contributes with a series resistance and substrate roughness (see AFM image), resulting in a peak separation of about 700 mV. TiO_2 layers that were deposited by spray-pyrolysis showed an excellent quenching behaviour, with hardly any noticeable currents (fig. 3-3b). This indicates a continuous and dense compact layer without pinholes that does not allow any current to leak through. AFM images show hardly any changes compared to the blank FTO sample (see fig. 3-3a), which is indicative of a dense and compact layer that is deposited on top of the substrate, and hence does not change its morphology.

These results were compared to our spin-coated samples, which indicated an incomplete suppression of current transport; an effect that can be modified by altering the cleaning procedure of the glass substrate. The signal intensity is decreased for the spin-coated samples for both substrate cleaning procedures. The peak to peak separation increased as well, which becomes most significant for the substrate that was additionally plasma cleaned. This indicates decreased electron transfer rate constant k_s in relation to the rate of mass transport to the electrode. The reason for this could be that the charge-carrier needs to pass the blocking layer by diffusion through small pores of the spin-coated layer, making the diffusion to the electrode the rate determining step. This new bottleneck for the charge transport decreases the measured current as well. Another explanation would be that the blocking layer forms a tunnelling barrier for electrons, which slows down the electron transfer rate, but tunnelling barriers are usually on the scale of several nanometres and the thickness in these samples are around

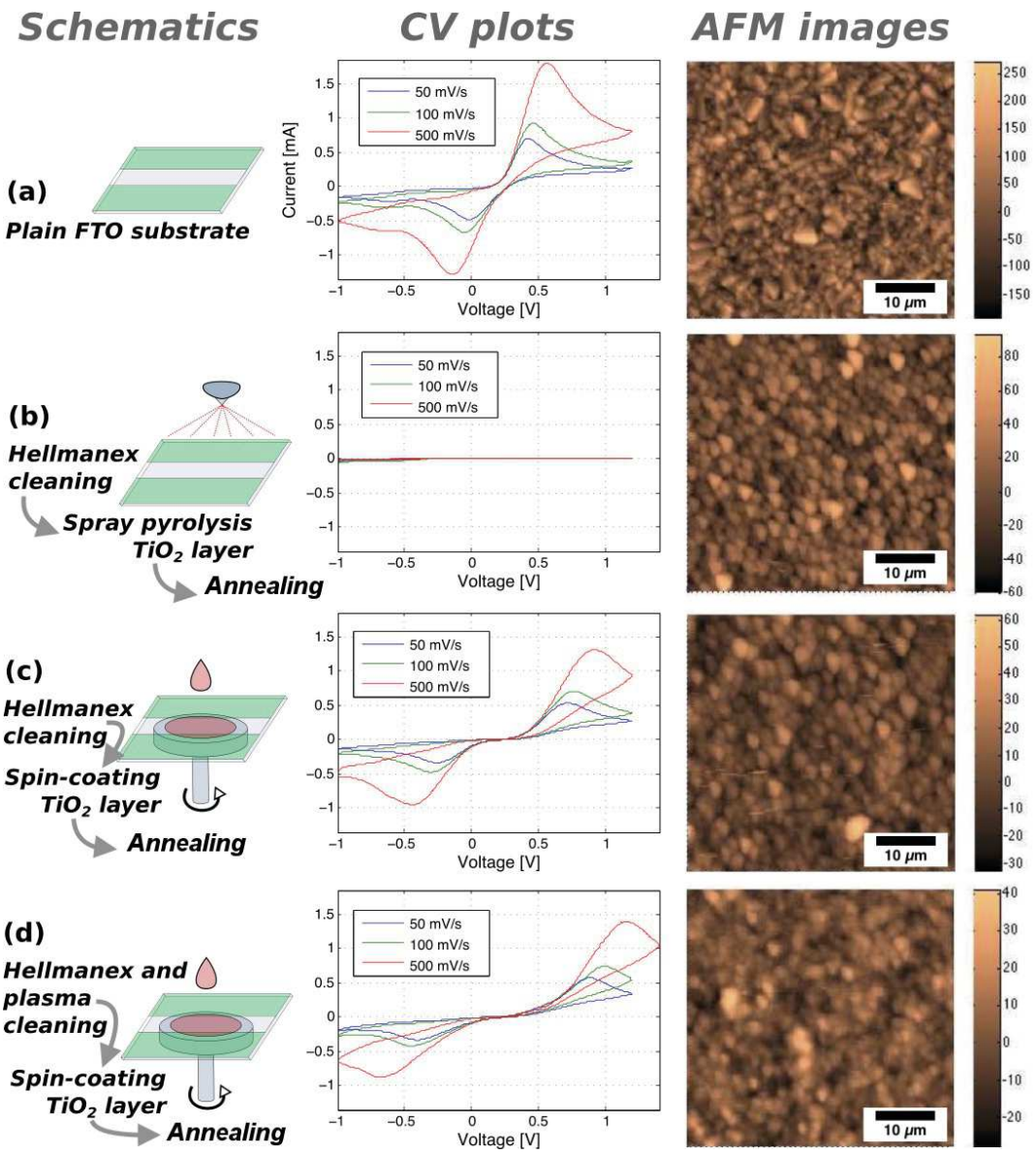

Figure 3-3: Comparison of different TiO_2 layer deposition methods and substrate cleaning procedures: (a) Plain FTO substrate; (b) spray-pyrolysis deposited layer; (c) spin-coated layer on a Hellmanex cleaned substrate; (d) spin-coated layer with an additional plasma cleaning step. Cyclic voltammetry measurements were performed against a Ag/AgCl (3 M KCl) reference with a Pt wire as counter electrode in a 100 mM solution of Fe^{+II}/Fe^{+III} with background electrolyte (10 mM KCl). Scans went from −1 V to 1.2 V at various scan rates, mentioned in the legend.

100x larger, which would make tunnelling nearly impossible.

Comparison of the AFM images (see fig. 3-3, right) shows a morphology that seems smoother than the blank FTO (note the decrease in z-scale) and a decreased film roughness (see fig. 3-4). The spin-coating seems to form a less continuous and dense layer than spraying and preferentially fills valleys of the rough FTO landscape to decrease surface tension.

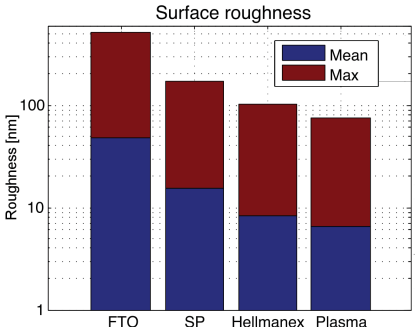

Figure 3-4: Comparison of substrate surface roughness for different surface treatments. FTO refers to blank substrate; SP spray pyrolysis; Hellmanex cleaned substrate with spin-coated layer and an additional Plasma cleaning step, before spin-coating.

It is known in literature that different deposition techniques cause different types of defects in the blocking layer.[19] The exact nature of the defect depends not only on deposition parameters but also post treatments, such as plasma or calcination can induce defects. The occurrence of the Fe^{+II}/Fe^{+III} redox signal in fig. 3-3c-d indicates an insufficient blocking behaviour for the observed system and is somewhat surprising, considering that spin-coating bl-TiO_2 is the most commonly used procedure for the creation of $MAPbI_3$ cells and produces an efficient SC with good blocking behaviour. It is known from recent studies that the spin-coated bl-TiO_2 can have different relative pinhole areas.[19] Therefore, one has to differentiate between charge transport in solution as for the measured system and a solid-state interface. Charge carriers in the former case have a size of approximately 0.47 nm (as calculated *via general AMBER force field*[5]) which could diffuse through small pores in the blocking layer. On the other hand, grain sizes of the crystallised $MAPbI_3$ layer are in the order of 1 μm,[3] and therefore substantially larger. This would explain a functioning $MAPbI_3$ cell without shunting across the spin-coated bl-TiO_2 layer. Despite the similarity regarding photovoltaic device performance values, blocking layers with porous defects give an amplification of photocurrent under reverse bias. This makes them a viable candidate for photo-detectors (PD). However, the underlying mechanism is as yet unknown.[20]

In conclusion, the cleaning procedure of FTO substrates was shown to benefit from an additional plasma cleaning step. Especially the spin-coated TiO_2 layer performs better, because of the increased wettability. The plasma-induced change of wettability seems to be reversible within several hours and a processing within 2 h after plasma cleaning is recommended. Usage of a spray pyrolysis TiO_2 layer gives a more dense and compact layer and shows a better charge-transport quenching in solution. Even though

spin-coated layers are easier and faster to fabricate, the results show that greater care needs to be taken during their deposition.

3.2.2 Low temperature $MAPbI_3$ fabrication in air

In order to obtain efficient devices, the charge transport and surface morphology of the $MAPbI_3$ thin-film is of crucial importance. However, the intrinsic instability of the thin-film for the desired film thickness of about 300 nm poses a problem, which makes the process control during fabrication complicated and an important issue.[3, 21, 22] Most reported fabrication routines employ either a convection oven or a hotplate for the annealing of the precursor thin-film, in order to drive out the solvent and crystallise the $MAPbI_3$ perovskite. Usually, the optimised conversion temperature that yields the best thin-film quality and most efficient devices is around 100 °C,[23, 24] with some variation including temperature ramp profiles or flash annealing steps in the end at higher temperatures,[25] or gas quenching steps after the spin-coating to homogenise the thin-film.[26] In this section a different PSC fabrication route was investigated, by creating a laminar flow setup with a heat-gun, that has a higher air flow rate than other routes. This setup allows a significant reduction of the fabrication temperature below 100 °C without residual precursor in the resulting thin-film. It incorporates the beneficial thin-film formation of a gas quenching step, which at the same time aides the crystallisation of the perovskite. A schematic of the process can be seen in figure 3-5. The properties of the thin-film

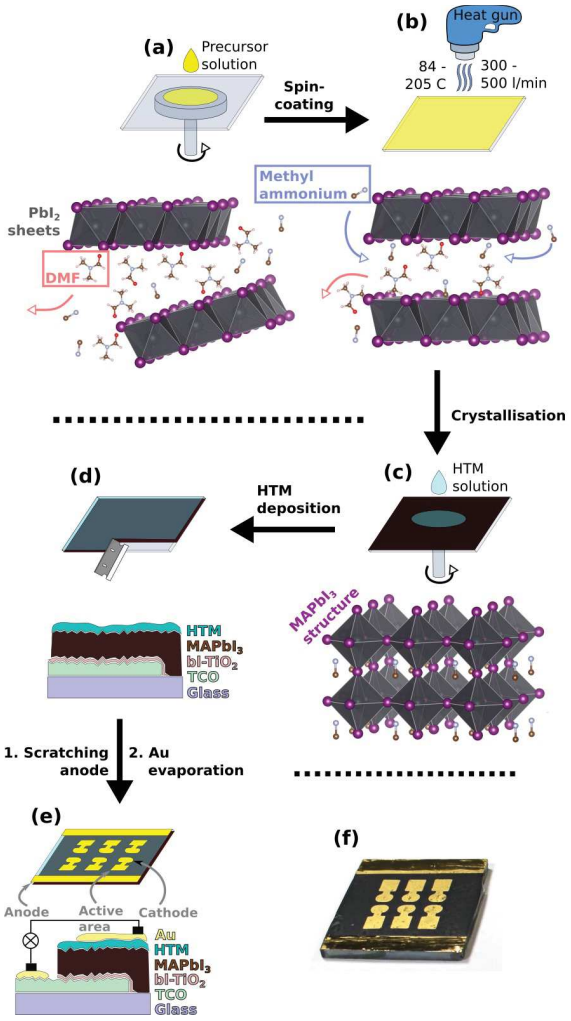

Figure 3-5: Schematic of the fabrication procedure. (a) Drop-casting and spin-coating of precursor solution in ambient environment; (b) temperature and air flow drives out solvent from intermediate state; (c) HTM solution drop-casted and spin-coated onto the crystallised $MAPbI_3$; (d) scratching of material at the anode before evaporating the Au contacts. (e) Shows the final cell with the real equivalent shown in (f).

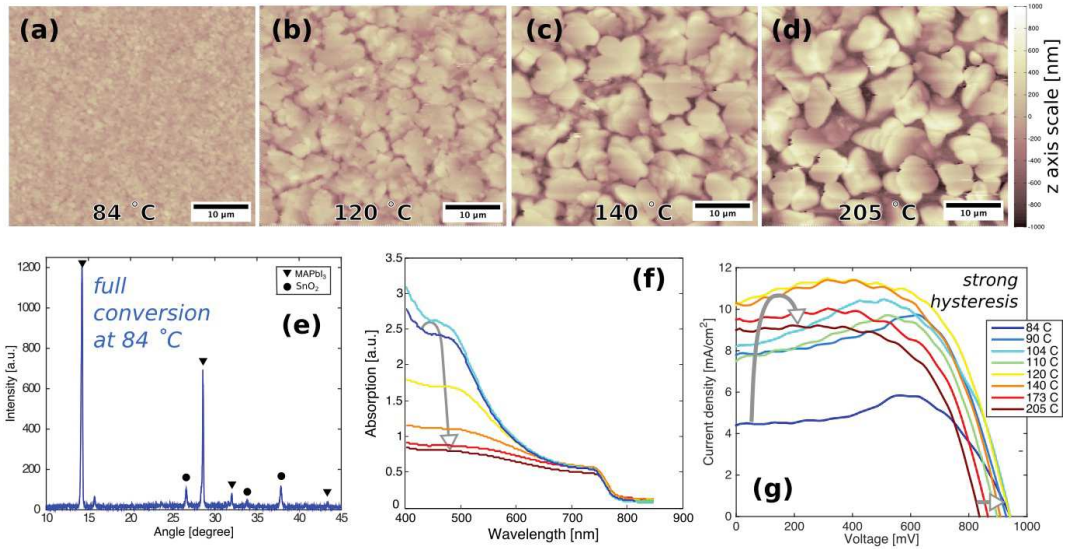

Figure 3-6: Measured film properties: (a-d) AFM images showing the morphology of different perovskite annealing temperature between 84 °C and 205 °C. (e) XRD diffractogram of low-temperature perovskite film annealed at 84 °C shows complete conversion. (f) UV-Vis Absorption spectrum of samples annealed at different temperatures. (g) Typical IV curves for different temperatures.

were analysed with respect to morphology, absorption behaviour as well as structural purity and finally also photovoltaic performance. AFM measurements give a fast and precise evaluation of film morphology and quality. The film roughness increased with annealing temperature, as can be seen in figure 3-6a-d. Smooth films were formed at lower temperatures (fig. 3-6d), while discontinuities started to develop at temperatures around 120 °C (fig. 3-6c): pinholes were forming, leaving shunt paths that decrease light absorption and have detrimental effects on the shunt resistance in the final cell. By further increasing the temperature shunt paths increase in size and start to separate into crystalline islands. Furthermore, the crystallite size increases. When approaching 200 °C, the domains became mostly separated, with many islands consisting of only a single large crystallite (fig. 3-6d). An overview of all obtained films made for this project is given in Appendix A (fig. A-1).

X-ray diffraction measurements (XRD) were taken in order to confirm the complete formation of the perovskite layer. Especially the sample annealed at 84 °C gave a smooth and continuous film having the characteristic $MAPbI_3$ absorption profile; however many reports in literature state that annealing temperatures < 95 °C give an incomplete conversion of the precursors.[22, 3] The reason for this discrepancy might be the differences in fabrication routine, with most literature reports referring to annealing on a hotplate where the temperature on the hotplate is higher than the

effective temperature of the thin-film on the substrate. Furthermore, the high laminar flow induced by the heat-gun helps to drive out solvent and assist the crystallisation, therefore decreasing the required annealing temperature. The XRD pattern shows that the precursors have fully converted into $MAPbI_3$ with a clear characteristic perovskite (110) reflection at around 14 ° and (220) reflection at around 28 °. Also, the most characteristic precursor reflections of the (111) plane of $PbCl_2$ at around 25 ° and the (002) plane of PbI_2 at 12.7 ° are not present. All reflections can be assigned to either $MAPbI_3$ or SnO_2, which forms the substrate, and only a small artefact at 15.7 ° remains unknown. Because of the absence of precursor signal, it can be assumed that even at the reduced temperature of 84 °C the film has fully converted to $MAPbI_3$.

UV-Vis measurements of the $MAPbI_3$ films show a sharp absorption onset at around 780 nm for all samples (see fig. 3-6f-g) and a very high absorption in the UV-region as a characteristic of this $MAPbI_3$ perovskite, which can be seen for low-temperature annealed samples and makes them appear dark reddish. This is consistent with the bulk absorption of $MAPbI_3$ and with the continuous film morphology measured *via* AFM. Films processed at higher temperatures appear lighter and greyish in colour and show a comparably flat UV-Vis profile. The reason for this appears to be the formation of crystalline islands, as seen in AFM. Strong light absorption of the thicker $MAPbI_3$ islands is opposed to low light absorption paths in the 'valleys'. This superposition of high and low light absorption leads to a neutral density light filtering, resulting in a grey colour and flat UV-Vis profile. One potential application of $MAPbI_3$ islands are semitransparent solar cells.[27] However, despite the complete conversion of the 84 °C annealed films (see fig. 3-6e), the absorption values are slightly higher for annealing temperatures just above 100 °C. This could indicate that the crystallisation process influences the quality of the film, as proposed previously (chapter 1) and defect states might affect the optical properties as well. This effect becomes more apparent when the photovoltaic performance is measured, as is discussed in the next paragraph.

The different $MAPbI_3$ films were made PV cells by spin-coating spiro as an HTM on top and finally evaporating a gold top contact. The resulting cells had a typical performance of around 5 to 6 % with a strong hysteretic contribution, which is not uncommon for planar cells with the given contact materials.[28] Therefore a quantitative evaluation of PV performance parameters does not seem useful (and might be misleading), but a qualitative comparison shows interesting trends. First of all, the photocurrent increases when comparing the high-temperature processed cells (173 and 205 °C) to slightly lower temperatures. This can be explained by the higher light absorption (see fig. 3-6f). But a maximum is reached at about 120 °C; despite a further increasing absorption, the photocurrent decreases. This indicates an inefficient charge transport,

e.g. carrier loss due to recombination, and is another indication that the quality strongly depends upon the crystallisation route. Secondly, the photovoltage increases steadily from about 820 to 950 mV (arrow in fig. 3-6g), which can be partially attributed to the increase in photocurrent and absorption, and causes the Fermi-level to rise, but might also be caused by the apparently increasing hysteretic contribution. A detailed analysis of hysteretic effects can not be given at this stage, because the measurements were taken before improving the measurement routine (described in the next section), which allowed for more comprehensive IV measurements. The IV curves given in this section are representative for cells obtained at that temperature, the full statistical distribution can be found in the Appendix A (fig. A-3).

In this section a new fabrication route for perovskite thin-films was developed that allowed a reduction of the already low processing temperature of perovskite solar cells to about 84 °C under a high gas flow rate. This approach is similar to the so called gas quenching method[29, 26] but keeps the high air flow rate throughout the whole annealing time. The process yielded a complete $MAPbI_3$ transformation, which is aided by enhanced solvent evaporation. The thin-film morphology is favourable at lower temperatures and influences the absorption and PV performance but with another contribution possibly stemming from the crystallisation condition (*e.g.* defect density). Thus, despite having a complete precursor conversion into a smooth and continuous film at 84 °C, the absorption and PV performance show their best values at higher temperatures. This indicates that defect formation seems to be more favourable (lower) at higher temperatures. The optimum fabrication conditions can be seen as a trade off between thin-film morphology, crystallinity and electronic structure.

3.2.3 Cell layout and measurement routine

After a thorough substrate preparation and blocking layer deposition (section 3.2.1), the next fabrication step is the deposition of the active (perovskite) layer. Even though experimental sections in scientific reports are habitually detailed regarding chemical procedures during this step, they are often poor regarding fabrication routines that are lab-specific, *e.g.* substrate size and cell layout. Hence the first perovskite cells produced in the course of this thesis had an unfavourable layout (see fig. 3-7, left). More specifically, a (too) large gold top-contact of about 1 cm^2 was sputtered by masking the cell with sticky tape (Kapton). Because the sputtering process damaged the HTM layer, initial cell efficiencies were mostly < 1 %. Improvements were made by evaporating the gold top-contact at low deposition rates (< 1 nm/min) as well as adapting evaporation masks. The initial size of the active area resembled the DSSC layout, but it was found that a decrease of the active area was advantageous because of the much thinner layers in $MAPbI_3$ cells (~ 400 nm) which give rise to short circuiting caused by small impurities (a dust spec), which are more likely to occur in a large area cell. This would not have a major impact on the performance of a DSSC (thickness ~ 15 μm), but significantly decreases the performance of a PSC. The active area was therefore divided into pixels with an individual area of about 0.1 cm^2 each (fig. 3-7, second from left). Usage of larger substrates of 12 pixels/cell made the fabrication easier and faster, but the distance between the pixels was found to be too small so that a conjunction of two pixels could be measured sometimes. This resulted in the measurement of surprisingly large current values, about twice of the expected value. Therefore the cell layout was reduced to 10 pixels/cell. In a last optimisation step the anode/cathode positioning was swapped, which facilitated scratching off the thin-film for the bottom electrode. Furthermore the outermost pixels were removed to exclude artefacts from the spin-coating at the substrate edges to influence the active area. Narrowing of the top contact in areas that are covered by the shadow mask is supposed to decrease dark currents during measurements.

Figure 3-7: Five different cell architectures, as of November/13, January/14, March/14, May/14 and November/15, respectively (left to right).

As mentioned earlier in chapter 1, typical voltage scanning protocols with scan speeds that were commonly used for DSSC and other solar cells resulted in a falsification of the obtained IV curve through the occurrence of anomalous hysteresis.[28] The scanning speed and direction of the measurement strongly effects the measured performance of the cell. This issue required and adjustment of the measurement software. For this purpose a program was created with LabView™, that was able to cope with this new phenomenon. In addition to that, the measurement system was upgraded to enable an inline measurement of up to four cells.

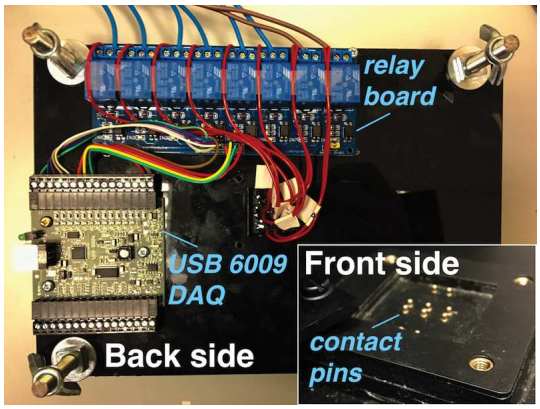

Figure 3-8: Front side and back side view of the home built IV measurement stage. Cell contact is made with spring loaded pins, which are adressed *via* a relay board that gets controlled with the USB 6009 DAQ device.

The developed software enabled a comprehensive control over the measurement procedure of the solar cell. Controllable settings include the pre-treatment (voltage bias and delay) and measurement parameters (scan speed and direction). Furthermore, the setup allowed for an automatised measurement of a whole cell, by coupling the written software to a home built hardware setup (see fig. 3-8). This setup consists of a sample holder that was adapted for the new perovskite cell layout. Contact to the individual pixels of the cell was made *via* spring-loaded pins (Mill-Max). Each pin can be individually selected with a relay board (Sainsmart 16-channel 12 V module), which is addressed with a USB 6009, National Instruments DAQ device. This enables an automated measurement of all pixels in one cell.

The improvement of the fabrication routine for PSC was done in multiple incremental steps, focusing mainly on the cell architecture and measurement routine. This section summarised the improvements of the measurement setup, that stretched through this whole study and form the foundation for other experiments in this thesis. Especially the fabrication and measurement of high-hysteresis cells in section 3.2.6 is based upon this routine.

3.2.4 Influence of solvent concentration

Fabrication of the perovskite thin-films in a fume hood (rather than a glovebox) offers a simple way to prepare PSC but it imposes a variety of problems regarding the reproducibility of results. It is well-known and widely reported in literature that humidity has a critical influence on the formation of the perovskite film as well as its stability.[30, 31, 32, 33, 34] And because the environmental humidity levels can vary depending on weather conditions, the efficiencies of cells made in ambient conditions can vary. Therefore it seems like moving the fabrication process into controlled environment (*e.g.* glovebox) is a solution to this problem, and in fact most reported PSC and virtually all high-performance PSC are produced in gloveboxes nowadays.[35, 36, 37, 38, 39] But even though moving the fabrication process into the glovebox removes the exposure to environmental atmosphere, it creates another problem due to the build-up of the precursor solvent that evaporates during the spin-coating and annealing process.[40] A fundamental issue when working in a glovebox is therefore the degree and dynamics of the solvent atmosphere build-up.

This issue was investigated in this work by building a self-made gas sensor. The device is based on two different sensors, that show sensitivity towards different types of solvents (see fig. 3-9). A MQ2 sensor was used that is sensitive for liquid propane gas and combustibles and a MQ9 sensor (both Seed Studio) that is sensitive for CO and combustibles. Both sensor are expected to be sensitive to the (combustible) solvents used for the perovskite precursor. The use of two sensors should cover a broader concentration regime and is more reliable as data is measured from two individual sources. For data acquisition the sensor was placed between spin-coater and hotplate and ran throughout a whole fabrication procedure as well as during solvent decay, covering in total 400 min (over 6 h). As shown in figure 3-9, the solvent starts to build up a few minutes after starting the spin-coating procedure. Another increase can be seen after starting the annealing of the thin-films. The build up to the maximum value takes a bit over 20 min. This can be explained by the retention of the solvent within an intermediate phase, where the solvents acts as a space holder in the network and gets gradually replaced by the organic cation.[36, 38] Once the residual solvent was replaced and the perovskite fully converted, the solvent concentration remains constant until the drying train is switched on. This initiates a steady decay, that slowly removes the solvent from the atmosphere. But despite measuring the solvent decay for more than 4 h, the atmosphere did still not recover to its initial value before spin-coating. It needs to be mentioned that the measured values only represent relative values of resistivity of the gas sensor, which are used to qualitatively evaluate the build-up and decay of solvents but do not allow a quantitative analysis of *e.g.* solvent concentrations.

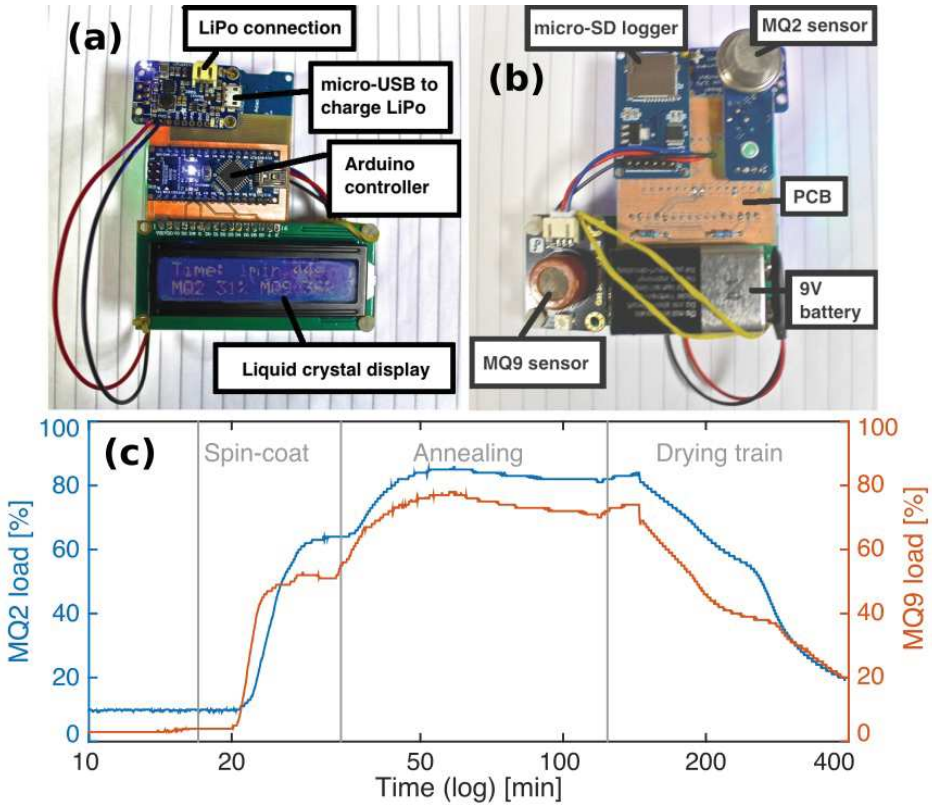

Figure 3-9: Home-built gas sensor: Front view (a) shows the display as well as controller and interfaces. The back view (b) reveals both sensors (MQ2 and MQ9) as well as the battery and the SD-card logger. (c) Qualitative measurement of the solvent concentration during a full deposition cycle.

In summary, a self-made sensor for the detection of organic solvents was built from DIY components to measure the solvent distribution and removal efficiency of the drying train. The results show fast build up that was partially retained by a solvent-intermediate phase and a very slow solvent removal. This experiment highlights that the atmosphere of the working place needs to be taken into consideration upon fabrication of PSC, even when working in a glovebox environment, because a complete removal of solvents can take a full day.

3.2.5 A Simple Approach for the Fabrication of Perovskite Solar Cells in Air

A key aspect of research in perovskite solar cells is the development of a reproducible production routine. This should ideally be done without the need for costly lab equipment, such as gloveboxes, which is opposed to the idea of a cheap and mass producible energy material. An examples of an alternative fabrication process is the vapour deposition, where both precursor salts are simultaneously sublimed onto the substrate in vacuum chamber.[41, 42] Another option is the solution-mediated intercalation of MAI into a spin-coated PbI_2 film,[35] which facilitates the thin-film formation because PbI_2 is easier to deposit than $MAPbI_3$. However, several environmental factors influence the conversion process, *e.g.* temperature or water content of the solvent.[43, 31] A modification was reported by exposing the PbI_2 film to MAI vapour, and therefore leaving out the liquid mediator.[44] This technique was labelled vapour assisted solution processing (VASP).

Our new technique consists of a modified VASP process, called vacuum-vapour assisted solution processing (V-VASP) technique. It enhances the VASP process by applying a static vacuum during the conversion step, which lowers the sublimation temperature of the MAI precursor and improves penetration into the PbI_2 layer. It makes do with only basic lab equipment: A vacuum pump, a hot plate, a desiccator lid and a spin-coater is all that is needed to produce perovskite solar cells. Moreover, the vacuum conversion process eliminates humidity as a variable from the process control and allows a better batch-to-batch reproducibility. To establish a dependable conversion process, the PbI_2 deposition was optimised to achieve a flat and shiny thin-film; therefore several solvents and annealing times were screened regarding the quality of the resulting PbI_2 film. An initial assessment can be done by comparing the 'shininess' of the sample, which correlates to microscopic surface smoothness. A quantitative evaluation was done by AFM, which was also used determine the thickness of the PbI_2 layer.

For the perovskite conversion, the MAI was assembled around the substrate on a hotplate and the lid was placed on top. As soon as the vacuum was applied, the timing was started and the valve closed. The static vacuum condition throughout the process was used to avoid contaminations from the pump. Optimum perovskite conversion parameters were developed with different deposition times and architectures. Perovskite cells achieved efficiencies of up to 12.7 % PCE and remained stable on a bench top for 14 days (about 50 % humidity).

3.2.5.1 Related publications

RGN contributed to this study by modifying the VASP process towards the (vacuum) V-VASP process together with SC. RGN carried out the AFM measurements and morphological optimisation of the PbI_2 precursor film, that formed the basis for the V-VASP conversion that was carried out by SC.

Journal of Power Sources 297 (2015) 504–510

Contents lists available at ScienceDirect

Journal of Power Sources

journal homepage: www.elsevier.com/locate/jpowsour

A simple approach for the fabrication of perovskite solar cells in air

Simone Casaluci [a], Lucio Cinà [a], Adam Pockett [b], Peter S. Kubiak [b], Ralf G. Niemann [b], Andrea Reale [a], Aldo Di Carlo [a], P.J. Cameron [b, *]

[a] CHOSE - Centre for Hybrid and Organic Solar Energy, Department of Electronic Engineering, University of Rome "Tor Vergata", Via del Politecnico 1, 00133, Rome, Italy
[b] Department of Chemistry, University of Bath, Bath, BA2 7AY, United Kingdom

HIGHLIGHTS

- Simple technique for the preparation of $MAPbI_3$ investigated.
- A glove box and an inert atmosphere were not necessary.
- Only a spin coater, hotplate, desiccator and low vacuum pump required.
- Glassy films were produced giving 12.7% efficiency for a planar device.

GRAPHICAL ABSTRACT

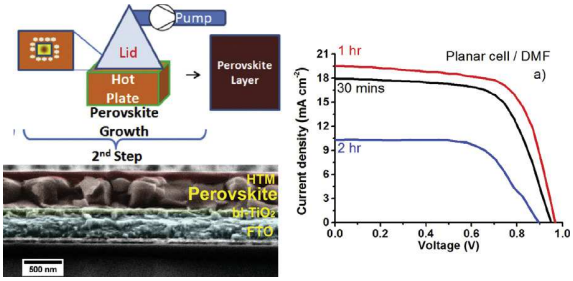

ARTICLE INFO

Article history:
Received 20 April 2015
Received in revised form
23 July 2015
Accepted 3 August 2015
Available online 25 August 2015

Keywords:
Stability
Perovskite solar cells
Ambient atmosphere
Vapor-assisted solution processing

ABSTRACT

Vacuum-vapor assisted solution processing has been investigated as a simple and low cost method for preparing perovskite solar cells without a glove box. The devices were prepared in ambient air without using a high vacuum or an inert atmosphere. A maximum efficiency of 12.7% for planar perovskite ($CH_3NH_3PbI_3$) devices was obtained. The perovskite films could be stored in air (20 °C, ~50% humidity) for up to 14 days without discoloration or the appearance of crystalline lead iodide in the films.

1. Introduction

The perovskite solar cell is emerging as a new type of photovoltaic technology which may become a widespread low-cost technology in the future [1]. Methylammonium (MA) lead halide $MAPbX_3$ (X = halogen) and mixed-halide perovskites are the most studied light absorber layers. Organometal halide perovskites have attracted attention due to very impressive electrical/optical properties such as: i) diffusion lengths of up to 1 μm in mixed halide perovskites [2,3], ii) good ambipolar transport of charge [4], iii) efficient absorption in the visible range [5–7], and iv) a very simple synthesis method [8]. Over the last 5 years the power conversion efficiency (PCE) of organometal halide perovskite-based solar cells has rapidly increased from 3.8% to certified 20.1% making this technology comparable to both crystalline silicon (c-Si) and thin film (CIGS, CdTe etc.) technologies [9,10]. A range of techniques have been developed to grow perovskite thin films. The most

* Corresponding author.
E-mail address: p.j.cameron@bath.ac.uk (P.J. Cameron).

http://dx.doi.org/10.1016/j.jpowsour.2015.08.010
0378-7753/

common procedure is the direct deposition of the perovskite precursor solution (called one-step solution deposition) on top of mesoscopic [8,11–15], or planar oxide [16–18]. In particular, a mixture of PbX (X: Cl, I) and CH_3NH_3I dissolved in different solvents such as N,N-Dimethylformamide (DMF), Dimethyl sulfoxide (DMSO), γ-butyrolactone (GBL) or N,N-dimethylacetamide (DMAc) is deposited on the substrate by spin-coating or drop-casting to realize the active layer after the annealing process [19]. This deposition procedure is critical to ensure perfect film morphology as the presence of pinholes and defects leads to lower photovoltaic performance (especially in terms of V_{oc} and J_{sc} values). To obtain more reproducible perovskite film morphology, two step deposition techniques have been developed. In the first-step of the sequential deposition, a PbI_2–based solution is directly deposited by spin-coating on the electron transport layer (ETL) [18,20], or onto a mesoporous scaffold [21,22]. Then, the perovskite film can be obtained by dip coating into methylammonium iodide (MAI) solution in isopropanol (IPA) (the second-step deposition). As reported by Ma et al. [23], and by Im et al. [5], the two step procedure is better than the one step procedure in terms of the perovskite morphology as more uniform and reproducible films are prepared [24]. Other strategies to produce the active layer are based on $MAPbX_3$ deposition using vapor techniques, where the perovskite growth is carried out without using any solvent. In fact, several different vapor deposition techniques are reported in literature, showing better film uniformity and surface coverage of the active layer compared to the solution processed films [18,25]. However vapor deposition has some problems as the source temperature must be tightly controlled due to the relatively low thermal stability of the perovskite precursors. Another kind of two-step deposition is the vapor-assisted solution processing technique in which a spin-coated PbI_2 sample is exposed to CH_3NH_3I vapor in an N_2 atmosphere to create the perovskite layer [26]. Using this approach good surface coverage, low surface roughness and excellent film quality is obtained, with Chen et al. preparing planar devices with a top efficiency of 12.1%. Recently, Leyden et al. developed hybrid vapor phase deposition (HVPV) to grow perovskite layers by chemical vapor deposition, preparing cells in an inert atmosphere with a top efficiency of 11.8%. The cells showed long term stabilities of up to 1100 h in an N_2 environment [27]. Hao et al. used a vapor deposition technique in a glove box to produce 10.6% efficient devices [28]. For all deposition and growth techniques the long term stability of the perovskite solar cell is the most critical issue that needs to be addressed, because as reported by Niu et al. $CH_3NH_3PbI_3$ decomposes rapidly in the presence of moisture [29].

This work is based on the two-step deposition technique using vapor-assisted solution processing (VASP) [26]. Our methodology, here called vacuum-vapor assisted solution processing (V-VASP), builds on the method developed by Chen and by Hao. V-VASP has been developed to avoid the use of a glove box or an inert environment during film preparation. In fact, the preparation of the active layer is performed in air with only a low vacuum to ensure a moisture "free" environment. We first optimized the annealing time of PbI_2 in air using different solvents (such as GBL, DMF or DMSO). The growth time of the perovskite layer during the second-step was then optimized for both Planar-Perovskite Solar Cells (P-PSC) and Mesoporous-Perovskite Solar Cells (M-PSC). Planar cells showed a maximum efficiency of 12.7% for a perovskite growth time of 1 h. After only 30 min of perovskite growth time the performance was still over 11%. $CH_3NH_3PbI_3$ layers prepared using the V-VASP procedure did not discolour when stored in air (14 days at 20 °C, humidity around 50%) without encapsulation and XRD showed an absence of crystalline lead iodide after 14 days. This result contrasts favourably with the reported stability of solution processed films [29,30].

2. Experimental section

The FTO/glass substrate (TEC 7, 8 Ohm $\square^{-1}$, 25 × 25 mm) was etched into the desired pattern with Zinc powder and 2 M HCl diluted in deionized water. The substrates were first cleaned with Hellmanex (2% solution) diluted in deionized water, then with isopropanol, and finally acetone. They were then treated with an oxygen plasma for 15 min to remove any remaining organic residues. Logical steps to fabricate the devices are shown in Fig. S10, ESI. A TiO_2 blocking layer (bl-TiO_2), made according to a reported procedure [31], was deposited onto the substrate by spin-coating at 2000 RPM for 60s and after drying at 150 °C for 15 min a sintering process at 500 °C for 30 min was done. To obtain a mesoporous layer, a TiO_2 paste (Dyesol 18NR-T) was diluted 1:5 with ethanol and spin coated on the substrate at 1000 RPM for 60s (thickness around 300 nm). The samples were dried in an oven at 100 °C for 10 min and then sintered at 500 °C for 30 min. PbI_2 powder (Aldrich, 99%) was dissolved either in DMF or in DMSO solvent (at a concentration of 400 mg ml^{-1}) and stirred at 70 °C. The hot PbI_2 solution was spin-coated on either a mesoporous scaffold to obtain mesoporous structure, or directly on the bl-TiO_2 to obtain a planar structure, at 4000 RPM for 30s on substrates preheated to 70 °C. These were then dried at 120 °C for 1 h in air to remove the solvent and drive the crystallization. For the perovskite growth, the sample was put on a hot plate and surrounded by MAI powder. The samples and the powder were put under low vacuum (desiccator lid attached to an Edwards 5 E2M5 Rotary Vane Dual Stage Mechanical Vacuum Pump) and heated at 150 °C for the desired time. For the hole transport material (HTM), 142.6 mg of Spiro-OMETAD was dissolved in 2 ml chlorobenzene (Aldrich, anhydrous 99.8%) and 4-tert Butylpyridine (17.5 μl, 96%, Aldrich) were added as well as previously prepared bis(trifluoromethane)sulfonimide lithium salt solution (37.5 μl of a 170 mg ml^{-1} LiTFSI, Aldrich, solution in acetonitrile). The HTM was spin coated at 4000 RPM for 45s and then left in air overnight in a closed box containing silica desiccant. Finally the samples were introduced into a high vacuum chamber to evaporate gold (Au) back contacts (thickness 80 nm). Each substrate has 10 pixels with 0.1 cm^2 of active area.

Powder X-ray diffraction (XRD) analysis was performed to investigate the phases of the samples, using a BRUKER D8-Advance. For the Atomic Force Microscope AFM measurements a Nanosurf AG, Easyscan 2 was used operating in dynamic force mode. Device performance was evaluated using a Class AAA solar simulator at AM 1.5G and 100 mW cm^{-2} connected to a source-meter (Keithley 2601A). For the measurements, the samples were covered with a shadow mask with an opening area of 0.1 cm^2 to illuminate only one cell at a time. Before measuring the reverse JV curve the sample was maintained for 5 s stabilization time at 1.2 V forward bias under illumination. A custom-made tool comprising a sourcemeter (Keithley 2612) and a monochromator (Newport 74000) was used to measure the external quantum efficiency (EQE) values of the device. For chronoamperometry measurements the cells were illuminated with a white LED (100 mW cm^{-2}, 3 Watts- 4200 K luxeon star).

3. Results and discussion

Vapor-assisted solution processing (V-VASP) involves the two-step deposition of methylammonium lead iodide (MAPI) films. A lead iodide layer is first spin-coated on top of a titania blocking layer before being converted to MAPI by exposure to MAI vapor under low vacuum. The lead iodide films were deposited and annealed in air (without any attempt to control the humidity, typical lab humidity was approx. 50%). The lead iodide films were then placed on a hot plate and covered with the lid of a vacuum

desiccator and a low vacuum applied. MAI vapor was created in situ to prepare the perovskite films. Finally the hole conductor was spin coated on top under ambient conditions. Despite carrying out the majority of the preparation steps under ambient conditions high quality MAPI films were made, the highest efficiency was 12.7% (OC-SC, see ESI for a discussion on hysteresis) for a planar device.

Firstly, the lead iodide deposition step was optimized. Spin-coated PbI_2 films were prepared using different solvents (GBL, DMF, DMSO); the annealing time (30 min, 1 h and 2 h) at 120 °C in air was also varied. As shown in Fig. 1c, the PbI_2 sample prepared from a GBL solution was paler than the others and poor coverage was attributed to the low solubility of the PbI_2 in GBL in the absence of other cations, ions, or other complexes as reported in the literature [23].

GBL deposited PbI_2 films didn't give good quality perovskite layers (Fig. S1a, ESI). For this reason, only PbI_2 films prepared from DMSO and DMF were studied further. The PbI_2 films prepared using DMSO appeared clearer and shinier than those prepared using DMF, in fact the roughness of the DMSO sample (average roughness, R_a, 6 nm) was lower than for the sample prepared from DMF (R_a 14 nm). PbI_2 layers were annealed for 1 h, after this time XRD (Fig. 1) showed a well resolved peak at 12.7°, corresponding to the (001) lattice [20]. Complete XRD spectra have been reported in supporting information (see Fig. S2a, ESI). The approximate PbI_2 crystal size was calculated from the full-width-at-half-maximum (FWHM) of the primary peak using the Scherrer formula [32]. Peak width is inversely proportional to crystallite size; in the case of films prepared using DMF, the crystallite size was calculated to be around 60 nm while in the DMSO case it was around 48 nm. The morphology of the PbI_2 layers was also studied by atomic force microscopy (AFM, Fig. S3(a) to S3(c) ESI). Films prepared from both DMF and DMSO showed a uniform surface morphology, however as outlined above the surface roughness was slightly lower for films deposited from DMSO than for films deposited from DMF. This result is consistent with the findings of Wu et al., and is thought to be due to a retardation of PbI_2 crystallization and the higher solubility of the lead in DMSO [20]. AFM images (not reported here) also showed that the morphology of the films did not change greatly with annealing time.

In the second step perovskite ($CH_3NH_3PbI_3$) film formation was optimized. In order to obtain a good photovoltaic performance a very uniform film, full coverage of the substrate and sufficient shunt resistance at the perovskite-electron transporting layer (ETL) interface are required [16]. Fig. 2 shows XRD spectra as well as photos and AFM images of perovskite samples prepared from PbI_2 films deposited from DMF (Fig. 2a) and DMSO (Fig. 2b). The substrates had a uniform dark-brown color (in web version). In both cases complete PbI_2 conversion was confirmed by the absence of PbI_2 peaks in the XRD spectra of the perovskite films. The principal peaks for $CH_3NH_3PbI_3$ were observed at 14.08°, 28° and 32° [21]. The principal peak at 2theta = 14.08° was narrow which suggested that in the case of both DMF and DMSO deposited films the grains showed good crystallinity and few defects [33]. In Fig. 2b it can be seen that when the perovskite was formed on PbI_2 prepared using DMSO, 30 min were enough to convert all the lead iodide. AFM images suggested a regular grain shape as well as good contact between neighbouring grains. Smooth films were obtained from DMSO and DMF (AFM analysis showed that the surface roughness was approx. 26 nm for DMF and 20 nm for DMSO) [26]. A smooth perovskite surface is important to make a good top contact without shunting through the HTM. In the cells presented here the hole transporting polymer layer was approx. 100 nm thick. Interestingly, at short times the perovskite grains follow the shape of the PbI_2 crystals (Figs. S4 and S5, ESI)) with relatively small grains formed on PbI_2-DMSO and slightly larger for PbI_2 DMF films. In both cases grain size increased (grain coarsening) with longer growth time [34].

Fig. 3 shows current–voltage curves for both planar perovskite solar cells (P-PSC) and mesostructured perovskite solar cells (M-PSC), measured under simulated AM 1.5G (100 mW cm^{-2}) solar irradiation in air. The solar cell parameters extracted from the J–V curves are summarized in Table 1.

We repeated the cell preparation twice and obtained the same trends both times. J–V curves for DMF based cells are shown in Fig. 3a. The performance of cells where the perovskite was grown for 30 min (V_{oc} = 950 mV, J_{sc} = 17.9 mA cm^{-2}, FF = 65.7%, PCE = 11.2%) and the best case of 1 h (V_{oc} = 967 mV, J_{sc} = 19.5 mA cm^{-2}, FF = 67.5%, PCE = 12.7%) was very similar. Fig. 3d shows a cross-section SEM image of the best device with 1 h of perovskite growth time on a PbI_2 film deposited from DMF

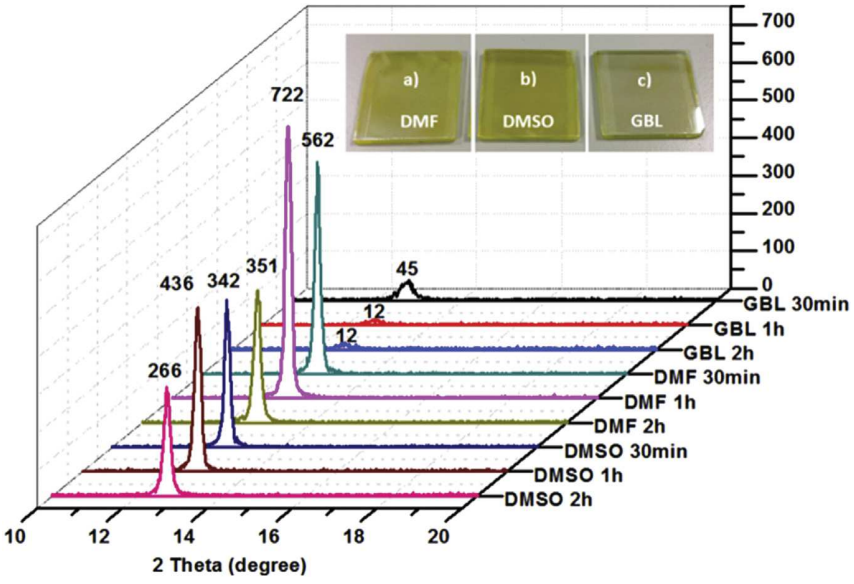

Fig. 1. Images and XRD pattern (from 10° to 20°) of FTO/bl-TiO_2 with layer of PbI_2 deposited from DMF a), DMSO b) and GBL c) solvent.

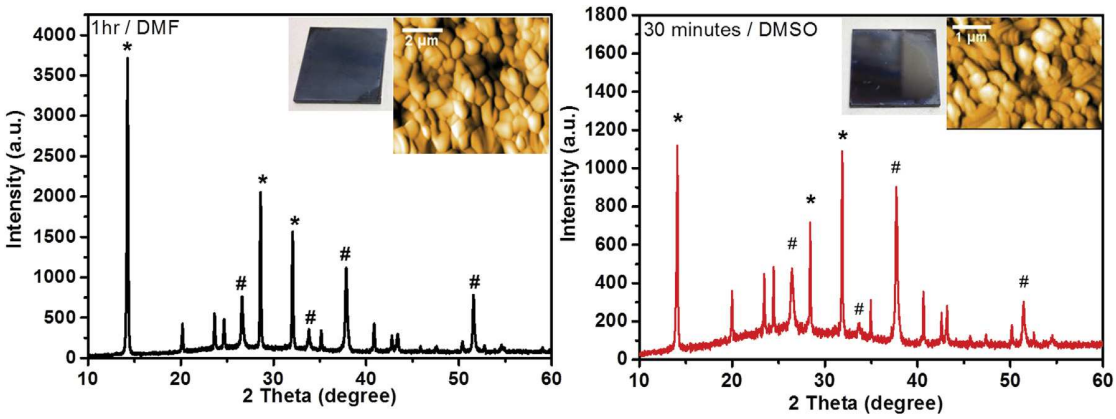

Fig. 2. XRD pattern, AFM image, Photo of PbI_2 films prepared from DMF a) and DMSO b) solutions. Best cases shown with perovskite growth for 1 h giving a roughness of 26 nm a), and growth for 30 min giving a roughness of roughness 20 nm b). Peaks labelled with a # are assigned to the fluorine-doped tin oxide substrate (2 theta = 26.5°, 33.7°, 37.7°, 51.5°), those with a * to principal perovskite peaks (2 theta = 14.08° (110), 28.5° (220), 32° (312)).

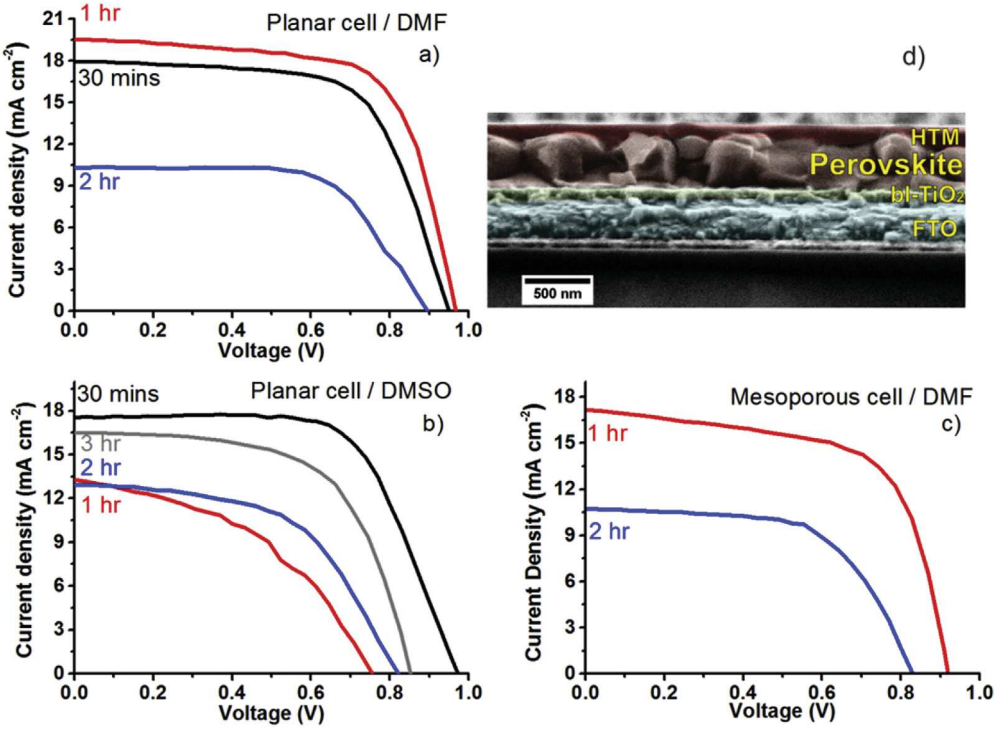

Fig. 3. Best JV characteristics for P-PSC and M-PSC under 100 mW cm^{-2} AM1.5 illumination and SEM image. Performance of planar perovskite films formed from PbI_2 solutions in DMF and DMSO a) and b) respectively, and c) performance of mesoporous structure with PbI_2 dissolved in DMF. d) Cross-section SEM image of planar perovskite solar cell with 1 h of perovskite growth time on PbI_2 DMF solvent (best case). The image reports a bl-TiO_2 thickness of 90 nm, $CH_3NH_3PbI_3$ layer of 400 nm, a Spiro-OMeTAD layer of 100 nm.

solvent. The perovskite grain size (around 400 nm) is in accordance with the AFM image (see Fig. 2a). In contrast, films formed over 2 h (V_{oc} = 900 mV, J_{sc} = 10.3 mA cm^{-2}, FF = 63.9%, PCE = 5.9%) had a lower performance especially in terms of the current density. These differences were related to different perovskite layer morphology as shown in Fig. S4 in the ESI. In the case of cells made from perovskite films grown for 30 min (PbI_2 from DMF), the films showed disorganized grains with varying shapes and sizes. In the case of films grown for 2 h, the grain dimensions increased but the contact between grains was poor and the film was not continuous. The performance of cells formed from PbI_2 dissolved in DMSO is shown in Fig. 3b. The best cell was for 30 min of perovskite growth time (V_{oc} = 972 mV, Jsc = 17.5 mA cm^{-2}, FF = 65.2%, PCE = 11%). AFM images (see Fig. S5, ESI), show that after 30 min the perovskite film appears to have a reasonably uniform morphology which is thought to greatly enhance the charge extraction process and is essential to reduce structural defects and electronic traps [16,35,36]. After 1 h (V_{oc} = 757 mV, J_{sc} = 13.3 mA cm^{-2}, FF = 44%, PCE = 4.4%) and 2 h (V_{oc} = 820 mV, J_{sc} = 12.8 mA cm^{-2}, FF = 54%, PCE = 5.7%) the grain size increased substantially and the cell efficiency dropped. As reported by Eperon et al. the V_{oc} value is strongly dependent on the coverage of the perovskite layer [16]. When the growth time was increased to 3 h (V_{oc} = 852 mV, J_{sc} = 16.5 mA cm^{-2}, FF = 61.2%, PCE = 8.6%), the performance

Table 1
Photovoltaic parameters of devices.

Cell Parameters - devices with 10 pixels				Performance of best pixel			
Solvent	Perovskite growth time	Cell type	Average PCE [%]	V_{oc} [mV]	J_{sc} [mA cm^{-2}]	Fill factor [%]	Best PCE [%]
DMF	30 min	Planar	10.2	950	17.9	65.7	11.2
	1 hr		11	967	19.5	67.5	12.7
	2 hr		5.3	900	10.3	63.9	5.9
	1 hr	Mesoporous	9.1	920	17.2	63.5	10
	2 hr		3.3	830	11.3	60	5.6
DMSO	30 min	Planar	9	972	17.5	65.2	11
	1 hr		3.5	757	13.3	44	4.4
	2 hr		5.5	820	12.8	54	5.7
	3 hr		7.1	852	16.5	61.2	8.6

improved again, it appeared that at longer times the grain size actually decreased again and the films become more uniform [16,35,37].

The V-VASP technique was also used to deposit a perovskite film on a mesoporous TiO_2 substrate. The optimum conditions for planar cells were chosen (PbI_2 powder dissolved in DMF). J–V curves are reported in Fig. 3c. 1 h of perovskite growth time (V_{oc} = 920 mV, J_{sc} = 17.2 mA cm^{-2}, FF = 63.5%, PCE = 10%) was much better than 2 h (V_{oc} = 830 mV, J_{sc} = 11.3 mA cm^{-2}, FF = 60%, PCE = 5.6%). The AFM images (Fig. S6, ESI) did not show a large change in grain structure as the annealing time increased; but both the V_{oc} and J_{sc} decreased severely. Fig. S7, (ESI) shows both the reverse (V_{oc} – short circuit) and forward scan (short circuit to V_{oc}) of current–voltage measurements under illumination with different delay times to investigate cell hysteresis. The P-PSC showed higher hysteresis, while for the M-PSC the effect was smaller.

Fig. 4 shows external quantum efficiency (EQE) spectra for P-PSC and M-PSC. Generation of photocurrent starts at 800 nm, in agreement with the bandgap of the $CH_3NH_3PbI_3$, and shows a good photocurrent response until 400 nm. Integrating the overlap of the EQE spectrum with the AM1.5G solar photon flux yields a current density of 16.3 mA cm^{-2} for the P-PSC and 17.2 mA cm^{-2} for the M-PSC. These values are in excellent agreement with the measured photocurrent density range (shown in Table 1) at the standard solar AM1.5G intensity of 100 mW cm^{-2}. The maximum EQE of the

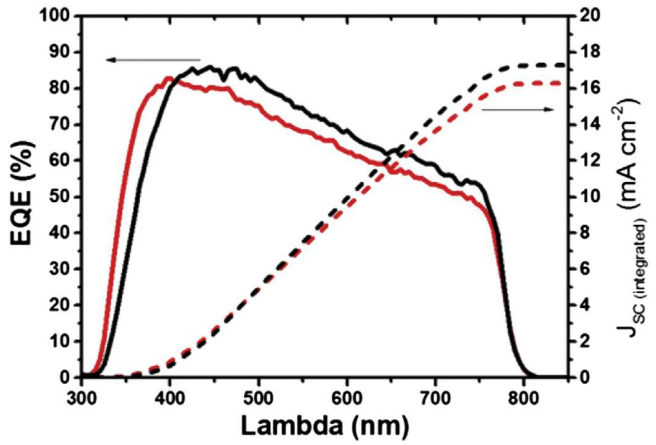

Fig. 4. EQE spectrum of planar and mesoporous perovskite solar cells. The right–hand axis indicates the integrated photocurrent that is expected to be generated under AM1.5G irradiation for M-PSC (black line and circle) and P-PSC (red line and square) with 1 h of perovskite growth from PbI_2 films formed using DMF solvent. (For interpretation of the references to colour in this figure legend, the reader is referred to the web version of this article.)

planar cell is blue shifted with respect to the mesostructured cell. The reason for this shift is not clear. A tentative explanation is that the mesostructured TiO_2 is absorbing light below 370 nm, but that the electrons are not escaping to be collected in the external circuit. This could be due to poor sintering contacts between the titania particles and surface recombination of electrons in the titania with the perovskite.

The mesostructured and planar cells prepared by V-VASP were further analysed by large amplitude Open Circuit Photovoltage Decay (OCVD). It has recently been shown that OCVD and Impedance spectroscopy do not generally give the recombination lifetime, τ_{rec}, for perovskite cells [38,39]. τ_{rec} is defined as the product of the chemical capacitance (due to photo-generated charge carriers, C_μ) and the recombination resistance (R_{rec}). In the majority of perovskite cells the geometric/contact capacitance, C_{geo}, appears to be larger than C_μ. As a result the relaxation lifetime, τ_{OCVD}, measured during OCVD decay appears to be related to $R_{rec}C_{geo}$ and doesn't contain information about the chemical capacitance. OCVD decay can however expose differences between devices, with some cells exhibiting 'persistent photovoltages' [44]. OCVD for the P-PSC and M-PSC is shown in Fig. 5(a–b) and the resulting lifetime τ_{OCVD} is shown in Fig. 5c [38]. τ_{OCVD} was slightly higher for the planar cells at the highest voltages, but overall the cells behaved very similarly to cells prepared in an inert atmosphere [38]. The most interesting feature of Fig. 5a is the long equilibration time needed to obtain the open circuit photovoltage for the planar cell (nearly 10 s) underlining the slow response of planar compared to mesostructured devices.

Although methylammonium lead iodide is very sensitive to oxygen and in particular to moisture, the films grown using V-VASP showed good stability [40–43]. XRD patterns may be used qualitatively to identify any new crystalline species formed during degradation. In Fig. 6 we show the XRD pattern taken immediately after deposition of a planar perovskite layer grown for 1 h on PbI_2 deposited from DMF(see Fig. S9, ESI for the DMSO case), and stored in air for up to 14 days (T = 20 °C, humidity = 50%) without encapsulation. The analysis confirms the absence of the typical signal at 2 theta = 12.7° associated with PbI_2 and other new peaks synonymous of film degradation, however amorphous degradation products could be formed which would not show up on the XRD spectrum. We believe that the relative stability of these unencapsulated devices is due to the compact and glassy nature of the vapor deposited films which may slow water induced degradation on this timescale, although as discussed above we do not rule out the formation of amorphous degradation products.

The evolution of the photocurrent with time for P-PSC and M-PSC is shown in Fig. 7. This technique was used to study the stability of the measured photocurrent when the device is under illumination at short circuit as many perovskite devices perform

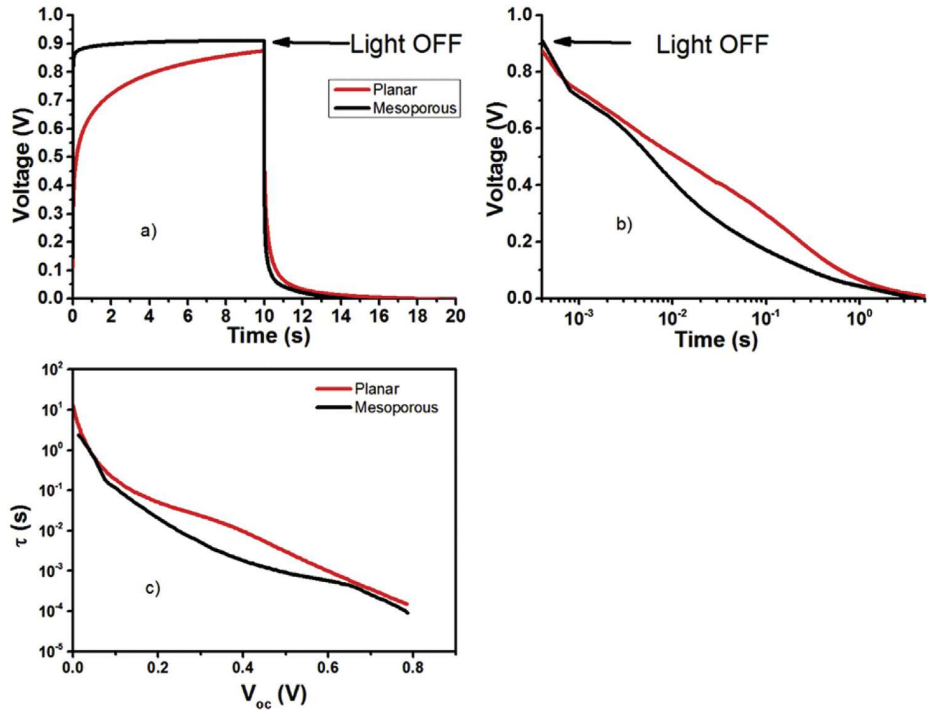

Fig. 5. Large perturbation open circuit voltage transient for M-PSC (black line) and P-PSC (red line) with 1 h of perovskite growth on PbI_2 in DMF solvent a). The light turned on at 0 s and turned off after 10 s. Open-circuit voltage decay on log(t) scale b). Lifetime extracted from open circuit voltage decay c). (For interpretation of the references to colour in this figure legend, the reader is referred to the web version of this article.)

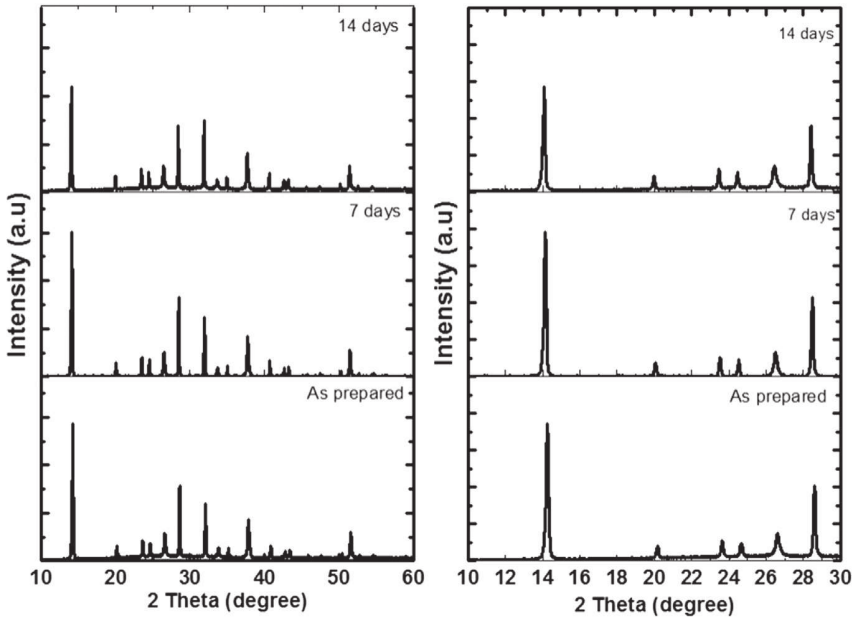

Fig. 6. XRD patterns of planar structure (FTO/bl-TiO_2/$CH_3NH_3PbI_3$) in DMF solvent and perovskite grown for 1 h, freshly deposited, after 7 days and after 14 days stored in air (20 °C, humidity about 50%). (Right) Magnification of the XRD patterns from 2 theta = 10°–30°.

poorly at short circuit. Other cell parameters (such as fill factor and global efficiency) were not continuously monitored as the constant biasing of the cell to the V_{OC} leads to complications in the J_{SC} measurements that we wanted to avoid. In cells that are degrading the J_{SC} typically drops extremely rapidly and so continuous monitoring of the J_{SC} was chosen as a good indicator of cell stability. In the case of both mesostructured and planar devices it was necessary to wait for a considerable time (about 100 s) to obtain steady state currents. The current from the M-PSC appears stable up to 1200s, whereas the planar structure exhibits an 18 μA min^{-1} decrease of photocurrent. The photocurrent decrease in P-PSC could be related to cell degradation, an increase in recombination process or due to a lowering of charge extraction efficiency as previously reported in literature [44].

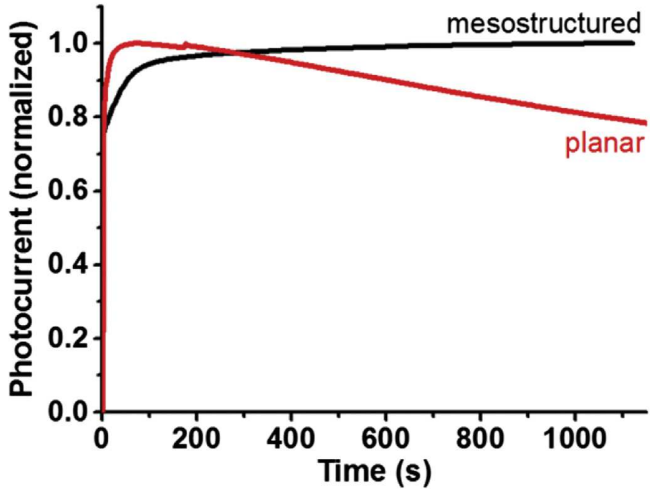

Fig. 7. Photocurrent of P-PSC and M-PSC against time under 1 Sun illumination in air. Both devices were held at short circuit for the duration of the measurement.

4. Conclusions

In summary, a cheap and rapid double step vapor deposition technique was developed, based on vapor-assisted solution processing at low pressures in air. We optimized both the first step of PbI_2 thin-film deposition from DMF and DMSO solvent and the second step of vapor-assisted perovskite conversion. A power conversion efficiency of over 12.7% has been realized with planar structure and over 11% with mesoporous structure for a 0.1 cm^2 active area. The $CH_3NH_3PbI_3$ film morphology was very uniform as confirmed by AFM images. PXRD analysis demonstrated a complete transformation of precursor in only 30 min of vapor exposure. Moreover, the optimized perovskite film showed good stability in air at 50% humidity and 20 °C without encapsulation after 14 days. In future we believe this simple vapor-assisted technique could be used to realize large area perovskite modules.

Acknowledgements

The research leading to these results has received funding from the European Union Seventh Framework Programme [FP7/2007-2013] under grant agreement 316494. We thank the EPSRC for funding (DTC studentship for Adam Pockett, Grant EP/G03768X/1). PJC also thanks the EPSRC for grant EP/H026304/1. All data created during this research (e.g. the raw data for IV curves and OCVD) are openly available from the University of Bath data archive at http://dx.doi.org/10.15125/BATH-00129.

Appendix A. Supplementary data

Supplementary data related to this article can be found at http://dx.doi.org/10.1016/j.jpowsour.2015.08.010.

References

[1] H.J. Snaith, J. Phys. Chem. Lett. 4 (2013) 3623.
[2] Samuel D. Stranks, Giles E. Eperon, G. Grancini, C. Menelaou, M.J.P. Alcocer, T. Leijtens, L.M. Herz, A. Petrozza, H.J. Snaith, Science 342 (2013) 341.
[3] G. Xing, N. Mathews, S. Sun, S.S. Lim, Y. Ming Lam, M. Grätzel, S. Mhaisalkar, T. Chien Sum, Science 342 (2013) 344.
[4] E. Edri, S. Kirmayer, A. Henning, S. Mukhopadhyay, K. Gartsman, Y. Rosenwaks, G. Hodes, D. Cahen, Nano Lett. 14 (2014) 21000.
[5] J. Hong Noh, S. Hyuk Im, J. Hyuck Heo, T.N. Mandal, S. Il Seok, Nano Lett. 13 (2013) 1764.
[6] Giles E. Eperon, Samuel D. Stranks, C. Menelaou, Michael B. Johnston, Laura M. Herz, Henry J. Snaith, Energy & Environ. Sci. 7 (2014) 982.
[7] S. De Wolf, J. Holovsky, Soo-Jin Moon, Philipp Lo per, B. Niesen, M. Ledinsky, Franz-Josef Haug, Jun-Ho Yum, C. Ballif, J. Phys. Chem. Lett. 5 (2014) 1035.
[8] Hui-Seon Kim, Chang-Ryul Lee, Jeong-Hyeok Im, Ki-Beom Lee, T. Moehl, A. Marchioro, Soo-Jin Moon, Robin Humphry-Baker, Jun-Ho Yum, Jacques E. Moser, M. Graetzel, Nam-Gyu Park, Sci. Rep. 2 (2012) 591.
[9] A. Kojima, K. Teshima, Y. Shirai, T. Miyasaka, J. Am. Chem. Soc. 131 (2009).
[10] http://www.nrel.gov/ncpv/images/efficiency_chart.jpg.
[11] K. Wojciechowski, M. Saliba, T.s Leijtens, A. Abate, H.J. Snaith, Energy & Environ. Sci. 7 (2014) 1142.
[12] J. Tse-Wei Wang, J.M. Ball, E.M. Barea, A. Abate, J.A. Alexander-Webber, J. Huang, M. Saliba, I. Mora-Sero, J. Bisquert, H.J. Snaith, R.J. Nicholas, Nano Lett. 14 (2014) 724.
[13] F. Di Giacomo, S. Razza, F. Matteocci, A. D'Epifanio, S. Licoccia, T.M. Brown, A. Di Carlo, J. Power Sources 251 (2014) 152.
[14] N.J. Jeon, J.H. Noh, Y. Chan Kim, W. Seok Yang, S. Ryu, S. Il Seok, Nat. Mater. 13 (2014) 897.
[15] M.M. Lee, J. Teuscher, T. Miyasaka, T.N. Murakami, H.J. Snaith, Science 338 (2012) 643.
[16] G.E. Eperon, V.M. Burlakov, P. Docampo, A. Goriely, H.J. Snaith, Adv. Funct. Mater. 24 (2014) 151–157.
[17] B. Conings, L. Baeten, C. De Dobbelaere, J. D'Haen, J. Manca, Hans-Gerd Boyen, Adv. Mater. 26 (2014) 2041–2046.
[18] D. Liu, T.L. Kelly, Nat. Photonics 8 (2014) 133.
[19] Z. Ku, Y. Rong, M. Xu, T. Liu, H. Han, Sci. Rep. 3 (2013) 3132.
[20] Y. Wu, A. Islam, X. Yang, C. Qin, J. Liu, K. Zhang, W. Peng, L. Han, Energy & Environ. Sci. 7 (2014) 2934.
[21] J. Burschka, N. Pellet, Soo-Jin Moon, R. Humphry-Baker, P. Gao, M.K. Nazeeruddin, M. Graetzel, Nature 499 (2013) 316.
[22] D. Bi, Soo-Jin Moon, L. Häggman, G. Boschloo, Lei Yang, Erik M.J. Johansson, Mohammad K. Nazeeruddin, M. Grätzel, A. Hagfeldt, RSC Adv. 3 (2013) 18762.
[23] Y. Ma, L. Zheng, Yao-Hsien Chung, S. Chu, L. Xiao, Z. Chen, S. Wang, Bo Qu, Q. Gong, Z. Wu, X. Houc, Chem. Commun. 50 (2014) 12458.
[24] Hui Seon Kim, Nam-Gyu Park, J. Phys. Chem. Lett. 5 (2014) 2927.
[25] H. Hu, D. Wang, Y. Zhou, J. Zhang, Siliu Lv, S. Pang, X. Chen, Z. Liu, Nitin P. Padture, G. Cui, RSC Adv. 4 (2014) 28964.
[26] Q. Chen, H. Zhou, Z. Hong, S. Luo, H.-Sheng Duan, H.-Hua Wang, Y. Liu, G. Li, Y. Yang, J. Am. Chem. Soc. 136 (2014) 622.
[27] M.R. Leyden, L.K. Ono, S.R. Raga, Y. Kato, S. Wang, Y. Qi, J. Mater. Chem. A 2 (2014) 18742.
[28] F. Hao, C.C. Stoumpos, Z. Liu, R.P.H. Chang, M.G. Kanatzidis, J. Am. Chem. Soc. 136 (2014) 16411.
[29] G. Niu, W. Li, F. Meng, L. Wang, H. Dong, Y. Qiu, J. Mater. Chem. A 2 (2014) 705.
[30] I.C. Smith, E.T. Hoke, D. Solis-Ibarra, M.D. McGehee, H.I. Karunadasa, Angew. Chem. Int. 53 (2014) 11232.
[31] A. Abrusci, S.D. Stranks, P. Docampo, Hin-Lap Yip, Alex K.-Y. Jen, H.J. Snaith, Nano Lett. 13 (2013) 3124.
[32] A.L. Patterson, Phys. Rev. 56 (1939) 978.
[33] R. Sharma, D.P. Bisen, U. Shukla, B.G. Sharma, Recent Res. Sci. Technol. 4 (2012) 77.
[34] C.V. Thompson, Annu. Rev. Mater. Sci. 30 (2000) 159.
[35] J.H. Im, H.S. Kim, Nam-Gyu Park, Apl. Mater. 2 (2014) 081510.
[36] Z. Xiao, Q. Dong, C. Bi, Y. Shao, Y. Yuan, J. Huang, Adv. Mater. 26 (2014) 6503.
[37] D. Bi, A.M. El-Zohry, A. Hagfeldt, G. Boschloo, ACS Appl. Mater Interfaces 6 (2014) 18751.
[38] A. Pockett, G.E. Eperon, T. Peltola, H.J. Snaith, A.B. Walker, L.M. Peter, P.J. Cameron, J. Phys. Chem. C 119 (2015) 3456.
[39] L. Bertoluzzi, R.S. Sanchez, L. Liu, Jin-Wook Lee, E. Mas-Marza, H. Han, Nam-Gyu Park, I. Mora-Sero, J. Bisquert, Energy & Environ. Sci. 8 (2015) 910.
[40] G. Niu, W. Li, F. Meng, L. Wang, H. Dong, Y. Qiu, J. Mater. Chem. A 2 (2014) 705.
[41] K.K. Bass, R. Eric McAnally, S. Zhou, P.I. Djurovich, M.E. Thompson, B.C. Melot, Chem. Commun. 50 (2014) 15819.
[42] G. Niu, X. Guo, L. Wang, J. Mater. Chem. A 3 (2015) 8970–8980.
[43] S. Ito, S. Tanaka, K. Manabe, H. Nishino, J. Phys. Chem. C 118 (2014) 16995.
[44] E.L. Unger, E.T. Hoke, C.D. Bailie, W.H. Nguyen, A.R. Bowring, T. Heumüller, M.G. Christoforo, M.D. McGehee, Energy & Environ. Sci. 7 (2014) 3690.

Supporting Information

A Simple Approach for the Fabrication of Perovskite Solar Cells in Air.

Simone Casaluci (a), Lucio Cinà (a), Adam Pockett (b), Peter S. Kubiak (b), Ralf G. Niemann (b), Andrea Reale (a), Aldo Di Carlo (a), P. J. Cameron (b)*

a) CHOSE - Centre for Hybrid and Organic Solar Energy- Department of Electronic Engineering, University of Rome Tor Vergata, Via del Politecnico 1, 00133 Rome, Italy
E-mail: p.j.cameron@bath.ac.uk

b) Department of Chemistry, University of Bath, Bath, BA2 7AY, United Kingdom

*) Corresponding Author: p.j.cameron@bath.ac.uk, Tel: +44 1225386116

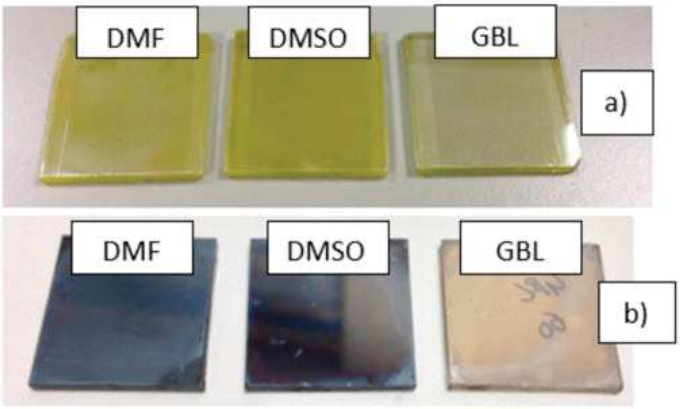

Figure S1: a) Photo of PbI_2 spin coating dissolve in DMF, DMSO and GBL solvent on FTO/bl-TiO_2. b) FTO/bl-TiO_2/PbI_2 in different solvent after exposure to CH_3NH_3I vapor using a V-VASP procedure.

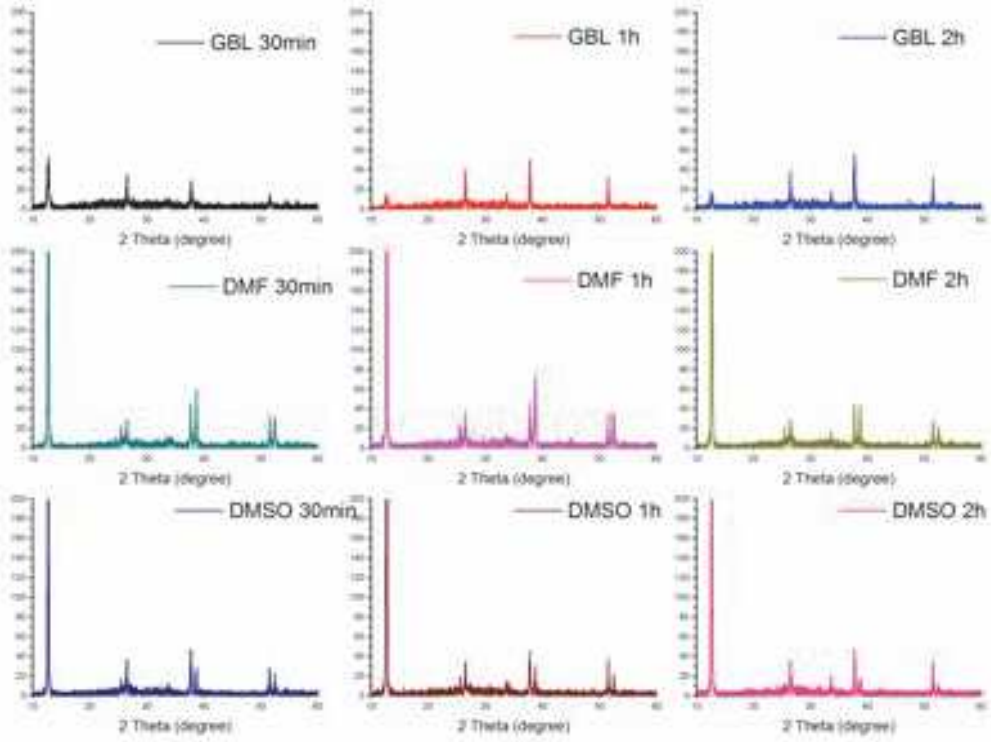

Figure S2a. XRD spectra of lead iodide dissolved in different solvent and with different annealing time. Lead iodide peaks: 2 theta 12.7 °, 25.6 °, 38.7 °, 52.5 °

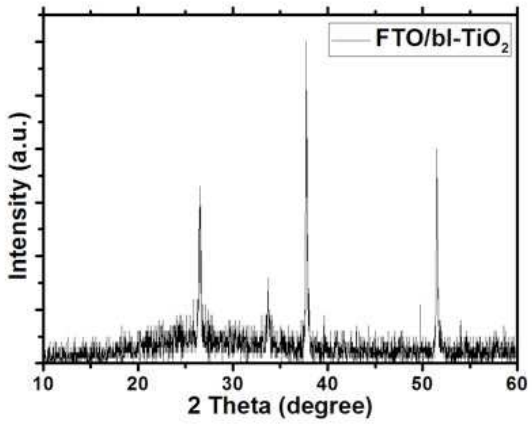

Figure S2b. XRD pattern from glass FTO/bl-TiO_2. Typical FTO peaks are at 2 theta =26.5 °, 33.7 °, 37.7 °, 51.5 °.

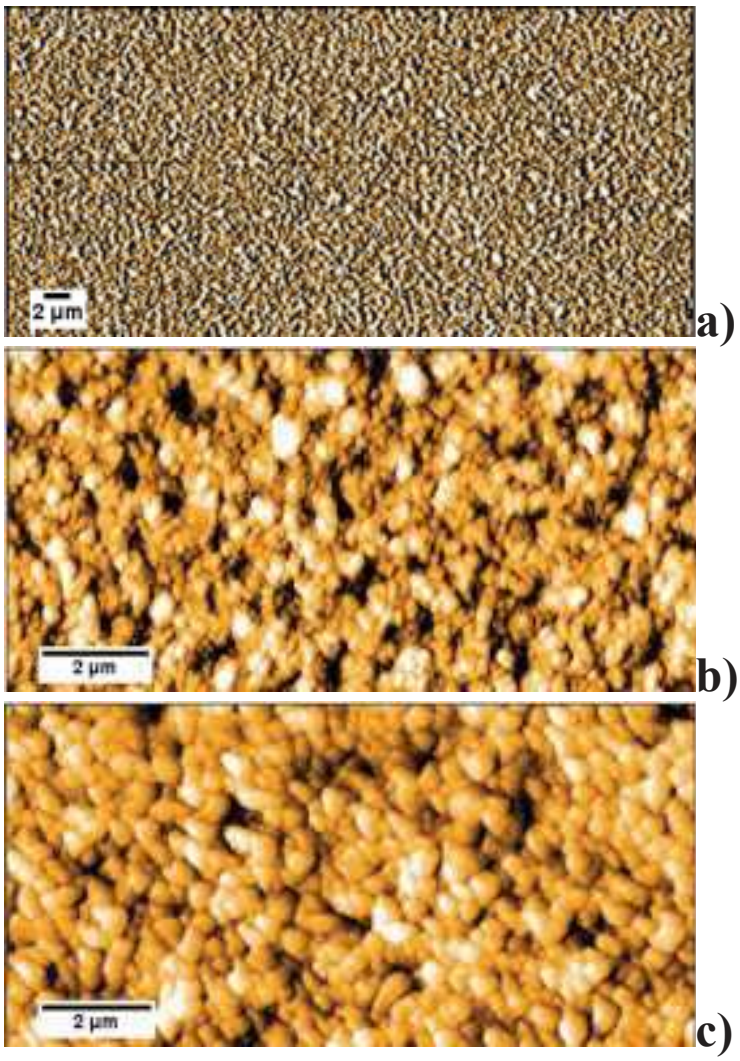

Figure S3. (a)AFM images of bl-TiO_2 on FTO roughness 13 nm, (b) PbI_2 in DMSO on FTO/bl-TiO_2 roughness 6 nm and (c) PbI_2 in DMF on FTO/bl-TiO_2 roughness 14 nm c), after 1h of annealing at 120 °C in air for b) and c).

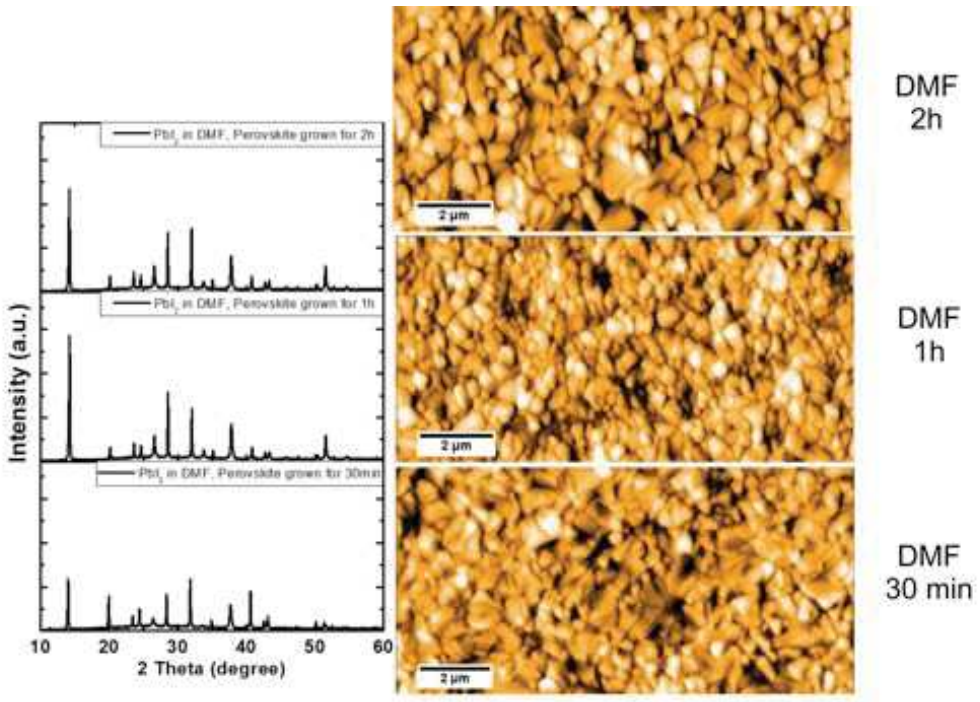

Figure S4. XRD and AFM images of evolution of perovskite film growth on a PbI_2 in DMF layer. Roughness 30 min: 30 nm, 1h: 26 nm, 2h: 30 nm

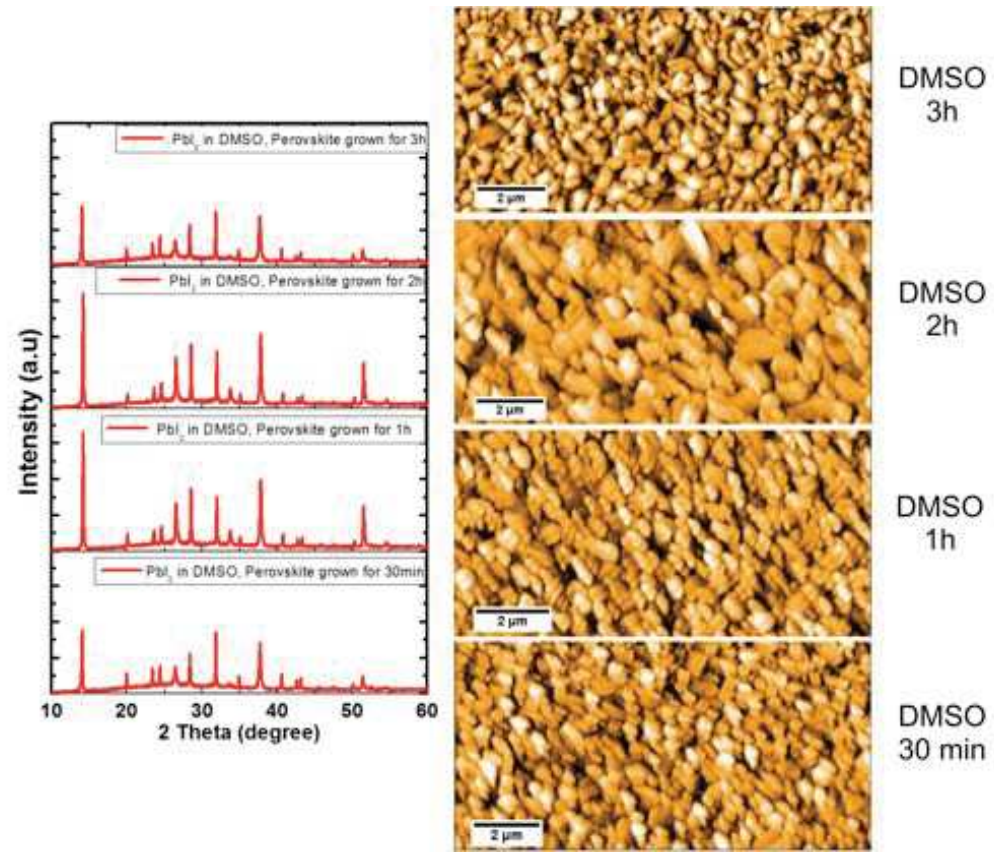

Figure S5. XRD and AFM images of evolution of perovskite film growth on a PbI_2 in DMSO layer. The images at 30 min, 1 h and particularly 2h show artifacts due to tip doubling, but the overall evolution of the nanoparticles can still be seen.

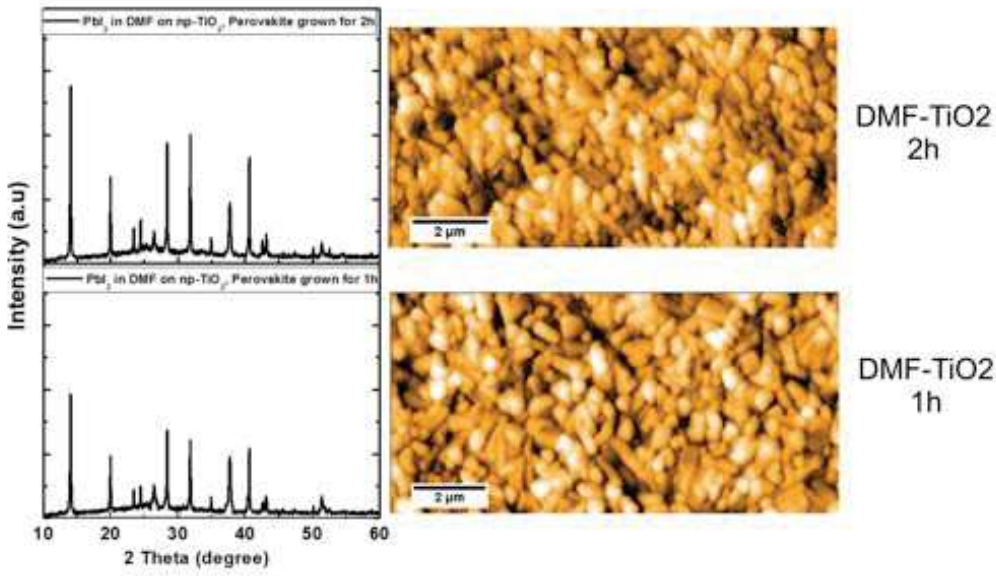

Figure S6. XRD pattern and AFM images of mesoporous structure. TiO_2 perovskite 1h, roughness 33 nm. TiO_2 perovskite 2h, roughness 34 nm.

HYSTERESIS PHENOMENA

Scan steps: Step: 20 mV - With delay 40ms: 500 mV/s - With delay 200ms: 100 mV/s
5 s on V_{oc} before start measure.
1°: reverse, 200 ms of delay on each point
2°: reverse 1, delay 40 ms
3°: forward delay 40 ms
4°: reverse 2, delay 40 ms

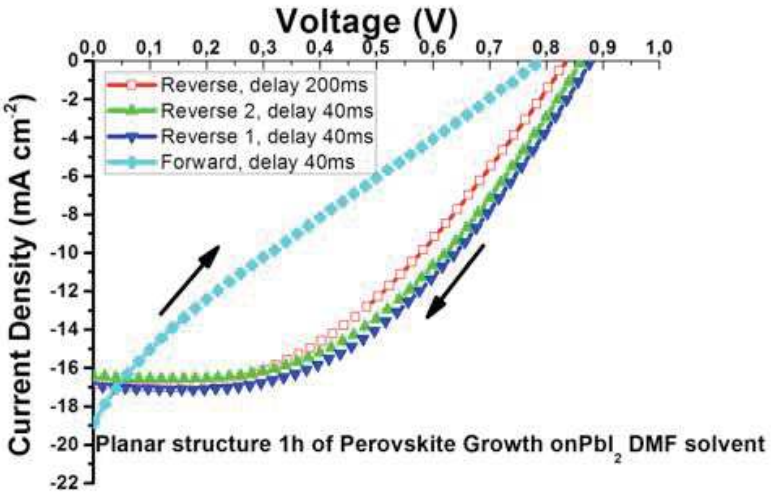

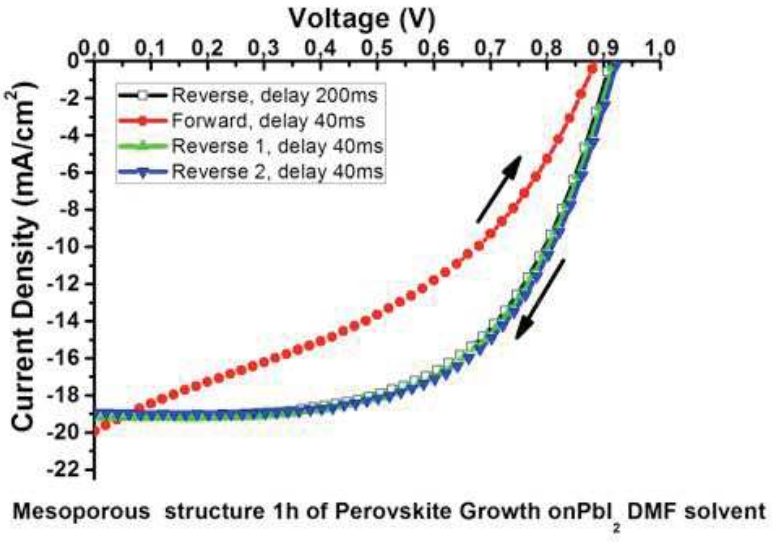

Scan steps: Step: 20 mV - With delay 40 ms: 500 mV/s - With delay 200 ms: 100 mV/s
5s on V_{oc} before start measure.

1°: reverse, 200 ms of delay on each point
2°: forward 200 ms
3° reverse 2, 200 ms
4°: reverse 1, delay 40 ms
5°: forward delay 40 ms
6°: reverse 2, delay 40 ms

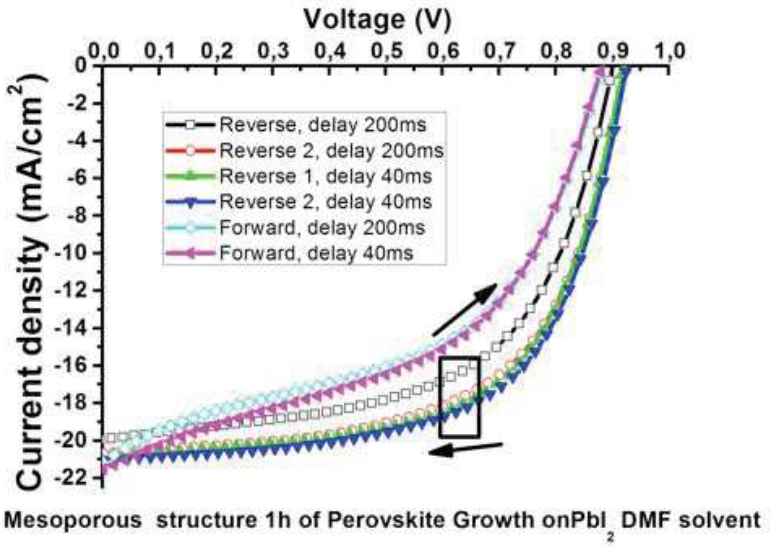

Figure S7. Current density- voltage measurements of P-PSC and M-PSC. Different scan direction (Forward: from 0 V to V_{oc}, Reverse: from V_{oc} to 0 V) and delay times (40 ms and 200 ms) are compared.

We didn't choose the 30 minutes time of grow the perovskite layer on TiO_2 mesoporous to fabricate device because this time was insufficient to have a complete formation of perovskite probably due to a large surface obtained with mesoporous TiO_2. The film was a mix brown/yellow colors, indicating incomplete perovskite formation. The AFM image (Figure S8) confirms an incomplete perovskite growth process and the presence of big holes. The XRD pattern shows a peak at 2 theta= 12.7 °, identified as unreacted PbI_2, and a typical yellow color of sample.

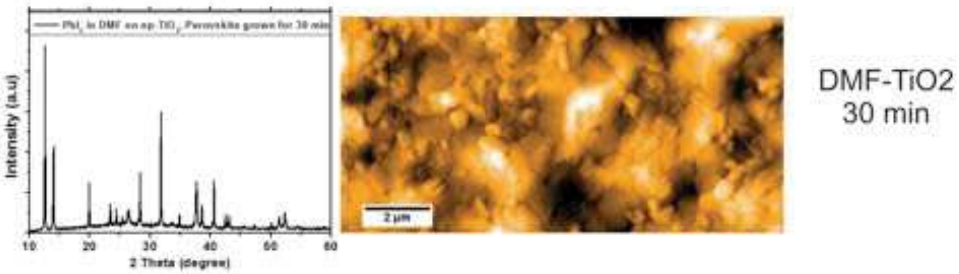

Figure S8. XRD and AFM image of sample glass FTO/bl-TiO_2/np-TiO_2/Perovskite with 30 minutes of grow time. The PbI_2 was dissolved in DMF solvent.

Degradation

XRD pattern of sample with PbI_2 dissolved in DMSO and perovskite growth for 1h. On right the magnification of pattern from 2 theta from 10 ° to 30 °. In this plot there aren't traces of "degradation" peaks like lead iodide at 2 theta=12.7 ° or other impurity.

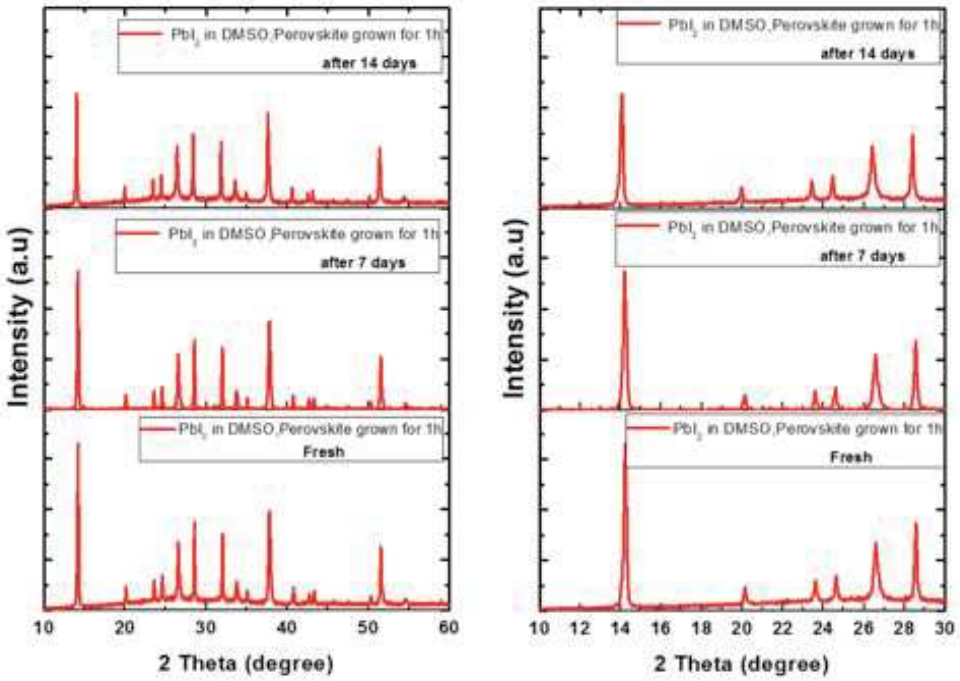

Figure S9. XRD pattern of perovskite layer fresh, after 7 days and after 14 days on a spin-coated PbI_2 film from DMSO. (Right) Magnified plot from 10 ° to 30 °.

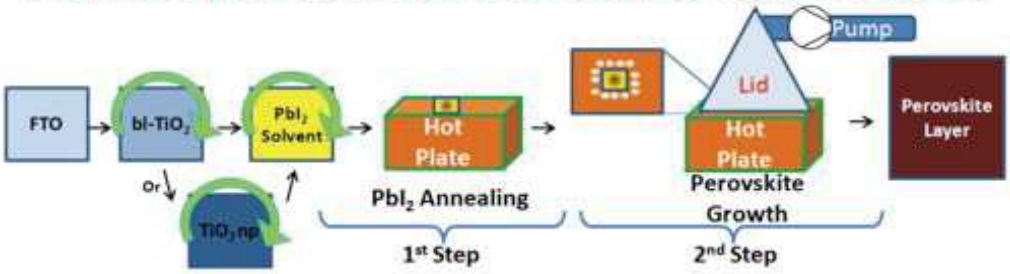

Figure S10. Steps used to fabricated a planar and mesoporous perovskite solar cells

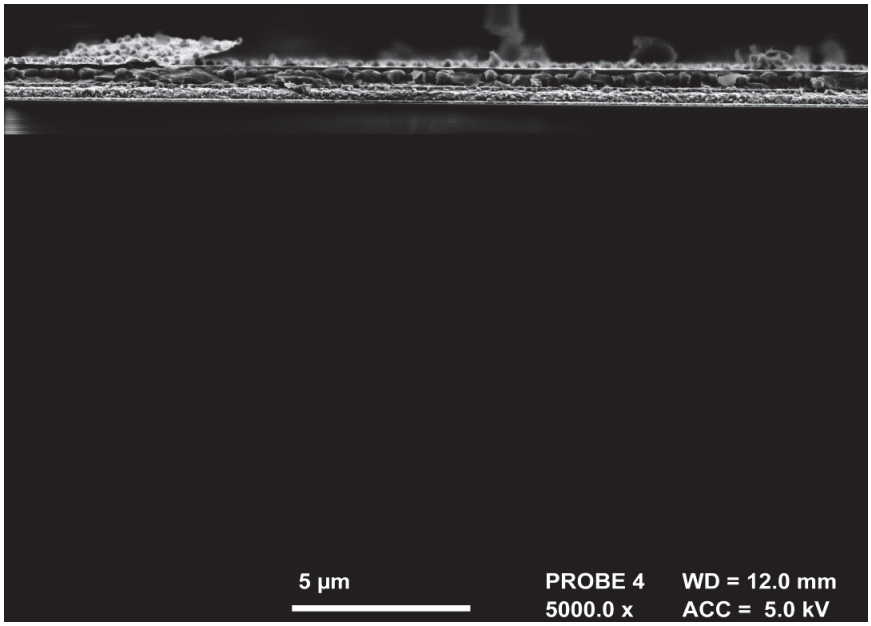

Figure S11. Original SEM cross sectionimage of planar cell, a close up of which is reproduced in Figure 3(d)

			Range of cell performance parameters			
Solvent	**Perovskite growth time**	**Cell type**	**Min-Max**	**Min-Max**	**Min-Max**	**Mean – (Max)**
			V_{oc} [mV]	J_{sc} [mA/cm^2]	FF [%]	PCE [%]
DMF	30 min	planar	874 - 976	16.5 - 17.9	63.4 - 65.7	10.2 - (11.2)
	1hr		**900 - 967**	**16.1 - 19.5**	**65 - 67.5**	**11 - (12.7)**
	2hr		854 - 900	8 - 10.3	63 - 70	5.3 - (5.9)
	1hr	mesoporous	853 - 942	14 - 17.2	63 - 63.5	9.1 - (10)
	2hr		788 - 830	7.3 - 11.3	50 - 60	3.3 - (5.6)
DMSO	30 min	planar	913 - 972	15 - 17.5	53 - 65.2	9 – (11)
	1hr		660 - 757	11.9 - 13.3	35 - 44	3.5 – (4.4)
	2hr		810 - 820	10 - 12.8	54 - 64	5.5 – (5.7)
	3hr		810 - 890	10.1 - 17.2	61.2 - 64	7.1 – (8.6)

Table S1. Performance range of cells presented in table 1 in the main text.

OCVD smoothing and fitting

To obtain the lifetime, τ_{OCVD}, the photovoltage decay data in Fig 5b (main text) was smoothed using Loess smoothing, and then fitted to an 11 parameter rational function. The lifetime was calculated using the formula (see ref 38 for details):

$$\tau_{OCVD} = -\frac{2k_BT}{q}\left(\frac{dV_{OC}}{dt}\right)^{-1} - \frac{dV_{OC}}{dt}\left(\frac{d^2V_{OC}}{dt^2}\right)^{-1}$$

3.2.5.2 Contemporary assessment

This paper has set out to facilitate the perovskite cell fabrication process and established a novel methodology for its production. Potential applications are research cell fabrication in labs without a glovebox and a possible upscaling to the level of small modules. Recent studies showed that the V-VASP technique can be used for the fabrication of large-area devices and even modules,[46, 47] which proves the scalability of this method. The quality of the films produced with V-VASP was analysed regarding interface and composition analysis by Matteocci *et al.* and it was found that V-VASP gives very compact films with well-defined interfaces, as compared to other sequential conversion techniques.[48] Other studies slightly altered the process, *e.g.* by flipping the substrate and placing it directly over the MAI powder to decrease the diffusion distance for the MAI vapour,[49] or by employing the vapour process after a solution conversion, so that it acts as a vapour healing process.[50] A possible limitation to this study is the vacuum pumping, which makes the process discontinuous, whereas a continuous procedure would be more desirable for up-scaling considerations. Another aspect is the conversion process itself, where the MAI powder is assembled around the substrate, which means that the central part of the substrate is exposed to a lower vapour concentration than the outer part. This effect can be visually observed as the conversion process starts at the edges and then progresses to the middle of the substrate. This can eventually affect bulk properties and defect densities. Other studies have shown that the ratio of MAI/PbI_2 plays a critical role in the crystallisation process.[51, 52, 53, 54, 55, 56] An alternative setup that could circumvent this problem would be to place the substrate directly over the MAI source,[49] ideally with a specially designed substrate holder to avoid direct contact to the MAI powder. Furthermore, it would be interesting to see further development of this process with a vapour pressure control, which is not quantified in the current study. First studies towards an up-scaling of this process show promising results and a better process control should enable further efficiency improvements.[46, 47]

3.2.6 High-hysteresis perovskite cells for the evaluation of ion motion

IV measurements are the most important characterisation technique for solar cells. With a relatively fast and easy measurement, they can give important information about both the performance (PCE) and working mechanism (V_{OC}, series-, and shunt-resistance) of the cell. In the case of measurements on DSSC and OPV, the IV curve was an unambiguous characterisation technique, which gives reliable results as long as care is taken during the measurements, e.g. by masking the active area.[57] This assumption does not apply to perovskite cells, which show a more complex behaviour. A common issue during IV measurements is so called anomalous hysteresis, which can make bad cells look good[58] and require attention and caution when measuring and interpreting IV curves. Factors that reportedly impact hysteresis are manifold and include interfaces and fabrication conditions.[28, 59, 60] However, the causes for this hysteretic effect have been the subject of intense debate within the scientific community and are unclear up to now.[61, 62] Snaith *et al.* proposed three possible causes, which may work individually or in conjunction:[28] (a) Interface effects, namely a large surface defect density may cause an accumulated of charges at grain boundaries and contacts; (b) another explanation is polarisation of ferroelectric domains,[63] which are caused by the organic cation and slowed down by the interaction with the inorganic cage to time constants that are in the same order of magnitude as IV measurement; (c) alternatively, a vacancy mediated migration of defect sides, which will be further elaborated in this section. Recent studies increasingly point towards (c) as the cause for the anomalous hysteresis.[64, 61] The first qualitative description of the effect of ion motion on hysteresis was given by Van Reenen *et al.*, but the grid spacing used of 4 nm is too coarse to accurately resolve the Debye layers in the devices.[65] A model that accounts for Debye layers and can give a quantitative description of experimental results was missing from literature.

As shown in chapter 1 (eqn. 1.1), the magnitude of hysteretic effects depends on the defect diffusion barrier ΔE_d, which intrinsic for each material, as well as the defect concentration $[D]$, which can be changed depending on the materials purity. Therefore hysteretic effects can be controlled by varying the processing conditions. This study intentionally employs cells with high defect concentrations, which were made by modifying the previously described V-VASP process, *e.g.* by using lower temperatures (120 °C instead of 150 °C) and shorter perovskite conversion times to increase the defect density.[66] The produced cells showed significant hysteresis and were well suited to study effects of the measurement routine on device performance and to compare measured results with an computational drift-diffusion model.

3.2.6.1 Related publications

RGN carried out the experimental part of this study. This includes the development of the PSC fabrication routine for high-hysteresis cells, as well as making and measuring of all devices.

Energy & Environmental Science

PAPER

View Article Online
View Journal | View Issue

Cite this: *Energy Environ. Sci.*, 2016, **9**, 1476

Can slow-moving ions explain hysteresis in the current–voltage curves of perovskite solar cells?†

Giles Richardson,*[a] Simon E. J. O'Kane,[b] Ralf G. Niemann,[c] Timo A. Peltola,[b] Jamie M. Foster,[d] Petra J. Cameron[c] and Alison B. Walker*[b]

Received 5th September 2015,
Accepted 12th February 2016

DOI: 10.1039/c5ee02740c

www.rsc.org/ees

The hypothesis that ion motion is responsible for anomalous hysteresis in the current–voltage curves of perovskite solar cells is investigated through a combination of electrical transport modelling and experimental measurements. In a combined computational and experimental study, good agreement is obtained between experiment and the results of a charge transport model covering mixed ionic-electronic conduction. Our model couples electrons, holes and defect mediated ion motion suggesting that slow moving ions are indeed the origin of the hysteresis. The magnitude of the ion diffusion coefficient required to match experiment and theory, $\sim 10^{-12}$ cm^2 s^{-1}, depends on the cell, but is similar to that predicted by microscopic theory of vacancy mediated diffusion. The investigation is extended to preconditioning procedures which are known to substantially influence the hysteresis. The method developed for solving the stiff equations in the drift diffusion model is widely applicable to other double layer problems occurring in electrochemical applications such as the evolution of transmembrane potentials in living cells.

Broader context

A perovskite solar cell is so-called because it includes a perovskite structured compound, most commonly a hybrid organic–inorganic lead or tin halide-based material, as the light-harvesting active layer. These cells were mentioned as an exciting development in the climate change conference in Paris in December 2015. The record certified power conversion efficiency for these cells is 21.0%. A well-known problem is hysteresis in which the cell current–voltage characteristics are strongly dependent on the voltage scan rate, direction and pre-conditioning treatments. Despite evidence from cell measurements identifying the likely cause of hysteresis as ion migration, there is no theoretical model capable of interpreting measured current–voltage characteristics that show hysteresis. Here, we report a combined theoretical–experimental investigation of hysteresis where we have identified the physical origin of the features seen in the measurements. Our model takes an approach to solving the charge transport equations that is widely applicable to other double layer problems occurring in electrochemical applications such as the evolution of transmembrane potentials in living cells. The model allows us to understand the effect of mobile defects on the operational mechanisms of the devices and paves the way for the development of cells with improved and reproducible performance.

1 Introduction

Since the first use of organolead halide perovskites as a sensitizer in a solar cell in 2009,[1] the power conversion efficiency, PCE, of perovskite solar cells has risen from 3%[2,3] to around 20% within five years. Recent reviews of perovskite solar cells are given by Stranks and Snaith,[4] Niu *et al.*,[5] Miyasaka,[6] and Park.[7]

Planar perovskite cells are produced by sandwiching a layer of perovskite, such as the compound $MAPbI_3$ (where MA is short for methylammonium, CH_3NH_3) between electron transporting and hole transporting contacts. The most common combination is titania (TiO_2) for the former and spiro, namely spiro-MeOTAD,2,2′7,7′-tetrakis-(*N*,*N*-di-*p*-methoxyphenyl amine)-9,9′-spirobifluorene as the latter.

A major weakness that undermines the credibility of measurements of perovskite solar cell PCEs is the choice of a voltage scanning protocol that takes advantage of hysteresis in the current density–voltage, *J*–*V*, curves to obtain apparent efficiencies that are in excess of the real efficiency of the cell. Indeed it was not until 2014, in the work of Snaith *et al.*,[8] and others,[9–12] that this source of inaccuracy was openly discussed in the literature. An understanding of the underlying working principles of perovskite cells is crucial to their future improvement,[10] not just the PCEs but also to achieve rapid energy payback time and sustainability.[13] Ion motion within the

[a] *Mathematical Sciences, University of Southampton, UK*
[b] *Department of Physics, University of Bath, UK. E-mail: a.b.walker@bath.ac.uk*
[c] *Department of Chemistry, University of Bath, UK*
[d] *Department of Mathematics and Statistics, McMaster University, Hamilton, Canada*

† Electronic supplementary information (ESI) available. See DOI: 10.1039/c5ee02740c

perovskite could lead to degradation of the perovskite material as it becomes depleted in I^-, and will inevitably lower the PCE of the cell by reducing the built-in electric field in the perovskite. Furthermore, ion motion is not an effect that can be averted by encapsulation.[14,15]

Snaith *et al.*[8] suggested three origins for hysteresis from the perovskite layer, either solely or in combination: (a) a large defect density close to interfaces with adjacent layers; (b) slow polarization of the material due to bias dependent motion or changes in configuration of the ferroelectric domains;[16] (c) vacancy aided migration of ions through the film. Mechanism (a) is unlikely since electronic transport to the layer takes $\sim$ns due to the high electronic mobility (though we note that charges could detrap on a timescale comparable to that associated with the hysteresis) and mechanism (b) is ruled out by electrical measurements.[17] Belstein-Edmands *et al.*[17] provide strong evidence for mechanism (c) estimating that motion of up to 3.7% of I^- contributes to the hysteresis. With a measured stored charge density of 2.5 mC cm^{-2} at 2 V, an ionic capacitance of 0.28 mF is inferred, similar to the low frequency capacitance reported elsewhere.[9] Recent work[18] has shown that hysteresis can be reduced by replacing the TiO_2 layer by PCBM and that this is associated with a reduction in the low frequency capacitance of the cell. Apparent PCEs of 11% and 13% have been measured from the *J–V* scans of *meso*-structured cells without a TiO_2 blocking layer but the cells have nevertheless been shown to have nearly zero stabilized power output.[19] Li *et al.*[15] have shown that by preconditioning similar cells that apparent PCEs increased from less than 1% to over 8% and that this can be attributed to ion motion. O'Regan *et al.*[20] found that that the apparent efficiency of a cell aged for 100 days varied between 0.1% and 9% depending on the time for which the cell was held at forward bias. In addition they were able to identify two distinct contributions to the transient response of the cell one of which (on a microsecond timescale) they ascribe to detrapping of electrons and the other (on the scale of 10 s of seconds) they ascribe to ion motion or dipole realignment. In terms of their capacitances the slow timescale response is much more significant than the fast timescale one.

Yang *et al.*[21] support the hypothesis that hysteresis arises from the motion of I^- ions in the perovskite, inferring an ionic diffusion coefficient of 2.4×10^{-8} cm^2 s^{-1}. Atomistic calculations by Eames *et al.*[22] using Density Functional Theory, DFT, methods employing an *ab initio* code showed the fastest ion motion is vacancy assisted I^- diffusion. Here the positively charged I^- vacancies are the mobile species rather than the I^- ions, with an activation energy E_A of 0.58 eV from which a diffusion coefficient $D_+ \sim 10^{-12}$ cm^2 s^{-1} was deduced at a temperature of 320 K. They postulated that this vacancy migration could help to explain hysteresis. Other ion species that could also explain hysteresis include negatively charged I^- interstitials, which would also explain the results of Yang *et al.*[21] and negatively charged MA^+ and Pb^{2+} vacancies. Eames *et al.*[22] calculated E_A to be 0.84 eV for MA^+ and to be 2.31 eV for Pb^{2+}, leading to corresponding diffusion coefficients of $D_+ \sim 10^{-16}$ cm^2 s^{-1} and effectively zero respectively. On the other hand, DFT calculations by Azpiroz *et al.*[23] yielded values of E_A of $\sim$0.16 eV, 0.5 eV and 0.8 eV for I^-, MA^+ and Pb^{2+} vacancies, respectively. They suggested that I^- vacancies and interstitials move too quickly to be responsible for the hysteresis and therefore MA^+ vacancies are a possible cause. However the value of $D_+ \sim 10^{-4}$ cm^2 s^{-1} for I^- vacancies (inferred from $E_A = 0.16$ eV) is so large that the electric field across the device would be fully compensated before the MA^+ vacancies had time to move. In turn this implies that no hysteresis would be observed over the 10 s timescale that characterizes this phenomenon. MA^+ and Pb^{2+} vacancy motion is also inconsistent with the results of Yang *et al.*[21] For both these reasons we can rule out mobile MA^+ and Pb^{2+} vacancies being the cause of the hysteresis.

The large number of results described above that lack a coherent explanation demonstrate that much perovskite research is based on a 'shake and bake' approach, uninformed by an understanding of the underlying mechanisms. Given the complexity of the proposed hysteresis mechanisms, a device model is essential and is one of 10 critical challenges posed in a recent review.[24] Atomistic models show considerable discrepancies in their predictions of the parameters governing ion motion as shown in the previous paragraph. Furthermore, the use of such models on the length scales required to study charge transport in solar cells is not feasible because of the huge computational cost involved; the appropriate tool for such studies (especially for planar devices) is the drift diffusion, DD, method.[25] DD models of coupled ion–electron conduction allow us to understand the effect of mobile ions on the operational mechanism of the device[8–12,19,22,23] and pave the way for the development of cells with improved and reproducible performance. The model reported here is a development of the DD model by Foster *et al.*[26] This model has guided developments in cell longevity *via* an equivalent circuit model that quantified the loss in charge arising from shunting where the metal electrode and the perovskite absorber layer make contact.[27]

Within our DD picture, a built-in voltage V_{bi}, determined by the difference in the Fermi levels in the TiO_2 and the spiro layers, gives rise to an electric field V_{bi}/b in the perovskite layer. This field drives positive charges towards the spiro layer and negative charges towards the TiO_2. At short circuit, free electron–hole pairs are separated by this field to create a current in which electrons are extracted through the TiO_2 layer and holes are extracted through the spiro layer. A positive applied bias, V, produces an electric field that opposes the built-in field. In the absence of charge build up within the perovskite there is a net electric field $(V_{bi} - V)/b$ from left to right. When $V < V_{bi}$, this field drives the positively charged iodide vacancies into the region of the perovskite adjacent to its interface with the spiro, where they create a narrow positively charged layer of total areal charge density Q_+. To maintain overall charge neutrality, there is also a negatively charged layer, created by depletion of the iodide vacancies of total areal charge density Q_-, in the region of the perovskite adjacent to its interface with the TiO_2. Fig. 1 illustrates the resulting electric potential and conduction band profile.

The charge accumulation layers, termed Debye layers, are examples of a diffuse double layer, such as seen in electrolytes.[28,29]

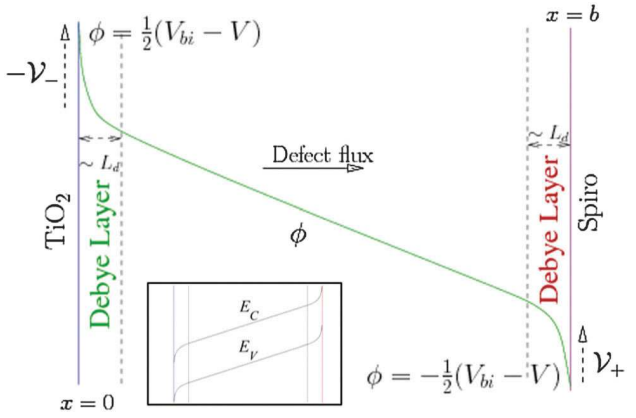

Fig. 1 Schematic of the electric potential ϕ in the perovskite. ϕ is linear across most of the perovskite film but varies rapidly across narrow Debye layers at its edges, jumping by an amount V_- across the left-hand layer and V_+ across the right-hand layer. We assume the applied bias V is zero at short circuit and is positive at the right hand contact relative to the left hand contact. The inset shows the equivalent band energy diagram in the perovskite. E_C and E_V depend upon ϕ *via* $E_C = -E_{ea} - q\,\phi$ and $E_V = -E_{ea} - E_g - q\,\phi$ where E_{ea} and E_g are the electron affinity and energy gap, respectively.

The width of the layers can (as for electrolytes) be estimated from the Debye length L_D, which is proportional to the reciprocal of the square root of the density of the mobile charged species. Ab initio theory[30] predicts an equilibrium I^- vacancy density of 1.6×10^{19} cm^{-3} and a corresponding Debye length $L_D \approx 1.5$ nm that is much smaller than the perovskite layer width $\approx$300 nm. Our approach explicitly accounts for ion motion and predicts charge accumulation in these layers on the time scales associated with mobile defect motion in the perovskite that are consistent with experimental measurements and theoretical estimates of D_+. Using the vacancy diffusion coefficient 10^{-12} cm^2 s^{-1} calculated by Eames *et al.*[22] leads to an estimate of the timescale for vacancy diffusion across a distance $5L_D$ of around 0.5 s which is consistent with experimental observations of hysteresis at scan rates of $\sim$1 V s^{-1} from open circuit to short circuit and back.

There are very few published DD models of perovskite cells.[31–34] Of these, only Van Reenen *et al.*[34] (published while this work was in review) addresses ion migration. In that work a finite difference based numerical scheme is employed. The constant grid spacing of 4 nm is far too coarse to resolve the Debye layers. Their assumed value of D_+ is 10^6 times greater than that of Eames *et al.*[22] and voltage scan rates around 10^6 times greater than the experimental scan rates at which hysteresis is observed, ruling out a quantitative comparison with experiment.

Our approach is more sophisticated and involves solving explicitly for the potential and ion distributions in the narrow (and problematic) Debye layers. By comparing our results to experiment, we can deduce the value of D_+, finding it to be close to the value of 10^{-12} cm^2 s^{-1} predicted by Eames *et al.*[22] With additional experimental *J–V* curves for different device structures and scan rates, our model would help resolve the question whether other mobile species, such as MA^+ and Pb^{2+} vacancies contribute to hysteresis. With a little additional work our model can also be used to address empirical observations showing that cells with fullerene (C60) derivative PCBM, [6,6]-phenyl-C61-butyric acid methyl ester, as an electron transport layer have reduced hysteresis.[18] This reduction is especially marked in inverted structures such as ITO/PEDOT:PSS/$MAPbI_3$/PCBM/C60/BCP/Al. Here ITO is Indium Tin Oxide, PEDOT:PSS is poly(3,4-ethylenedioxythiophene) polystyrene sulfonate and BCP is bathocuproine.[18,35] The reduction in hysteresis in these devices is also predicted by our model and is the subject of a current study, but is outside the scope of this paper which focuses on the conventional TiO_2 and spiro based devices.

It is possible that illumination levels may also influence vacancy concentration. Hoke *et al.*,[36] for example, speculate that photoexcitation may cause halide segregation in mixed halide perovskites resulting in photoinduced trap formation that could influence hysteresis. However, since no clear experimental evidence exists for such effects, we omit them from our model.

To validate our model, we compare its predictions with experimental measurements on two cells chosen to demonstrate high levels of hysteresis. Features seen in the measured *J–V* curves at varying scan rates, such as a shallow peak on scans from 1.2 V to short circuit, can be explained in terms of a time varying internal electric field across the perovskite layer. These measurements, and their interpretation, are extended to include discussion of the influence of preconditioning. By reporting on the two cells, we show how much *J–V* characteristics vary for cells fabricated in the same way but with different preconditioning. Validation of our methodology through this comparison opens the way to study other solar cells containing mixed ionic electronic conductor materials, such as $CuInSe_2$ in which Cu^+ can migrate.[14]

2 Methods

Choice of model parameters

Table 1 shows parameter definitions and values adopted in our model. All values are for room temperature, set as 298 K. Values for n_0 and p_0 were calculated from the effective density of states $\hat{g}_c$, $\hat{g}_v$, the conduction and valence band edges E_C and E_V and the Fermi levels in the TiO_2 and spiro E_{Ft}, E_{Fs}.

Parameters fit to experiment are shown in Table 2. Our treatment of light absorption *via* the Beer–Lambert law with a single value for the absorption coefficient is approximate so we have used a value of F_{ph} that gives short circuit current densities in the range 5–15 mA cm^{-2}, reproducing measurements by Sanchez *et al.*[9] and the measurements reported in the Results section. Tress *et al.*[11] find that hysteresis is independent of illumination, motivating our assumption that D_+ is similarly independent of illumination despite its soft structure. The perovskite film nanoscale morphology, in the form of its grain boundary structure, influences D_+ and accounts for differences between cells fabricated in the same way. Fitting predicted *J–V* characteristics for varying scan rates to experiment gives an estimate of D_+ that differs by a factor of three between the two cells. Our estimates for D_{1+} and D_{2+} are both within a factor of 10 of

Table 1 Parameters used in the drift-diffusion simulations fixed a *priori*

Symbol	Description	Value
N_0	I^- vacancy equilibrium density	1.0×10^{17} cm^{-3} Fig. 3, 4 1.6×10^{19} cm^{-3} Fig. 5–8[30]
n_0	Density of free electrons at TiO_2	6.9×1013 cm^{-3} ref. 37, 38
p_0	Density of free holes at spiro	1.0×1012 cm^{-3} ref. 37, 38
$\hat{g}_c$	Conduction band density of states	8.1×10^{18} cm^{-3} ref. 38
$\hat{g}_v$	Valence band density of states	5.8×10^{18} cm^{-3} ref. 38
$\hat{D}_n$	Electron diffusion coefficient	1.7 cm^2 s^{-1} ref. 39
$\hat{D}_p$	Hole diffusion coefficient	1.7 cm^2 s^{-1} ref. 39
E_C	Conduction band minimum	−3.7 eV ref. 37
E_V	Valence band maximum	−5.4 eV ref. 37
E_{Ft}	TiO_2 Fermi level	−4.0 eV ref. 37
E_{Fs}	Spiro Fermi level	−5.0 eV ref. 37
L_d	Debye length = $(\varepsilon_p V_T/(qN_0))^{1/2}$	1.5 nm
b	Perovskite layer width	6×10^{-5} cm ref. 39
ε_0	Vacuum permittivity	8.85187×10^{-12} F m^{-1}
ε_p	Static dielectric constant	$24.1\varepsilon_0$ ref. 38
q	Electron charge magnitude	1.602×10^{-19} C
V_T	Thermal voltage	0.0257 V
V_{bi}	Built-in voltage	1 V
ν_{scan}	Scan rate	See figure caption
α	Absorption coefficient	1.3×10^5 cm^{-1} ref. 40

Table 2 Parameter values derived from fitting the drift-diffusion simulations to experiment

Symbol	Description	Value
F_{ph}	Intensity at $x = 0$	9.45×10^{16} cm^{-2} s^{-1}
D_{1+}	Cell 1 I^- vacancy diffusion coefficient	1.0×10^{-11} cm^2 s^{-1}
τ_{n1}	Cell 1 electron pseudo-lifetime	0.38 ns
τ_{p1}	Cell 1 hole pseudo-lifetime	3.8 ps
D_{2+}	Cell 2 I^- vacancy diffusion coefficient	3.7×10^{-12} cm^2 s^{-1}
τ_{n2}	Cell 2 electron pseudo-lifetime	0.30 ns
τ_{p2}	Cell 2 hole pseudo-lifetime	3.0 ps

that calculated by Eames *et al.*[22] but are further away from that determined by Yang *et al.*[21]

The differences in the values of τ_n and τ_p between the cells can be accounted for by the strong influence of perovskite morphology on recombination. These values were chosen to give an open circuit voltage around 0.9 V, which approximately matches the experimentally measured values on the scan from 1.2 V to 0 V. The predicted *J–V* curves for this scan are sensitive to τ_p/τ_n (ESI,† note 2).

Modelling charge transport in the perovskite layer by drift diffusion, DD

Vacancy mediated ion transport is modelled in a single layer of perovskite sandwiched between highly doped spiro and TiO_2 buffer layers. It is assumed that the doping levels in the buffer layers are sufficiently high to force them to be at the same electric potential as their respective contacts. The potentials at the perovskite-buffer layer interfaces are thus approximately equal to the potentials at their respective contacts. This allows the problem to be simplified to one in the perovskite layer only. In line with Eames *et al.*[22] who estimate the diffusion coefficient of the I^- vacancies to be four orders of magnitude greater than that of the other ionic constituents (Pb^{2+} and MA^+) we assume that the only mobile charged species in the perovskite, other than holes and electrons, are the I^- vacancies. Furthermore we assume that these vacancies do not migrate into the blocking layers. Whilst in some cells there is evidence that the I^- ions pass through pinholes in the spiro to the metal contact,[41] our overall conclusions still hold, and we are currently looking to how to extend our model to this case.

The narrowness of the Debye layers that ensue from the high ion density, and the very strong variations of ion concentration and potential within them, render direct numerical solution of a drift-diffusion (DD) model extremely challenging, see for example.[29] Even with a highly tailored numerical approach, such as the one adopted here, it is not possible on a practical timescale to compute an accurate representation of the solution. Here, in order to circumvent these difficulties an approximate approach is adopted based on asymptotic expansions.

The validity of this approach is demonstrated by comparing the potentials and ion densities obtained from a numerical solution to the DD model (ESI,† note 1) with the asymptotic approximation (briefly described below) to the same model, albeit for unrealistically low iodide vacancy concentrations. A brief description of the asymptotic method follows. Matched asymptotic expansions (*cf.* Foster *et al.*[26]) can be used to derive a capacitance relation between the charge Q per unit area in a Debye layers and the potential drop V across it; for a single mobile positively charged species (*i.e.* an I^- vacancy)

$$Q(V) = \frac{\varepsilon V_T}{L_d}\mathrm{sign}(V)\left[2\left(e^{V/V_T} - 1 - \frac{V}{V_T}\right)\right]^{1/2}, \qquad (1)$$

and is plotted in Fig. 2 (a similar capacitance relation has been derived, in a different context, by Richardson[42]). Eqn (1) is valid for diffuse layers in which the density of vacancy sites does not limit vacancy density (*i.e.* volume exclusion effects are insignificant) and is thus analogous to the capacitance relation calculated from Gouy–Chapman theory for a 1:1 electrolyte. The fact that only one ion species is mobile is reflected in the asymmetry of the capacitance curve in Fig. 2, which contrasts to the symmetric capacitance curve predicted for a 1:1 electrolyte by Gouy–Chapman theory. The diffuse layer approximation holds well for $N_0 = 1.0 \times 10^{17}$ cm^{-3} used in Fig. 3 and 4 but can start to break down for the higher equilibrium vacancy density, $N_0 = 1.6 \times 10^{19}$ cm^{-3} predicted by Walsh *et al.*[30] This breakdown occurs if Q_+, the charge per unit area in the vacancy accumulation layer (the right-hand layers in Fig. 3 and 4), becomes sufficiently large to result in vacancy densities comparable to the density of vacancy sites (*i.e.* volume exclusion effects become significant). Nevertheless this effect is not strong enough, with $N_0 = 1.6 \times 10^{19}$ cm^{-3}, to alter the results qualitatively.

In practice it is easier to solve directly for surface charge densities stored in the left- and right-hand Debye layers (Q_- and Q_+, respectively) rather than for the potential drops across these layers, V_- and V_+ (illustrated in Fig. 1). In order to do this it is necessary to invert the capacitance relation (1) to obtain expressions for V_- and V_+ in terms of Q_- and Q_+ of the form

$$V_- = V(Q_-),\ V_+ = V(Q_+) \quad \text{where} \quad V(\cdot) = Q^{-1}(\cdot). \qquad (2)$$

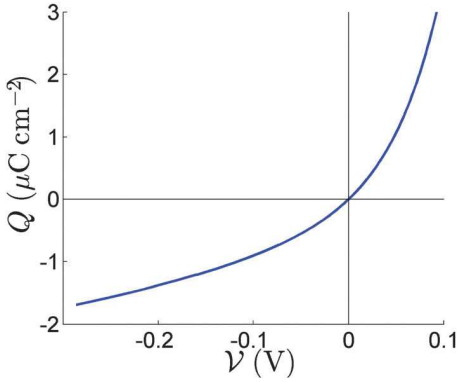

Fig. 2 The relation between the charge Q in the Debye layer and the potential drop V across the layer.

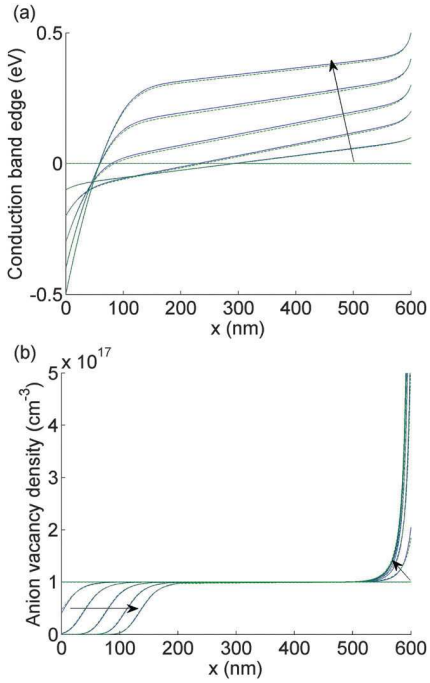

Fig. 3 Comparison between the numerical (solid blue) and the asymptotic (dashed green) solutions to $E_C(x)$ (panel a) and $P(x)$ (panel b) as the applied voltage $V(t)$ is scanned from 1 V to 0 V taking values in V of 0.8, 0.6, 0.4, 0.2, 0. At time t = 0, $E_C(x)$ = 0 for all x. The arrow indicates the direction of increasing time. For this figure and Fig. 4, $N_0 = 10^{17}$ cm^{-3}.

The density of generated electron–hole pairs is insufficient to screen the electric field in the perovskite between the Debye layers so that the potential profile is linear, as shown in Fig. 1, and the electric field $E_{\mathrm{bulk}}(t)$ is spatially uniform; $E_{\mathrm{bulk}}(t)$ can therefore be evaluated from the potential difference between points just inside the two Debye layers and is thus given by

$$E_{\mathrm{bulk}}(t) = \frac{V_{\mathrm{bi}} - V(t) - V_+ + V_-}{b}. \quad (3)$$

as can be seen from Fig. 1. Furthermore since the mobile ion concentration is uniform (and equal to N_0) within the perovskite bulk, the corresponding ion current density is well-approximated

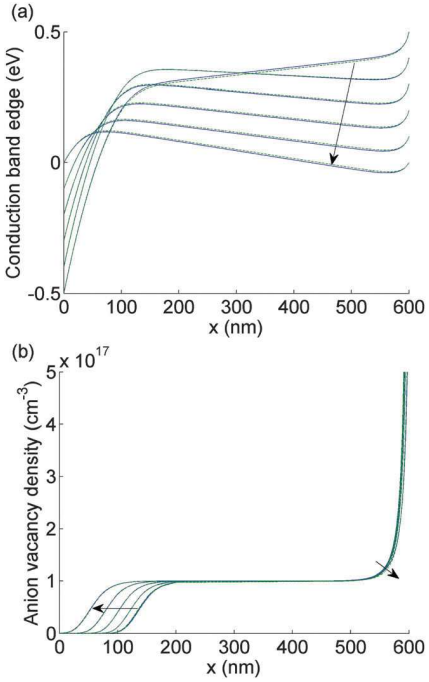

Fig. 4 As for Fig. 3 but here $V(t)$ is scanned from 0 V to 1 V and plotted at values in V 0, 0.2, 0.4, 0.6, 0.8, 1.0.

by $j_{\mathrm{ion}} = \sigma E_{\mathrm{bulk}}(t)$, where $\sigma = qD_+N_0/V_{\mathrm{T}}$ is the ionic conductivity. It follows, from the assumption that ions cannot migrate into the blocking layers, that the rates of change of Q_- and Q_+ are given by the ion currents flowing from the perovskite into the Debye layers

$$\frac{\mathrm{d}Q_-}{\mathrm{d}t} = -j_{\mathrm{ion}}(t), \quad \frac{\mathrm{d}Q_+}{\mathrm{d}t} = j_{\mathrm{ion}}(t). \quad (4)$$

Given initial charge neutrality these equations imply the charge conservation relation

$$Q_- = -Q_+. \quad (5)$$

It therefore suffices to solve only for Q_+ from the equation obtained by substituting for j_{ion} in (4), namely

$$\frac{\mathrm{d}Q_+}{\mathrm{d}t} = \frac{qD_+N_0}{V_{\mathrm{T}}}E_{\mathrm{bulk}}(t) \quad (6)$$

Here $E_{\mathrm{bulk}}(t)$, V_- and V_+ are obtained, in terms of Q_+, from (2), (3) and (5) and are used as input to a 1-d DD model for electron and hole densities (n and p) within the perovskite. Multiple ion species can be introduced by providing a contribution for each species on the right hand side of eqn (6).

The equations for the drift diffusion model are well known and so are provided in ESI,† note 2 rather than the main paper. Eqn (1) and (2) of ESI,† note 2 are the continuity equations for electrons and holes combined with the equations for the current densities in terms of their diffusion and drift components. The generation rate used in this DD model is the Beer–Lambert law while charge recombination is assumed to be predominantly trap assisted and to obey Shockley–Read–Hall theory. Its numerical

solution is determined by using the package Chebfun[43] and yields electron and hole current densities (j_n and j_p, respectively) which are used to obtain an expression for the total current density across the cell $J(t)$. Plots of $J(t)$ *versus* the applied voltage $V(t)$ yield the predicted hysteresis curves which are compared to measurements from 2 cells. The latter are made using the same process which is described in the Cell fabrication and characterization section below.

Since device history affects the measured *J–V* curves it is important to capture its effects accurately. After light soaking at open circuit, both cells were preconditioned at 1.2 V for 5 s, then swept from 1.2 V to 0 V and back again three times (these measurements are described below and the full results shown in ESI,† Fig. S1). The scan rate, ν_{scan}, was assigned values 1 V s^{-1}, 500 mV s^{-1}, 250 mV s^{-1} and 100 mV s^{-1}. Further *J–V* curves, reported in ESI,† Fig. S2(b), were measured from cell 2, which was subsequently preconditioned for 5 s at 0 V immediately after the initial set of measurements were performed.

Two different protocols were used to model: (I) the *J–V* curve obtained from the third scan after the effects of the preconditioning have worn off and (II) the *J–V* curve obtained from the first scan immediately after the preconditioning step. Since simulating all three scans is computationally intensive we choose in case (I) to start the simulation by letting the cell equilibrate at V = 1 V (*i.e.* V_{bi}) so that the Debye layers are initially uncharged (*i.e.* the sweep begins at t = 0 with Q_+ = 0) and then scan the voltage down from 1 V to 0 V by setting $V(t)$ = 1 V$-\nu_{scan}t$ between t = 0 to t = (1 V)/ν_{scan} and then scan back again at the same rate. Although this procedure may appear *adhoc* we can justify it by noting that after two cycles the preconditioning effects have worn off so that the Debye layers will be close to being uncharged ($Q_+ = Q_- \approx 0$) at $V = V_{bi}$. In case (II) the pre-conditioning step is explicitly accounted for by starting the simulation at t = −5 s with Q_+ = 0 and then immediately increasing V to 1.2 V where it remains for 5 s until t = 0, after which the downward scan is commenced with $V(t)$ = 1.2 V $- \nu_{scan}t$ from t = 0 to t = (1.2 V)/ν_{scan}; when V reaches 0 at t = (1.2 V)/ν_{scan} the direction of the scan is reversed by choosing $V(t) = \nu_{scan}t$ −1.2 V between t = (1.2 V)/ν_{scan} and t = (2.4 V)/ν_{scan}. ESI,† Fig. S2(a), (c) and (d) shows predictions from our model where we follow a similar procedure to case (II), but here the preconditioning is at 0 V for 5 s before scanning to 1.2 V and back.

Cell fabrication and characterization

Methylammonium iodide was synthesized by drop-wise addition of 10 mL of HI (57 wt% in water, Sigma-Aldrich) to a cooled solution of 24 mL methylamine (33 wt% in EtOH, Sigma-Aldrich) in 100 mL ethanol under steady stirring. The solvent was removed in a rotary evaporator and then the salt was recrystallized from ethanol. Upon slowly cooling the ethanol solution, white crystals formed. Washing with diethylether and drying at 70 °C for 6 hours gave a pure product. For the compact layer of TiO_2 a solution with 35 μL of 2 M HCl in 2.5 mL IPA was drop-wise added to a solution with 369 μL titanium isopropoxide (97%, Sigma-Aldrich) in 2.5 mL of IPA under heavy stirring. The solution for the hole transporting layer was mixed by dissolving 72.3 mg of spiro-MeOTAD (99%, Borun chemicals) in 1 mL chlorobenzene at ∼60 °C for 30 min and then adding 8.75μL 4-*tert*-butyl pyridine (tBP) and 18.75 μL Li-TFSI solution (170 mg mL^{-1} in acetonitrile).

For device fabrication, substrates of FTO/glass (TEC7, 7 μ cm^{-2}, Pilkington) were partially etched with Zn and 2 M HCl and cut into device sizes. Cleaning was done with Hellmanex solution (2 wt% in water), deionized water, acetone and oxygen plasma treatment for 30 min. A compact layer of TiO_2 was spin-coated from the TTIP solution for 60 s at 2000 rpm (2000 rpm s^{-1} ramp rate) then annealed at 500 °C for 30 min.

The perovskite layer was deposited *via* vapour assisted solution processing, VASP.[44] First, a hot solution of PbI_2 (99%, Sigma-Aldrich) in DMSO (1 M, 70 °C) was spin-coated onto the heated FTO/glass substrate (70 °C) for 60 s at 2000 rpm. The PbI_2 film was then annealed at 100 °C for 10 min. Conversion into perovskite films was done by vapor deposition of MAI. Therefore the MAI powder was put onto a hotplate together with the substrates and sealed with a desiccator lid. A temperature of 120 °C and low-vacuum were applied. Sublimation of the MAI converted the PbI_2 into $MAPbI_3$ within 30 min. The perovskite films were rinsed with IPA and blow-dried with nitrogen. For the hole-transporting layer the spiro solution was spread on the sample and left for 10 s before spin-coating at 4000 rpm for 45 s. Finally, a gold cathode was deposited *via* thermal evaporation with a shadow mask, resulting in a active area of 0.1 cm^2.

A TS Space Systems solar simulator was used with a 200 W metal halide lamp and an internal AM1.5 filter, which is calibrated against a *Fraunhofer* reference cell (ISE, RS-OD-4). The solar simulator is classified according IEC 60904-9 Edition2 and ASTM E927-10 standards as class A. *Keithley* 2600A SourceMeter was used for the *J–V* measurements.

Two cells were prepared using the above methods, each containing ten pixels. Both cells were measured with the following protocol. The cells were connected to the solar simulator and held at open circuit, V_{oc}, in the dark for several minutes. Then the cells were then held at V_{oc} for 30 s under illumination to allow a steady photovoltage to be achieved. In a preconditioning stage, the cells were held at 1.2 V for 5 s. Following this stage, the cells were swept from 1.2 V to 0 V and back to 1.2 V three times. The scan rate was then reduced and the scans repeated. In ESI,† Fig. S2(b), cell 2 *J–V* characteristics were measured in the same way except that the preconditioning voltage was 0 V. These cell 2 measurements followed immediately after the measurements for preconditioning at 1.2 V.

3 Results

The evolution of E_{bulk} is illustrated in Fig. 3(a) and 4(a) and the I^- vacancy concentration profile $P(x,t)$ in Fig. 3(b) and 4(b). These figures show a series of snapshots of the solution at evenly spaced time intervals in the scans down from V = 1 V to V = 0 V and back from V = 0 V to V = 1 V, respectively. Comparison between the uniformly valid asymptotic solution

and the numerical solution to the ion transport problem (green dashed and blue solid curves, respectively) is made in these figures (the agreement is extremely good).

The bulk electric field $E_{bulk}(t)$ is equal to the gradient of $E_C(x,t)/q$ within the central portion of the perovskite layer and is positive as $V(t)$ is decreased from 1 V to 0 V (Fig. 3(a)), driving holes to the spiro layer and electrons to the TiO_2 layer. Sharp changes in $E_C(x)$ (of magnitude qV_-, qV_+) are seen across the left-hand and right-hand Debye layers, respectively. Positively charged I^- vacancies flow into the right-hand Debye layer, increasing Q_+, and away from the left-hand Debye layer. The latter layer acquires its negative charge through vacancy depletion. Its width L_- is determined by the need to maintain charge neutrality, so that

$$Q_+(t) = |Q_-(t)| = q\int_0^{L_-} P(x,t)\mathrm{d}x = q\int_{b-L_+}^{b} P(x,t)\mathrm{d}x, \qquad (7)$$

where L_+ is the width of the right-hand Debye layer. Since $0 < P(x,t) < N_0$ in the left hand layer while $P(x,t) \gg N_0$ in the right-hand layer, the extent of the left-hand layer L_- is greater than that of the right-hand one L_+ in order to fit the same amount of charge into both. As Q_+ and $|Q_-|$ increase, L_- also increases significantly, see Fig. 3. The greater extent of the left-hand layer in comparison to that of the right-hand one gives a greater magnitude of potential drop $|V_-|$ across it compared to that across the right-hand one V_+.

Note that $E_{bulk}(t)$ becomes negative as $V(t)$ returns from 0 V to 1 V (Fig. 4(a)). This change in the sign of E_{bulk} can be used, in part, to explain the difference between the measured current in the 1.2 V to 0 V scan from that in the 0 V to 1.2 V scan. When $E_{bulk} < 0$, the field drives the free charge carriers away from the contacts where they are extracted, into the bulk of the device, leading to large carrier concentrations and increased recombination. The charge density accumulations from the mobile vacancies Q_- and Q_+ influence the free charge carrier densities at the boundaries, causing diffusion currents towards or away from the contacts. These diffusion currents can exceed the drift component. In spite of this diffusion contribution, the current is typically smaller on the 0 V to 1.2 V scan than it is on the 1.2 V to 0 V scan.

Experimental J–V data from 3 complete scan cycles of cell 1 which has been preconditioned for 5 s at 1.2 V are shown in ESI,† Fig. S1(a)–(c). Fig. 5(b) plots experimental J–V data from the third scan cycle performed on cell 1. The agreement between these results and the model solutions, computed as described above, case (I) in the Methods section, and plotted in Fig. 5(a), is very good.

Fig. 6 depicts the evolution of the bulk electric field E_{bulk} and the Debye layer surface charge density Q_+ arising from the vacancy motion predicted by the model used to simulate the J–V curves in Fig. 5(a). As noted previously where $E_{bulk}(t) > 0$, positively charged I^- vacancies flow into the right-hand Debye layer, increasing Q_+. For large positive Q_+, the potential drop across the left-hand Debye layer, $-V_-$, is large and positive and screens out the field from the potential across the contacts. In the subsequent 0 V to 1 V scan the screening, which lags behind

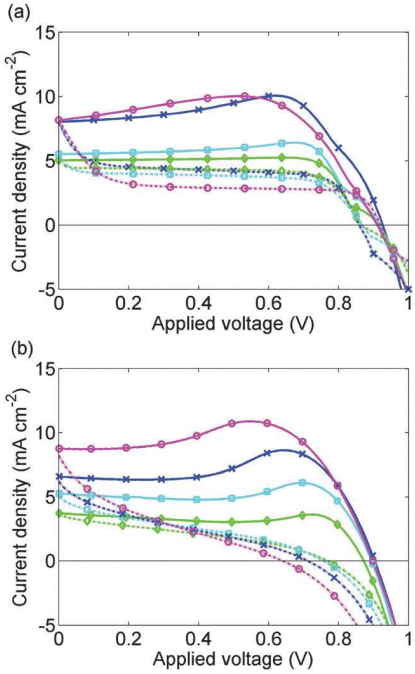

Fig. 5 (a) Calculated J–V curves for cell 1 without allowing for preconditioning; (b) measured J–V curves for cell 1 after an initial preconditioning at 1.2 V and two scan cycles. Solid lines show the 1.2 V to 0 V scan; broken lines show the 0 V to 1.2 V scan. Scan rates are 1 V s^{-1} (magenta, circles), 500 mV s^{-1} (blue, crosses), 250 mV s^{-1} (cyan, filled squares), 100 mV s^{-1} (green, diamonds). As discussed in the text the third scans are shown as the effect of the 1.2 V preconditioning is removed.

the scan, typically leads to negative E_{bulk}, putting the cell into effective forward bias and leading to high recombination rates.

The model is able to predict the maximum in the current density on the 1 V to 0 V scan, seen in measurements reported here and elsewhere.[9,11] This is closely associated with a maximum in E_{bulk} the field that drives the charge carriers apart. This result strengthens the hypothesis that large positive values of E_{bulk} suppress recombination, increasing current output.

The vacancy mediated ion motion hypothesis provides a clear explanation for the influence of scan rate on J–V curves. For slower scan rates, the vacancies have more time to respond to the change in applied voltage than for faster scans. Hence, the vacancy charge screens the bulk electric field more effectively on slower scans than on fast ones, so $|E_{bulk}|$ remains relatively small on such slow scans, resulting in limited hysteresis. For intermediate scan rates, hysteresis is strongest. At the other extreme, if the scan is sufficiently fast, the ions do not have a chance to build up in the Debye layers so that there is very limited screening and consequently little hysteresis (and increased short circuit current). This effect is not addressed here but is reported elsewhere.[10,11]

Snaith *et al.*[8] also report an increase in hysteresis with reduction in scan rate even at scan rates as low as 11 mV s^{-1}. This observation contrasts with our data which suggests that hysteresis is reduced by a decrease in scan rates below about 1 V s^{-1}. The 1.4 V to 0 V scans in ref.[8] vary little with scan rate, which could be a result of the strong preconditioning (60 s at 1.4 V) used. It may be the case that

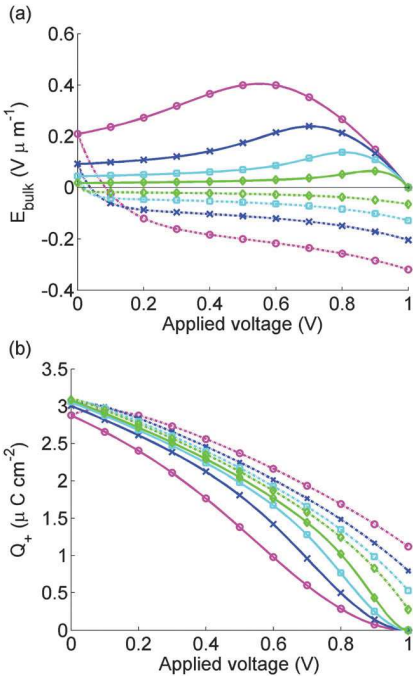

Fig. 6 Electric field between the Debye layers E_{bulk} (panel a) and charge per unit area in the Debye layer next to the spiro Q_+ (panel b) used to find calculated J–V curves for cell 1 shown in Fig. 5. Scan rates and solid and dashed lines as for Fig. 5.

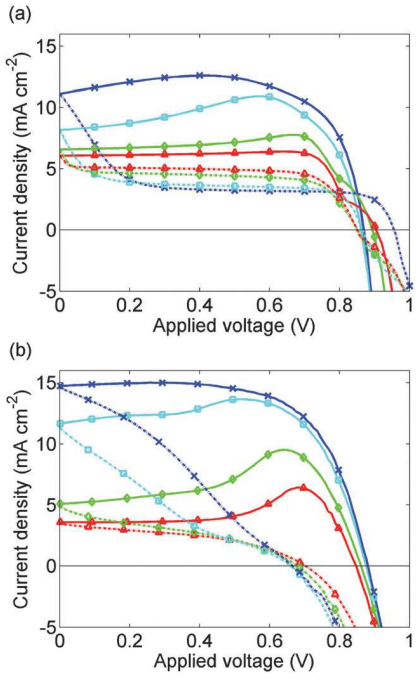

Fig. 7 (a) Calculated J–V curves for cell 2 allowing for 5 s preconditioning at 1.2 V. (b) Measured J–V curves for cell 2 on the 1st scan cycle immediately after preconditioning for 5 s at 1.2 V. Solid lines show the 1.2 V to 0 V scan; broken lines show the 0 V to 1.2 V scan. Scan rates are as for Fig. 5 with the addition of a scan rate of 50 mV s^{-1} (red, triangles). In the fastest scans the shapes of the J–V curves are improved by the preconditioning.

this strong preconditioning makes E_{bulk} high enough to yield a large current for the whole of 1.4 V to 0 V and 0 V to 1.4 V scans, unless the scan rate is very slow. Only when Snaith *et al.*[8] decreased the scan rate to 11 mV s^{-1} did the current maximum reappear.

Deviations between the experimental and theoretical results occur for the fastest scan rate, 1 V s^{-1}, and when the applied voltage is increasing from 0 V to 1 V. For the calculated 0 V to 1 V scans, J is nearly independent of V except for sharp changes in J close to open circuit. In contrast, the measured 0 V to 1.2 V scans have a continuously varying slope. Evidence from an analytic solution to the DD carrier equations that we have derived when $\tau_p = 0$ suggests that decreasing τ_p towards zero could help correct this discrepancy between experiment and theory. However for $\tau_p < \tau_n/100$, the DD equations for the free charge carriers become so stiff that numerical solutions become very difficult to find.

Experimental J–V data from 3 complete scan cycles of cell 2, which like cell 1 has been preconditioned for 5 s at 1.2 V, are shown in ESI,† Fig. S1(d)–(f). These plots show how the effects of the preconditioning step diminish over successive scan cycles. In Fig. 7(b), this data is shown for the first scan cycle. Preconditioning plays a significant role in the subsequent evolution of the J–V curve in contrast to the data presented in Fig. 5(b) for the third scan cycle.

The simulated J–V curve for cell 2, computed using case (II) in the Methods section, is plotted in Fig. 7(a) while the solution for E_{bulk} and Q_+ are plotted in Fig. 8. Comparison to experimental data, though still good, is not as good as in Fig. 5. This discrepancy may arise because the preconditioning step occurs

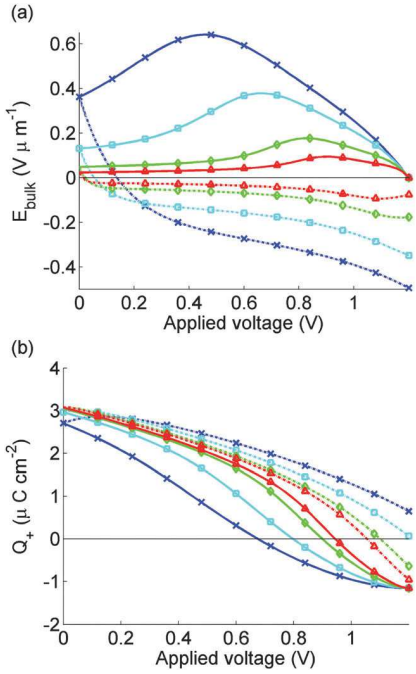

Fig. 8 As for Fig. 6, but for calculated J–V curves for cell 2 shown in Fig. 7 where we model effects of 5 s preconditioning at FB = 1.2 V.

at 1.2 V, outside the range $V \leq 1$V in which the effect of electrons and holes on the potential can be neglected. The model therefore overpredicts the charge accumulation (negative Q_+) in the preconditioning step. The sensitivity to preconditioning seen in Fig. 7(a) and (b) was also observed by O'Regan *et al.*[20]

On commencing preconditioning, $Q_+ = 0$. Since the preconditioning occurs at 1.2 V which exceeds V_{bi}, the net field in the bulk of the perovskite layer E_{bulk} is negative. As a consequence, the I^- vacancies drift towards the TiO_2 layer. A net negative charge is left next to the spiro layer, causing Q_+ to become progressively more negative. This negative Q_+ gives a negative V_+ and a positive V_- which is opposite to the signs depicted in Fig. 1. By the end of the relatively short preconditioning period, the net voltage drop of -0.2 V is nearly all accounted for by V_+ and V_- so that $E_{bulk} \approx 0$.

Once the scan begins, $V(t)$ begins to drop. However it takes time for the vacancies to move away from their accumulation layer and for Q_+ to increase from its negative value, so the reduction in E_{bulk} from V_+ and V_- is less than it would have been without the preconditioning. This result aids extraction of electrons into the TiO_2 and holes into the spiro and explains the widely reported observation that preconditioning at a voltage exceeding V_{bi} improves the apparent solar cell performance.

4 Conclusions

In conclusion, a time-dependent drift-diffusion model has been developed to explore the effects of defect mediated ion motion on the *J–V* curves of planar perovskite solar cells. We have shown that an accurate representation of the ionic charge buildup in narrow Debye layers close to the blocking layers is crucial to understanding the experimental *J–V* curves reported here.

Our model predicts hysteresis that compares well to the experimental data reported here and which is similar to that reported in the literature. The hypothesis that mobile ions in the perovskite are responsible for hysteresis is confirmed, although other explanations, such as large-scale trapping of electrons,[45] are not ruled out. We have also shown why apparently high efficiencies, obtained from measurements at fast scan rates, are not a useful indicator of device performance, even over several voltage cycles. Our approach can be generalized to explore recombination schemes other than the one considered here, to accommodate multiple ion species with different mobilities and to study why hysteresis effects increase as the temperature decreases, even in low hysteresis cells.[46,47]

The markedly lower hysteresis observed in perovskite solar cells employing a 60-PCBM hole blocking layer has been attributed by Shao *et al.*[35] to passivation of perovskite grain boundaries by the PCBM. This explanation has been questioned by Tao *et al.*[48] who note that the PCBM layer is so thin ($\sim$40 nm) in comparison to the perovskite layer ($b \approx$ 300–600 nm) that the amount of PCBM leakage required for effective passivation is enough to cause degradation of the PCBM layer and reduce device performance. The moving ion hypothesis, however, points to an alternative explanation for the lower hysteresis in these cells. Under normal operating conditions (*i.e.* $V < V_{bi}$), vacancies drift towards the spiro (PEDOT:PSS for inverted structures) and away from the PCBM, *i.e.* I^- ions move towards the PCBM. Since PCBM is made up of small molecules of functionalized C_{60} it is quite possible that I^- ions could drift across the interface entering gaps between the PCBM molecules. This cannot happen in titania, which is crystalline. It is also possible that positively charged ions, *e.g.* Li^+ from the spiro, protons or MA^+, could enter the PCBM, compensating the negative charge of the iodide ions and causing the hysteretic effect to be further reduced.

Acknowledgements

The authors wish to acknowledge helpful discussions with Laurie Peter, Saiful Islam and Aron Walsh. The research leading to these results has received funding from the European Union Seventh Framework Programme FP7/2007-2013 under grant agreement 316494 and the UK Engineering and Physical Sciences Research Council grants EP/J017361/1 & EP/I01702X/1.

References

1 A. Kojima, K. Teshima, Y. Shirai and T. Miyasaka, *J. Am. Chem. Soc.*, 2009, **131**, 6050–6051.
2 M. M. Lee, J. Teuscher, T. Miyasaka, T. N. Murakami and H. J. Snaith, *Science*, 2012, **338**, 643–647.
3 H.-S. Kim, C.-R. Lee, J.-H. Im, K.-B. Lee, T. Moehl, A. Marchioro, S.-J. Moon, R. Humphry-Baker, J.-H. Yum, J. E. Moser, M. Graetzel and N.-G. Park, *Sci. Rep.*, 2012, **2**, 591.
4 S. D. Stranks and H. J. Snaith, *Nat. Nanotechnol.*, 2015, **10**, 391–402.
5 G. Niu, X. Guo and L. Wang, *J. Mater. Chem. A*, 2015, **3**, 8970–8980.
6 T. Miyasaka, *Chem. Lett.*, 2015, **44**, 720.
7 N.-G. Park, *J. Phys. Chem. Lett.*, 2013, **4**, 2423–2429.
8 H. J. Snaith, A. Abate, J. M. Ball, G. E. Eperon, T. Leijtens, N. K. Noel, S. D. Stranks, J. T.-W. Wang, K. Wojciechowski and W. Zhang, *J. Phys. Chem. Lett.*, 2014, **5**, 1511–1515.
9 R. S. Sanchez, V. Gonzalez-Pedro, J.-W. Lee, N.-G. Park, Y. S. Kang, I. Mora-Sero and J. Bisquert, *J. Phys. Chem. Lett.*, 2014, **5**, 2357–2363.
10 E. L. Unger, E. T. Hoke, C. D. Bailie, W. H. Nguyen, A. R. Bowring, T. Heumuller, M. G. Christoforo and M. D. McGehee, *Energy Environ. Sci.*, 2014, **7**, 3690–3698.
11 W. Tress, N. Marinova, T. Moehl, S. M. Zakeeruddin, M. K. Nazeeruddin and M. Grätzel, *Energy Environ. Sci.*, 2015, **8**, 995–1004.
12 T. C. Sum, S. Chen, G. Xing, X. Liu and B. Wu, *Nanotechnology*, 2015, **26**, 342001.
13 J. Gong, S. B. Darling and F. You, *Energy Environ. Sci.*, 2015, **8**, 1953–1968.
14 J. Berry, T. Buonassisi, D. A. Egger, G. Hodes, L. Kronik, Y.-L. Loo, I. Lubomirsky, S. R. Marder, Y. Mastai, J. S. Miller, D. B. Mitzi, Y. Paz, A. M. Rappe, I. Riess, B. Rybtchinski,

O. Stafsudd, V. Stevanovic, M. F. Toney, D. Zitoun, A. Kahn, D. Ginley and D. Cahen, *Adv. Mater.*, 2015, **35**, 5102.
15 X. Li, X. Wang, W. Zhang, Y. Wu, F. Gao and J. Fang, *Org. Electron.*, 2015, **18**, 107–112.
16 J. M. Frost, K. T. Butler, F. Brivio, C. H. Hendon, M. van Schilfgaarde and A. Walsh, *Nano Lett.*, 2014, **14**, 2584–2590.
17 J. Beilsten-Edmands, G. E. Eperon, R. D. Johnson, H. J. Snaith and P. G. Radaelli, *Appl. Phys. Lett.*, 2015, **106**, 173502.
18 H.-S. Kim, I.-H. Jang, N. Ahn, M. Choi, A. Guerrero, J. Bisquert and N.-G. Park, *J. Phys. Chem. Lett.*, 2015, **6**, 4633–4639.
19 Y. Zhang, M. Liu, G. E. Eperon, T. C. Leijtens, D. McMeekin, M. Saliba, W. Zhang, M. de Bastiani, A. Petrozza, L. M. Herz, M. B. Johnston, H. Lin and H. J. Snaith, *Mater. Horiz.*, 2015, **2**, 315–322.
20 B. C. O'Regan, P. R. F. Barnes, X. Li, C. Law, E. Palomares and J. M. Marin-Beloqui, *J. Am. Chem. Soc.*, 2015, **137**, 5087–5099.
21 T.-Y. Yang, G. Gregori, N. Pellet, M. Grätzel and J. Maier, *Angew. Chem., Int. Ed.*, 2015, **54**, 7905.
22 C. Eames, J. M. Frost, P. R. F. Barnes, B. C. O'Regan, A. Walsh and M. S. Islam, *Nat. Commun.*, 2015, **6**, 7497.
23 J. M. Azpiroz, E. Mosconi, J. Bisquert and F. De Angelis, *Energy Environ. Sci.*, 2015, **8**, 2118–2127.
24 A. Walsh, *J. Phys. Chem. C*, 2015, **119**, 5755–5760.
25 J. Nelson, *The physics of solar cells*, Imperial College Press, London, UK, 2003.
26 J. M. Foster, H. J. Snaith, T. Leijtens and G. Richardson, *SIAM J. Appl. Math.*, 2014, **74**, 1935–1966.
27 S. Guarnera, A. Abate, W. Zhang, J. M. Foster, G. Richardson, A. Petrozza and H. J. Snaith, *J. Phys. Chem. Lett.*, 2015, **6**, 432–437.
28 J. O. Bokris, A. K. Reddy and M. E. Gamboa-Aldeco, *Modern Electrochemistry 2A*, Springer US, New York, 2000.
29 R. Morrow and D. R. McKenzie, *Proc. R. Soc. A*, 2011, **468**, 18–34.
30 A. Walsh, D. O. Scanlon, S. Chen, X. G. Gong and S.-H. Wei, *Angew. Chem.*, 2015, **127**, 1811.
31 T. Minemoto and M. Murata, *J. Appl. Phys.*, 2014, **116**, 054505.
32 F. Liu, J. Zhu, J. Wei, Y. Li, M. Lv, S. Yang, B. Zhang, J. Yao and S. Dai, *Appl. Phys. Lett.*, 2014, **104**, 253508.
33 X. He, K. Juan Jin, C. Ge, C. Wang, H. Bin Lu and G. Zhen Yang, *EPL*, 2013, **102**, 37007.
34 S. van Reenen, M. Kemerink and H. J. Snaith, *J. Phys. Chem. Lett.*, 2015, **6**, 3808–3814.
35 Y. Shao, Z. Xiao, C. Bi, Y. Yuan and J. Huang, *Nat. Commun*, 2014, **5**, 5784.
36 E. T. Hoke, D. J. Slotcavage, E. R. Dohner, A. R. Bowring, H. I. Karunadasa and M. D. McGehee, *Chem. Sci.*, 2015, **6**, 613–617.
37 P. Schulz, E. Edri, S. Kirmayer, G. Hodes, D. Cahen and A. Kahn, *Energy Environ. Sci.*, 2014, **7**, 1377–1381.
38 F. Brivio, K. T. Butler, A. Walsh and M. van Schilfgaarde, *Phys. Rev. B: Condens. Matter Mater. Phys.*, 2014, **89**, 155204.
39 A. Pockett, G. E. Eperon, T. Peltola, H. J. Snaith, A. Walker, L. M. Peter and P. J. Cameron, *J. Phys. Chem. C*, 2015, **119**, 3456–3465.
40 S. Sun, T. Salim, N. Mathews, M. Duchamp, C. Boothroyd, G. Xing, T. C. Sum and Y. M. Lam, *Energy Environ. Sci.*, 2014, **7**, 399–407.
41 Y. Kato, L. K. Ono, M. V. Lee, S. Wang, S. R. Raga and Y. Qi, *Adv. Mater. Interfaces*, 2015, **2**, 1500195.
42 G. Richardson, *Mathematical Medicine and Biology*, 2009, **26**, 201–224.
43 T. A. Driscoll, N. Hale and L. N. Trefethen, *Chebfun Guide*, Panufty Publications, Oxford, 2014.
44 Q. Chen, H. Zhou, Z. Hong, S. Luo, H.-S. Duan, H.-H. Wang, Y. Liu, G. Li and Y. Yang, *J. Am. Chem. Soc.*, 2014, **136**, 622–625.
45 J. H. Heo, D. H. Song, H. J. Han, S. Y. Kim, J. H. Kim, D. Kim, H. W. Shin, T. K. Ahn, C. Wolf, T.-W. Lee and S. H. Im, *Adv. Mater.*, 2015, **27**, 3424–3430.
46 D. Bryant, S. Wheeler, B. C. O'Regan, T. Watson, P. R. F. Barnes, D. Worsley and J. Durrant, *J. Phys. Chem. Lett.*, 2015, **6**, 3190–3194.
47 L. K. Ono, S. R. Raga, S. Wang, Y. Kato and Y. Qi, *J. Mater. Chem. A*, 2015, **3**, 9074–9080.
48 C. Tao, S. Neutzner, L. Colella, S. Marras, A. R. Srimath Kandada, M. Gandini, M. D. Bastiani, G. Pace, L. Manna, M. Caironi, C. Bertarelli and A. Petrozza, *Energy Environ. Sci.*, 2015, **8**, 2365–2370.

ESI Electronic Supplementary Information, ESI

Can slow-moving ions explain hysteresis in the current-voltage curves of perovskite solar cells?

Giles Richardson,[a], Simon E. J. O'Kane,[b], Ralf G. Niemann[c], Timo A. Peltola[b], Jamie M. Foster[d], Petra J. Cameron[c] and Alison B. Walker[e]

[a]*Mathematical Sciences, University of Southampton, UK,* [b]*Department of Physics, University of Bath, UK,* [c]*Department of Chemistry, University of Bath, UK,* [d]*Department of Mathematics and Statistics, McMaster University, Hamilton, Canada,*[e]*Department of Physics, University of Bath, UK. E-mail: a.b.walker@bath.ac.uk*

ESI Note 1: Drift-diffusion (DD) model for iodide vacancies

Figs. 3 and 4 in the main article compare the conduction band edge $E_C(x,t)$ and the iodide vacancy density $P(x,t)$ obtained via two different methods: the asymptotic method outlined in the main article and a numerical drift-diffusion method, which is outlined here. The drift-diffusion method is centred around solving the continuity equations

$$\frac{\partial P}{\partial t}+\frac{\partial F_p}{\partial x}=0, \quad \text{where} \quad F_p=D_+\left(\frac{P}{k_BT}\frac{\partial E_C}{\partial x}-\frac{\partial P}{\partial x}\right) \tag{1}$$

and Poisson's equation of electrostatics

$$\frac{\partial^2 E_C}{\partial x^2}=\frac{q^2}{\varepsilon_p}(P-N_0) \tag{2}$$

simultaneously, where F_p is the vacancy flux, k_B is the Boltzmann constant, T is absolute temperature (assumed here to be 298 K) and q is the electronic charge. Descriptions and values for ε_p and D_+ are given in Tables 1 and 2 of the main article respectively. Equations (1) and (2) are usually given in terms of the electrostatic potential $\phi(x,t)$ as opposed to the conduction band edge $E_C(x,t)$. It is possible to switch between the two formulations by noting that $E_C(x,t)=E_0-q\phi(x,t)$, where E_0 is the energy relative to which $E_C(x,t)$ is defined. For the purposes of this work $E_0=E_C(x,0)\,\forall x$, *i.e.* the conduction band edge under flat band conditions.

ESI Note 2: Drift-diffusion (DD) model for electrons and holes

Equations (1) and (2) of this Note are the continuity equations for electrons and holes combined with the equations for the current densities in terms of their diffusion and drift components. The current-voltage, *J-V*, curves are obtained by solving a one-dimensional transport model for the charge carriers (electrons and holes) within the perovskite ($0<x<b$). This takes the standard form

$$\frac{\partial p}{\partial t}+\frac{1}{q}\frac{\partial j_p}{\partial x}=G(x)-R(n,p), \quad \text{where} \quad j_p=q\hat{D}_p\left(\frac{p}{V_T}E_{bulk}-\frac{\partial p}{\partial x}\right), \tag{3}$$

$$\frac{\partial n}{\partial t}-\frac{1}{q}\frac{\partial j_n}{\partial x}=G(x)-R(n,p), \quad \text{where} \quad j_n=q\hat{D}_n\left(\frac{n}{V_T}E_{bulk}+\frac{\partial n}{\partial x}\right), \tag{4}$$

in which the variables: n and p denote electron and hole densities, respectively; j_n and j_p denote electron and hole currents, respectively; and $E(x,t)$ denotes the electric field. The parameters $\hat{D}_n$, $\hat{D}_p$ and V_T are described in Table 1 of the main article. The latter, as discussed in the main article, is well-approximated, in the central region of the perovskite (away from the Debye layers) by $E_{bulk}(t)$ as defined in equation (3) of the main article. The charge generation term $G(x)$ is given by the Beer-Lambert law of light absorption which, since the light enters from the left of the device (through the TiO_2 layer), has the form

$$G=F_{ph}\alpha\exp[-\alpha x], \tag{5}$$

where F_{ph} is the incident photon flux and α is the light absorption coefficient of the perovskite. Charge carrier recombination is modelled by a Shockley-Read-Hall term of the form

$$R=\frac{np-n_i^2}{\tau_n n+\tau_p p}; \tag{6}$$

where n_i is the intrinsic carrier density. We have ignored the term n_i^2 as we are always well away from equilibrium. Estimates for the electron and hole pseudo-lifetimes (τ_n and τ_p) are given in Table 2 in the main article. The physical origin of the pseudo-lifetimes is are given by[1]

$$\tau_n=\frac{1}{N_t v_{th}\sigma_p} \quad \text{and} \quad \tau_p=\frac{1}{N_t v_{th}\sigma_n}, \tag{7}$$

where N_t is the density of traps, v_{th} is the thermal velocity and σ_n and σ_p are the electron and hole capture cross-sections respectively. Crucially, the psuedo-lifetime of one carrier type is inversely proportional to the capture cross-section of the other type.

Since we believe that bulk recombination, rather than interfacial recombination, is the source of the hysteresis we neglect the effects of recombination via surface traps on the perovskite-TiO_2 and the perovskite-spiro interfaces and impose zero hole current on the former and zero electron current on the latter. It is assumed that the doping levels in the buffer layers are sufficiently high so that they are at the same potential as their respective contacts. It follows that the potentials at the perovskite-buffer layer interfaces are equal to the potentials at the respective contacts. The boundary conditions on (3)-(4) thus read

$$\left.\begin{array}{c} n = n_0 \\ j_p = 0 \end{array}\right\} \text{ on } x = 0, \qquad \left.\begin{array}{c} p = p_0 \\ j_n = 0 \end{array}\right\} \text{ on } x = b. \tag{8}$$

Numerical solution to the carrier transport equations (3)-(8) proves difficult for the same reasons that the solution to the ionic one proves problematic, that is because of the presence of the narrow Debye layers adjacent to the edges of the perovskite (on $x = 0$ and $x = b$) over which the solutions to n and p vary extremely rapidly. This difficulty may be overcome by noting that there is minimal band bending within the Debye layers so that n and p vary exponentially (in the standard fashion) with the potential in these layers. It follows that the boundary conditions at the interfaces (8) can be replaced by the standard approximate ones

$$\left.\begin{array}{c} n = n_0 \exp\left(\dfrac{\boldsymbol{\mathcal{V}}_-(t)}{V_T}\right) \\ j_p = 0 \end{array}\right\} \text{ on } x = 0^+, \qquad \left.\begin{array}{c} p = p_0 \exp\left(-\dfrac{\boldsymbol{\mathcal{V}}_+(t)}{V_T}\right) \\ j_n = 0 \end{array}\right\} \text{ on } x = b^-, \tag{9}$$

which hold on the interior of the respective Debye layers (denoted by $x = 0^+$ and $x = b^-$ to highlight the fact that these regions lie just inside the perovskite layer). Here $\boldsymbol{\mathcal{V}}_- = \boldsymbol{\mathcal{V}}(-Q_+)$ is the potential drop from the TiO_2 interface (on $x = 0$) to the interior of the adjacent Debye layer at $x = 0^+$ and $\boldsymbol{\mathcal{V}}_+ = \boldsymbol{\mathcal{V}}(Q_+)$ is the potential drop from the spiro interface (on $x = b$) to the interior of the adjacent Debye layer at $x = b^-$. Solution of (3)-(4) is then made throughout the bulk region $0^+ < x < b^-$ with the appropriate asymptotic expression for the electric field in the bulk, namely

$$E = E_{bulk}(t) = \frac{V_{bi} - V(t) - \boldsymbol{\mathcal{V}}(Q_+(t)) + \boldsymbol{\mathcal{V}}(-Q_+(t))}{b}. \tag{10}$$

and used to calculate $J(t) = j_n + j_p$ as the applied potential $V(t)$ varies and hence to obtain J-V curves for particular scanning profiles. The timescales used for generating these hysteresis curves are nearly always much greater than the timescale for relaxation of the charge carrier concentrations and consequently the error made in neglecting the time derivatives in (3)-(4) is negligible.

Here numerical solution of (3)-(4) and (9)-(10) is accomplished using the same package used for the ionic problem, namely Chebfun, because although the effects of the Debye layers have been accounted for using an asymptotic technique the problem is stiff (and therefore hard to resolve numerically) when E is large.

References

[1] S. Sze, *Physics of Semiconductor Devices, 2nd Edition*, John Wiley & Sons, New York, 2002.

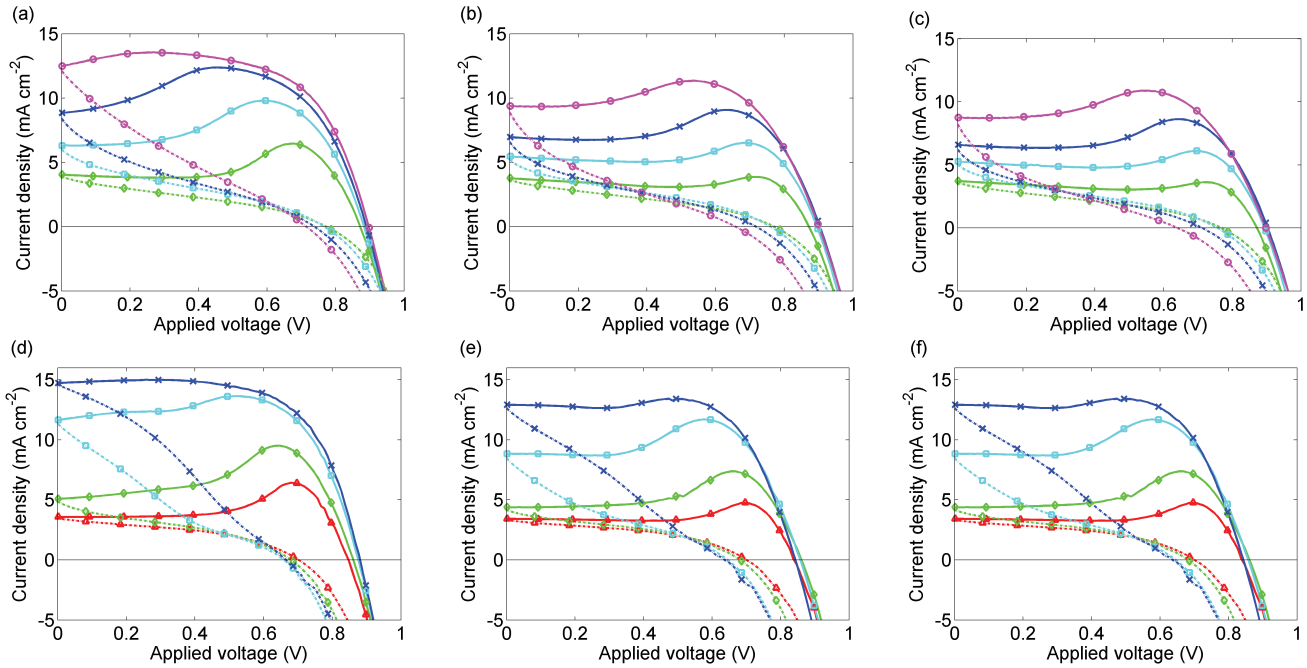

ESI Fig.1.

Measured J-V curves for cells 1 and 2 preconditioned for 5s at 1.2V. Cell 1: (a) first scan, (b) second scan, (c) third scan. Cell 2: (d) first scan, (e) second scan, (f) third scan. Solid lines show the 1.2 V to 0 V scan; broken lines show the 0V to 1.2 V scan. Scan rates are 1 V/s (magenta, circles), 500 mV/s (blue, crosses), 250 mV/s (cyan, filled squares), 100 mV/s (green, diamonds). For cell 2, we also show results for a scan rate of 50 mV/s (red, triangles)

ESI Note 3: Preconditioning at short circuit

ESI Fig. 2 contains measurements (a) and simulations (b),(c),(d) of cell 2 for the case where the cell was preconditioned at short circuit as opposed to 1.2 V. For faster scans, Q_+ at $V \approx 1.2$ V in ESI Fig. 2 (d) for the 1.2 V to 0 V scan is larger for preconditioning at 0 V compared to Q_+ where preconditioning is at 1.2 V shown in Fig. 8 (b) in the main article. This difference in Q_+ has little effect on the current J predicted by the model due to inaccuracies in the diffusion currents when there is a large amount of electronic charge in the cell, as discussed in the main article. However, the measured currents differ significantly between the two preconditioning experiments even for the slow scans where Q_+ is predicted to be similar for both types of preconditioning. It is possible that D_+ has been overestimated so that the simulated I^- vacancies respond too quickly to changes in the voltage compared to in the experiments. Some degradation may have taken place during the measurement for preconditioning at 1.2 V, which were performed first, although we would not expect significant changes in cell output over this short period.

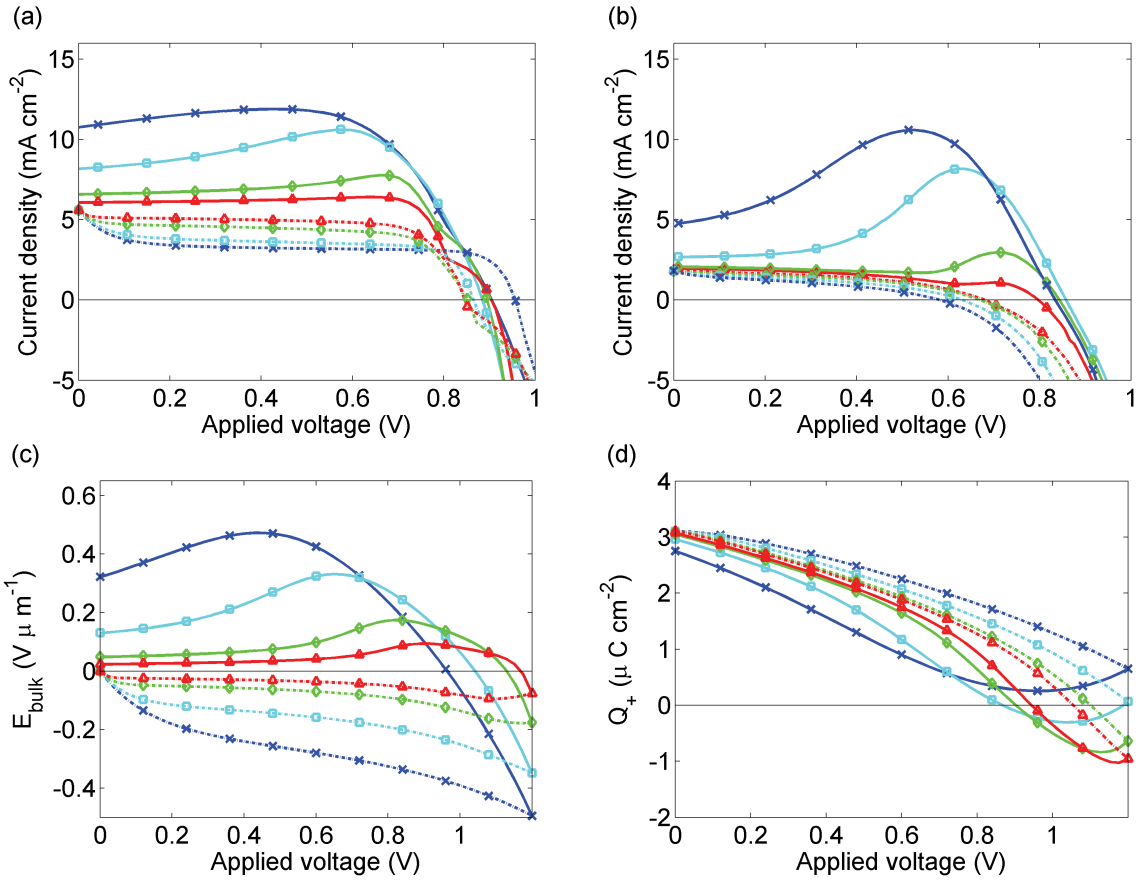

ESI Fig. 2.

$J-V$ curves, fields and accumulated ionic charge for the first scan of cell 2. Scan rates are 500 mV s^{-1} (blue), 250 mV s^{-1} (cyan), 100 mV s^{-1} (green) and 50 mV s^{-1} (red). Solid lines show the 1.2 V to 0 V scan dashed lines the 0V to 1.2V scan. Top panels: J-V curves with 5 s preconditioning at 0 V; (a) calculated, (b) measured. Bottom panels: (c) Electric field E_{bulk} between the Debye layers and (d) charge per unit area Q_+ in the Debye layer next to the spiro. When $E_{bulk} > 0$, holes drift towards the spiro and electrons towards the TiO_2.

3.2.6.2 Contemporary assessment

The previously described V-VASP process was modified, by using lower temperatures (120 instead of 150 °C) and shorter perovskite conversion times to increase the defect density,[66] which yielded cells with higher hysteresis. While defects easily arise during the crystallisation process, there are several ways to cure those defects to avoid detrimental effects on cell performance. In this work however the aim was to maximise hysteresis. Gouda *et al.* also reported on MAI vapour healing,[67] which is minimised in this case by decreasing the conversion time. This would explain the underlying mechanism on why the V-VASP treatment with our new parameters forms cells with a very high hysteresis contribution. However, this does not lighten the significance of this study for 'normal' cells with less hysteresis, because the increase in defect density does not affect the activation barrier of ion diffusion, which was a critical parameter in this study. Following our intial work, several other studies have recently pointed out that the degree of hysteresis critically depends on processing conditions. Factors like PbI_2 deficiency and defect density are directly linked to several processes, including hysteresis, recombination processes and even shelf-lifetime.[68, 69, 70] While it seems widely accepted in literature that vacancy-mediated iodide transport is intrinsically present in $MAPbI_3$ perovskites,[71, 72, 73, 74, 61] the degree of hysteresis in the devices seems to vary on processing conditions. Especially inter-facial recombination processes seem to play a critical role regarding the dominance of hysteresis in the device;[70] thus passivating the contact recombination would screen the ionic charge and decrease hysteretic effects. However, the exact activation energy is still uncertain. Pockett *et al.* recently measured an Arrhenius activation energy for low frequency processes in IMVS and EIS measurements of 0.68 eV and 0.55 eV, respectively, which is very close to the values of Eames *et al.*[64, 75] Other reports give different activation energies, for example a study by Meloni *et al.* that measured temperature dependent IV scans and deduces a value of $314 \leq E_A \leq 333$ meV.[76] It remains uncertain up to now to which extent interfaces participate in hysteresis. It is known that hysteresis itself can be changed by manipulating the interface material, which is unlikely to influence bulk properties, such as defect density and activation energy.[70] This suggests that the hysteretic effects are not confined to the perovskite layer but diffusion extends across the interface boundaries. This could mean that either ionic species from the perovskite can diffuse into one of the blocking layers or that ionic dopants from the interface (*e.g.* Li^+) diffuse into the perovskite. In summary, it could be shown that the V-VASP process does not only offer opportunities for up-scaling,[46, 47] as shown in the last section, but also allows a control of bulk properties. Even though this section intentionally maximised the undesirable defect density, it also shows the delicacy of this type of

material and demonstrates the importance of a thorough optimisation of processing conditions.

3.3 Conclusions

This chapter described aspects of perovskite cell fabrication, from basic principles up to a judicious fabrication procedure for cells with specific properties. The results given in this chapter elaborate on basic principles of perovskite solar cell production and give further evidence to the theory that vacancy mediated ion diffusion is responsible for the anomalous hysteresis effect.

More specifically, the results on substrate treatment and bl-TiO_2 deposition methods compliment a study by Moehl *et al.* about photocurrent amplification with a porous blocking layers,[20] by confirming the porosity of spin-coated TiO_2 layers and showing that the degree of this effect can be varied through different pre-treatments of the substrate. The development of a hardware and software setup allowed for an automated measurement of IV curves and adjustment of voltage scanning protocol to take hysteretic effects into account. A home-build gas sensor showed the fast build-up of a solvent atmosphere in the dry box environment, which equally stems from the spin-coating and annealing of the thin-film. Furthermore, the development of different fabrication routes for PSC devices shows the versatility and complexity of this perovskite material, with many factors influencing its performance. Using a high air-flow rate decreases the conversion temperature of the precursor solution. A further development of the VASP process[44] to vacuum-VASP in this work allows for a perovskite conversion in air with efficiencies up to 12.7 % PCE. The fabrication process was modified to produce cells with a high defect density that give a pronounced anomalous hysteresis, which was compared to a numerical drift-diffusion model.

These findings help to improve basic fabrication steps of the perovskite cell making process and understand anomalous hysteresis effect, which remains an enigmatic bottleneck towards a further implication of this technology. For example substrate pre-treatment routines, annealing conditions of the $MAPbI_3$ thin-film and conversion times in the V-VASP process. The qualitative modelling of hysteresis aided the further understanding of the working principles of perovskite cells, for example the Debye layer thickness was estimated to about 1.5 nm from the chosen parameters, based on the measured IV curves.[77] This layer could give rise to substantial recombination at the interface.[78]

3.4 Bibliography

[1] W. Ramsay, "Radium and its products," *Harper's Magazine*, 1904.

[2] A. Kojima, K. Teshima, Y. Shirai, and T. Miyasaka, "Organometal halide perovskites as visible-light sensitizers for photovoltaic cells.," *Journal of the American Chemical Society*, vol. 131, pp. 6050–6051, may 2009.

[3] G. E. Eperon, V. M. Burlakov, P. Docampo, A. Goriely, and H. J. Snaith, "Morphological Control for High Performance, Solution-Processed Planar Heterojunction Perovskite Solar Cells," *Advanced Functional Materials*, pp. 151–157, 2013.

[4] S. Shoaee, J. Briscoe, J. R. Durrant, and S. Dunn, "Acoustic enhancement of polymer/ZnO nanorod photovoltaic device performance," *Advanced Materials*, vol. 26, no. 2, pp. 263–268, 2014.

[5] P. Kollman, "Assisted Model Building with Energy Refinement." http://ambermd.org [Online; accessed: 5-Aug-2014], 2014.

[6] P. J. Cameron, L. M. Peter, and S. Hore, "How important is the back reaction of electrons via the substrate in dye-sensitized nanocrystalline solar cells?," *Journal of Physical Chemistry B*, vol. 109, no. 2, pp. 930–936, 2005.

[7] P.-W. Liang, C.-Y. Liao, C.-C. Chueh, F. Zuo, S. T. Williams, X.-K. Xin, J. Lin, and A. K.-Y. Jen, "Additive Enhanced Crystallization of Solution-Processed Perovskite for Highly Efficient Planar-Heterojunction Solar Cells," *Advanced Materials*, vol. 26, no. 22, pp. 3748–54, 2014.

[8] E. Edri, S. Kirmayer, S. Mukhopadhyay, K. Gartsman, G. Hodes, and D. Cahen, "Elucidating the charge carrier separation and working mechanism of CH3NH3PbI3xClx perovskite solar cells," *Nature Communications*, vol. 5, p. 3461, 2014.

[9] V. Gonzalez-Pedro, E. J. Juarez-Perez, W.-S. Arsyad, E. M. Barea, F. Fabregat-Santiago, I. Mora-Sero, and J. Bisquert, "General Working Principles of CH3NH3PbX3 Perovskite Solar Cells.," *Nano Letters*, vol. 14, no. 2, pp. 888–893, 2014.

[10] K. Wojciechowski, M. Saliba, T. Leijtens, A. Abate, and H. J. Snaith, "Sub-150C processed meso-superstructured perovskite solar cells with enhanced efficiency," *Energy & Environmental Science*, vol. 7, pp. 1142–1147, 2014.

[11] M. M. Lee, J. Teuscher, T. Miyasaka, T. N. Murakami, and H. J. Snaith, "Efficient hybrid solar cells based on meso-superstructured organometal halide perovskites," *Science*, vol. 338, no. 6107, pp. 643–647, 2012.

[12] I. Chung, B. Lee, J. He, R. P. H. Chang, and M. G. Kanatzidis, "All-solid-state dye-sensitized solar cells with high efficiency," *Nature*, vol. 485, pp. 486–489, may 2012.

[13] A. S. Subbiah, A. Halder, S. Ghosh, N. Mahuli, G. Hodes, and S. K. Sarkar, "Inorganic Hole Conducting Layers for Perovskite-Based Solar Cells," *Journal of Physical Chemistry Letters*, vol. 5, pp. 1748–1753, may 2014.

[14] Z. Li, S. Kulkarni, P. Boix, E. Shi, and A. Cao, "Laminated Carbon Nanotube Networks for Metal Electrode-Free Efficient Perovskite Solar Cells," *ACS Nano*, vol. 8, no. 7, pp. 6797 – 6804, 2014.

[15] S. Colella, E. Mosconi, P. Fedeli, A. Listorti, F. Gazza, F. Orlandi, P. Ferro, T. Besagni, A. Rizzo, G. Calestani, G. Gigli, F. D. Angelis, and R. Mosca, "MAPbI(3-x)Clx Mixed Halide Perovskite for Hybrid Solar Cells : The Role of Chloride as Dopant on the Transport and Structural Properties," *Chemistry of Materials*, vol. 25, no. 22, pp. 4613–4618, 2013.

[16] A. Calloni, A. Brambilla, G. Berti, G. Bussetti, E. V. Canesi, M. Binda, A. Petrozza, M. Finazzi, F. Ciccacci, and L. Duò, "X-ray photoemission spectroscopy investigation of the interaction between 4-mercaptopyridine and the anatase TiO2 surface," *Langmuir*, vol. 29, no. 26, pp. 8302–8310, 2013.

[17] J. M. Ball, M. M. Lee, A. Hey, and H. J. Snaith, "Low-temperature processed meso-superstructured thin-film perovskite solar cells," *Energy & Environmental Science*, vol. 6, no. 6, pp. 1739–1743, 2013.

[18] M. G. Helander, M. T. Greiner, Z. B. Wang, W. M. Tang, and Z. H. Lu, "Work function of fluorine doped tin oxide," *Journal of Vacuum Science & Technology A*, vol. 29, p. 011019, 2011.

[19] L. Kavan, N. Tetreault, T. Moehl, and M. Grätzel, "Electrochemical Characterization of TiO2 Blocking Layers for Dye- Sensitized Solar Cells," *Journal of Physical Chemistry C*, vol. 118, pp. 16408 – 16418, 2014.

[20] T. Moehl, J. H. Im, Y. H. Lee, K. Domanski, F. Giordano, S. M. Zakeeruddin, M. I. Dar, L.-p. Heiniger, M. K. Nazeeruddin, N.-g. Park, and M. Gra, "Strong Photocurrent Amplification in Perovskite Solar Cells with a Porous TiO2 Blocking Layer under Reverse Bias," *Journal of Physical Chemistry Letters*, vol. 5, pp. 3931–3936, 2014.

[21] B. Conings, L. Baeten, C. De Dobbelaere, J. D'Haen, J. Manca, and H.-G. Boyen, "Perovskite-Based Hybrid Solar Cells Exceeding 10% Efficiency with High Reproducibility Using a Thin Film Sandwich Approach," *Advanced Materials*, vol. 26, no. 13, pp. 2041–2046, 2013.

[22] A. Dualeh, N. Tétreault, T. Moehl, P. Gao, M. K. Nazeeruddin, and M. Grätzel, "Effect of Annealing Temperature on Film Morphology of Organic-Inorganic Hybrid Pervoskite Solid-State Solar Cells," *Advanced Functional Materials*, pp. 1–6, 2014.

[23] M. J. Carnie, C. Charbonneau, M. L. Davies, J. Troughton, T. M. Watson, K. Wojciechowski, H. Snaith, and D. Worsley, "A one-step low temperature processing

route for organolead halide perovskite solar cells," *Chemical Communications*, vol. 49, no. 72, pp. 7893–7895, 2013.

[24] N. Ahn, D.-Y. Son, I.-H. Jang, S. M. Kang, M. Choi, and N.-G. Park, "Highly Reproducible Perovskite Solar Cells with Average Efficiency of 18.3% and Best Efficiency of 19.7% Fabricated via Lewis Base Adduct of Lead(II) Iodide," *Journal of the American Chemical Society*, vol. 137, no. 27, pp. 8696–8699, 2015.

[25] M. Saliba, K. Tan, and H. Sai, "Influence of Thermal Processing Protocol upon the Crystallization and Photovoltaic Performance of Organic - Inorganic Lead Trihalide Perovskites," *Journal of Physical Chemistry C*, vol. 118, no. 30, pp. 17171 – 77, 2014.

[26] C. O. Ramírez Quiroz, I. Levchuk, C. Bronnbauer, M. Salvador, K. Forberich, T. Heumüller, Y. Hou, P. Schweizer, E. Spiecker, and C. J. Brabec, "Pushing efficiency limits for semitransparent perovskite solar cells," *Journal of Materials Chemistry A*, vol. 3, no. 47, pp. 24071–24081, 2015.

[27] G. Eperon, V. Burlakov, A. Goriely, and H. Snaith, "Neutral Color Semitransparent Microstructured Perovskite Solar Cells," *ACS Nano*, vol. 8, no. 1, pp. 591–598, 2014.

[28] H. Snaith, A. Abate, and J. Ball, "Anomalous Hysteresis in Perovskite Solar Cells," *Journal of Physical Chemistry Letters*, vol. 5, pp. 1511–1515, 2014.

[29] K. Hwang, Y.-s. Jung, Y.-j. Heo, F. H. Scholes, S. E. Watkins, J. Subbiah, D. J. Jones, D.-y. Kim, and D. Vak, "Toward Large Scale Roll-to-Roll Production of Fully Printed Perovskite Solar Cells," *Advanced Materials*, vol. 27, no. 7, p. 1521, 2015.

[30] G. E. Eperon, S. N. Habisreutinger, T. Leijtens, B. J. Bruijnaers, J. J. van Franeker, D. W. DeQuilettes, S. Pathak, R. J. Sutton, G. Grancini, D. S. Ginger, R. A. J. Janssen, A. Petrozza, and H. J. Snaith, "The Importance of Moisture in Hybrid Lead Halide Perovskite Thin Film Fabrication," *ACS Nano*, vol. 9, no. 9, pp. 9380–9393, 2015.

[31] A. M. A. Leguy, Y. Hu, M. Campoy-Quiles, M. I. Alonso, O. J. Weber, P. Azarhoosh, M. van Schilfgaarde, M. T. Weller, T. Bein, J. Nelson, P. Docampo, and P. R. F. Barnes, "Reversible Hydration of CH3NH3PbI3 in Films, Single Crystals, and Solar Cells," *Chemistry of Materials*, vol. 27, no. 9, pp. 3397–3407, 2015.

[32] D. Li, S. A. Bretschneider, V. W. Bergmann, I. M. Hermes, J. Mars, A. Klasen, H. Lu, W. Tremel, M. Mezger, H.-J. Butt, S. A. L. Weber, and R. Berger, "Humidity-Induced Grain Boundaries in MAPbI3 Perovskite Films," *The Journal of Physical Chemistry C*, vol. 120, no. 12, pp. 6363–6368, 2016.

[33] C. Muller, T. Glaser, M. Plogmeyer, M. Sendner, S. Doring, A. A. Bakulin, C. Brzuska, R. Scheer, M. S. Pshenichnikov, W. Kowalsky, A. Pucci, and R. Lovrincic, "Water Infiltration in Methylammonium Lead Iodide Perovskite: Fast and Inconspicuous," *Chemistry of Materials*, vol. 27, no. 22, pp. 7835–7841, 2015.

[34] M. K. Gangishetty, R. W. J. Scott, and T. L. Kelly, "Effect of Relative Humidity on Crystal Growth, Device Performance and Hysteresis in Planar Heterojunction Perovskite Solar Cells," *Nanoscale*, vol. 8, pp. 6300–6307, 2016.

[35] J. Burschka, N. Pellet, S.-J. Moon, R. Humphry-Baker, P. Gao, M. K. Nazeeruddin, and M. Grätzel, "Sequential deposition as a route to high-performance perovskite-sensitized solar cells.," *Nature*, vol. 499, no. 7458, pp. 316–320, 2013.

[36] N. Jeon, J. Noh, Y. Kim, W. Yang, S. Ryu, and S. Seok, "Solvent engineering for high-performance inorganic-organic hybrid perovskite solar cells," *Nature Materials*, vol. 13, pp. 897–903, 2014.

[37] N. J. Jeon, J. H. Noh, W. S. Yang, Y. C. Kim, S. Ryu, J. Seo, and S. I. Seok, "Compositional engineering of perovskite materials for high-performance solar cells," *Nature*, vol. 517, no. 7535, pp. 476–480, 2015.

[38] W. S. Yang, J. H. Noh, N. J. Jeon, Y. C. Kim, S. Ryu, J. Seo, and S. I. Seok, "High-performance photovoltaic perovskite layers fabricated through intramolecular exchange," *Science*, vol. 348, pp. 1234–1237, may 2015.

[39] M. Saliba, T. Matsui, J.-Y. Seo, K. Domanski, J.-P. Correa-Baena, N. Mohammad K., S. M. Zakeeruddin, W. Tress, A. Abate, A. Hagfeldt, and M. Grätzel, "Cesium-containing Triple Cation Perovskite Solar Cells: Improved Stability, Reproducibility and High Efficiency," *Energy & Environmental Science*, vol. 9, pp. 1989–1997, 2016.

[40] S. Pathak, A. Sepe, A. Sadhanala, F. Deschler, A. Haghighirad, N. Sakai, K. C. Goedel, S. D. Stranks, N. Noel, M. Price, S. Hu, N. A. Hawkins, R. H. Friend, U. Steiner, and H. J. Snaith, "Atmospheric Influence upon Crystallization and Electronic Disorder and Its Impact on the Photophysical Properties of Organic-Inorganic Perovskite Solar Cells," *ACS Nano*, vol. 9, no. 3, pp. 2311–2320, 2015.

[41] M. Liu, M. B. Johnston, and H. J. Snaith, "Efficient planar heterojunction perovskite solar cells by vapour deposition.," *Nature*, vol. 501, no. 7467, pp. 395–398, 2013.

[42] M. Era, T. Hattori, T. Taira, and T. Tsutsui, "Self-organized growth of PbI-based layered perovskite quantum well by dual-source vapor deposition," *Chemistry of Materials*, vol. 4756, no. 16, pp. 8–10, 1997.

[43] P. Docampo, F. C. Hanusch, N. Giesbrecht, P. Angloher, A. Ivanova, and T. Bein, "Influence of the orientation of methylammonium lead iodide perovskite crystals on solar cell performance," *APL Materials*, vol. 2, p. 081508, 2014.

[44] Q. Chen, H. Zhou, Z. Hong, S. Luo, H.-S. Duan, H.-H. Wang, Y. Liu, G. Li, and Y. Yang, "Planar heterojunction perovskite solar cells via vapor-assisted solution process.," *Journal of the American Chemical Society*, vol. 136, no. 2, pp. 622–625, 2014.

[45] S. Casaluci, L. Cina, A. Pockett, P. S. Kubiak, R. G. Niemann, A. Reale, A. Di Carlo, and P. J. Cameron, "A Simple Approach for the Fabrication of Perovskite Solar Cells in Air," *Journal of Power Sources*, vol. 297, pp. 504–510, 2015.

[46] A. Fakharuddin, A. L. Palma, F. D. Giacomo, S. Casaluci, F. Matteocci, Q. Wali, M. Rauf, A. D. Carlo, T. M. Brown, and R. Jose, "Solid state perovskite solar modules by vacuum-vapor assisted sequential deposition on Nd:YVO 4 laser patterned rutile TiO 2 nanorods," *Nanotechnology*, vol. 26, no. 49, p. 494002, 2015.

[47] T. Gatti, S. Casaluci, M. Prato, M. Salerno, F. Di Stasio, A. Ansaldo, E. Menna, A. Di Carlo, and F. Bonaccorso, "Boosting Perovskite Solar Cells Performance and Stability through Doping a Poly-3(hexylthiophene) Hole Transporting Material with Organic Functionalized Carbon Nanostructures," *Advanced Functional Materials*, vol. 26, no. 41, pp. 7443–7453, 2016.

[48] F. Matteocci, Y. Busby, J.-J. Pireaux, G. Divitini, S. Cacovich, C. Ducati, and A. Di Carlo, "Interface and Composition Analysis on Perovskite Solar Cells," *ACS Applied Materials and Interfaces*, vol. 7, no. 47, pp. 26176–26183, 2015.

[49] D. Cui, Z. Yang, D. Yang, X. Ren, Y. Liu, Q. Wei, H. Fan, J. Zeng, and S. F. Liu, "Color-Tuned Perovskite Films Prepared for Efficient Solar Cell Applications," *The Journal of Physical Chemistry C*, vol. 120, no. 1, pp. 42–47, 2016.

[50] L. Gouda, R. Gottesman, A. Ginsburg, D. A. Keller, E. Haltzi, J. Hu, S. Tirosh, A. Y. Anderson, A. Zaban, and P. P. Boix, "Open Circuit Potential Build-Up in Perovskite Solar Cells from Dark Conditions to 1 Sun," *The Journal of Physical Chemistry Letters*, vol. 6, no. 22, pp. 4640–4645, 2015.

[51] D. H. Cao, C. C. Stoumpos, C. D. Malliakas, M. J. Katz, O. K. Farha, J. T. Hupp, and M. G. Kanatzidis, "Remnant PbI2, an unforeseen necessity in high-efficiency hybrid perovskite-based solar cells?," *APL Materials*, vol. 2, no. 9, p. 091101, 2014.

[52] Y. C. Kim, N. J. Jeon, J. H. Noh, W. S. Yang, J. Seo, J. S. Yun, A. Ho-Baillie, S. Huang, M. A. Green, J. Seidel, T. K. Ahn, and S. I. Seok, "Beneficial Effects of PbI2 Incorporated in Organo-Lead Halide Perovskite Solar Cells," *Advanced Energy Materials*, vol. 6, p. 1502104, 2016.

[53] T. J. Jacobsson, J.-P. Correa-Baena, E. Halvani Anaraki, B. Philippe, S. D. Stranks, M. E. F. Bouduban, W. Tress, K. Schenk, J. Teuscher, J.-E. Moser, H. Rensmo, and A. Hagfeldt, "Unreacted PbI2 as a Double-Edged Sword for Enhancing the Performance of Perovskite Solar Cells," *Journal of the American Chemical Society*, vol. 138, no. 32, pp. 10331–10343, 2016.

[54] C. Roldan Carmona, P. Gratia, I. Zimmermann, G. Grancini, P. Gao, M. Gratzel, and N. Mohammad K., "High efficiency methylammonium lead triiodide perovskite solar cells: the relevance of non-stoichiometric precursors," *Energy & Environmental Science*, vol. 8, pp. 3550–3556, 2015.

[55] J. Teuscher, A. Ulianov, O. Muntener, M. Gratzel, and N. Tetreault, "Control and Study of the Stoichiometry in Evaporated Perovskite Solar Cells," *ChemSusChem*, vol. 8, no. 22, pp. 3847–3852, 2015.

[56] S. Wang, W. Dong, X. Fang, Q. Zhang, S. Zhou, Z. Deng, R. Tao, J. Shao, R. Xia, C. Song, L. Hu, and J. Zhu, "The credible evidence for passivation effect of remnant PbI2 in CH3NH3PbI3 films for improving the performance of perovskite solar cells," *Nanoscale*, vol. 8, pp. 6600–6608, 2016.

[57] H. J. Snaith, "How should you measure your excitonic solar cells?," *Energy & Environmental Science*, vol. 5, no. 4, p. 6513, 2012.

[58] J. A. Christians, J. S. Manser, and P. V. Kamat, "Best practices in perovskite solar cell efficiency measurements. Avoiding the error of Making Bad Cells Look Good," *Journal of Physical Chemistry Letters*, vol. 6, no. 5, pp. 852–857, 2015.

[59] E. L. Unger, E. T. Hoke, C. D. Bailie, W. H. Nguyen, A. R. Bowring, T. Heumuller, M. G. Christoforo, and M. D. McGehee, "Hysteresis and transient behavior in current-voltage measurements of hybrid-perovskite absorber solar cells," *Energy & Environmental Science*, vol. 7, no. 11, pp. 3690–3698, 2014.

[60] H. Kim and N. Park, "Parameters Affecting I-V Hysteresis of CH3NH3PbI3 Perovskite Solar Cells: Effects of Perovskite Crystal Size and Mesoporous TiO2 Layer," *Journal of Physical Chemistry Letters*, vol. 5, no. 17, pp. 2927–2934, 2014.

[61] J. M. Frost and A. Walsh, "What Is Moving in Hybrid Halide Perovskite Solar Cells?," *Accounts of Chemical Research*, vol. 49, no. 3, pp. 528–535, 2016.

[62] W. Tress, N. Marinova, T. Moehl, S. M. Zakeeruddin, M. K. Nazeeruddin, and M. Grätzel, "Understanding the rate-dependent J-V hysteresis, slow time component, and aging in CH3NH3PbI3 perovskite solar cells: the role of a compensated electric field," *Energy & Environmental Science*, vol. 8, no. 3, pp. 995–1004, 2015.

[63] J. M. Frost, K. T. Butler, and A. Walsh, "Molecular ferroelectric contributions to anomalous hysteresis in hybrid perovskite solar cells," *APL Materials*, vol. 2, no. 8, p. 081506, 2014.

[64] C. Eames, J. M. Frost, P. R. F. Barnes, B. C. O'Regan, A. Walsh, and M. S. Islam, "Ionic transport in hybrid lead iodide perovskite solar cells," *Nature Communications*, vol. 6, p. 7497, 2015.

[65] S. van Reenen, M. Kemerink, and H. J. Snaith, "Modeling Anomalous Hysteresis in Perovskite Solar Cells," *The Journal of Physical Chemistry Letters*, pp. 3808–3814, 2015.

[66] W. Peng, B. Anand, L. Liu, S. Sampat, B. E. Bearden, A. Malko, and Y. J. Chabal, "Influence of growth temperature on bulk and surface defects in hybrid lead halide perovskite films," *Nanoscale*, vol. 8, pp. 1627–1634, 2015.

[67] L. Gouda, R. Gottesman, S. Tirosh, E. Haltzi, J. Hu, A. Ginsburg, D. A. Keller, Y. Bouhadana, and A. Zaban, "Vapor and Healing Treatment for CH3NH3PbI3-xClx Films toward Large-Area Perovskite Solar cells," *Nanoscale*, vol. 8, pp. 6386–6392, 2016.

[68] Y. Cheng, H.-W. Li, J. Qing, Q. Yang, Z. Guan, C. Liu, S. H. Cheung, S.-K. So, C.-S. Lee, and S. W. Tsang, "The Detrimental Effect of Excess Mobile Ions in planar CH3NH3PbI3 Perovskite Solar Cells," *Journal of Materials Chemistry A*, vol. 4, pp. 12748–12755, 2016.

[69] J. T. Jacobsson, J. P. Correa Baena, M. Pazoki, M. Saliba, K. Schenk, M. Graetzel, and A. Hagfeldt, "An exploration of the compositional space for mixed lead halogen perovskites for high efficiency devices," *Energy & Environmental Science*, vol. 9, pp. 1706–1724, 2016.

[70] P. Calado, A. M. Telford, D. Bryant, X. Li, J. Nelson, C. Brian, O. Regan, and P. R. F. Barnes, "Evidence for ion migration in hybrid perovskite solar cells with minimal hysteresis," *Nature Communications*, vol. 7, p. 13831, 2016.

[71] A. Walsh, "Principles of Chemical Bonding and Band Gap Engineering in Hybrid Organic-Inorganic Halide Perovskites," *Journal of Physical Chemistry C*, vol. 119, pp. 5755–5760, 2015.

[72] J. Haruyama, K. Sodeyama, L. Han, and Y. Tateyama, "First-Principles Study of Ion Diffusion in Perovskite Solar Cell Sensitizers," *Journal of the American Chemical Society*, vol. 137, no. 32, pp. 10048–10051, 2015.

[73] Z. Yang, A. Rajagopal, S. B. Jo, C.-C. Chueh, S. T. Williams, C.-C. Huang, J. K. Katahara, H. W. Hillhouse, and A. K. Y. Jen, "Stabilized wide bandgap perovskite solar cells by Tin substitution," *Nano Letters*, vol. 16, no. 12, pp. 7739–7747, 2016.

[74] I. Levine, P. K. Nayak, J. Tse, W. Wang, N. Sakai, S. Van Reenen, T. M. Brenner, S. Mukhopadhyay, H. J. Snaith, G. Hodes, D. Cahen, and S. V. Reenen, "Interface-Dependent Ion Migration/Accumulation Controls Hysteresis in MAPbI 3 Solar Cells," *Journal of Physical Chemistry C*, vol. 120, no. 30, pp. 16399–16411, 2016.

[75] A. Pockett, G. Eperon, N. Sakai, H. Snaith, L. M. Peter, and P. J. Cameron, "Microseconds, milliseconds and seconds: deconvoluting the dynamic behaviour of planar perovskite solar cells," *Phys. Chem. Chem. Phys.*, vol. 19, pp. 5959 – 5970, 2017.

[76] S. Meloni, T. Moehl, W. Tress, M. Franckevičius, M. Saliba, Y. H. Lee, P. Gao, M. K. Nazeeruddin, S. M. Zakeeruddin, U. Rothlisberger, and M. Graetzel, "Ionic polarization-induced current-voltage hysteresis in CH3NH3PbX3 perovskite solar cells," *Nature Communications*, vol. 7, no. May 2015, p. 10334, 2016.

[77] G. Richardson, S. E. J. O'Kane, R. G. Niemann, T. A. Peltola, J. M. Foster, P. J. Cameron, and A. B.Walker, "Can slow-moving ions explain hysteresis in the

current-voltage curves of perovskite solar cells?," *Energy & Environmental Science*, vol. 9, pp. 1476–1485, 2016.

[78] B. Chen, M. Yang, S. Priya, and K. Zhu, "Origin of J-V Hysteresis in Perovskite Solar Cells.," *The Journal of Physical Chemistry Letters*, vol. 7, pp. 905–917, 2016.

Chapter 4

Compositional diversity: Chemical derivations and structural limitations

In the history of science we often find the study of some natural phenomenon has been the starting point in the development of a new branch of knowledge

Sir C.V. Raman
Nobel Lecture, 1930

In recent years, the efficiencies of perovskite cells have experienced a steady growth from 3.8 % in 2009[1] to currently 22.1 % with the potential for further improvement.[2] In fact, perovskites are the fastest advancing PV technology up to date, as can be seen on the NREL chart.[2] It serves as an excellent indicator for the state of current PV technologies and their development. Even besides the view on performance data, one can get a good impression about the technological development when comparing the chemical composition of record cells from the NREL chart. After an initial improvement of the processing conditions and thin-film morphology, further improvements for cell efficiencies of > 15 % were done with chemical derivatives (*e.g.* organic cation or halide replacements) to increase voltage, quantum efficiency and stability of the cells. Up to date, the plain $MAPbI_3$ perovskite failed to achieve efficiencies > 20 %,[3] a milestone that was already passed in 2014 by its mixed-ion derivatives. This shows that the main challenge for a further improvement of PSC lies in the material's chemistry.[4] I_{SC} and FF are already close to their theoretical maximum. Further work should aim for an improvement of the V_{OC} as well as stability.

The specific objective of this chapter is to elaborate on two approaches that use

different cations, namely Cs^+ and Az^+, and their respective mixtures with MA^+ in order to broaden the compositional space of $MAPbI_3$ derivatives.

More specifically, the $Cs_xMA_{1-x}PbI_3$ perovskite was systematically investigated for a broad range of compositions and different fabrication methods. We found that most compositions are not stable and experience spinodal decomposition into pure δ-$CsPbI_3$ and a solid-state solution of $Cs_xMA_{1-x}PbI_3$ with an estimated substitution limit of $x = 0.13$. This result is irrespective of the fabrication route and therefore of thermodynamic origin. Furthermore, we showed that material compositions of $x < 0.13$ increase the stability and V_{OC}.

The introduction of Az^+ as a new organic cation instead of MA^+ leads to a destruction of the three-dimensional perovskite network, despite the Az^+ formally fitting into the predictions given by the Goldschmidt tolerance factor. An evaluation of the different mixtures of $Az_xMA_{1-x}PbI_3$ showed that even small incorporation of a few percent ($0.05 \leq x \leq 0.1$) show indications of phase separation. A spectroscopic analysis and comparison of the AzI precursor with the $AzPbI_3$ orange phase indicates a bridging function of the Az^+, which might serve as an alternative linker between the inorganic $[PbI_6]_n^{4-}$ units, in the orange non-perovskite phase.

4.1 Experimental methods

The substrate cleaning and deposition for the $AzPbI_3$ perovskite study was done in the same way as described in the previous chapter. However, for the $Cs_xMA_{1-x}PbI_3$ we used larger substrates by the size of 7.1×7.1 cm^2 and a modified fabrication procedure that is described in detail in the appendix. Briefly, the $MAPbI_3$ perovskite was deposited by a two-step solution conversion, as described elsewhere in literature.[5] The conversion into $Cs_xMA_{1-x}PbI_3$ by cation exchange was done in analogy to recent reports,[6, 7] by dipping the $MAPbI_3$ into a supersaturated solution of CsI in IPA. A home-made dip coater was used to submerge the substrate into the supersaturated solution; the substrate was then partially lifted out of the solution at different conversion times of 1, 3, 10, 25 and 40 min for different conversion stages. After the conversion finished, the film was annealed at 100 °C for 10 min. Elemental analysis was performed directly on the perovskite layer. For the solar cell fabrication, a Li-TFSI doped layer of spiro was spin-coated at 4000 rpm for 30 s and left in a dry atmosphere overnight for oxygen-doping. For the top electrode, an array of 13×13 separate silver contacts (100 nm thickness) were thermally evaporated. Sonication soldering was used for the bottom contact.

For the one-step deposited perovskite films (reference cells), two equimolar precursor

solutions were prepared from MAI with PbI_2 (each 1 mol/L in DMSO) and CsI with PbI_2 (each 1 mol/L in DMSO), by stirring at 60 °C over 6 h. The mixed cation solutions were prepared by mixing the $CsPbI_3$ and $MAPbI_3$ precursor solutions with the respective ratios $x = 0.05$, 0.1, 0.15, 0.2, 0.25, 0.3, 0.4, 0.5 and 0.75. Finally, the prepared precursor solutions were spin-coated at 2000 rpm for 60 s and then annealed at 100 °C for 10 min.

For the analysis, IV scans were performed on a Keithley 2400 source measurement unit at a scan rate of 50 mV/s and an active area of 0.026 cm^2 of each of the 169 cells.[8] The in-situ absorption measurements were recorded with a CARY UV-Vis-NIR spectrophotometer. The thin-film absorbance mapping was measured on a home-build optical scanner, measuring total transmission, total reflection, and specular reflection.[9] The x-ray diffraction (XRD) was measured on a Bragg Brentano geometry diffractometer (CuKα1 with $\lambda = 1.5406$ Å and CuKα2 with $\lambda = 1.5443$ Å; intensity ratio of 2). Diffractograms were corrected against FTO as an internal standard. Baseline removal was performed with *fityk 0.9.8.*[10] For the time-resolved XRD measurements, the cation exchange setup was placed inside the diffractometer to be able to take measurements at different stages of the conversion process from the same position of the sample. The native $MAPbI_3$ sample was loaded and 1 mL of CsI in IPA solution were placed on top. At a set of conversion times (0, 3, 8, 18, 28 and 38 min) the solution was removed and the sample blow-dried in order to measure a diffractogram, after which fresh solution was applied again. Peak fitting was done manually with CrystalDiffract 6.5 (CrystalMaker Software Ltd., Oxford, UK), using a Pseudo-Voigt peak profile. The geometrical broadening was 0.1 °. The occupancy fitting was done against single crystal data published by Stoumpos *et al.*,[11] comparing the dominant reflection peaks (002) and (110). For the used fitting model the Cs^+ was assumed to incorporate into the entire $MAPbI_3$ grains forming $Cs_xMA_{1-x}PbI_3$. Other options like two separate phases of $MAPbI_3$ and $Cs_xMA_{1-x}PbI_3$ with shared boundaries were tested. In this case the fitting converged to a complete domination of $Cs_xMA_{1-x}PbI_3$ upon $MAPbI_3$. We concluded that the two-phase model is not necessary. Each fitting was done at least three times; the reported values are an average of those three fittings and their standard deviation as an error. SEM images were measured with a FEI Helios 600 high resolution scanning electron microscope. The energy-dispersive X-ray analysis (EDX) was measured with a 80 mm^2 X-max, Oxford Instruments. Raman measurements were performed with a Renishaw inVia Reflex micro-Raman spectrometer equipped with solid state lasers emitting at 514 and 785 nm with a resolution of < 2 cm^{-1}. The laser beam was focused with a x50 magnification lens, giving a laser spot size of about 1 μm in diameter. Rayleigh scattering was rejected with a 110 cm^{-1} cutoff dielectric edge

filter. We measured the AzI sample with the 514 nm laser and the orange $AzPbI_3$ with the 785 nm laser in order to avoid resonant effects in the sample, which could change the spectroscopic response. All measurements were performed in air and with different laser powers to ensure that the laser probe did not induce damage or changes in the sample.

4.2 Results and discussion

4.2.1 $Cs_xMA_{1-x}PbI_3$ perovskite: Substitution limit and stability enhancement

A key aspect of research on HOIP materials for photovoltaics is to bring the cell performance as close to its theoretically achievable maximum efficiency as possible to be able to compete with silicon solar cells. The recent evolution in research went from an initial exploration of fabrication methods to a chemical optimisation of the material, as described in chapter 1. It was shown that the incorporation of a halide mixture improves the stability towards water, but also moves the bandgap into an unfavourable region.[12] The usage of cations, that are slightly larger than MA^+ allows for an extension of the bandgap towards more favourable longer wavelengths.[13] Many potential HOIP cation systems that could be suitable for photovoltaics were explored.[14, 15] However, most candidates did not achieve a favourable bandgap paired with an acceptable stability of the (usually cubic) dark phase of the perovskite.[16] The only promising candidate that performs comparable to the MA^+ system seems to be the FA^+, which forms a yellow δ-phase at RT, but can be stabilised in its dark phase as well.[17, 18, 19] The FA^+ cation radius (253 pm) is at the the upper end of the favourable window described by the Goldschmidt tolerance factor with $t = 0.99$ (see fig. 4-1, explained in chapter 1). Another candidate cation that is within the predicted stable perovskite Goldschmidt range is the inorganic Cs^+; but opposed to the FA^+, which is on the upper end of the range, the Cs^+ ($r_{ion} = 167$ pm) is at the lower range with $t = 0.81$. This causes the material to transform into an orthorhombic yellow phase at temperatures < 310 °C. But, just like the FA^+ system, it can be stabilised in its dark phase at lower temperatures.[16, 20] The aforementioned 'stabilisation' of the photoactive dark phase usually refers to a relative enhancement and stabilisation for several hours or days. The thermodynamically stable form of both materials remains the yellow non-perovskite phase, but solid-state solutions offer a way to stabilise the dark perovskite phase. As pointed out in chapter 1, recent research activities covered the FA-MA and Cs-FA cation mixture, as well as the ternary Cs-FA-MA system that yielded a world-record efficiency (at that time) of 21 %,[21] that was beaten by a new NREL entry after just 3 days.[2]

However, the dual cation mixture Cs-MA seems to be under-represented in literature with only one report from 2014, that shows a significant ($\sim$ 100 mV) increase in photovoltage for all Cs-MA compositions. In that study, the photocurrent increases for small incorporations ($x \leq 0.1$) but a sharp drop of photocurrent for Cs-ratios $x \geq 0.2$. This goes along with new features in the XRD and UV-Vis measurements arising at ratios $x \geq 0.2$, that indicate a discontinuity for Cs-MA mixtures. These effects are not specifically addressed in that report, but seem to be crucial for the photovoltaic performance.

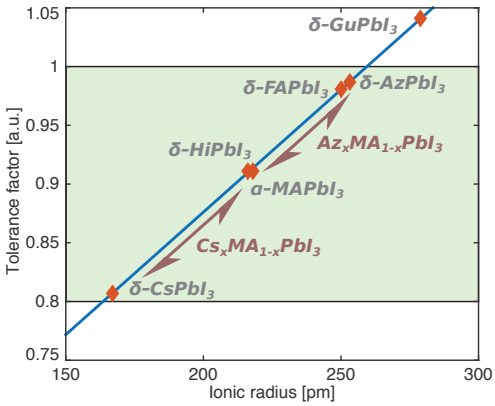

Figure 4-1: Comparison of different cations for HOIPs. A tolerance factor between $\sim$ 0.8 and 1 (marked green) is expected to yield a cubic perovskite structure. However, many systems fall short of that prediction. The octahedral factor for all lead iodide systems listed below is $\mu = 0.54$.

Our study gave the first comprehensive exploration of the Cs-MA system and explains the discontinuity that underlies many of the systems properties. We propose a substitution limit (miscibility gap) to be intrinsic to the Cs-MA system and underlay the performance of the corresponding perovskites. A similar miscibility gap was proposed for mixed halide systems as well, *e.g.* $MAPbI_xBr_{1-x}$.[22] These results indicate that the empirical Goldschmidt tolerance factor only describes one aspect of perovskite formability, which is steric. Other factors that significantly influence the formability of perovskite structures may include *e.g.* chemical bonding effects or polarisability of the cation.[23]

4.2.1.1 Related publications

RGN contributed to this study in several ways. The experiments and measurements connected to the one-step deposited $Cs_xMA_{1-x}PbI_3$ were carried out by RGN. Experiments and measurements related to the two-step cation exchange were carried out by LG and RGN; the $MAPbI_3$ reference cell was fabricated and measured by JH. The writing of the manuscript and creation of figures was done by RGN.

Journal of Materials Chemistry A

PAPER

Cite this: *J. Mater. Chem. A*, 2016, **4**, 17819

Cs^+ incorporation into $CH_3NH_3PbI_3$ perovskite: substitution limit and stability enhancement†

Ralf G. Niemann,*[a] Laxman Gouda,[b] Jiangang Hu,[b] Shay Tirosh,[b] Ronen Gottesman,*[b] Petra J. Cameron[a] and Arie Zaban[b]

In this study we systematically explored the mixed cation perovskite $Cs_x(CH_3NH_3)_{1-x}PbI_3$. We exchanged the A-site cation by dipping $MAPbI_3$ films into a CsI solution, thereby incrementally replacing the MA^+ in a time-resolved dipping process and analysed the resulting thin-films with UV-Vis, XRD, EDAX, SEM and optical depth-analysis in a high-throughput fashion. Additional *in situ* UV-Vis and time-resolved XRD measurements allowed us to look at the kinetics of the formation process. The results showed a discontinuity during the conversion. Firstly, small amounts of Cs^+ are incorporated into the structure. After a few minutes, the Cs content approaches a limit and grains of δ-$CsPbI_3$ occur, indicating a substitution limit. We compared this cation exchange to a one-step crystallisation approach and found the same effect of phase segregation, which shows that the substitution limit is an intrinsic feature rather than a kinetic effect. Optical and structural properties changed continuously for small Cs incorporations. Larger amounts of Cs result in phase segregation. We estimate the substitution limit of $Cs_xMA_{1-x}PbI_3$ to start at a Cs ratio $x = 0.13$, based on combined measurements of EDAX, UV-Vis and XRD. The photovoltaic performance of the mixed cation perovskite shows a large increase in device stability from days to weeks. The initial efficiency of mixed $Cs_xMA_{1-x}PbI_3$ devices decreases slightly, which is compensated by stability after a few days.

Received 12th July 2016
Accepted 26th October 2016

DOI: 10.1039/c6ta05869h

www.rsc.org/MaterialsA

The recent surge in the field of ABX_3-type hybrid inorganic–organic perovskite solar cells has led to a rise of efficiencies from 3.8% in 2009 to currently 22.1%.[1–10] Numerous adjustments were made to the initial structure $MAPbI_3$ (MA = methylammonium $CH_3NH_3^+$) in order to obtain a more stable, non-toxic and efficient solar cell material.[11–15] Current record-cells usually employ a mixture of different cations and halides, as in $FA_xMA_{1-x}PbBr_yI_{3-y}$ (FA = formamidinium $(CH_3)_2NH^+$).[16–18] In fact, the plain $MAPbI_3$ has up to now failed to reach efficiencies exceeding 20%, a benchmark that its derivatives reached in 2014.[10] This shows the importance of a judicial exploration of structural derivatives and a thorough analysis of their properties.

Halide derivatives of the plain $MAPbX_3$ span a broad compositional range (I, Br and Cl) and allow for a continuous adjustment of the bandgap from around 1.56 eV to 3.06 eV, as smaller halides are introduced into the structure.[11,19–21] This adjustment brings about an increasing stability towards high ambient humidity but also moves the bandgap into an unfavourable high energy region, that reduces the light harvesting range of the solar cell.[11] Furthermore the use of mixed halides is put into question because many Br–I compositions segregate upon light exposure,[22] possibly caused by thermodynamic instability of the solid solution.[23]

On the other hand, A-site cation derivatives of ABX_3 perovskites show various enhancements. The $FAPbI_3$ perovskite has a more favourable red-shifted bandgap and is less prone to thermal degradation compared to its MA equivalent.[24] However, its photoactive α-phase is only stable at elevated temperature and it tends to transform into the inactive δ-phase at room temperature. More recently, the inorganic caesium lead halide perovskite $CsPbI_3$ has drawn a lot of attention.[12,25–32] This material shows great potential, considering that a main reason for the decomposition of perovskites is the high volatility of the organic MA^+ cation.[33] Cs salts are less volatile than their organic counterparts, which renders the material stable at high temperatures and can yield perovskite solar cells with an impressive thermal stability.[34,35] However, $CsPbI_3$ also suffers from poor structural stability of its α-phase, and tends to transform into the non-perovskite yellow δ-phase at room temperature.[25] Several attempts have been made to stabilise the α-$CsPbI_3$ with different additives.[18,26,32] The only long-term conservation of the dark phase at room temperature was done by co-depositing colloidal nanocrystals, that were sintered to obtain a supersaturation of Cl^- dopant.[36]

[a]*Department of Chemistry, University of Bath, Bath BA27AY, UK. E-mail: rgn23@bath.ac.uk; Tel: +44 (0)1225 38 6116*

[b]*Center for Nanotechnology & Advanced Materials, Bar-Ilan University, Ramat Gan 52900, Israel. E-mail: ronen.gottesman@biu.ac.il*

† Electronic supplementary information (ESI) available. See DOI: 10.1039/c6ta05869h

Clearly, the options for plain ternary perovskites are limited and even more so within the range of properties that are desirable for photovoltaic applications. Therefore it seems important to further investigate mixed perovskite materials.

A substitution of the halide in the $CsPbX_3$ perovskite can be done for the halide series X = I, Br, Cl, just as in their MA derivatives.[27,28] Besides continuous tunability in colour, $CsPbX_3$ materials are viable candidates for applications in tandem cells and exhibit an improved thermal stability.[29,30] But just as for $MAPbX_3$ compounds, usage of smaller halide derivatives shifts the bandgap into an unfavourable spectral region. Solid solutions of $Cs_xFA_{1-x}PbX_3$ have been shown to maintain a desirable absorption onset and stabilise the photoactive α-phase due to a gain in mixing entropy.[18] This improves their resistance against photo- and moisture-induced degradation.[12,31,32] On the other hand, mixtures of Cs^+ with the MA cation as in $Cs_xMA_{1-x}PbX_3$ seem to be under-explored with only one report by Choi *et al.*, which shows an improved efficiency from 5.5 to 7.7% for a Cs-doping concentration of 10 mol%.[37] Interestingly, the more complicated ternary cation mixture $Cs_x(FA_{0.87}MA_{0.13})_{1-x}PbBr_{0.17}I_{0.87}$ was recently investigated by Saliba *et al.* and cells reached efficiencies of >20% with an impressive improvement of stability under operating conditions.[38] In this study we want to shed more light onto the less explored $Cs_xMA_{1-x}PbX_3$ system by refining the material's compositional space and demonstrating its benefits for photovoltaic applications.[17] Therefore, we analysed large-area substrates (7.1 × 7.1 cm^2) to facilitate the dipping process and reduces edge effects (*e.g.* capillary forces) during the cation conversion process. The large conversion area allows for a statistical treatment of the photovoltaic properties, with 169 cells on one substrate (13 × 13 anodic contacts), with otherwise identical processing conditions, therefore creating a continuous compositional spread. We have produced multiple batches to ensure batch-to-batch reproducibility.

1 Experimental

1.1 Substrate preparation

FTO on glass substrates of the size 7.1 × 7.1 cm^2 were cleaned by rinsing with a soap solution (2 vol% Hellmanex III in water), deionised water, ethanol and then etched in an argon plasma. A 100 nm layer of TiO_2 was coated on top *via* spray pyrolysis. A mesoporous TiO_2 layer was deposited from a 1 : 10 diluted titania paste (18NR-T, Dyesol) in ethanol *via* spin-coating at 5000 rpm for 30 s and sintered at 500 °C for 30 min, resulting in a 250 nm thick layer.

1.2 Cation exchange

A solution of 460 mg mL^{-1} PbI_2 and 23 mg mL^{-1} $PbCl_2$ in DMSO was deposited by spin-coating at 4000 rpm for 60 s and annealed at 100 °C for 60 min. Dipping the lead halide film into a solution of methylammonium iodide (MAI) in 2-propanol (IPA) (32 mg mL^{-1}) for 2 min converted the film into the $MAPbI_3$ perovskite. The films were then washed in an IPA bath and annealed with MAI vapor at 140 °C for 60 min according to our previous report.[39] To sublime the excess MAI, we then annealed the cells for another 60 min on the hotplate. The Cs^+ cation exchange was done in analogy to recent reports.[40,41] A supersaturated solution of CsI in IPA was prepared by heating a saturated mixture with excess salt and sonicating it for 60 min. The solution was heated to 80 °C for 30 min and cooled down to 30 °C just before using it. The substrate was dipped into the supersaturated solution with a home-made dip coater. The substrate was partially lifted out of the CsI solution at conversion times of 1, 3, 10, 25 and 40 min in order to get different conversion stages. The film was annealed at 100 °C for 10 min. Thin-film substrates were directly used for elemental analysis. For solar cell fabrication spiro-MeOTAD (72 mg mL^{-1} in chlorobenzene) was used as a hole transport contact, doped with 34 μL Li-bis-(trifluoromethylsulfonyl)imide (540 mg mL^{-1} in acetonitrile) and 58 μL 4-*tert*-butylpyridine (80 mM) and spin coated at 4000 rpm for 30 s. The cells were kept in a dry atmosphere overnight to oxygen-dope the spiro-MeOTAD layer. Finally, an array of 13 × 13 separate silver back contacts (100 nm thickness) were thermally evaporated, thus forming 169 individual solar cells per substrate; an example of a so called library can be found in the ESI (see Fig. E1†). For the anodic contact the perovskite was scratched off the edges of the substrate and the contact was strengthened with sonication soldering. The solar cell fabrication procedure is identical to our previous report, except for the cation exchange.[39] Full statistics on cell performance can be found in the ESI (see Fig. E2†) including a comparison to another batch in order to address reproducibility of the results. For the stability testing the cells were stored in clean dry air (about 0.6% humidity) in darkness at room temperature.

1.3 One-step deposition

Equimolar precursor solutions of MAI with PbI_2 and CsI with PbI_2 were dissolved in DMSO with a concentration of 1 mol L^{-1}, by stirring at 60 °C over 6 h. The mixed cation solutions were prepared by mixing the $CsPbI_3$ and $MAPbI_3$ precursor solutions with the respective ratios x = 0.05, 0.1, 0.15, 0.2, 0.25, 0.3, 0.4, 0.5 and 0.75. Solutions were spin-coated at 2000 rpm for 60 s and then annealed at 100 °C for 10 min.

1.4 Analysis

An overview of measurements performed thin-films and solar cells is given in the ESI (see Fig. E3†). IV performance was measured with a home-build and automated scanner, using a Keithley 2400 source measurement unit at a scan rate of 50 mV s^{-1} and an active area of 0.026 cm^2 of each of the 169 cells, as defined by the size of the metal back contact and the shadow mask. Measurements were performed in forward and backward direction; details about the measurement system can be found in our recent study.[42] *In situ* absorption measurements were recorded on thin-films in a cuvette with a CARY UV-Vis-NIR spectrophotometer. Thin-film absorbance was measured on a home-build optical scanner, measuring total transmission, total reflection, and specular reflection with millimeter spatial resolution in a high-throughput fashion. A line scan was measured, including 11 points along the dipping axis, therefore

measuring more datasets than conversion stages. Details of the optical scanning system can be found elsewhere.[43] X-ray diffraction (XRD) measurements were performed on a Bragg Brentano geometry X-ray diffractometer (CuKα_1 with $\lambda = 1.5406$ Å and CuKα_2 with $\lambda = 1.5443$ Å; intensity ratio of 2). All diffractograms were corrected against FTO as an internal standard. Baseline removal was performed with fityk 0.9.8.[44] For the time-resolved XRD measurements, the cation exchange setup was placed inside the diffractometer and measurements were taken at different stages of the conversion process. The native $MAPbI_3$ sample was loaded and 1 mL of CsI in IPA solution were placed on top. At a set of conversion times (0, 3, 8, 18, 28 and 38 min) the solution was removed and the sample blow-dried in order to measure a diffractogram, after which fresh solution was applied again. SEM images were measured with a field-emission, FEI, Helios 600 high resolution scanning electron microscope. The energy-dispersive X-ray analysis (EDAX) was done on a 80 mm^2 X-max, Oxford Instruments, scanning the entire substrate in analogy to the optical scanning system mentioned above.

2 Results and discussion

The first step for the $MAPbI_3$ A-site cation exchange with Cs^+ was to find a solvent that dissolved the CsI salt without decomposing the $MAPbI_3$ perovskite. We screened several solvents that do not dissolve the $MAPbI_3$ (so called anti-solvents). Solvents that were tested include toluene, chlorobenzene, acetonitrile, IPA and mixture of IPA/methanol, but none of them solubilised the CsI to levels close to the commonly used concentrations for cation exchanges (*e.g.* around 10 mg mL^{-1} or 63 mmol L^{-1} for MAI).[5] Therefore, the sample was dipped into a supersaturated solution of CsI in IPA (that has a low solubility of CsI) for the conversion. We would like to specify that in this study we used a mixed halide precursor solution of PbI_2 and $PbCl_2$. However, we are using the nomenclature $MAPbI_3$ and $Cs_xMA_{1-x}PbI_3$ to refer to all species made from iodide–chloride mixed halide precursors, for the sake of simplicity. Nevertheless, the Cl does play a critical role during film formation,[45–48] and has recently been shown to stabilise the photoactive α-phase of the Cs-perovskite.[36] The organic cation exchange was done by dipping the $MAPbI_3$ films into a CsI solution in discreet steps at conversion times of 1, 3, 10, 25 and 40 min, resulting in a partially converted thin-film. The thin-film were characterised using UV-Vis, XRD, EDAX, SEM and optical depth-analysis techniques. We applied line scans or mappings of the whole substrate (details in the Experimental section) in a high-throughput fashion. The perovskite film showed a constant uptake of Cs cations with increasing dipping time. This can be seen from the EDAX line scan that increases up to a Cs ratio of $x = 0.5$ for 40 min dipping time (see Fig. 1). However, this steady uptake of Cs^+ into the structure is opposed by a discontinuity of both structural and optical properties.

The UV-Vis analysis showed an initial blue-shift of the absorption edge (see Fig. 1d), caused by an increasing Cs ratio. The same trend was reported for the same material by Choi *et al.*[37] and also for a mixed cation systems with FA.[18,38] Longer conversion times (>3 min) resulted in a visible change of colour

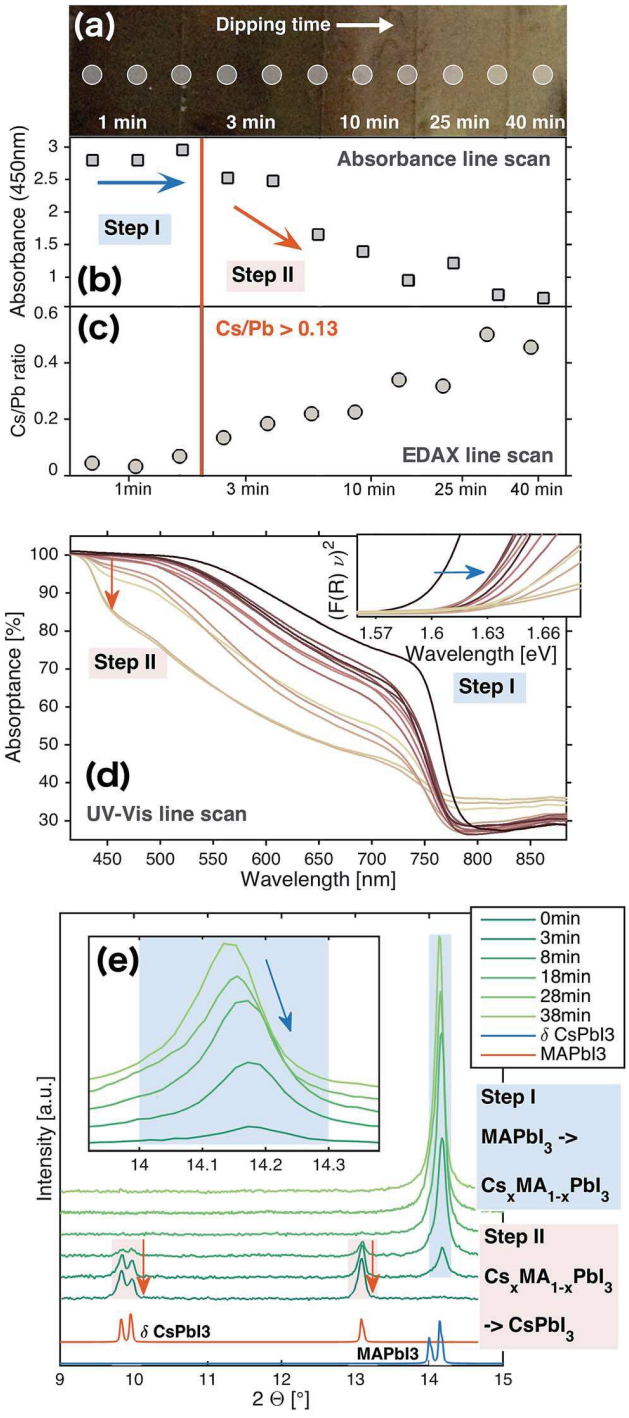

Fig. 1 (a) Photograph of measured region along sample. (b) Absorbance for wavelength 450 nm along the dipping axis stays first constant and then decreases. (c) An EDAX line scan shows a continuous increase of the Cs-ratio and correlates the drop of absorbance to a Cs ratio $x = 0.13$, indicating the formation of δ-$CsPbI_3$. (d) The full absorptance spectra of Cs^+ intercalation into $MAPbI_3$ film for different dipping times (0–40 min). Inset shows Tauc plot and bandgap shift. (e) Time-resolved XRD of Cs^+ incorporation into $MAPbI_3$ shows two steps. First the (110) reflection shifts (inset), indicating incorporation of Cs^+. In the second step pure δ-$CsPbI_3$ builds up at the expense of $Cs_xMA_{1-x}PbI_3$.

from dark brown of the $MAPbI_3$ to a bright yellow that can be attributed to either PbI_2 or the δ-phase of $CsPbI_3$. Accordingly, the UV-Vis spectrum showed a decrease of the $MAPbI_3$ absorption together with an intensifying absorption around 440 nm. This wavelength corresponds to the signature absorption of δ-$CsPbI_3$ and indicates a discontinuity of the material, which is indicative of a substitution limit. The terminology substitution limit in this context can interchangeably used with miscibility gap. It refers to an intrinsic feature of the material, as we will show later on. PbI_2 should show an absorption onset around 510 nm. A more detailed look shows a shifting absorption onset for initial dipping times (≤3 min) of $MAPbI_3$. This indicates incremental changes, namely small inclusions of Cs before the substitution limit. Throughout this work we labelled the incremental conversion of $MAPbI_3$ into the solid solution $Cs_xMA_{1-x}PbI_3$ as step I, while the transformation of $Cs_xMA_{1-x}PbI_3$ into the $CsPbI_3$ caused by the substitution limit is labelled as step II. In order to quantify the beginning of the substitution limit (transition from step I to step II), we plotted the absorbance at 450 nm, as a region that is strongly absorbed by the $MAPbI_3$ and below the bandgap of δ-$CsPbI_3$. The absorbance shows a drop after about 3 min conversion, which correlates to a Cs ratio $x = 0.13$, as measured *via* EDAX.

Time-resolved analysis of the native $MAPbI_3$ conversion was measured with XRD, as opposed to the spatially resolved analysis of the dipped films in the last section. Two distinctive regions can be seen in the measurement, which correspond to the Cs- and MA-perovskites. An excerpt that shows characteristic peaks of both perovskite domains is shown in Fig. 1e, while the full diffractograms before and after conversion are shown in the ESI (Fig. E4†). During the course of the conversion we observed a decreasing peak intensity of the MA-containing perovskite alongside an increasing intensity of the δ-phase $CsPbI_3$, indicating a substitution limit (step II) in the same fashion as discussed for the UV-Vis spectra above. Another important feature in the X-ray diffractogram is a shift of the MA-perovskite signal towards larger angles, indicating a decrease of the unit cell size. This is an effect of adding small amounts of Cs^+ into the perovskite structure, as mentioned before for the step I formation of $Cs_xMA_{1-x}PbI_3$. The same trend is observed for Cs^+ incorporations into $FAPbI_3$ perovskites.[49] It shows that the material, despite having a substitution limit, allows for small incorporations of Cs cations. The (110) reflection shifts from 14.137° (at 0 min) to 14.180° (at 28 min), which corresponds to *d*-spacing values of 6.2598 Å and 6.2409 Å, respectively (assuming $\lambda = 1.5406$ Å). This corresponds to a decrease in *d*-spacing of 1.89 pm. The reduction in *d*-spacing is following the reduction in unit cell volume, caused by the fact that Cs^+ is smaller than MA^+. Direction and magnitude of the structural change lines up with our expectations. Tabulated values of ionic radii and changes of structural parameters can be found in the ESI (Table E3†). A more detailed quantitative discussion of this finding will be given later in this text. A blank measurement with IPA and without CsI salt has also been run, which showed a constant peak position. An out of plane movement of the focal plane caused by a layer-by-layer conversion can be excluded because the resulting shift would be beyond the detection limit.

The only comparable study on the system $Cs_xMA_{1-x}PbI_3$ was done by Choi *et al.* in 2014, for the full compositional range of $Cs_xMA_{1-x}PbI_3$ of one-step deposited perovskites.[37] In contrast to this work, that study does not consider any phase segregation or substitution limit. Therefore, we conducted analogous measurements on one-step deposited films of the mixed perovskite $Cs_xMA_{1-x}PbI_3$ in order to address this discrepancy and to ascertain that the substitution limit is an intrinsic thermodynamic feature, rather than a kinetic product. The one-step deposited films all crystallised in their dark phase first, then the pure $CsPbI_3$ changed its colour to yellow after a few seconds on the hotplate, indicating the transition of the α-phase into the δ-phase.[26] Perovskites with Cs-contents of 75% and 50% endured several hours and days, respectively, before changing their colour to yellow. This indicates that MA^+ cations can stabilise the α-phase for a limited time, as has been reported for several other additives before.[18,26,36] UV-Vis analysis of the $CsPbI_3$ shows the distinct absorption onset around 450 nm,

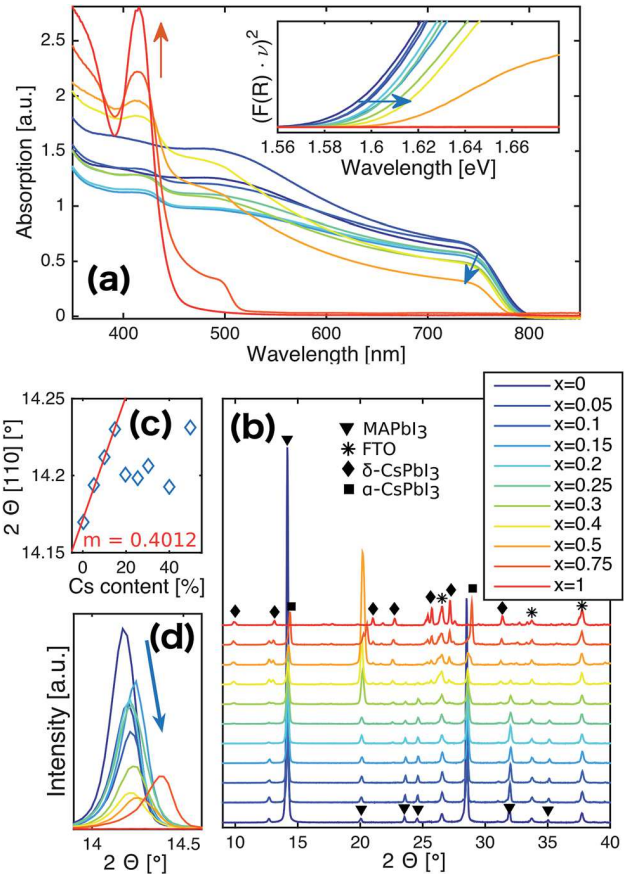

Fig. 2 (a) One-step deposited mixtures $Cs_xMA_{1-x}PbI_3$ show build up of the absorption onset of δ-$CsPbI_3$ for high Cs ratios *x* as well as a shifting bandgap for small Cs incorporations, that can also be seen in the Tauc plot (inset). (b) X-ray diffractogram shows pure $MAPbI_3$ and $CsPbI_3$ at the top and bottom with their respective solid solutions in between. (c) The fitted (110) reflection shifts continuously for Cs ratios $0 \geq x \geq 0.15$. (d) A close up of the $MAPbI_3$ (110) reflection. The Intensity of $x = 0$ is reduced for the sake of clarity.

which remains conspicuous for decreasing Cs ratios down to $x \geq 0.25$. The absorption onset does not show any apparent change in wavelength (see Fig. 2a). On the other hand, the bandgap of MA-rich $Cs_xMA_{1-x}PbI_3$ compounds blue-shifts continuously, from around 780 nm (1.59 eV) for $MAPbI_3$ to about 770 nm (1.61 eV), as shown in the Tauc plot (see Fig. 2a, inset). Materials with a high Cs content also show an absorption onset around 510 nm, presumably relating to PbI_2 as a decomposition product during phase segregation. Analysis with XRD illustrates how the (110) reflection of the $MAPbI_3$ phase decreases in intensity and shifts towards larger angles as a result of Cs-inclusion. We fitted the (110) reflection, assuming a pseudo-cubic structure. The fitted peak position is linear for Cs-ratios $x \geq 0.15$ with a slope of 0.4012° (see Fig. 2b and c), which is used later to determine the Cs ratio after various dipping times. We would like to point out that this is beyond the estimated miscibility limit reported in this study (see Table 1) and can be attributed to a kinetic effect, similar to the spinodal segregation reported for mixed halide perovskites.[23]

A peculiarity is the diffraction peak at 20°, which soars for Cs ratios $x = 0.4$–0.5, presumably relating to the (110) reflection of the cubic α-$CsPbI_3$ structure. This suggests a stabilisation of the α-phase, which has been demonstrated before for different additives.[18,26,36] However, all significant peaks of that phase, coincide with the tetragonal $MAPbI_3$ diffraction pattern, which facilitates a definite conclusion. For Cs ratios $x \geq 0.25$ we can see characteristic peaks of the δ-$CsPbI_3$ alongside the mixed phase $Cs_xMA_{1-x}PbI_3$. Interestingly the peak positions of the δ-$CsPbI_3$ from Cs-rich mixed cation precursors ($x \geq 0.25$) are slightly shifted with respect to its pure phase, which could indicate a small solubility of MA^+ in the δ-$CsPbI_3$. In conclusion, both synthesis routes, the one-step crystallisation and two-step conversion show continuous structural and optical changes for small inclusion of Cs and a segregation of δ-$CsPbI_3$ alongside $Cs_xMA_{1-x}PbI_3$ for larger Cs ratios. This indicates that the substitution limit is an intrinsic feature rather than a kinetic effect during the cation exchange. A similar effect of spinodal decomposition has recently been shown for halide mixtures $MAPbBr_xI_{1-x}$, caused by a substitution limit.[23]

In order to investigate the depth-profile of the conversion process we exfoliated the thin-films with adhesive tape over 15 cycles. Profilometer measurements showed that the exfoliation removed a layer with a total thickness of 60–70 nm after 15 cycles, indicating a partial removal of the capping layer. We measured the optical absorption after each exfoliation for 15 cycles. The full absorption spectra show a decrease in absorption with each exfoliation cycle and can be found in the ESI.†

Table 1 Comparison of three different methods to estimate the start of the substitution limit for $Cs_xMA_{1-x}PbI_3$

Measurement	Analysis method	Substitution limit
UV-Vis	Tauc plot	$x = 0.14 \pm 0.08$
EDAX	Comparison to absorption	$x = 0.13 \pm 0.04$
XRD	External standard	$x = 0.12 \pm 0.03$
	Estimated limit (average)	$x = 0.13 \pm 0.03$

Most interesting are small changes around the bandgap region, which are sensitive to changes in the material, such as the bandgap shift with increasing Cs ratio shown earlier (see Fig. 1d). Therefore, we subtracted the spectrum of the initial spectrum from the exfoliated sample for different time regimes of the dipping (Abs_{exfol}–$Abs_{initial}$). We can see two types of features in the subtracted spectra: (1) plateau-like regions which are caused by changes in absorbance because we take away material and (2) peaks that are caused by a shifted absorption onset between native and exfoliated thin-film. We corrected the baseline in order to have a direct comparison of the latter. The resulting spectra are shown in Fig. 3. Full absorption spectra and differential spectra with baseline can be found in ESI Fig. E5.† Intuitively, we would expect a faster conversion on the interface between thin-film and solution, because of the direct exposure to the solution and a potentially faster mass transport of Cs^+. This would red-shift the absorption onset of $MAPbI_3$ in the converted interface layer and therefore result in a positive peak of the differential spectrum after exfoliation. However, the experiment reveals the opposite effect. A negative peak in the bandgap regime of $MAPbI_3$ (760 nm) demonstrates a Cs-enrichment in the underlying layer. This effect can be seen only for short dipping times < 10 min, which indicates a faster cation exchange in the mesoscopic region. We assume that the increased surface of the underlying mesoscopic layer is responsible for a faster Cs^+ uptake. This negative peak also shows a blue-shift which affirms the continuous formation of a solid solution $Cs_xMA_{1-x}PbI_3$ for small x. Spectra of films formed at longer dipping times ≥ 10 min do not exhibit this peak any more, which indicates Cs-saturation of the $Cs_xMA_{1-x}PbI_3$ phase. Instead, two peaks appear at around 510 nm and 440 nm, that are allocated to PbI_2 and δ-$CsPbI_3$, respectively. *Vice versa*, their positive signature

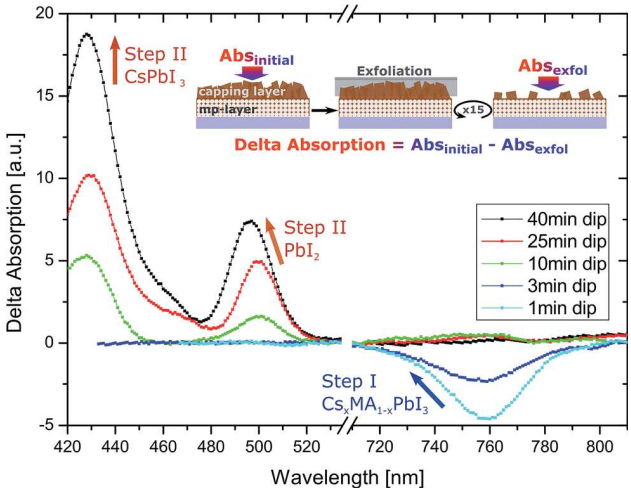

Fig. 3 Optical analysis *via* exfoliation of the capping layer shows a preferential formation of Cs^+ rich domains in lower sections. The spectra of the difference in absorbance ($Abs_{initial}$–Abs_{exfol}, baseline removed) shows peaks in the range of the bandgaps of $Cs_xMA_{1-x}PbI_3$, PbI_2 and $CsPbI_3$. Negative magnitude of the $Cs_xMA_{1-x}PbI_3$ peak indicates a higher MA content in the capping layer for short dipping times (t < 10 min). Positive peaks for PbI_2 and $CsPbI_3$ indicate and enrichment in the lower mesoporous layer ($t \geq 10$ min).

indicates an enrichment of those species in the mesoscopic layer that is left after exfoliation. The position of the $CsPbI_3$ peak does not shift, which is an indication for the formation of a pure phase without MA inclusions. On the other hand, the PbI_2 phase does show a blue-shift for increasing dipping times, which can be explained by intercalation dynamics, that occur during the conversion from the 3D perovskite to a 2D PbI_2 structure.[50,51] We further would like to add that the presence of PbI_2 in the optical measurements stems from the sensitivity of the measurement, opposed to our XRD measurements which show only the perovskite structures $Cs_xMA_{1-x}PbI_3$ and $CsPbI_3$. SEM images before and after exfoliation can be found in the ESI (Fig. E6†).

To quantify the stable region of the mixed phase $Cs_xMA_{1-x}PbI_3$ we associated the previously described measurements to estimate a limit for the substitution limit in three different ways. Using a Tauc plot, we extracted an absorption onset of 1.618 eV for $Cs_xMA_{1-x}PbI_3$ after the cation exchange. We related this value to the pure phases of $MAPbI_3$ and α-$CsPbI_3$ in order to conclude the Cs ratio, assuming a linear bandgap shift for small dopant concentrations. For $MAPbI_3$ we measured a bandgap of 1.598 eV (see Fig. 1d) and for α-$CsPbI_3$ we used a value of 1.73 eV (taken from Stoumpos *et al.*).[25] This correlates to a Cs ratio of $x_{\mathrm{Tauc}} = 0.14 \pm 0.08$. Details about the estimation and an error calculation can be found in the ESI.† The previously discussed thin-film analysis gives an estimate composition of $x_{\mathrm{EDAX}} = 0.13 \pm 0.04$ as the elemental composition before the absorbance of $Cs_xMA_{1-x}PbI_3$ starts to drop as a result of the substitution limit step II conversion (see Fig. 1b). Finally, we estimated the composition from the shifting XRD signal of the time-resolved analysis of the conversion, by comparing the obtained shift with one-step deposited films with a known Cs ratio. As mentioned earlier, we assumed a pseudo-cubic peak profile and fitted the peak shift against the Cs ratio of the thin-film. The resulting linear slope (see Fig. 2c) was related to the obtained shift during cation exchange (0.048° after 28 min) and gave an estimated Cs ratio of $x = 12 \pm 0.03$. Averaging those three methods, we assess the stable regime of $Cs_xMA_{1-x}PbI_3$ to be between $0 \leq x \leq 0.13$, as the average of our three methods, and a broad substitution limit for $x > 0.13$. It is worthwhile mentioning that there are contradicting reports about the mixing Cs^+ with $FAPbI_3$ perovskite, with some reports stating continuous miscibility,[18] while others report on segregation for Cs ratios $x \geq 10\%$.[12] The formation dynamics of perovskites can be, at least empirically, very well described by the thermochemical radii of the respective elements. The mathematical description of this correlation is given with the Goldschmidt tolerance factor t and octahedral factor μ.[52,53] One might argue that the size difference between the Cs cation and MA is too large with 1.81 Å and 2.17 Å as cation radii, respectively.[54] However, the FA cation is even larger with 2.53 Å and has been reported to improve stability and reproducibility as a ternary cation perovskite $Cs_x(FA_{0.17}MA_{0.83})_{1-x}PbX_3$.[38] This points towards bonding effects that go beyond the radii of the respective ABX_3 ions and shows the temperamental nature of this class of perovskite. Possible contributions are manifold and could include factors such as mixing entropy, cation shape and polarisation as well as chemical effects like hydrogen bonding, ion movements, spin–orbit coupling or orbital hybridisation.[55–58]

A Cs-MA cation exchange for perovskite solar cells is useful to overcome the intrinsic instability of the $MAPbI_3$ perovskite,[59] which remains a major obstacle towards its commercialisation. We measured decomposition rates of the $Cs_xMA_{1-x}PbI_3$ solid solution in comparison to the plain $MAPbI_3$ perovskite. Therefore, the respective thin-films were dipped into an IPA solution with different water concentrations between 0 and 5 vol% and *in situ* UV-Vis transmission was measured. Upon decomposition, the transmission spectra show a drop in the absorbance due to the conversion of the $MAPbI_3$ and an increasing baseline caused by the roughness of the formed PbI_2, resulting in an increase in light scattering. Two explanatory spectra are shown in Fig. 4a and b, a listing of all spectra is given in ESI Fig. E7.† We labelled a film as decomposed when the transmission at 450 nm drops below 80% of its initial value. Fig. 4c summarises the time before the films started to degrade. The plain $MAPbI_3$ degraded relatively quickly, within 30 min in anhydrous IPA. As we increased the water concentration in IPA the films decomposed quicker, within 5 min in a solution of 5 vol% water in IPA. The $Cs_xMA_{1-x}PbI_3$ solid solution showed a significant increase in stability. For water concentrations ≥ 2 vol% the films remained intact for about twice as long. An even better performance was

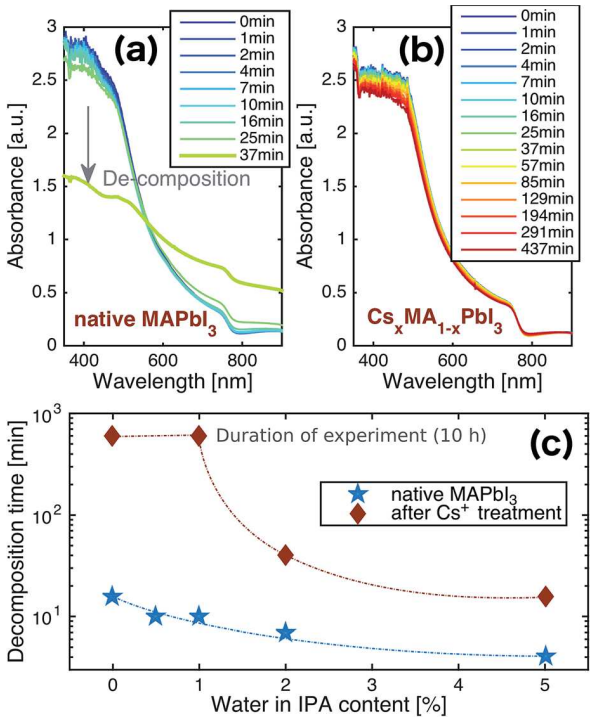

Fig. 4 *In situ* UV-Vis of thin-film degradation. $MAPbI_3$ and $Cs_xMA_{1-x}PbI_3$ in IPA solvent with different concentrations of water (0–5 vol%). $MAPbI_3$ decomposes in less than 30 min for any water concentration, while the $Cs_xMA_{1-x}PbI_3$ was stable in water concentrations $c_{H_2O} \leq 10$ wt% throughout the whole measurement (10 hours). (a and b) Shows an example of a decomposition of $MAPbI_3$ in anhydrous IPA, while $Cs_xMA_{1-x}PbI_3$ remains stable throughout the whole measurement (10 h). (c) Shows a summary of all measured compositions.

found for water concentrations ≤ 1 vol%, where the films remained stable over the duration of the measurement (10 h) and also did not show any visible decomposition after being kept another 7 days in the same solution. We would like to point out that for the $Cs_xMA_{1-x}PbI_3$ perovskite the broad spectral absorption remains intact, as opposed to changes in the halide composition that come along with a blue-shifting bandgap.[11]

Finally we wanted to investigate the photovoltaic properties of this compound. Our $MAPbI_3$ reference cell showed an average power conversion efficiency PCE of 12.1 ± 1.4% with the best cell achieving 14.2%. The cells had an average photovoltage V_{OC} = 1.01 V, photocurrent I_{SC} = 19.2 mA and fill factor FF = 62.0%.

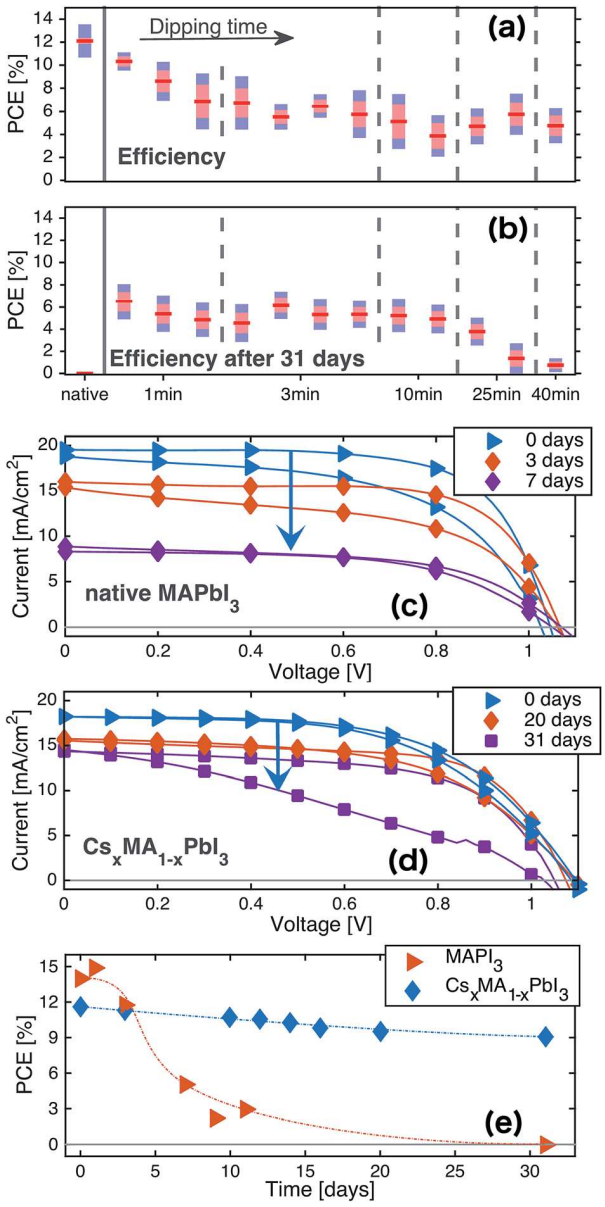

Fig. 5 (a and b) A summary is given of power conversion efficiencies PCE for different dipping times, on day 1 and after 31 days. (c and d) The respective IV curves for a native $MAPbI_3$ reference sample and $Cs_xMA_{1-x}PbI_3$ after 1 min cation exchange, over a months. (e) Shows the PCE for the best performing device over a period of 31 days.

The Cs-containing samples were produced with a cation exchange for 1 min, that resulted in a Cs concentration within the stable region $0 < x < 0.13$. A precise estimation of the composition can not be done due to the propagation error of $\Delta x = 0.04$ (see Table 1 and ESI† for calculations). The cells showed a slight increase in V_{OC} for all dipping times (see ESI Fig. E2†), which is in agreement with a small blue-shift of the bandgap. The I_{SC} showed a linear drop with dipping time, which is probably caused by the decrease in absorption as the proportion of the yellow δ-$CsPbI_3$ increased (see Fig. 1a). The PCE also drops with increasing dipping time but the decrease in photocurrent is partially compensated by a higher FF for long dipping times. An overview of all PCE values is given in Fig. 5. A full listing of photovoltaic parameters (V_{OC}, I_{SC}, FF and PCE) including distribution histograms is given in the ESI (Fig. E2†). We also evaluated the cell stability over a period of 31 days; during this time the cells were stored in a dark and dry environment (2% humidity) and taken out only for IV testing. Here we saw a trade-off when increasing the Cs-content: a decrease of photocurrent I_{SC} is countered by a markedly improved stability. Dipping the sample for 1 min decreases the average efficiency from 12.1 to 10.3% which decays to 6.48% after 31 days. Dipping for 3 min gives an initial efficiency of 6.73% that changes to 4.56% after 31 days. In comparison, the native $MAPbI_3$ sample decreased in PCE from 12.1% to 2.81% within only a week and went dead after 31 days. A comparison of the decomposition for the best performing native sample and the best performing Cs^+ dipped sample can be found in Fig. 5c–e. This shows that even short Cs conversion times have an appreciable impact on stability. Even though the initial PCE is lower for Cs^+ treated samples, this is been compensated by an increased stability after about 3 days, when the efficiency of the native sample drops below the mixed cation perovskite $Cs_xMA_{1-x}PbI_3$.

3 Conclusions

In summary, our study has investigated the incorporation of Cs^+ into the $MAPbI_3$ perovskite structure. Dipping the thin-film into a solution of CsI resulted in a continuous uptake of Cs^+ over time. We found that an increasing Cs ratio results in a conversion into the δ-$CsPbI_3$, leaving a substitution limit. We compared this cation exchange to a one-step crystallisation procedure for different stoichiometric mixtures $Cs_xMA_{1-x}PbI_3$ and found an analogous and continuous change of optical and structural properties for small Cs incorporations and a phase segregation for larger Cs contents. We estimate the substitution limit of $Cs_xMA_{1-x}PbI_3$ to start at a Cs ratio $x = 0.13$, based on combined measurements of EDAX, UV-Vis and XRD. We believe that these results have important implications for the fabrication of mixed cation perovskites, that are commonly employed in record cells. Furthermore, we looked at stability improvement of the $Cs_xMA_{1-x}PbI_3$ material itself and in solar cells. Thin-films exposed to a mixture of water/IPA increased their stability from minutes to days. Solar cells showed an improvement in cell lifetime from days to a month, even for small incorporations of Cs^+. This study refines the compositional

space and gives further manifestation to the temperamental nature of this class of perovskite with implications reaching from material design to solar cell fabrication.

Acknowledgements

For enlightening conversations we thank Oliver Weber and Peter Kubiak. The research is funded from the European Union Seventh Framework Programme [FP7/2007–2013] (DESTINY project) under grant agreement 316494.

References

1 A. Kojima, K. Teshima, Y. Shirai and T. Miyasaka, *J. Am. Chem. Soc.*, 2009, **131**, 6050–6051.
2 J.-H. Im, C.-R. Lee, J.-W. Lee, S.-W. Park and N.-G. Park, *Nanoscale*, 2011, **3**, 4088–4093.
3 M. M. Lee, J. Teuscher, T. Miyasaka, T. N. Murakami and H. J. Snaith, *Science*, 2012, **338**, 643–647.
4 H.-S. Kim, C.-R. Lee, J.-H. Im, K.-B. Lee, T. Moehl, A. Marchioro, S.-J. Moon, R. Humphry-Baker, J.-H. Yum, J. E. Moser, M. Grätzel and N.-G. Park, *Sci. Rep.*, 2012, **2**, 591.
5 J. Burschka, N. Pellet, S.-J. Moon, R. Humphry-Baker, P. Gao, M. K. Nazeeruddin and M. Grätzel, *Nature*, 2013, **499**, 316–320.
6 M. Liu, M. B. Johnston and H. J. Snaith, *Nature*, 2013, **501**, 395–398.
7 J. M. Ball, M. M. Lee, A. Hey and H. J. Snaith, *Energy Environ. Sci.*, 2013, **6**, 1739–1743.
8 G. Xing, N. Mathews, S. Sun, S. S. Lim, Y. M. Lam, M. Grätzel, S. Mhaisalkar and T. C. Sum, *Science*, 2013, **342**, 344–347.
9 S. D. Stranks, G. E. Eperon, G. Grancini, C. Menelaou, M. J. P. Alcocer, T. Leijtens, L. M. Herz, A. Petrozza and H. J. Snaith, *Science*, 2013, **342**, 341–344.
10 NREL, Research Cell Efficiency Records, http://www.nrel.gov/ncpv/, online, accessed, 17-June-2016, 2016.
11 J. H. Noh, S. H. Im, J. H. Heo, T. N. Mandal and S. I. Seok, *Nano Lett.*, 2013, **13**, 1764–1769.
12 J.-W. Lee, D.-H. Kim, H.-S. Kim, S.-W. Seo, S. M. Cho and N.-G. Park, *Adv. Energy Mater.*, 2015, **5**, 1614–6840.
13 E. T. McClure, M. R. Ball, W. Windl and P. M. Woodward, *Chem. Mater.*, 2016, **28**, 1348–1354.
14 A. H. Slavney, T. Hu, A. M. Lindenberg and H. I. Karunadasa, *J. Am. Chem. Soc.*, 2016, **138**, 2138–2141.
15 G. Volonakis, M. R. Filip, A. A. Haghighirad, N. Sakai, B. Wenger, H. J. Snaith and F. Giustino, *J. Phys. Chem. Lett.*, 2016, 1254–1259.
16 N. J. Jeon, J. H. Noh, W. S. Yang, Y. C. Kim, S. Ryu, J. Seo and S. I. Seok, *Nature*, 2015, **517**, 476–480.
17 J. T. Jacobsson, J. P. Correa Baena, M. Pazoki, M. Saliba, K. Schenk, M. Graetzel and A. Hagfeldt, *Energy Environ. Sci.*, 2016, **9**, 1706–1724.
18 C. Yi, J. Luo, S. Meloni, A. Boziki, N. Ashari-Astani, C. Grätzel, S. M. Zakeeruddin, U. Röthlisberger and M. Grätzel, *Energy Environ. Sci.*, 2015, **9**, 656–662.
19 Y. Zhao and K. Zhu, *J. Am. Chem. Soc.*, 2014, **136**, 12241–12244.
20 B. Suarez, V. Gonzalez-Pedro, T. S. Ripolles, R. S. Sanchez, L. Otero and I. Mora-Sero, *J. Phys. Chem. Lett.*, 2014, **5**, 1628–1635.
21 R. G. Niemann, A. G. Kontos, D. Palles, E. I. Kamitsos, A. Kaltzoglou, F. Brivio, P. Falaras and P. J. Cameron, *J. Phys. Chem. C*, 2016, **120**, 2509–2519.
22 E. T. Hoke, D. J. Slotcavage, E. R. Dohner, A. R. Bowring, H. I. Karunadasa and M. D. McGehee, *Chem. Sci.*, 2015, **6**, 613–617.
23 F. Brivio, C. Caetano and A. Walsh, *J. Phys. Chem. Lett.*, 2016, **7**, 1083–1087.
24 G. E. Eperon, S. D. Stranks, C. Menelaou, M. B. Johnston, L. M. Herz and H. J. Snaith, *Energy Environ. Sci.*, 2014, **7**, 982–988.
25 C. C. Stoumpos, C. D. Malliakas and M. G. Kanatzidis, *Inorg. Chem.*, 2013, **52**, 9019–9038.
26 G. E. Eperon, G. M. Paterno, R. J. Sutton, A. Zampetti, A. A. Haghighirad, F. Cacialli and H. J. Snaith, *J. Mater. Chem. A*, 2014, **3**, 19688–19695.
27 L. Protesescu, S. Yakunin, M. I. Bodnarchuk, F. Krieg, R. Caputo, C. H. Hendon, R. X. Yang, A. Walsh and M. V. Kovalenko, *Nano Lett.*, 2015, **15**, 3692–3696.
28 Q. A. Akkerman, V. D'Innocenzo, S. Accornero, A. Scarpellini, A. Petrozza, M. Prato and L. Manna, *J. Am. Chem. Soc.*, 2015, **137**, 10276–10281.
29 R. E. Beal, D. J. Slotcavage, T. Leijtens, A. R. Bowring, R. A. Belisle, W. H. Nguyen, G. Burkhard, E. T. Hoke and M. D. McGehee, *J. Phys. Chem. Lett.*, 2016, 746–751.
30 R. J. Sutton, G. E. Eperon, L. Miranda, E. S. Parrott, B. A. Kamino, J. B. Patel, M. T. Hörantner, M. B. Johnston, A. A. Haghighirad, D. T. Moore and H. J. Snaith, *Adv. Energy Mater.*, 2016, **6**, 1502458.
31 X. Xia, W. Wu, H. Li, B. Zheng, Y. Xue, J. Xu, D. Zhang, C. Gao and X. Liu, *RSC Adv.*, 2016, **6**, 14792–14798.
32 Z. Li, M. Yang, J.-S. Park, S.-H. Wei, J. Berry and K. Zhu, *Chem. Mater.*, 2016, **28**, 284–292.
33 B. Conings, J. Drijkoningen, N. Gauquelin, A. Babayigit, J. D'Haen, L. D'Olieslaeger, A. Ethirajan, J. Verbeeck, J. Manca, E. Mosconi, F. D. Angelis and H. Boyen, *Adv. Energy Mater.*, 2015, 1500477.
34 D. M. Trots and S. V. Myagkota, *J. Phys. Chem. Solids*, 2008, **69**, 2520–2526.
35 M. Kulbak, D. Cahen and G. Hodes, *J. Phys. Chem. Lett.*, 2015, **6**, 2452–2456.
36 S. Dastidar, D. A. Egger, L. Z. Tan, S. B. Cromer, A. D. Dillon, S. Liu, L. Kronik, A. M. Rappe and A. T. Fafarman, *Nano Lett.*, 2016, **16**, 3563–3570.
37 H. Choi, J. Jeong, H. B. Kim, S. Kim, B. Walker, G. H. Kim and J. Y. Kim, *Nano Energy*, 2014, **7**, 80–85.
38 M. Saliba, T. Matsui, J.-Y. Seo, K. Domanski, J.-P. Correa-Baena, N. Mohammad K, S. M. Zakeeruddin, W. Tress, A. Abate, A. Hagfeldt and M. Grätzel, *Energy Environ. Sci.*, 2016, **9**, 1989–1997.
39 L. Gouda, R. Gottesman, S. Tirosh, E. Haltzi, J. Hu, A. Ginsburg, D. A. Keller, Y. Bouhadana and A. Zaban, *Nanoscale*, 2016, **8**, 6386–6392.

40 G. Nedelcu, L. Protesescu, S. Yakunin, M. I. Bodnarchuk, M. J. Grotevent and M. V. Kovalenko, *Nano Lett.*, 2015, **15**, 5635–5640.
41 G. E. Eperon, C. E. Beck and H. J. Snaith, *Mater. Horiz.*, 2016, **3**, 63–71.
42 S. Ruhle, H. N. Barad, Y. Bouhadana, D. a. Keller, A. Ginsburg, K. Shimanovich, K. Majhi, R. Lovrincic, a. Y. Anderson and A. Zaban, *Phys. Chem. Chem. Phys.*, 2014, **16**, 7066–7073.
43 A. Y. Anderson, Y. Bouhadana, H. N. Barad, B. Kupfer, E. Rosh-Hodesh, H. Aviv, Y. R. Tischler, S. Ruhle and A. Zaban, *ACS Comb. Sci.*, 2014, **16**, 53–65.
44 M. Wojdyr, *J. Appl. Crystallogr.*, 2010, **43**, 1126–1128.
45 S. Colella, E. Mosconi, G. Pellegrino, A. Alberti, V. L. P. Guerra, A. Listorti, A. Rizzo, G. G. Condorelli, F. D. Angelis and G. Gigli, *J. Phys. Chem. Lett.*, 2014, 3532–3538.
46 M. I. Dar, N. Arora, P. Gao, S. Ahmad, M. Grätzel and M. K. Nazeeruddin, *Nano Lett.*, 2014, **14**, 6991–6996.
47 V. L. Pool, A. Gold-Parker, M. D. McGehee and M. F. Toney, *Chem. Mater.*, 2015, **27**, 7240–7243.
48 C. Cao, C. Zhang, J. Yang, J. Sun, S. Pang, H. Wu, R. Wu, Y. Gao and C. Liu, *Chem. Mater.*, 2016, **28**, 2742–2749.
49 D. P. McMeekin, G. Sadoughi, W. Rehman, G. E. Eperon, M. Saliba, M. T. Hörantner, A. Haghighirad, N. Sakai, L. Korte, B. Rech, M. B. Johnston, L. M. Herz and H. J. Snaith, *Science*, 2016, **351**, 151–155.
50 N. Preda, L. Mihut, M. Baibarac, I. Baltog and S. Lefrant, *J. Phys.: Condens. Matter*, 2006, **18**, 8899–8912.
51 I. Baltog, M. Baibarac and S. Lefrant, *J. Phys.: Condens. Matter*, 2009, **21**, 025507.
52 H. D. B. Jenkins and K. P. Thakur, *J. Chem. Educ.*, 1979, **56**, 576–577.
53 H. K. Roobottom, H. D. B. Jenkins, J. Passmore and L. Glasser, *J. Chem. Educ.*, 1999, **76**, 1570–1573.
54 G. Kieslich, S. Sun and T. Cheetham, *Chem. Sci.*, 2015, **6**, 3430–3433.
55 G. Richardson, S. E. J. O'Kane, R. G. Niemann, T. A. Peltola, J. M. Foster, P. J. Cameron and A. B. Walker, *Energy Environ. Sci.*, 2016, **9**, 1476–1485.
56 F. Wang, J. Ma, F. Xie, L. Li, J. Chen, J. Fan and N. Zhao, *Adv. Funct. Mater.*, 2016, **26**, 3417–3423.
57 A. Amat, E. Mosconi, E. Ronca, C. Quarti, P. Umari, M. K. Nazeeruddin, M. Grätzel and F. De Angelis, *Nano Lett.*, 2014, **14**, 3608–3616.
58 A. Walsh, *J. Phys. Chem. C*, 2015, **119**, 5755–5760.
59 Y.-Y. Zhang, S. Chen, P. Xu, H. Xiang, X.-G. Gong, A. Walsh and S.-H. Wei, arXiv preprint, arXiv:1506.01301, 2015.

Supporting Information

Cs^+ incorporation into $CH_3NH_3PbI_3$ perovskite: Broad miscibility gap and stability enhancement

Ralf G. Niemann[a], Laxman Gouda[b], Jiangang Hu[b], Shay Tirosh[b], Ronen Gottesman[b], P.J. Cameron[a] and Arie Zaban[b]

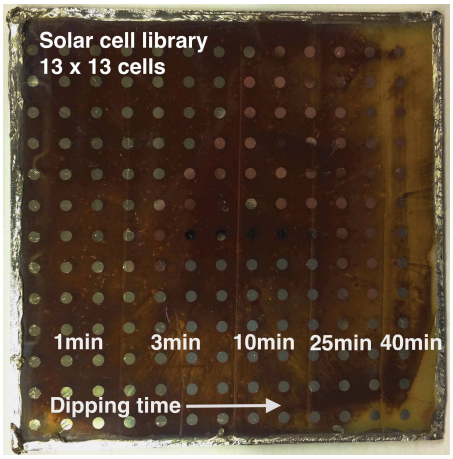

Figure E1: An example of a solar cell library (13 x 13 cells) with a gradient perovskite layer after dipping into a CsI in IPA solution.

Table E1: Fittings of the (110) reflection during in-situ cation exchange.

Time	2Θ [°]
0min	14.13
3min	14.16
8min	14.17
18min	14.17
28min	14.18
38min	no peak

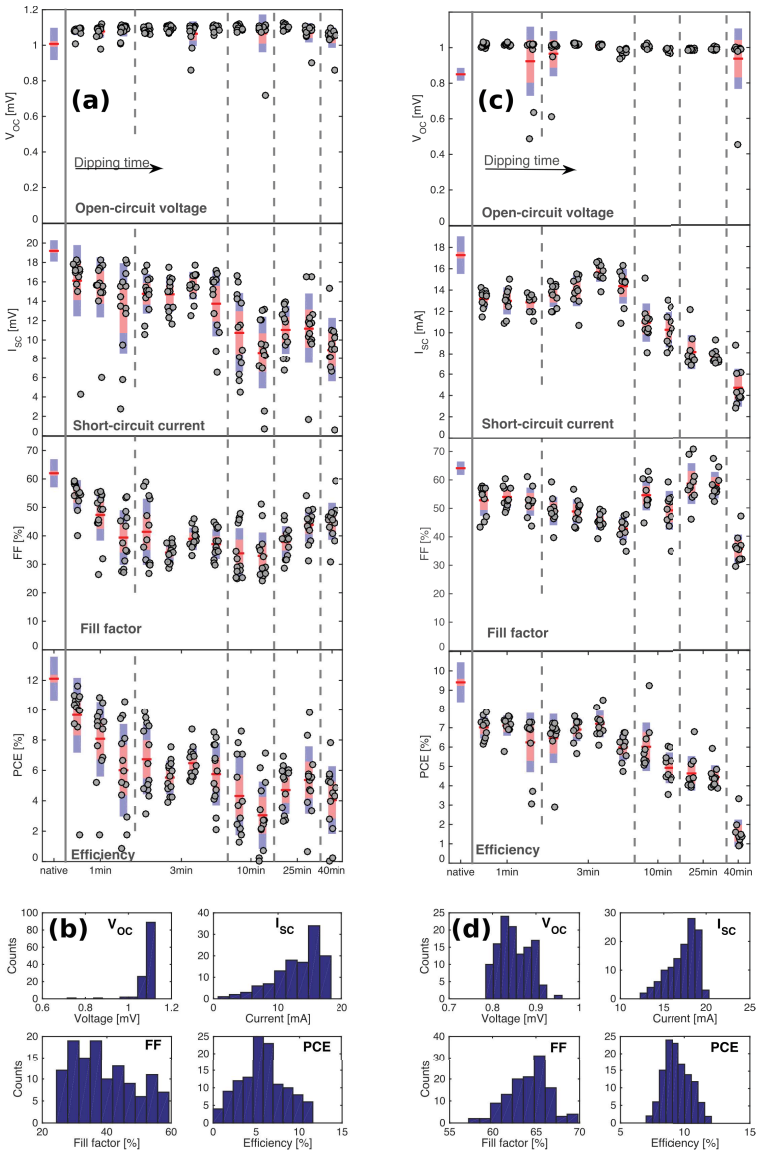

Figure E2: A summary is given of the photovoltaic parameters over dipping time for two different batches, namely open-circuit voltage V_{OC}, short-circuit current I_{SC}, fill factor FF and power conversion efficiency PCE, respectively. (a+c) shows the full parameter distribution with each cell indicated as a dot, while (b+d) shows the distribution of those parameters for the native sample in form of a histogram. The qualitative trend is the same in that the V_{OC} increases upon Cs-incorporation and I_{SC} (and therefore PCE continuously drop for increasing dipping times. The blank sample shown in (d) shows a broader distribution of most PV parameters, but the qualitative response of the parameters for the Cs^+ dipping remains the same.

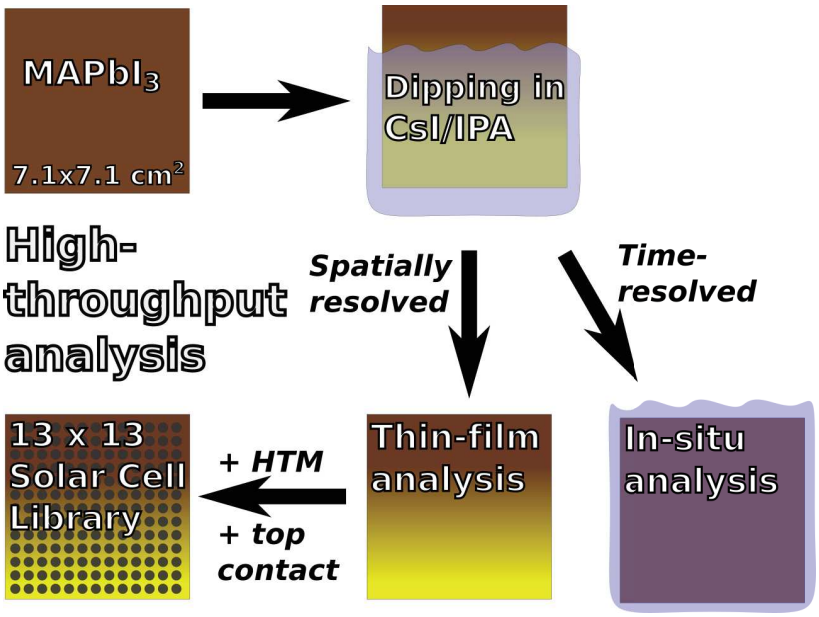

Figure E3: Synthesis and analysis of Cs+ incorporated MAPbI3 solar cells. A gradual dipping conversion was done on 7 7 cm2 substrates. The optical, electronic and structural properties of the material were tested in a high-throughput fashion. In-situ measurements were taken to clarify the conversion mechanism and show the improved stability of CsxMA1-xPbI3. Analysis of the thin-films and solar cells gave information about the material and its photovoltaic performance.

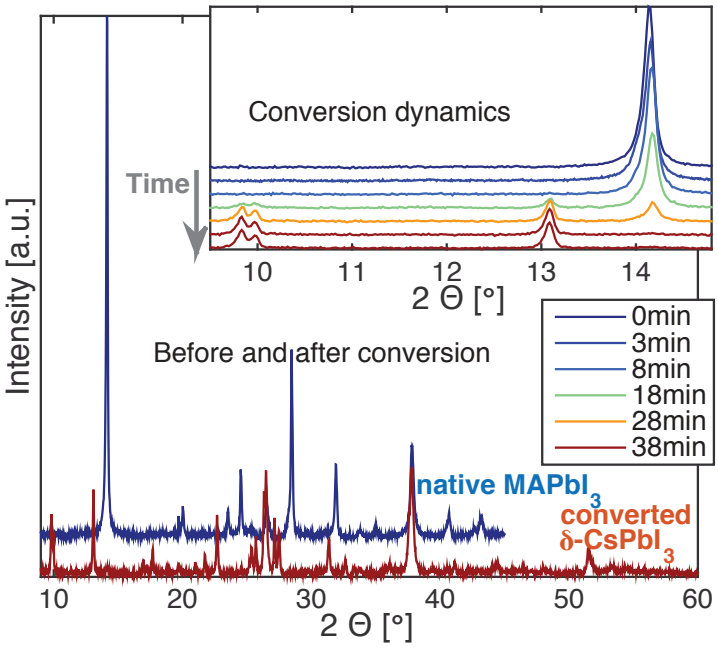

Figure E4: full XRD spectra of the in-situ cation exchange shows the complete conversion within the 38min of the experiment. The inset shows zoomed-in diffractograms at different stages of the conversion process.

Table E2: Peak position of (110) reflection found in diffractions done for different $Cs_xMA_{1-x}PbI_3$ compositions made with a one-step deposition. Peak position obtained using fittings of the (110) reflection peak to a calculated pseudoVogit intensity profile done in CrystalMaker. The full diffractograms can be found in fig. 2 in the main document.

Composition	2Θ [°]
x=0	14.17
x=5	14.19
x=10	14.21
x=15	14.23
x=20	14.20
x=25	14.20
x=30	14.21
x=40	14.19
x=50	14.23
x=75	14.34
x=100	-

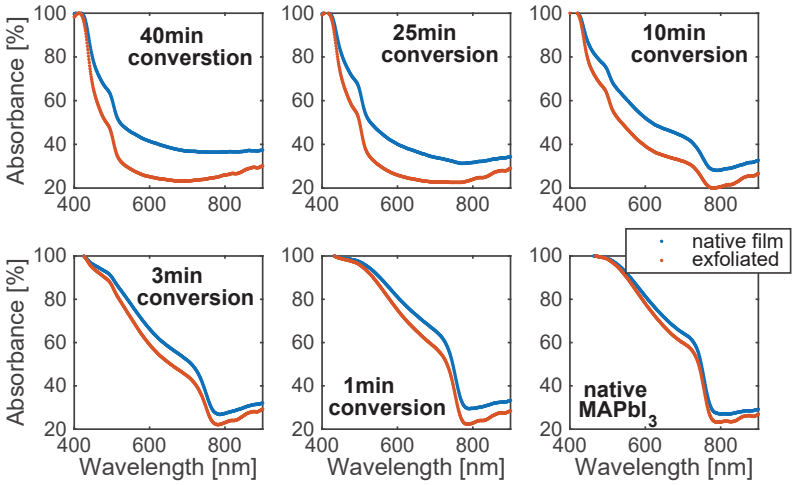

(a)

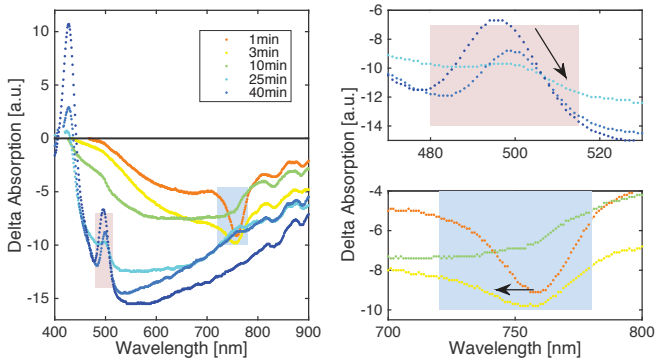

(b)

Figure E5: (a) UV-Vis spectra of different conversion stages of the native thin-films (native $MAPbI_3$ and different conversion times in CsI solution). (b) The subtracted spectra before baseline removal. The baseline corrected spectra are shown in fig. 5 in the main document.

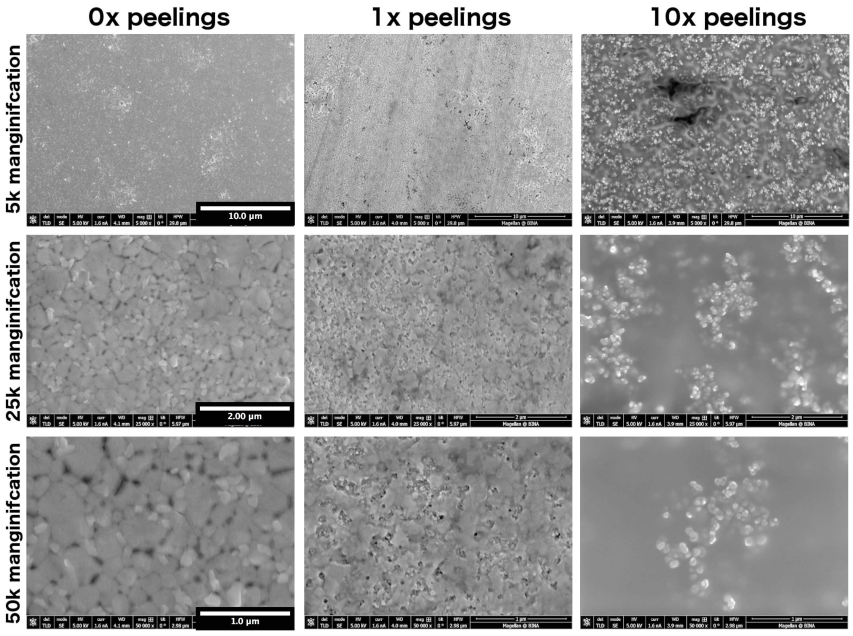

Figure E6: SEM images taken at different stages of the peeling process on $MAPbI_3$ ting(before, after one peeling and ten peelings). Results show the incremental removal of the capping layer.

Table E3: Structural parameters of the plain perovskites $MAPbI_3$ and $CsPbI_3$ as well as the mixed cation $Cs_xMA_{1-x}PbI_3$ in their cubic phase. Namely the cation radii r_{cation} [1] and unit cell volume $V_{UC,cubic}$ [2] were taken from literature. The values of the (110) reflection in XRD (2 Θ) and corresponding d-spacing as measured in this study.

Perovskite cation		MA	Cs_xMA_{1-x}	Cs	Rel. diff.
Literature	r_{cation} [1]	2.17 Å		1.81 Å	-16.6 %
	$V_{UC,cubic}$ [2]	251.6 $Å^3$		248.8 $Å^3$	-1.12 %
Measured	2 Θ (110)	14.14 °	14.18 °		0.30 %
	d-spacing	6.26 Å	6.24 Å		-0.30 %

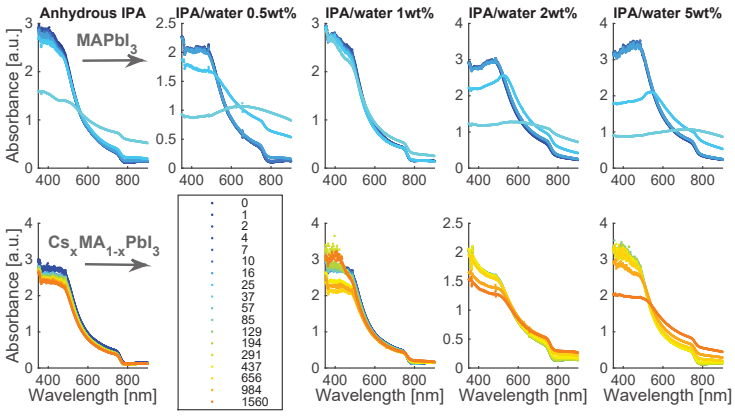

Figure E7: UV-Vis absorption spectra of thin-films (native $MAPbI_3$ above and $Cs_xMA1-xPbI_3$ below) dipped into a solution of IPA with different concentrations of water. The absorption in the blue regime dropped significantly as the thin-films decomposed into PbI_2, alongside an increase of the red regime, caused by scattering. A drop of the signal at 450 nm of 80 % was defined as the time of degradation. $Cs_xMA1-xPbI_3$ in solutions of water/IPA < 0.02 were stable over the full duration of the measurement (10h) and remained without visible color change for more than a week.

Error analysis

The propagation of error calculations were calculated individually for the three different approaches that were taken in this study (Tauc plot, EDAX and XRD).

Tauc plot error: The shift of the bandgap was determined via Tauc plot. Therefore, we fitted a first order polynomial to the linear region of the Tauc plot of the $Cs_xMA_{1-x}PbI_3$ after cation conversion (Tauc 1 with bandgap T_1) and for the blank $MAPbI_3$ (Tauc 2 with T_2). The linear fit parameters for Tauc 1 plot curve with standard deviation are $a_1 = 0.1775 \pm 0.0009 \cdot 10^{-23}$ and $c_1 = -0.2851 \pm 0.0014 \cdot 10^{-23}$. The intersection with the x axis and corresponding error function are:

$$T_1 = \frac{c_1}{a_1} \qquad \Rightarrow \Delta T_1 = \pm\sqrt{\left(\Delta c_1 \frac{1}{a_1}\right)^2 + \left(\Delta a_1 \frac{c_1}{a_1^2}\right)^2}$$

$$\Rightarrow T_1 = 1.618 \pm 0.012 \text{ eV}$$

For the blank $MAPbI_3$ sample we performed and analogous calculation with the fit parameters of the linear region of Tauc 2 of $a_2 = 0.1842 \pm 0.00015 \cdot 10^{-23}$ and $c_2 = -0.2946 \pm 0.0002 \cdot 10^{-23}$. The intersection with the x axis and corresponding error function are:

$$T_2 = \frac{c_2}{a_2} \qquad \Rightarrow \Delta T_2 = \pm\sqrt{\left(\Delta c_2 \frac{1}{a_2}\right)^2 + \left(\Delta a_2 \frac{c_2}{a_2^2}\right)^2}$$

$$\Rightarrow T_2 = 1.598 \pm 0.0018 \text{ eV}$$

The value for the bandgap of pure $CsPbI_3$ is taken from literature[2] $T_3 = 1.73$ eV. Combining these values we can calculate the composition from our UV-Vis measurements and the corresponding error function:

$$x_{Tauc} = \frac{T_2 - T_1}{T_3 - T_1} \qquad \Rightarrow \Delta x_{Tauc} = \pm\sqrt{\left[\Delta T_2 \frac{T_1 - T_2}{(T_3 - T_2)^2}\right]^2 + \left(\Delta T_1 \frac{1}{T_3 - T_2}\right)^2}$$

$$\Rightarrow \Delta x_{Tauc} = \pm 0.081$$

EDAX error: The constant regime (*step I*) of the absorbance at 450 nm is evaluated by forming the mean average $c_1 = 2.850 \pm 0.047$, while the slope that occurs during the *step II* conversion is fitted with a first order polynomial ($y = a \cdot x + b$) with $a_2 = 0.407 \pm 0.021$ and $b_2 = -1.47 \pm 0.18$. The slope of the EDAX Cs signal was also fitted with a first order polynomial with $a_3 = -0.0466 \pm 0.0018$ and $b_3 = 0.602 \pm 0.016$. The formula to determine composition x_{EDAX} derives from simple geometric consideration to:

$$x_{EDAX} = a_3 \frac{c_1 - b_2}{a_2} + b_3$$

$$\Rightarrow \Delta x_{EDAX} =$$

$$\pm\sqrt{\left[\Delta a_3\frac{c_1-b_2}{a_2}\right]^2+\left[\Delta c_1\frac{a_3}{a_2}\right]^2+\left[\Delta b_2\frac{a_3}{a_2}\right]^2+\left[\Delta a_2\frac{a_3}{a_2^2}(c_1-b_2)\right]^2+\Delta b_3^2}$$

$$\Rightarrow \Delta x_{EDAX} = \pm 0.042$$

XRD error: The miscibility gap estimation from XRD was done by measureing the (110) reflection peak of different stoichiometric $Cs_xMA_{1-x}PbI_3$ thin-films. The shifting reflection peaks were fitted with a first order polynomial with a slope $a = 0.4012 \pm 0.048$. This slope was compared to the obtained shift during the cation conversion, with (110) reflection before conversion of $\Theta_1 = 14.137 \pm 0.0037\ ^\circ$ and after 28 min conversion $\Theta_2 = 14.184 \pm 0.0098\ ^\circ$. The function to calculate the composition and the according error function are:

$$x_{XRD} = \frac{\Theta_2 - \Theta_1}{a}$$

$$\Rightarrow \Delta x_{XRD} = \pm\sqrt{\left[\Delta a\frac{\Theta_2-\Theta_2}{a^2}\right]^2+\left(\Delta\Theta_1\frac{1}{a}\right)^2+\left(\Delta\Theta_2\frac{1}{a}\right)^2}$$

$$\Rightarrow \Delta x_{XRD} = \pm 0.030$$

References

[1] G. Kieslich, S. Sun, and T. Cheetham. An Extended Tolerance Factor Approach for Organic-Inorganic Perovskites. *Chem. Sci.*, 6:3430–3433, 2015.

[2] C. C. Stoumpos, C. D. Malliakas, and M. G. Kanatzidis. Semiconducting tin and lead iodide perovskites with organic cations: phase transitions, high mobilities, and near-infrared photoluminescent properties. *Inorganic chemistry*, 52(15):9019–9038, aug 2013.

4.2.1.2 Further work: Structural and electronic response

To further support the XRD measurements and structurally analyse the $Cs_xMA_{1-x}PbI_3$ perovskite, we performed a manual fitting with CrystalDiffract covering both deposition methods, the cation exchange and the crystallisation from stoichiometric precursors (also called calibration sample in this context). The fitting focused on the (200) and (110) reflections and was done manually, as described in the experimental section. Our model assumes the formation of a homogeneous $Cs_xMA_{1-x}PbI_3$ alloy forming on the expense of $MAPbI_3$, therefore assuming a continuous solid-state solution. Other models that incorporate two phases of $MAPbI_3$ and $Cs_xMA_{1-x}PbI_3$ that share boundaries were tested but have been found to be inaccurate. The fitting was done with five free parameters: (1) Degree of orientation (March coefficient); (2) Grain Size; (3) Unit cell volume; (4) Cs-occupancy; (Cs occupied C positions in crystal structure file); (5) η parameter in Pseudo-Voigt profile. The unit cell volume was changed independently of the Cs occupancy in order to improve the fitting between the calculated curve and the measured data and was found to decreases with dipping time and with Cs-content in the calibration sample. The grain sizes used during the fitting are consistent with SEM results. The occupancies match well with the calibration sample as well as EDX measurements. The structural and morphological implications of the two main parameters will be discussed in the following paragraph: unit cell size and grain size.

From a structural point of view, the incorporation of the relatively small Cs^+ cation in $MAPbI_3$ shrinks the unit cell size, which shifts the diffraction pattern towards larger angles 2Θ, as can be seen in fig. 4-2a-b. We accounted for this shift by varying the unit cell size upon fitting. Both deposition methods show a similar change of the unit cell size over Cs ratio (see fig. 4-2). Small Cs incorporations $x \leq 0.1$ give a minor decrease of the unit cell size, while ratios $0.1 \leq x \leq 0.2$ result in a more drastic change of the unit cell, possibly resulting in considerable strains within the structure. This effect levels off for even larger ratios $x \geq 0.2$, which might be caused by the aforementioned disintegration of the structure. Morphologically, the grain size correlates to the peak width of the diffraction pattern, which we fitted as a third parameter. The results showed a decrease in grain size for Cs ratios $0.15 \leq x \leq 0.2$ (see fig. 4-2). This can be explained by the phase segregation for high Cs ratios, which segregates the structure into smaller grains. Interestingly, the calibration sample increases in grain size for small incorporations of Cs^+. This is consistent with the $Cs_xFA_{1-x}PbI_3$ system, which improves crystallinity, photo-stability and electronic properties for small ($x < 0.2$) Cs^+ contents.[25] The calculated decrease in grain size is consistent with SEM results.

We characterised the cells using large amplitude open-circuit photovoltage decay (OCVD), the full decay is shown in figure 4-3a. The OCVD shows three distinctive

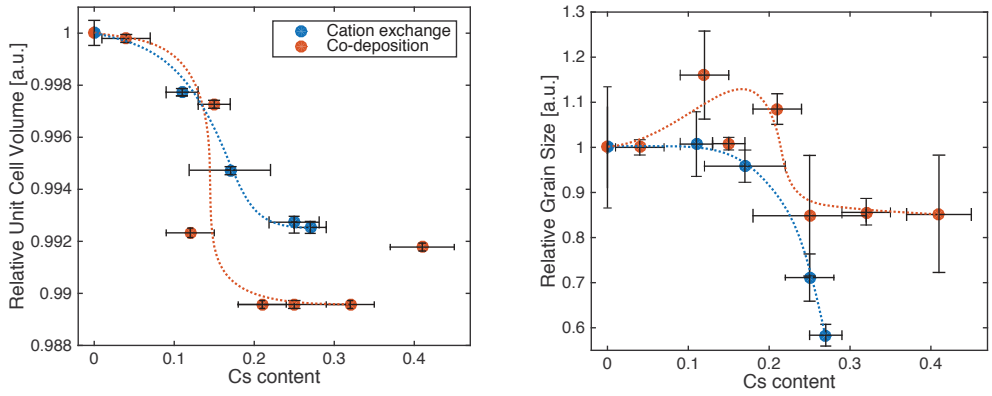

(a) (b)

Figure 4-2: Both graphs present fitting results of the XRD pattern in CrystalMaker. (a) Normalised unit cell volume evolution for both deposition techniques. (b) Evolution of grain size with increasing Cs^+ content. The dashed lines serve to visualise the trend and do not represent fit-functions.

regions in the decay curve: Immediately after switching the cell, we observe a *fast regime*, with a steep voltage decay. After about 1 ms the decay curve experiences a kink for all samples and changes its slope towards the *medium regime*, as can be seen figure 4-3b. Finally the curve changes into the *slow regime*.

For a more detailed evaluation of the data we need to treat each regime individually and regarding the process that is dominating at that specific time regime. Pockett *et al.* recently investigated planar PSC at a variety of temperatures and showed that the OCVD consists of two distinctive processes.[26] The free carrier recombination happens within fast time domains (e.g. ns).[27, 28] Slower time domains are therefore not related to free carrier recombination but rather relaxation processes,[29, 30] most likely through the movement of ion vacancies that equilibrate according to the change in electric field.[31] However, the cells analysed in this work contain an additional mp-TiO_2 scaffold and therefore the decay measurement is more complex with more time domains during the large perturbation decay. A fast initial decay can be seen over the first $\approx$ 100 mV in less than 1 ms (see fig. 4-3b). According to recent studies this time scale includes the processes of charge carrier recombination as well as depopulation of trap states.[28, 27] The plot shows a linear decay after an initial curvature, which was fitted with a first order polynomial in the range between 300 and 800 μs, in order to compare the decay of the different Cs^+ conversion times. The comparison of the fitted values can be seen in figure 4-4a, which will be further discussed later. The next time regime has a distinctive transition with a kink at 1 ms and lasts for about 200 ms. Assignment

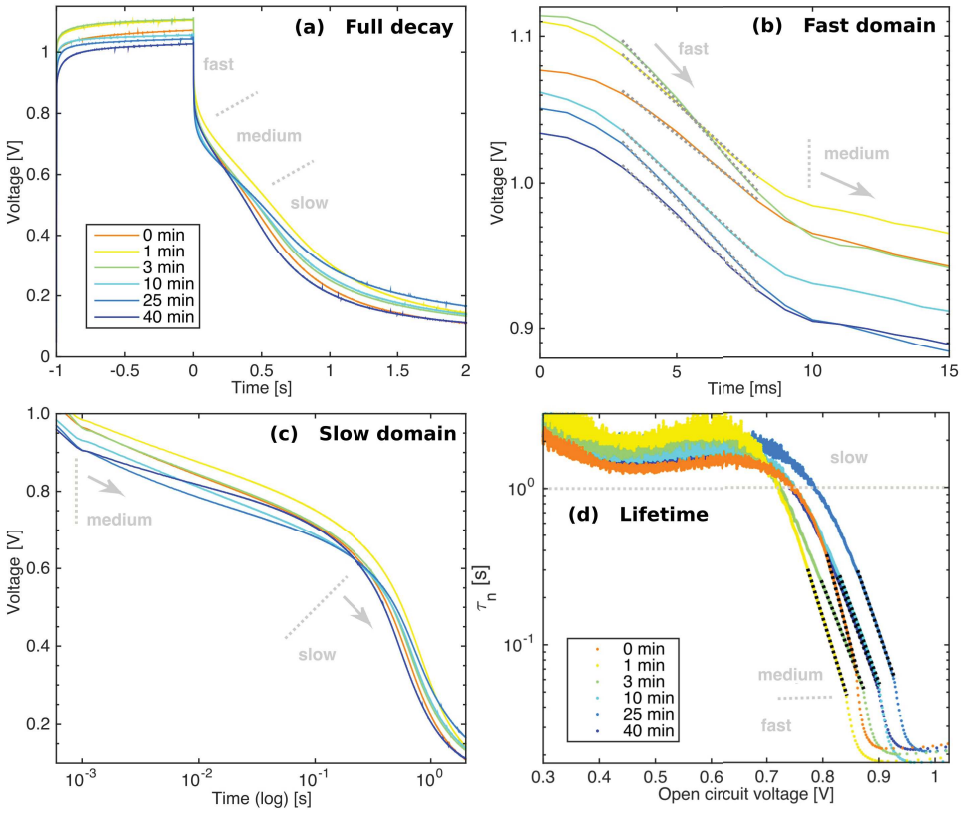

Figure 4-3: (a) Full photo-voltage decay for different perovskite conversion times; (b) linear plot of the fast decay and (c) semi-log plot of the medium and slow decay. (d) The full decay plotted as lifetime over voltage, where the upper constant regime (< 700 mV) shows a constant value which is attributed to ion diffusion.

of the underlying process is difficult because it lies between the electronic response that can still be seen in the fast domain and the ionic response in the slow domain. The distinctive transition is very similar to a '*bounce back*' effect that was reported by Pockett *et al.* for planar cells that strongly depends on temperature.[26] Finally, the transition to the slow domain can be observed as a change of slope in figure 4-3c and is even more significant when plotting the lifetime (see fig. 4-3d). This regime is probably dominated by drifting ions that respond to the change in electrical field as a result of the carrier depopulation.[31, 26]

The transformation of the OCVD into a lifetime τ_n needs to be given special attention at this point. The conversion was done according to equation 2.3, described in chapter 2:

$$\tau_n = -\left(\frac{kT}{q} \cdot \frac{dV}{dt}\right)^{-1}$$

The lifetime τ_n was initially derived as a lifetime of charge-carriers in DSSC,[32] where the electrons and holes recombine across the interface between TiO_2 and liquid electrolyte. Applied to PSC, it includes several cooperative effects,[30] which complicates the interpretation and demands caution for the interpretation. We assume that the fast initial decay is dominated by recombination and depopulation of trap states, and therefore this regime can be represented by the lifetime. The linear decrease of V_{OC} translates into a curved lifetime for the fast regime. The initial decay then turns into a linear regime after a small kink between $850 - 950$ mV. This is where fast recombination and de-trapping processes become entangled with relaxation processes caused by the movement of ions and possible contributions from ferroelectric alignments. This process starts at time constants of about $\tau_n \approx 55$ ms for all compositions $Cs_xMA_{1-x}PbX_3$ but differs in their further slope. Therefore a first order polynomial was fitted to that region to compare their development. The resulting slopes are shown in figure 4-4, bottom. Finally, the slow domain shows a broad but almost constant value and dominates the lifetime plot for voltages < 700 mV. It should be stressed that this value does not correspond to an actual lifetime. The transition from medium to slow domain is at about 700 mV.

We fitted the slopes of figure 4-3b+d in order to quantify the changes of the OCVD regarding Cs^+ content, as described above. The results are shown in figure 4-4. For the fast regime we can see that the slope becomes significantly steeper (about 40 %) over the first 3 min of cation exchange. Correlation of this time domain to recombination and depopulation of trap states shows that either the de-trapping becomes faster (traps become more shallow) for increasing Cs^+ contents or that the density of trap states is lower. Considering the increase in V_{OC} of about 100 mV (see supporting information of paper in section 4.2.1.1), it seems likely that the mixed cation perovskite has an intrinsically lower density of traps. For higher cation concentrations, the values level off, which is consistent with our assumption of a substitution limit, where the Cs-content remains constant. The medium regime slope is based on the lifetime against voltage and, different to the OCVD slope, becomes less steep with increasing Cs^+ content up to values where the substitution limit lies. Then they start levelling at a more or less constant value. This suggests that the Cs incorporation slows down the relaxation process. The unpolar Cs^+ could increase the defect diffusion barrier ΔE_b (equation 1.1 in chapter 1) and therefore reduce the ion movement. Thus contributing to the organic cation's molecular dynamics and hydrogen bonding, that plays a central role for structural dynamics of the perovskite scaffold and also assists the ion diffusion process.[33] The decrease of hysteresis in the IV curves reported in the paper in section 4.2.1.1 supports this assumption.

To sum up, we acquired additional structural information about the $Cs_xMA_{1-x}PbI_3$ composite through a manual fitting of the diffraction peak position, relative height and width. Those values correlate to the parameters unit cell size and grain size. The reliability of the fitting was assured by comparison to independent methods such as HRSEM, EDAX and calibration samples. The results show that Cs^+ cations can exchange with MA^+ in $MAPbI_3$ to form a continuous phase of $Cs_xMA_{1-x}PbI_3$. Small Cs incorporations ($x \leq 0.1$) result in minor changes of the $MAPbI_3$ structure, while larger Cs ratios of $x \geq 0.15$ leave a strained $Cs_xMA_{1-x}PbI_3$ structure. After the substitution limit, the structure decomposes into smaller fractions of $CsPbI_3$. Furthermore, the V_{OC} decay of different $Cs_xMA_{1-x}PbI_3$ compositions was analysed and showed three distinctive regions. The fast decay domain shows an increasingly quicker decay which indicates a lower trap density for higher Cs^+ contents. This is opposed by slower decay rates for the > 1 ms time domain which might be caused by slower relaxation processes, possible due to a hindered I^- ion movement.

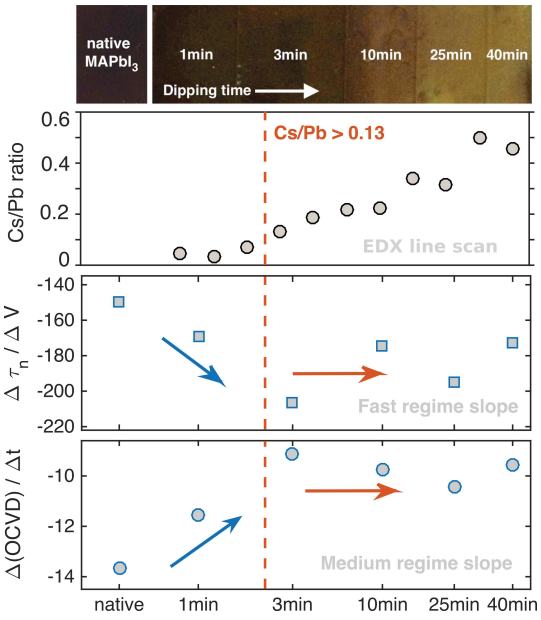

Figure 4-4: (top) Photograph of the native $MAPbI_3$ as well as different conversion times for $Cs_xMA_{1-x}PbI_3$. (middle) Linear fitting of the fast regime of the OCVD $[V \cdot s^{-1}]$. (bottom) Linear fitting of the lifetime plot τ_n over voltage $[V^{-1} \cdot s^{-1}]$.

4.2.1.3 Contemporary assessment

Even though the publication presented above was published relatively recently, it can already be compared to a number of related studies. A qualitative confirmation was given by Niu *et al.* when they reported on a '*remarkable improvement*' of stability and a segregation of $CsPbI_3$ for higher Cs-contents.[34] An opposing view was given by Dong *et al.* who reported the synthesis of $Cs_xMA_{1-x}PbI_3$ nanowires for the whole compositional spectrum.[35] This contradicts our findings, which found a substitution limit for different deposition methods. However, the synthesis method used by Dong *et al.* is a water-based conversion of PbI_2 plates into single-crystalline one-dimensional nanowires of $Cs_xMA_{1-x}PbI_3$, grown in [001] direction. Our study on the other hand used two different methods for the synthesis but both of them being (two-dimensional) thin-

film methods. Hence a major contribution for the instability of the solid-state solution might be facet-dependent, possibly with the (001)-side initiating the degradation. Such a facet-dependent activity and stability is known from other perovskites as well as other crystal systems.[36, 37]

4.2.2 Azetidinium: A new organic cation as an A-site derivative

As explained in the last section, the three main candidates for high performance perovskite materials for PV are Cs^+-, FA^+- and MA^+-based lead iodide perovskites. Each of those systems has its own advantages and disadvantages, but none combines a good PV performance with sufficient stability. Therefore, an ongoing research effort is put into the search for a favourable cation replacement. A noticeable approach was done by Kieslich *et al.* recently,[14] who screened 13 protonated amines with over 2500 possible perovskite permutations regarding their eligibility to form the perovskite structure according to the Goldschmidt tolerance factor. Of the 13 suggested cations, only a few have been implemented into PV devices.

One example is the hydrazinium ($H_2NNH_3^+$, Hi^+),[38] which however has a high internal energy caused by the N-N bond, rendering it a useful candidate for rocket fuel and therefore raising questions about its stability. Hi-based PSC showed an optimum performance for a cation ratio of 0.1, with further substitutions resulting in a decrease of photocurrent. The structural evolution shows a shift of the (110) reflection for $x \leq 0.1$, indicating an increase in unit cell size, which remains constant for higher incorporations. The UV-Vis spectra indicate the rise of two new species, namely the hydrazinium lead iodide and PbI_2. All these effects indicate a similar behaviour to the Cs-MA perovskite system, with the presence of a miscibility gap that supposedly starts between $0.1 \leq x \leq 0.2$.

Another experimental implementation of the organic cations computationally suggested by Kieslich *et al.* is the guanidinium ($(NH_2)_2C(NH_3)^+$, Gu^+), which however is too large to form a perovskite structure and does not seem to incorporate into the $MAPbI_3$ structure. But it can presumably act as an additive that enhances the crystallisation process and increases carrier lifetime.[39]

Azetidinuim-based ($(CH_2)(NH_2)^+$, Az^+) perovskites already drew attention for their intriguing magnetic, ferroelectic, multiferroic properties and glassy behaviour.[40, 41] Those properties are at least partially based on the Az^+ cation that plays a central role for bonding motives, supports strong hydrogen bonding and can adopt both a planar and ring-puckered form under different conditions.[42, 41] Based on the Goldschmidt rules, $AzPbI_3$ is expected to form a perovskite structure, but it has not been reported as an A-site cation up to now. In the approach presented in this work, we investigated the Az^+ as an A-site derivative on its own and for mixed cation systems with MA^+. Small incorporations ($x < 0.05$) form a solid-state solution that shows enhanced photovoltaic properties. A Raman spectroscopic analysis of the $AzPbI_3$ shows red-shifted signals of the amine group compared to the AzI salt, which is indicative of significant bonding interaction (*e.g.* hydrogen bonding) with the inorganic $[PbI_3]^-$ framework. This study

represents pioneering work on compositional derivatives of the $MAPbI_3$ perovskite system, aiming to overcome its intrinsic instability.

4.2.2.1 Related publications

RGN contributed to this study by analysing the powder XRD and discussing the results from the structural point of view; furthermore RGN measured and analysed the Raman results.

Azetidinium Lead Iodide for Perovskite Solar Cells

Samuel R. Pering[a], Wentao Deng[a], Joel R. Troughton[c], Ralf G. Niemann[a], Federico Brivio[a], Peter S. Kubiak[a,b], Florence E. Jeffrey[d], Trystan M. Watson[c], Paul.R. Raithby[a], Andrew L. Johnson[a,d], Simon E. Lewis[a,d], & PJ. Cameron[a,d]
[a]: Department of Chemistry, University of Bath, Claverton Down, Bath, BA2 7AY, UK
[b]: Centre for Doctoral Training in New and Sustainable Photovoltaics, University of Liverpool
[c]: SPECIFIC, Swansea University College of Engineering, Bay Campus, Swansea, SA1 8EN, UK
[d]: Centre for Sustainable Chemical Technologies, University of Bath, Claverton Down, Bath, BA2 7AY, UK

Email: S.R.Pering@bath.ac.uk, P.J.Cameron@bath.ac.uk

Hybrid organic-inorganic perovskites have been established as good candidate materials for emerging photovoltaics, with device efficiencies of over 22 % being reported. There are currently only two organic cations, methylammonium and formamidinium, which produce 3D perovskites with band gaps suitable for photovoltaic devices. Numerous computational studies have identified azetidinium as a potential third cation for synthesizing organic-inorganic perovskites, but to date no experimental reports of azetidinium containing perovskites have been published. Here we prepare azetidinium lead iodide for the first time and show that it is a stable, bright orange material that can be successfully used as the absorber layer in solar cells. We also show that it is possible to make mixed cation devices by adding the azetidinium cation to methylammonium lead iodide. Mixed azetidinium-methylammonium cells show improved performance and reduced hysteresis compared to methylammonium lead iodide cells.

1. Introduction

The amount of research into Organo Lead Halide Perovskites for Perovskite Solar Cells (PSC) has increased rapidly since 2012.[1-3] The benefits of PSC include fabrication using facile solution processing methods,[2,4] and the ability to easily tune properties like band gap and colour.[5,6] Methylammonium lead iodide (MAPI) solar cells have reached efficiencies of over 15 %.[7] MAPI has a bandgap of 1.6 eV,[8] which is higher than the optimum band gap for

solar cells of 1.1 – 1.4 eV.[9,10] Band gap engineering is possible by mixing halide ions to form $MAPbI_{3-y}X_y$, where X is either chloride or bromide.[6,8] Alternatively the lead cation can be exchanged for tin. $MASnI_3$ has a lower bandgap of 1.3 V, and $MASnI_3$ PSC can reach efficiencies of 5.7 %.[11] However $MASnI_3$ has been shown to be more unstable and more toxic than $MAPbI_3$.[12,13]

To date, variation of the organic cation has received much less attention compared to variation of the halide and group 14 metal components of the perovskite. This is likely due to the perceived lack of alternatives to methylammonium. Formamidinium (FA) is the only alternative organic cation that has been shown to produce a 3D perovskite. $FAPbI_3$ has a band gap of 1.48 eV, and solar cells have been prepared with efficiencies of up to 16 %.[14,15] An nalternative approach is to replace the organic cation with an inorganic caesium cation. $CsPbI_3$ cells have reached 2.9 % efficiency;[16] Cs^+ has also been used as an aditive in MAPI cells, improving both the efficiency and stability.[16,17] Mixed cation perovskites, e.g. containing formamidinium and methylammonium show efficiencies of over 18 %, and a band gap more closely aligned to that of its contact layers.[18] Trication perovskites with the formula $Cs_5(MA_{0.17}FA_{0.83})_{95}Pb(I_{0.83}Br_{0.17})_3$ have shown high efficiencies of 22.1 % and improved stability relative to single cation perovskites.[19,20] Methylammonium and formamidinium are by far the most common cations that are used in high efficiency 3D perovskite solar cells. Organo-lead halide perovskites have been produced using *n*-butylammonium cations, but the larger size of the cation means that a 2D rather than a 3D perovskite is created.[21] Guanidinium lead iodide also forms a 2D perovskite, but the addition of small amounts of guanidinium to MAPI can improve the open-circuit voltage in the resulting devices.[22] 2D perovskites have been investigated as absorber layers in PSC and show enhanced stability compared to devices made with 3D perovskites.[21] 2D materials are very promising, although to date the efficiencies are lower than for devices containing 3D perovskites; 2D perovskites can also require high temperature processing.[23]

Substitution of any of the ions in a 3D perovskite will cause a change in the lattice parameters, and band gap of the material.[24] There are three perovskite phases, the α, β, and γ, as well as a non- perovskite δ phase; which are stable at different temperatures and dictate electronic properties.[25] A tolerance factor, which is calculated based on the size of the ions present, can be used to predict whether or not a 3D perovskite phase will form:

$$t = \frac{(r_A + r_X)}{\sqrt{2}(r_B + r_X)} \quad (1)$$

where r_A, r_B and r_x are the ionic radii of the components in the general perovskite formula ABX_3. The tolerance factor approach has been used to predict the likely structure of new perovskites, where a value of $t = 0.9 – 1.0$ suggests a cubic perovskite phase will be formed. Compensating for the effect of the halide anions on the radius of the inorganic cation yields a modified factor.[26] Cations with radii that are too large to fit within the cubic perovskite parameters (i.e. r_A gives $t > 1$) form 2D perovskites.[23] The tolerance factor approach has been used to identify other possible ions that could be used to prepare 3D cubic lead halide perovskites suitable for PSC. Suggested organic cations include azetidinium, $[(CH_2)_3NH_2]^+$, hydrazinium $[H_3N\text{-}NH_2]^+$ and guanidinium, $[(NH_2)_3C]^+$.[27,28] Hydrazinium was used recently to improve the efficiency of mixed cation inverted structure perovskite cells.[29] The azetidinium (Az) cation has a computationally derived ionic radius of 250 pm, which lies between the ionic radii of MA (217 pm) and FA (253 pm).[30] A simple tolerance factor calculation yields a *t* value of 0.98, within the region that a perovskite structure could be predicted. Factoring in the effect of the halide ions on the $[PbI_6]^{4-}$ octahedra produces a tolerance factor of 1.03, still within the region where a perovskite could be predicted to form.[31] Several computation papers have now predicted that azetidinium should produce stable lead iodide perovskites. The azetidinium cation has been previously been used in metal-organic perovskites which were not for photovoltaic applications.[32,33] In this paper we

demonstrate that azetidinium lead iodide (AzPI) is stable and easy to produce. It is a bright orange solid that can be used to prepare PSC both on its own and when combined in a mixed cation solar cell with MA. We show experimentally for the first time that the Az cation is a good option for the engineering of high-efficiency and stable perovskite solar cells.

2. Results & Discussion

In this project we prepared both single crystals and thin films of azetidinium lead iodide (AzPI). The properties of the Az cation are compared to those of the commonly used MA and FA cations in Table 1.

Table 1. Comparison of three organic cations for PSC regarding ionic size, Goldschmidt tolerance factor, perovskite structure at RT, dipole moment and chemical structure. Dipole moments were calculated for this study.

Cation	Methylammonium	Formamidinium	Azetidinium
Effective radius[30]	217	253	250
Tolerance Factor[27]	0.912	0.987	0.980
RT Structure	tetragonal	hexagonal	unresolved
Dipole moment (DFT calc.)	2.176 D	0.605 D	2.519 D
Chemical Structure	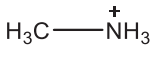	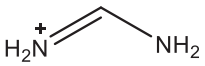	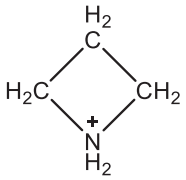

We found that azetidinium iodide was not soluble in either DMF or DMSO, so a sequential deposition approach was used to produce films of AzPI. A solution of azetidinium iodide in isopropanol was spin-coated on top of a PbI_2 film. The PbI_2 film rapidly turned a glassy orange colour at room temperature (Figure 1a), the colour did not change with annealing. Powder XRD was performed on both MAPI and AzPI films formed by the two-step deposition route. Major reflections in the AzPI diffractogram were at 11.5 °, 24.9 °, 26.2 ° and 30.1 °, and although there is a feature close to the (002) lead iodide peak at 12.7 °, the

diffractogram is clearly different from that of pure PbI_2.[2] A comparison of the thin film X-ray diffractograms for MAPI and AzPI shows a large difference in the patterns obtained. The peaks in the MAPI spectrum were more intense and had a narrower peak width, suggesting that the MAPI film is more crystalline than the AzPI film. It is likely that chemical bonding effects play an important role in the interactions between cation and inorganic cage, which results in the formation of a more disordered AzPI phase.

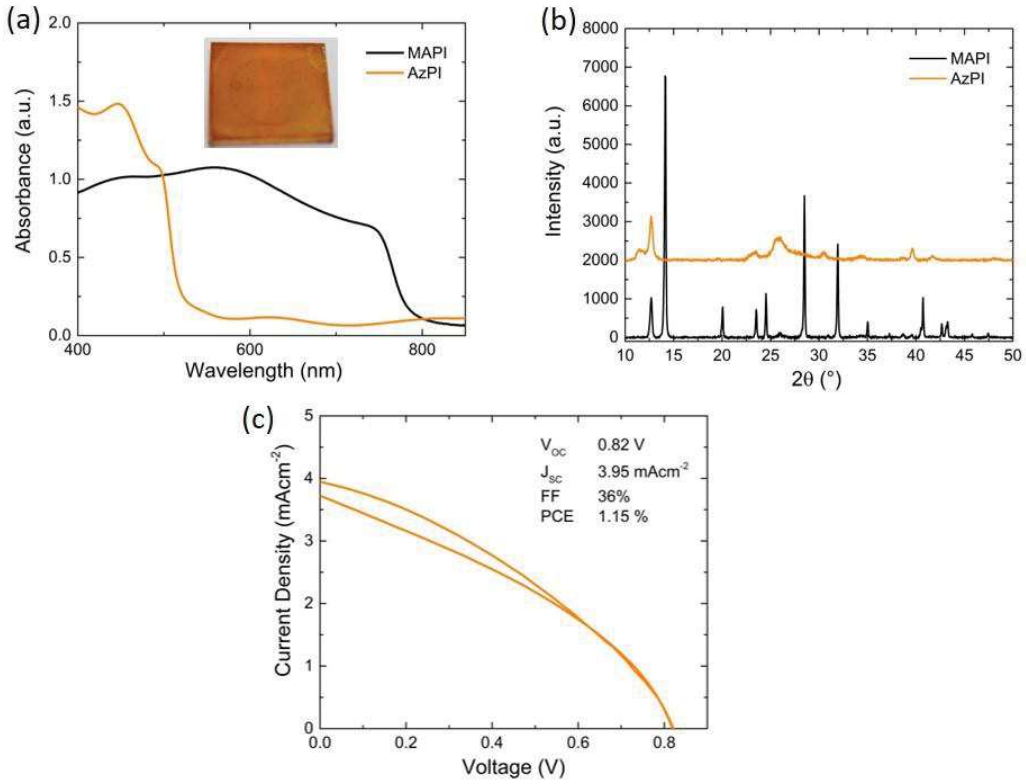

Figure 1: Azetidinium Lead Iodide (a) UV/Vis spectroscopy of an AzPI film with MAPI for comparison and (inset) photograph of an AzPI film, (b) XRD patterns of AzPI and MAPI, (c) a J-V curve of an AzPI solar cell with inset cell parameters

Single crystals of AzPI were grown for analysis, but unfortunately a complete description of the atomic positions in AzPI could not be determined by single crystal XRD as all the crystals obtained suffered from severe twinning.

SEM images of the AzPI film (Figure S2) showed that the layer consisted of a large number of small crystals, each around 100 nm in size. There was also a high surface coverage with few noticeable pinholes, which should aid solar cell performance by increasing shunt resistance. A low surface roughness of around 100 nm was observed by AFM (Figure S2).

To estimate the band gap of AzPI, UV/Vis absorbance of the film on glass was measured and compared with a MAPI film (Figure 1a). As expected for an orange film, the absorption onset for AzPI is at shorter wavelengths than for MAPI, with a difference of just over 200 nm. The band gap of AzPI was estimated to be 2.15 eV – significantly higher than the optimum band gap for solar cell materials. Mesoporous PSC were made using the bright orange azetidinium lead iodide layers (Figure 1d) The best cell exhibited an efficiency of just over 1 % (with an average over 8 pixels of 0.96 % and a standard deviation of 0.08), demonstrating that pure AzPI exhibits reasonable efficiencies for a new photovoltaic material in unoptimised solar cells.

Due to the difficulties in resolving the single crystal structure of AzPI it is not possible to say which perovskite phase has been formed. In order to see if AzPI was photoactive, a cyclic voltammogram was measured under chopped illumination. This voltammogram is shown in Figure S3. In order to stabilise the AzPI film, the electrolyte was 0.1 M azetidinium iodide in isopropanol. A positive photocurrent was observed above 0.2 V (versus Ag/AgCl); at 0.2 V the photocurrent switched and became negative. The response suggests that like other organolead halide perovskites, AzPI is ambipolar.[30]

Raman spectroscopy was performed to elicit more information about the possible role of the azetidinium cation in the structure. AzPI is compared to AzI and Az^+ in Figure 2 (A full listing of measured modes is in Table S1).[36] The results show a continuous red-shift for most modes in AzPI with respect to AzI. The magnitude of this shift is mostly based upon a

chemical Stark shift as well as increased interaction of the Az^+ with its direct environment, due to the spatial constraint; thus increasing the interaction between the Az^+ cation and the $[PbI_3]_n$ cage. The magnitude of this shift is mostly between 5 to 10 cm^{-1}, with few exceptions. Specifically strong shifts can be seen for the ring deformation (ν_3) and the NH_2 wagging (ν_{13}). Firstly, the ν_3 mode shows a red-shift of 15 cm^{-1} in the AzPI structure, potentially caused by sterical hindrance of the inorganic cage. Moreover, the ν_{13} NH_2 wagging mode shows a strong red-shift of 61 cm^{-1}, which is significantly larger than any other observed shift. The decrease in frequency suggests a weakening of the bond-strength, presumably through a strengthening interaction with the inorganic scaffold. Besides the increased interaction caused by the higher dipole moment (Table S1) and favourable out-of-ring position of hydrogen atoms for bonding with the inorganic scaffold, the Az^+ also possesses fewer internal degrees of freedom because of its limited conformational isomerism. One way to compensate for this would be the formation of a lower-dimensional (not 3D) AzPI structure with higher entropy. Strong hydrogen bonding from the organic cation would offer an alternative bonding motif for this structure, as opposed to the three-dimensional I-Pb-I perovskite scaffold. The strong shift of the NH_2 wagging mode ν_{12} indicates strong bonding action from the amine group (e.g. hydrogen bonding) in the orange AzPI phase. The generally stronger shifts in modes associated with the 2C-position and the ambivalent behavior of 1C-positioned modes suggests that the Az^+ has a bridging function in the orange phase.

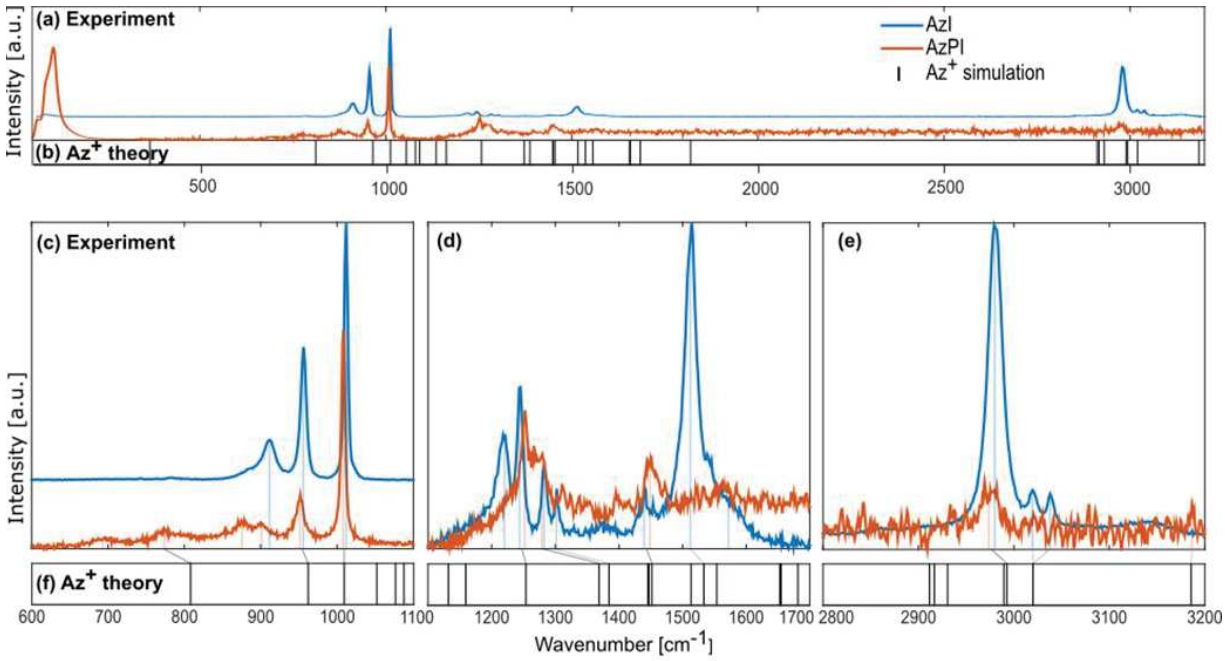

Figure 2: (a-b) Full spectra of AzI and AzPI including comparison to Az^+ modes (c-e) zoomed region with shifts of assigned peaks against Az^+

Both MAPI and FAPI are known to be unstable in even low humidity conditions.[37] To test the stability of AzPI films towards water, both an AzPI film and MAPI film were submerged in water for a few seconds. As might be expected the MAPI film immediately turned yellow on contact with water and part of the film detached into the solution. In contrast the azetidinium film remained fully intact and the bright orange colour was unchanged. To investigate the degree of degradation of each film, thin film XRD was run before and after the dipping experiment. The results are shown in Figure 3a. The AzPI spectrum was largely unaffected by dipping and most importantly there was no increase in the intensity of the PbI_2 reflection at 12 °, showing that, unlike MAPI and FAPI, the photoactive phase of AzPI is stable even in the presence of extreme amounts of water. In contrast the MAPI had clearly degraded and the PbI_2 peak increased in intensity by more than four times after exposure to water. 2D perovskites have generally been shown to have an improved stability to 3D perovskites with exposure to humidity,[34] but in our study we chose a more extreme test.

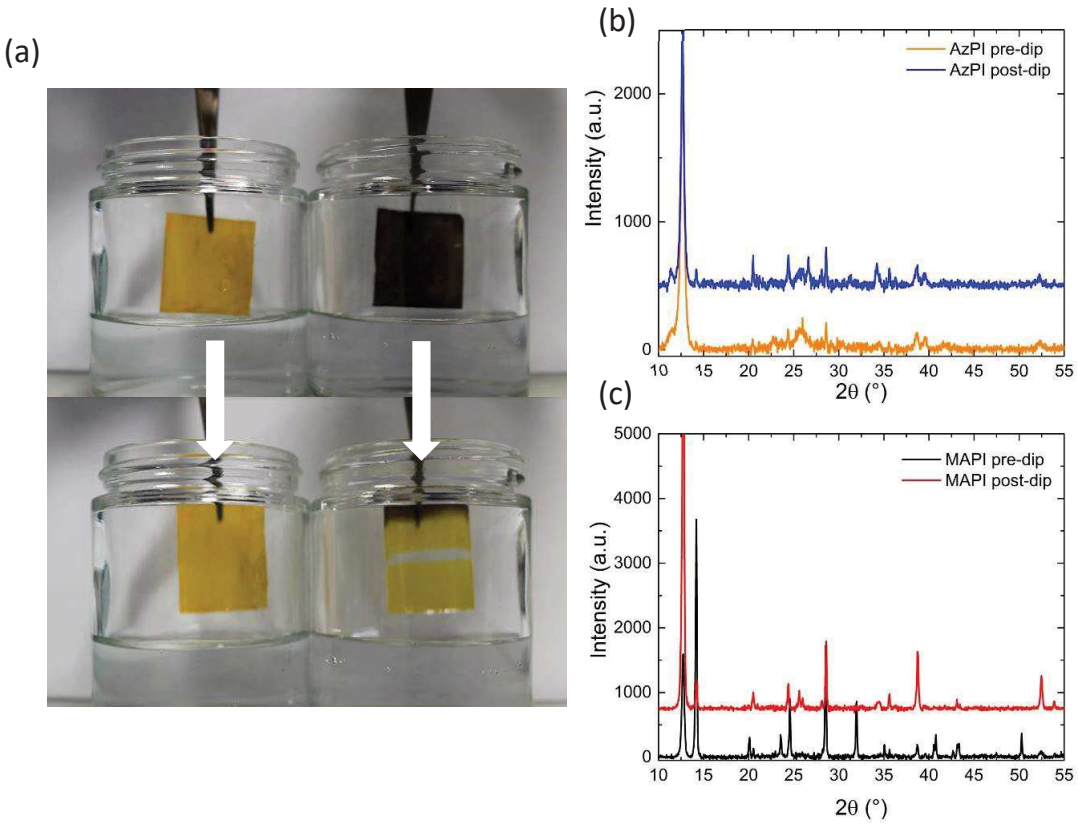

Figure 3. The effect of water on AzPI and MAPI: (a) photographs of AzPI (left) and MAPI (right) before (above) and after (below) dipping in water; (b) pre- and post-dip XRD for AzPI, and (c) pre- and post-dip XRD for MAPI

Mixed azetidinium-methylammonium lead iodide PSC were prepared and characterised. Tuning the proportion of different cations in the perovskite is known to alter the band gap and other properties of the material.[20,35] Mixed cation films were prepared by two step deposition; spin-coating methylammonium iodide solutions containing an increasing mole percentage of azetidinium iodide onto a pre-prepared PbI_2 film. The resulting films are shown in Figure 4a. The black colour of the MAPI was maintained until 10 mol% AzI was included in the solution. At this concentration the film became visibly lighter in colour. Increasing the mol% of AzI in the solution caused the film to continue lightening towards the orange colour of azetidinium lead iodide. This is evident in the UV/Vis spectra of the films (Figure 4b), in

which there is little change in the absorbance until 5 mol% AzI is present in the solution. As the percentage of azetidinium increases further, the absorption onset is slightly blue shifted and there is a reduction in the overall absorbance between 800-600 nm, then an increase in the absorbance at shorter wavelengths.

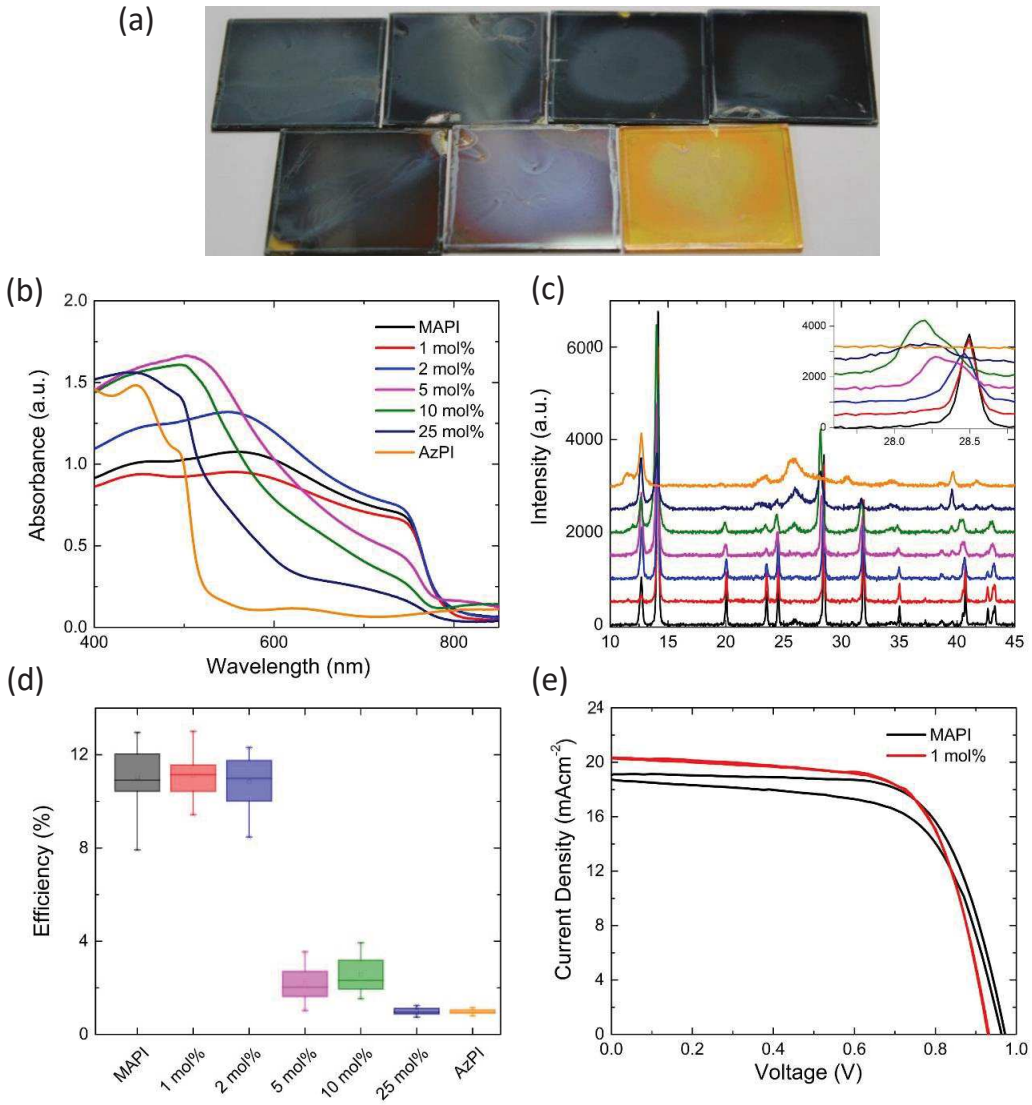

Figure 4. A study of the effects of azetidinium on methylammonium lead iodide (a) photographs of the AzMAPI films on glass with different mol% Azetidinium iodide in the spin-coating solution, from left to right: (top row) MAPI, 1 mol% AzI , 2 mol % AzI, 5 mol% AzI; (bottom row) 10 mol% AzI, 25 mol% AzI and AzPI; (b) UV/Vis spectroscopy and (c) X-ray diffraction patterns for the films on glass with inset tracking of the movement of the (2,2,0) peak at 28.5 °; (d) Box-chart for the efficiencies of cells made using AzMAPI and (e) JV curves for the best performing MAPI and AzMAPI cells showing both the forward and reverse scan.

In the thin film X-ray diffractograms there are clear trends that appear with the increasing mole percentage of azetidinium in the spin-coating solution. For compositional ratios of $x \leq 0.02$, the diffraction pattern shifts towards smaller angles, caused by an increase in unit cell size. There is a single peak at 28.5 ° without shoulder, suggesting that there is a continuous phase of $Az_xMA_{1-x}PbI_3$. For larger Az ratios $0.05 \leq x \leq 0.1$, the perovskite reflections indicate splitting into two domains. The primary AzPI peak at 26.2 ° appears at $x = 0.1$, and upon further increasing the Az ratio to $x \geq 0.25$, the intensities of the MAPI phase reflections decrease, while the AzPI reflections become more intense. Taking the MAPI (2,2,0) reflection as an example (inset in Figure 4c), there is a broadening and leftward shift – with the appearance of shoulders in the peak for the 5 mol% AzI sample. The apparent phase separations in the films made with a larger proportion of AzI explains the shape of the UV/Vis spectrum, with separate AzPI phases within the MAPI film causing shoulders in the absorbance, rather than completely shifting the band gap.

For solar cell fabrication PbI_2 films were dipped into solutions of mixed AzI and MAI, to allow the organic cation solution to fully penetrate the mesoporous layer (Figure S4). MAPI cells were used as the control. Until recently the highest reported efficiency for a pure $MAPbI_3$ cell was 15%, [2] however using a multi-step Lewis base adduct method, the efficiency can be increased to 19.7 %. [38] The highest efficiency perovskite devices are mixed cation and contain MA, FA and Cs. We chose to work with lower efficiency $MAPbI_3$ cells to allow us to fully characterise any changes introduced by the Az cations. The cells were made by a standard two-step deposition method and were not optimised for efficiency.

Table 2. Photovoltaic parameters for MAPI and 1 mol% Azetidinium solar cells (averaged over **15 pixels**)

	V_{OC} (mV)	J_{SC} (mAcm^{-2})	FF (%)	Champion Cell (%)	Efficiency (%)
MAPI	948 ± 13	18.6 ± 0.70	62 ± 5.1	12.9	11.0 ± 1.35
$Az_{0.01}MA_{0.99}PI$	925 ± 16	18.1 ± 0.95	65 ± 4.0	13.0	11.1 ± 0.95

AzMAPI mixed cation cells deposited from a solution containing more than 5 mol% AzI show a lower efficiency than pure MAPI cells (Figure 4d). This agrees with the UV/Vis spectra, XRD (Figure 3b & 3c) and EQE (Figure S5) measurements which all show phase separation into MAPI and AzPI regions when 5 mol% AzI is present in the precursor solution. A discontinuous phase may hinder charge transfer through the lattice. With lower percentages of azetidinium in solution there is an improvement in the average efficiency of the cells, which is largely due to an improved fill factor (Figure S6). This, as well as a significant reduction in the hysteresis, is evident in the JV curves displayed in Figures 4(e) and S7, where, as in Table 2, the best performing MAPI and AzMAPI pixels are compared. There is a reduction in the standard deviation of the cell efficiency, from 1.35 in the MAPI control to 0.95 in the $Az_{0.01}MA_{0.99}PbI_3$ set. The stabilised power output of the devices also increased, shown in Figure S8. The best performing cell, from the $Az_{0.01}MA_{0.99}PbI_3$ set had an efficiency of 13.00 % in the reverse sweep, and 12.98 % in the forward sweep.

3. Conclusion

In conclusion, we have synthesised and characterised the new compound, azetidinium lead iodide (AzPI). We have determined that this compound exists as a stable, bright orange film and exhibits some photovoltaic capability, with an optical band gap of 2.15 eV. This tests the application of tolerance factor calculations to these materials, as azetidinium lead iodide is predicted to be within the range where a 3D perovskite should form. Chemical differences in the cation itself (dipole, acidity of the N-H group) are likely to be a key factor that needs to be brought into consideration when making predictions. Azetidinium can be co-deposited with

methylammonium to further improve the properties of the MAPI perovskite. These AzMAPI perovskites show an enhanced efficiency and stability compared to pure MAPI, with a reduced hysteresis at low percentages of azetidinium.

4. Experimental

4.1. Dipole calculations

The calculated dipoles have been obtained using the NWChem code. [39] The initial input obtained by geometrical intuition has been optimized. To express the wavefunction we used the cc-pVTZ basis set provided within the package and the as exchange correlation functional we used the B3lyp. The obtained values are in good agreement with other reports in literature. [40,41]

4.2. Azetidinium iodide preparation

5 ml of Azetidine (Alfa Aesar) at 0 °C had 55 mL hydroiodic acid (Sigma) added to it under argon atmosphere **(Caution! Exotherm)**. The ice bath was subsequently removed, and the solution was stirred for one hour. The solution was then left on a rotary evaporator until dry, leaving a bright orange solid. This was washed with diethyl ether to remove the iodine, and recrystallized in isopropanol, leaving white needle-like crystals. The identity of azetidinium iodide (AzI) was confirmed by ^{1}H NMR (Figure S1): (300 MHz, D_2O, δ): 2.46 (quin, J = 8.29 Hz, 2 H) δ 4.04 (t, J = 8.5 Hz, 4 H)

4.3. Crystal formation

0.1 mmol PbI_2 and AzI were dissolved in 1 mL *N*,*N*-dimethylformamide, and single crystals were grown by the solvent evaporation method.

4.4. Film deposition

For optical and structural measurements the perovskite films were deposited on to microscope glass following a method by Zheng *et al.*[35] Before film deposition, the substrates were

cleaned by sonication in 2% Hellmanex solution in water, followed by deionised water, acetone and isopropanol at 90 °C. Lastly they were treated with UV/Ozone for 20 minutes. 100 µL of a 1 M solution of PbI_2 (Sigma-Aldrich) in *N*,*N*-dimethylformamide was spin-coated at 2000 rpm for 60 seconds, followed immediately by 100 µL of isopropanol spun at the same rate. The resulting PbI_2 film was dried at 60 °C for 30 minutes. Solutions containing varying mole percentages of azetidinium iodide compared to methylammonium iodide were prepared in isopropanol, with a concentration of 20 $mgml^{-1}$. 100 µL of these solutions were pipetted onto the PbI_2 films, and spun for 60 seconds at 2000 rpm. The perovskite films were annealed at 100 °C for 20 minutes.

4.5. Solar cell fabrication

Pre-etched FTO glass (Kintek) was cleaned in 2% Hellmanex solution in water, followed by deionised water, acetone and isopropanol. A compact TiO_2 layer was deposited by spray pyrolysis. A hand held atomiser was used to spray a solution of 10 vol% solution of titanium isopropoxide (bisacetylacetonate) (Sigma-Aldrich) in isopropanol onto the substrates, which were kept at 550 °C for the procedure, and sintered for 30 minutes at the same temperature. A mesoporous layer consisting of a 2:7 mixture of 30 NR-D TiO_2 paste (Dyesol) in ethanol was spun onto the compact layer with a further 30 minute sintering step at 550 °C. After cooling, to improve conductivity a 0.1 M solution of Li-TFSI (Sigma) solution was spin-coated at 3000 rpm for 10 seconds and the substrates were then re-sintered at 550 °C for 30 minutes. Perovskite deposition was performed in a nitrogen filled glove box. A two-step dip-coating method was used to fabricate the solar cells. 1M PbI_2 in DMF was kept at 70 °C for spin-coating. 100 µL of PbI_2 solution was spin-coated at 6500 rpm for 30s, then dried at 100 °C for 30 minutes. A 5 minute dipping step in the MAI or mixed MAI/AzI in IPA solution (10 $mgml^{-1}$, AzI fractions in mol% with respect to MAI). The films were annealed at 100 °C for 1 hour.

The hole transport layer solution consisted of 85 $mgml^{-1}$ Spiro-OMeTAD (Ossila) in chlorobenzene, with additives of: 30 μLml^{-1} *t*-butyl pyridine (Sigma), 20 μLml^{-1} of 520 $mgmL^{-1}$ Li-TFSI in acetonitrile and 30 μgmL^{-1} FK209-TFSI solution. This was spin-coated onto the perovskite at 4000 rpm for 30 seconds.

To establish the contacts, 2 mm of perovskite was removed from the centre of the substrate. 100 nm of gold (Kurt J Lesker) was deposited by thermal evaporation.

4.6. SCXRD, PXRD

Crystal X-ray diffraction was performed on an Agilent Technologies EOS S2 Supernova, using a Cu X-ray source.

A Bruker axs D8 advance powder x-ray diffractometer with a Cu Kα source and Ge monochromator was used for Powder X-ray diffraction. Measurements were taken from 2θ values of 10 ° to 80 °.

4.7. UV/vis spectroscopy

Thin film optical Transmission and Reflectance measurements were performed on a Perkin-Elmer Lambda 750S UV/Vis spectrometer, from 1000 nm to 250 nm. Absorption was calculated as incident light– (transmission + reflectance).

4.8. Raman spectroscopy

Raman measurements were performed with a Renishaw in via Reflex microRaman spectrometer equipped with solid state lasers emitting at 514 and 785 nm with a resolution of $< 2\ cm^{-1}$. The laser beam was focused with a x50 magnification lens, giving a laser spot size of about 1 μm in diameter. Rayleigh scattering was rejected with a 110 cm−1 cutoff dielectric edge filter. The AzI sample was measured with a 514 nm laser and the orange AzPI with the 785 nm laser in order to avoid resonant effects in the sample. All measurements were performed in air and with different laser powers to ensure that the laser probe did not induce damage or changes in the sample

4.9. Electrochemical measurements

An Autolab potentiostat/galvanostat was used for solution based electrochemistry, using an Ag/AgCl reference electrode and a platinum counter electrode. 0.1 mol azetidinium iodide in isopropanol was used as the electrolyte. For Mott-Schottky measurements the frequency was 27 Hz and the voltage was swept stepwise from -0.1 to 0.75 V vs Ag/AgCl.

4.10. J-V curves

J-V curves were measured using a Keithley 2601A potentiostat, under 1 Sun intensity and at AM 1.5. The cell was sweeped at 100 mVs^{-1} from 1.1 V to -0.1 V and back to 1.1 V. The 8 pixels with a 0.1 cm^2 active area (obtained using a mask) were measured independently.

A Newport Oriel 91150-KG5 reference cell with a KG5 filter was used for instrument calibration.

EQE measurements were taken in 10 nm steps from 380-850 nm.

4.11. Scanning Electron Microscopy

SEM images were taken on a JEOL SEM 6480LV, at an acceleration voltage of 10kV.

4.12 Atomic Force Microscopy

AFM images were taken on a Nanosurf easyscan 2 FlexAFM system in dynamic mode using a force of 20 nN. A ContAl-G Tip was used for measurements.

Acknowledgements

We thank the University of Bath (studentship for SRP), EPSRC Centre for Doctoral Training in New and Sustainable Photovoltaics (studentship for PSK under Grant EP/LO1551X/1) EPSRC Centre for Doctoral Training in Sustainable Chemical Technologies (studentship for FEJ under Grant EP/L016354/1), the EPSRC (PRR under grant EP/K004956 and PJC under grant EP/H026304/1) and the European Union Seventh Framework Programme (RGN [FP7/2007–2013] (DESTINY project)) under grant agreement 316494.

References

[1] A. Kojima, K. Teshima, Y. Shirai and T. Miyasaka, *J. Am. Chem. Soc.*, 2009, **131**, 6050–6051.

[2] J. Burschka, N. Pellet, S.-J. Moon, R. Humphry-Baker, P. Gao, M. K. Nazeeruddin and M. Grätzel, *Nature*, 2013, **499**, 316–9.

[3] C. Roldan-Carmona, P. Gratia, I. Zimmermann, G. Grancini, P. Gao, M. Graetzel and M. K. Nazeeruddin, *Energy Environ. Sci.*, 2015, **8**, 3550–3556.

[4] M. Liu, M. B. Johnston and H. J. Snaith, *Nature*, 2013, **501**, 395–8.

[5] A. Walsh, *J. Phys. Chem. C*, 2015, **119**, 5755–5760.

[6] J. H. Noh, S. H. Im, J. H. Heo, T. N. Mandal and S. Il Seok, *Nano Lett.*, 2013, **13**, 1764–1769.

[7] M. Yang, Y. Zhou, Y. Zeng, C.-S. Jiang, N. P. Padture and K. Zhu, *Adv. Mater.*, 2015, **27**, 6363-6370.

[8] J. M. Frost, K. T. Butler, F. Brivio, C. H. Hendon, M. Van Schilfgaarde and A. Walsh, *Nano Lett.*, 2014, **14**, 2584–2590.

[9] H.-S. Kim, C.-R. Lee, J.-H. Im, K.-B. Lee, T. Moehl, A. Marchioro, S.-J. Moon, R. Humphry-Baker, J.-H. Yum, J. E. Moser, M. Grätzel and N.-G. Park, *Sci. Rep.*, 2012, **2**, 591.

[10] F. Meillaud, A. Shah, C. Droz, E. Vallat-Sauvain and C. Miazza, *Sol. Energy Mater. Sol. Cells*, 2006, **90**, 2952–2959.

[11] F. Hao, C. C. Stoumpos, D. H. Cao, R. P. H. Chang and M. G. Kanatzidis, *Nat. Photonics*, 2014, **8**, 489–494.

[12] D. B. Mitzi, in *Progress in Inorganic Chemistry*, 2007, pp. 1–121.

[13] A. Babayigit, D. Duy Thanh, A. Ethirajan, J. Manca, M. Muller, H.-G. Boyen and B. Conings, *Sci. Rep.*, 2016, **6**, 18721.

[14] G. E. Eperon, S. D. Stranks, C. Menelaou, M. B. Johnston, L. M. Herz and H. J. Snaith, *Energy Environ. Sci.*, 2014, **7**, 982.

[15] J.-W. Lee, D.-J. Seol, A.-N. Cho and N.-G. Park, *Adv. Mater.*, 2014, **6**, 1–8.

[16] G. E. Eperon, G. M. Paterno, R. J. Sutton, A. Zampetti, A. A. Haghighirad, F. Cacialli, H. J. Snaith, *J. Mater. Chem. A*, 2015, **3**, 19688–19695.

[17] R. G. Niemann, L. Gouda, J. Hu, S. Tirosh, R. Gottesman, P. J. Cameron and A. Zaban, *J. Mater. Chem. A*, 2016, **4**, 17819–17827.

[18] J. P. C. Baena, L. Steier, W. Tress, M. Saliba, S. Neutzner, T. Matsui, F. Giordano, T. J. Jacobsson, A. R. S. Kandada, S. M. Zakeeruddin, A. Petrozza, A. Abate, M. K. Nazeeruddin, M. Grätzel, A. Hagfeldt, *Energy Environ. Sci.*, 2015, **8**, 2928–2934.

[19] C. Yi, J. Luo, S. Meloni, A. Boziki, N. Ashari-Astani, C. Grätzel, S. M. Zakeeruddin, U. Rothlisberger and M. Grätzel, *Energy Environ. Sci.*, 2015, **9**, 656-662

[20] M. Saliba, T. Matsui, J.-Y. Seo, K. Domanski, J.-P. Correa-Baena, N. Mohammad K., S. M. Zakeeruddin, W. Tress, A. Abate, A. Hagfeldt and M. Grätzel, *Energy Environ. Sci.*, 2016, **9**, 1989-1997

[21] I. C. Smith, E. T. Hoke, D. Solis-Ibarra, M. D. McGehee and H. I. Karunadasa, *Angew. Chemie*, 2014, **126**, 11414–11417.

[22] N. De Marco, H. Zhou, Q. Chen, P. Sun, Z. Liu, L. Meng, E.-P. Yao, Y. Liu, A. Schiffer and Y. Yang, *Nano Lett.*, 2016, **16**, 1009–1016

[23] H. Tsai, W. Nie, J.-C. Blancon, C. C. Stoumpos, R. Asadpour, B. Harutyunyan, A. J. Neukirch, R. Verduzco, J. J. Crochet, S. Tretiak, L. Pedesseau, J. Even, M. A. Alam, G. Gupta, J. Lou, P. M. Ajayan, M. J. Bedzyk, M. G. Kanatzidis and A. D. Mohite, *Nature*, 2016, **536**, 312-316

[24] A. Amat, E. Mosconi, E. Ronca, C. Quarti, P. Umari, M. K. Nazeeruddin, M. Grätzel and F. De Angelis, *Nano Lett.*, 2014, **14**, 3608–3616.

[25] C. C. Stoumpos, C. D. Malliakas and M. G. Kanatzidis, *Inorg. Chem.*, 2013, **52**, 9019–9038.

[26] W. Travis, E. N. K. Glover, H. Bronstein, D. O. Scanlon and R. Palgrave, *Chem. Sci.*, 2016, **7**, 4548-4556

[27] G. Kieslich, S. Sun and A. K. Cheetham, *Chem. Sci.*, 2014, **5**, 4712–4715.

[28] G. Kieslich, S. Sun and A. K. Cheetham, *Chem. Sci.*, 2015, **6**, 3430–3433.

[29] J. Brgoch, A. J. Lehner, M. L. Chabinyc and R. Seshadri, *J. Phys. Chem. C*, 2014, **18**, 27721–27727.

[30] A. F. Akbulatov, L. A. Frolova, D. A. Anokhin, K. L. Gerasimov, N. N. Dremova and P. Troshin, *J. Mater. Chem. A*, 2016, Advance Article.

[31] W. Travis, E. N. K. Glover, H. Bronstein, D. O. Scanlon and R. Palgrave, *Chem. Sci.*, 2016 7, 4548-4556

[32] M. Becker, T. Kluner and M. Wark, *Dalt. Trans.*, 2017, **46**, 3500–3509.

[33] B. Zhou, Y. Imai, A. Kobayashi, Z.-M. Wang and H. Kobayashi, *Angew. Chemie Int. Ed.*, 2011, **50**, 11441–11445.

[34] I. C. Smith, E. T. Hoke, D. Solis-Ibarra, M. D. McGehee and H. I. Karunadasa, *Angew.*

Chemie, 2014, **126**, 11414–11417.

[35] H. Zheng, W. Wang, S. Yang, Y. Liu and J. Sun, *RSC Adv.*, 2016, **6**, 1611–1617.

[36] Dutler, R., Rauk, A., & Shaw, R. A. *J. Phys. Chem.*, 1990, *94*, 118–124

[37] T. M. Koh, K. Fu, Y. Fang, S. Chen, T. C. Sum, N. Mathews, S. G. Mhaisalkar, P. P. Boix and T. Baikie, *J. Phys. Chem. C*, 2014, **118**, 16458–16462

[38] N. Ahn, D.-Y. Son, I.-H. Jang, S. M. Kang, M. Choi and N.-G. Park, *J. Am. Chem. Soc.*, 2015, **137**, 8696–8699

[39] M. Valiev, E.J. Bylaska, N. Govind, K. Kowalski, T.P. Straatsma, H.J.J. Van Dam, D. Wang, J. Nieplocha, E. Apra, T.L. Windus, W.A. De Jong *Comput. Phys. Commun.* 2010, **181** (9), 1477–1489.

[40] J. Frost, K. Butler, F. Brivio, Atomistic Origins of High-Performance in Hybrid Halide Perovskite Solar Cells. *Nano Lett.* 2014, **14** (5), 2584–2590

[41] F. Zheng, H. Takenaka, F. Wang, N.Z. Koocher, A.M. Rappe *J. Phys. Chem. Lett.* 2015, **6** (23), 31–37.

Supporting Information

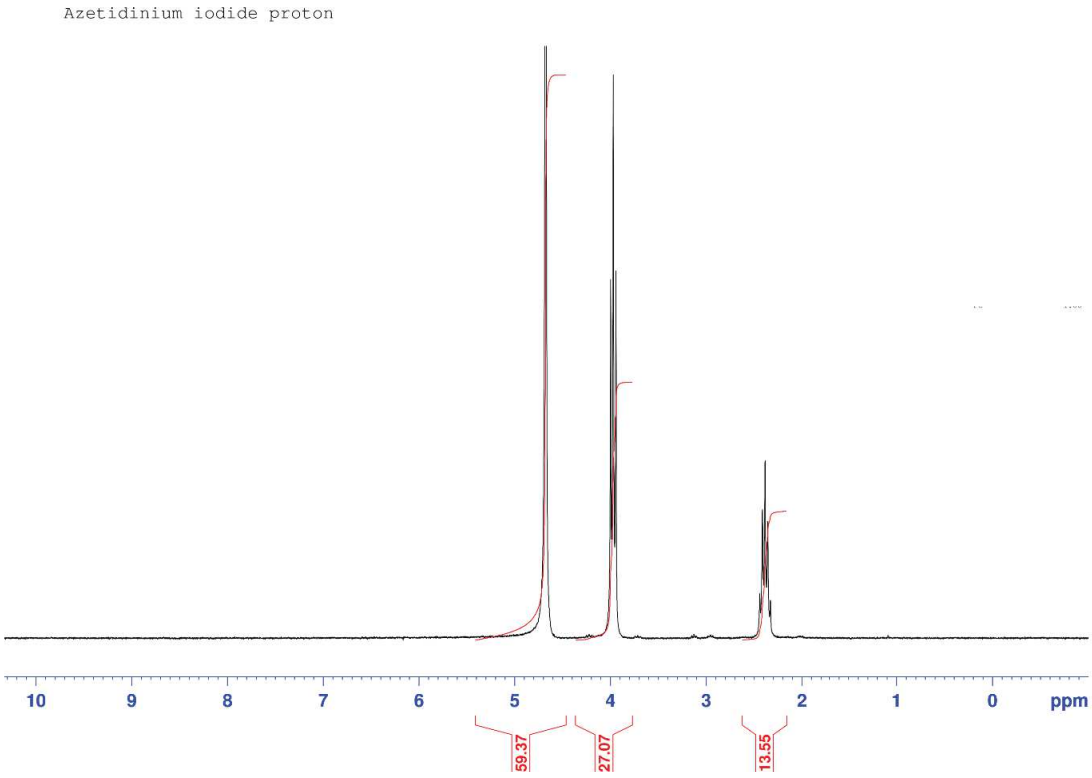

Figure S1: Azetidinium Iodide ^{1}H NMR Spectrum (Taken in D_2O on a 300 MHz Spectrometer)

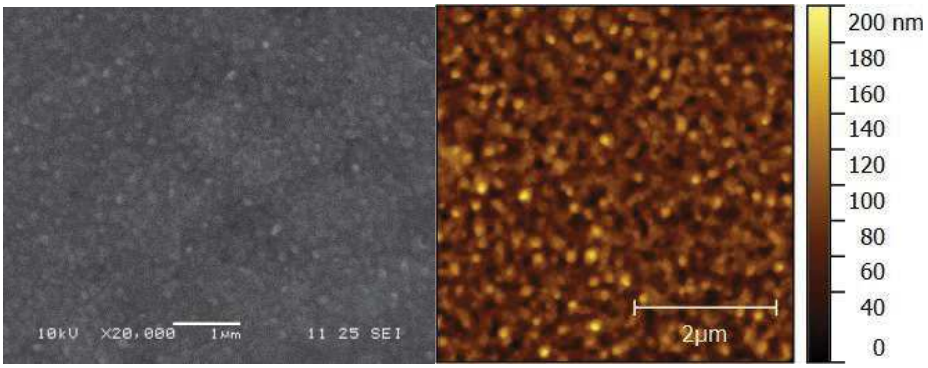

Figure S2: SEM image (left) and AFM image (right) of an AzPI film

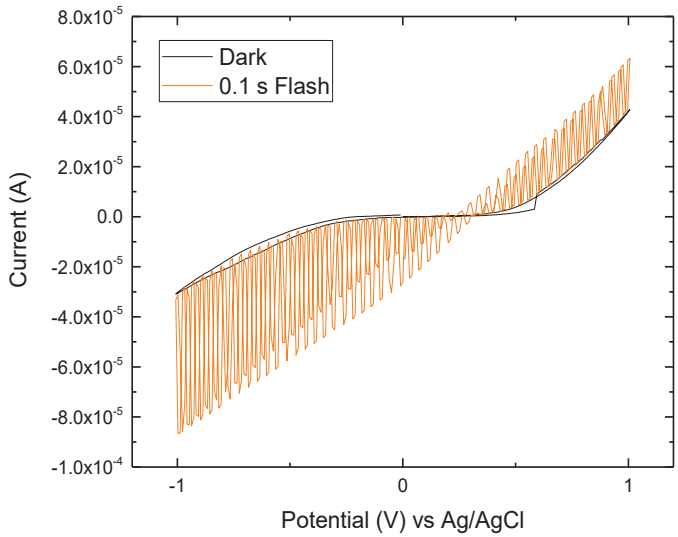

Figure S3: Chopped photocurrent measurement of AzPI on FTO, in 0.1 M AzI in IPA electrolyte, with Pt counter electrode and Ag/AgCl reference.

Table S1. Comparison of all measured Raman modes of $AzPbI_3$, AzI and Az with provisional peak assignment.

Az (DFT)	AzI	rel. shift	AzPI	Assignment	
361				ν_1	Ring pucker
			693	ν_2	N-H bend (in plane)
808	785	↓ 15	770	ν_3	Ring deform
	883	↓ 8	875	ν_4	2-CH_2 twist
	911	↓ 12	899	ν_5	2-CH_2 rock
961	956	↓ 5	951	ν_6	1-CH_2 rock
1009	1012	↓ 4	1008	ν_7	2-CH_2 rock
	1217			ν_8	1-CH_2 wag
1254	1245	↑ 7	1252	ν_9	1-CH_2 twist
1313	1283	↓ 6	1277	ν_{10}	2-CH_2 twist
1385	1302			ν_{11}	1-CH_2 twist
1452	1455			ν_{12}	1-CH_2 wag
1534	1511	↓ 61	1450	ν_{13}	NH_2 wag
1655	1582			ν_{14}	2-CH_2 scissor
2982	2980	↓ 8	2972	ν_{15}	1-C-H stretch
3020	3019			ν_{16}	2-C-H-stretch

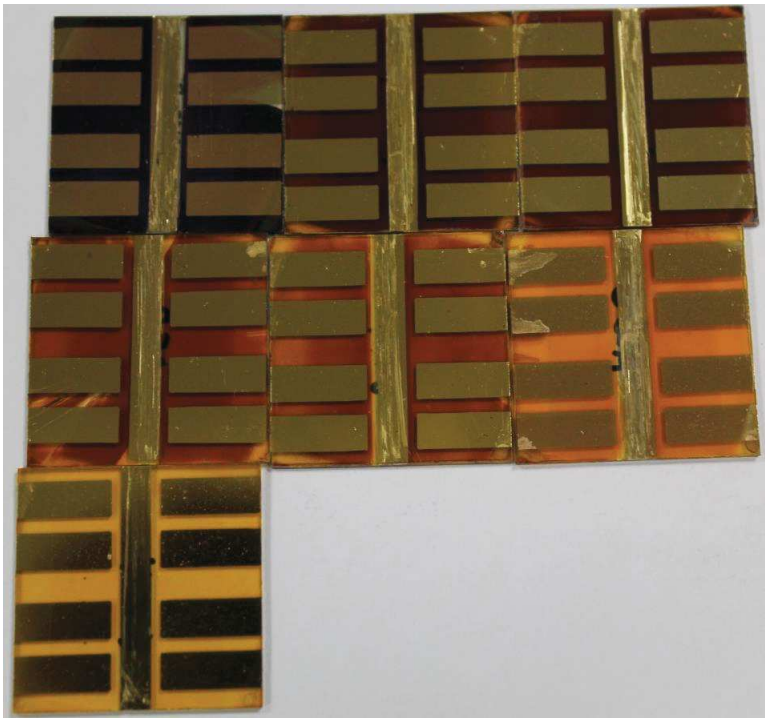

Fig. S4: A photograph of the MAPI/AzMAPI solar cell, from left to right: (top) MAPI, A1, A2 (middle) A5, A10, A25 (bottom), AzPI

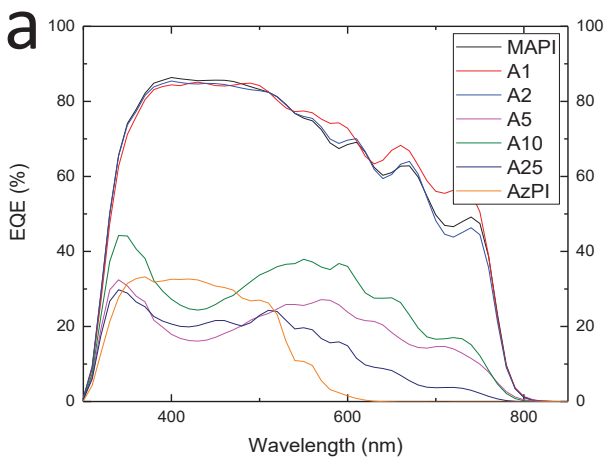

Fig. S5: (a) EQE measurements for the best performing pixels for each mixture of MAPI, AzMAPI or AzPI and

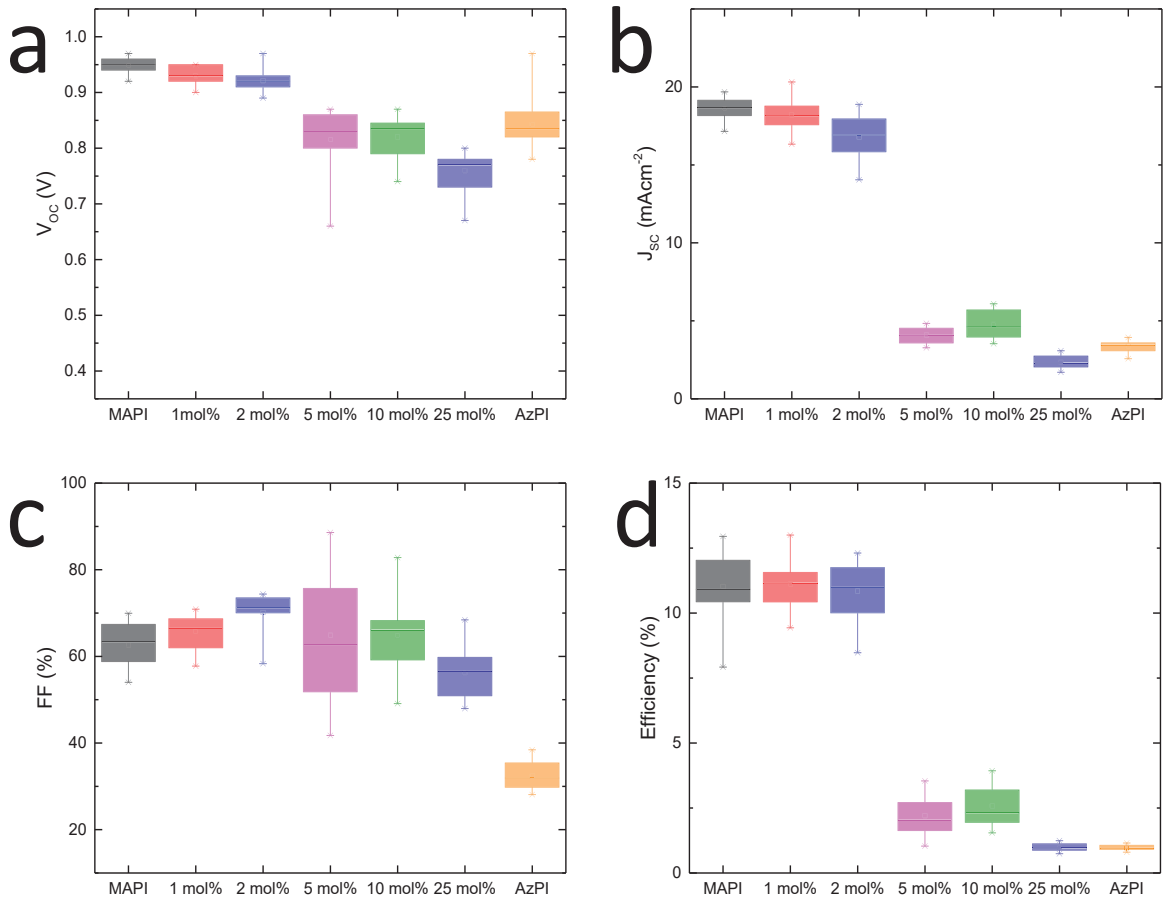

Fig. S6 Box plots for the cell parameters of AzMAPI cells: (a) V_{OC} (b) J_{SC} (c) Fill Factor and (d) Efficiency

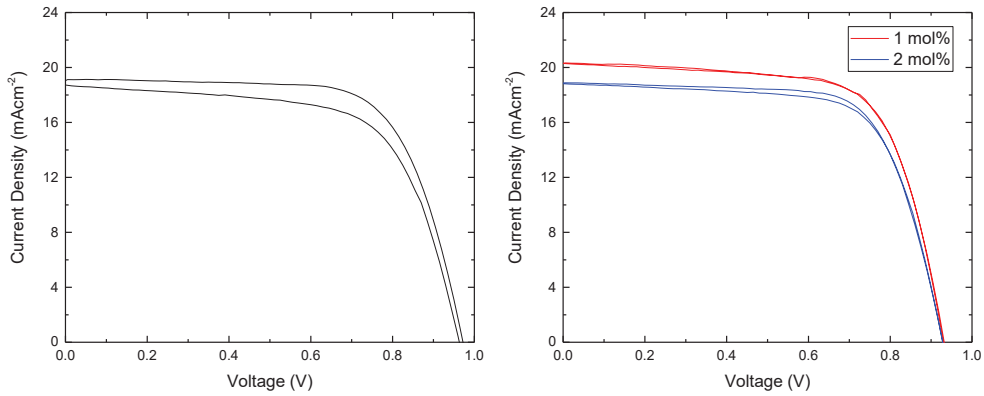

Figure S7. A comparison of the hysteresis in the JV curves for MAPI cells (left) and those with azetidinium additives

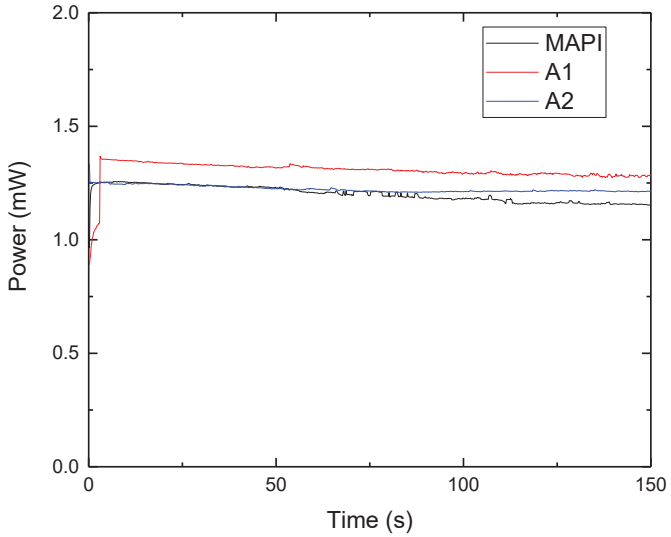

Figure S8. Stabilised power output measurements for the best performing AzMAPI and MAPI pixels

4.2.2.2 Contemporary assessment

Due to the recent submission of this publication (January 2017) an evaluation of the impact on other literature is not possible at this stage.

4.3 Conclusions

The work in this chapter was designated to expand the compositional space of the $MAPbI_3$ perovskite, regarding an improvement of the materials stability through a partial or complete replacement of the MA^+ cation with Cs^+ or Az^+. Our results can be described twofold, because they redefine the boundaries of a known perovskite system ($Cs_xMA_{1-x}PbI_3$), and also widen the compositional space by introducing a new constituent (Az^+ cation).

We showed that for the case of the Cs^+ most cation mixtures are not obtainable. This is caused by a substitution limit for $x > 0.13 \pm 0.03$, that has not been reported in literature so far. Nevertheless, we showed that for mixtures that form a solid state solution ($x < 0.13$), the Cs-incorporation has a beneficial effect on device stability. By redefining the boundaries of the $Cs_xMA_{1-x}PbI_3$ system, we were able point out the reason for the apparent under-representation of this perovskite system in literature and give important guidelines for the further design of novel perovskite mixtures with multiple cation constituents. An extended structural analysis is given in this thesis and indicates that the incorporation of Cs^+ induces strain on the perovskite lattice that could lead to the miscibility limit. OCVD results indicate that the inclusion of the Cs^+ cation causes a decrease of defects in the perovskite lattice.

The formulation of a new $APbI_3$ compound with the Az-cation resulted in the formation of an orange (presumably non-perovskite) phase on its own. However, an inclusion of small amounts into the $MAPbI_3$ perovskite structure to form a solid-state solution was shown to be feasible; this however comes along with similar limitations as in the Cs-MA system, as shown by peak separation in XRD at about $x = 0.05$. A spectroscopic analysis of this compound was done regarding bonding motives and gave indications of strong bonding effects with the inorganic scaffold that could play a decisive role for the instability of the $AzPbI_3$ perovskite phase.

Current research seems to spark interest in perovskites with multiple cation systems (mainly MA^+, FA^+, Cs^+), which can be dual, triple or even quadruple,[43, 44, 21, 45] and supposedly cause an entropic stabilisation of the system. The research presented in this study gives important guidelines and offers new possibilities for the further design of improved cation mixtures.

4.4 Bibliography

[1] A. Kojima, K. Teshima, Y. Shirai, and T. Miyasaka, "Organometal halide perovskites as visible-light sensitizers for photovoltaic cells.," *Journal of the American Chemical Society*, vol. 131, pp. 6050–6051, may 2009.

[2] NREL, "Research Cell Efficiency Records." http://www.nrel.gov/ncpv/ [Online; accessed: 17-December-2016], 2016.

[3] N. Ahn, D.-Y. Son, I.-H. Jang, S. M. Kang, M. Choi, and N.-G. Park, "Highly Reproducible Perovskite Solar Cells with Average Efficiency of 18.3% and Best Efficiency of 19.7% Fabricated via Lewis Base Adduct of Lead(II) Iodide," *Journal of the American Chemical Society*, vol. 137, no. 27, pp. 8696–8699, 2015.

[4] J. Seo, J. H. Noh, and S. I. Seok, "Rational Strategies for Efficient Perovskite Solar Cells," *Accounts of Chemical Research*, vol. 49, no. 3, pp. 562–572, 2016.

[5] L. Gouda, R. Gottesman, S. Tirosh, E. Haltzi, J. Hu, A. Ginsburg, D. A. Keller, Y. Bouhadana, and A. Zaban, "Vapor and Healing Treatment for CH3NH3PbI3-xClx Films toward Large-Area Perovskite Solar cells," *Nanoscale*, vol. 8, pp. 6386–6392, 2016.

[6] G. Nedelcu, L. Protesescu, S. Yakunin, M. I. Bodnarchuk, M. J. Grotevent, and M. V. Kovalenko, "Fast Anion-Exchange in Highly Luminescent Nanocrystals of Cesium Lead Halide Perovskites (CsPbX3, X = Cl, Br, I)," *Nano Letters*, vol. 15, no. 8, pp. 5635–5640, 2015.

[7] G. E. Eperon, C. E. Beck, and H. J. Snaith, "Cation exchange for thin film lead iodide perovskite interconversion," *Materials Horizons*, vol. 3, pp. 63–71, 2016.

[8] S. Ruhle, H. N. Barad, Y. Bouhadana, D. Keller, A. Ginsburg, K. Shimanovich, K. Majhi, R. Lovrincic, Y. Anderson, and A. Zaban, "Combinatorial solar cell libraries for the investigation of different metal back contacts for TiO2-Cu2O hetero-junction solar cells.," *Physical Chemistry Chemical Physics*, vol. 16, no. 15, pp. 7066–7073, 2014.

[9] A. Y. Anderson, Y. Bouhadana, H. N. Barad, B. Kupfer, E. Rosh-Hodesh, H. Aviv, Y. R. Tischler, S. Ruhle, and A. Zaban, "Quantum efficiency and bandgap analysis for combinatorial photovoltaics: Sorting activity of Cu-O compounds in all-oxide device libraries," *ACS Combinatorial Science*, vol. 16, no. 2, pp. 53–65, 2014.

[10] M. Wojdyr, "Fityk: A general-purpose peak fitting program," *Journal of Applied Crystallography*, vol. 43, no. 5, pp. 1126–1128, 2010.

[11] C. C. Stoumpos, C. D. Malliakas, and M. G. Kanatzidis, "Semiconducting tin and lead iodide perovskites with organic cations: phase transitions, high mobilities, and near-infrared photoluminescent properties.," *Inorganic Chemistry*, vol. 52, no. 15, pp. 9019–9038, 2013.

[12] J. H. Noh, S. H. Im, J. H. Heo, T. N. Mandal, and S. I. Seok, "Chemical management for colorful, efficient, and stable inorganic-organic hybrid nanostructured solar cells.," *Nano Letters*, vol. 13, no. 4, pp. 1764–1769, 2013.

[13] A. Amat, E. Mosconi, E. Ronca, C. Quarti, P. Umari, M. K. Nazeeruddin, M. Grätzel, and F. De Angelis, "Cation-induced band-gap tuning in organohalide perovskites: Interplay of spin-orbit coupling and octahedra tilting," *Nano Letters*, vol. 14, no. 6, pp. 3608–3616, 2014.

[14] G. Kieslich, S. Sun, and A. K. Cheetham, "Solid-state principles applied to organic-inorganic perovskites: new tricks for an old dog," *Chemical Science*, vol. 5, pp. 4712–4715, 2014.

[15] G. Kieslich, S. Sun, and T. Cheetham, "An Extended Tolerance Factor Approach for Organic-Inorganic Perovskites," *Chemical Science*, vol. 6, pp. 3430–3433, 2015.

[16] G. E. Eperon, G. M. Paterno, R. J. Sutton, A. Zampetti, A. A. Haghighirad, F. Cacialli, and H. J. Snaith, "Inorganic caesium lead iodide perovskite solar cells," *Journal of Materials Chemistry A*, vol. 3, pp. 19688–19695, 2014.

[17] G. E. Eperon, S. D. Stranks, C. Menelaou, M. B. Johnston, L. M. Herz, and H. J. Snaith, "Formamidinium lead trihalide: a broadly tunable perovskite for efficient planar heterojunction solar cells," *Energy & Environmental Science*, vol. 7, pp. 982–988, 2014.

[18] M. T. Weller, O. J. Weber, J. M. Frost, and A. Walsh, "The Cubic Perovskite Structure of Black Formamidinium Lead Iodide, a-[HC(NH2)2]PbI3, at 298 K," *Journal of Physical Chemistry Letters*, vol. 6, pp. 3209–3212, 2015.

[19] Z. Zhou, S. Pang, F. Ji, B. Zhang, and G. Cui, "Fabrication of formamidinium lead iodide perovskite thin films via organic cation exchange," *Chemical Communications*, vol. 52, pp. 3828–3831, 2016.

[20] L. A. Frolova, D. V. Anokhin, A. A. Piryazev, S. Y. Luchkin, N. N. Dremova, K. J. Stevenson, and P. A. Troshin, "Highly Efficient All-Inorganic Planar Heterojunction Perovskite Solar Cells Produced by Thermal Coevaporation of CsI and PbI2," *The Journal of Physical Chemistry Letters*, vol. 8, pp. 67–72, 2016.

[21] M. Saliba, T. Matsui, J.-Y. Seo, K. Domanski, J.-P. Correa-Baena, N. Mohammad K., S. M. Zakeeruddin, W. Tress, A. Abate, A. Hagfeldt, and M. Grätzel, "Cesium-containing Triple Cation Perovskite Solar Cells: Improved Stability, Reproducibility and High Efficiency," *Energy & Environmental Science*, vol. 9, pp. 1989–1997, 2016.

[22] F. Brivio, C. Caetano, and A. Walsh, "Thermodynamic Origin of Photoinstability in The CH3NH3Pb(I1-xBrx)3 Hybrid Halide Perovskite Alloy," *The Journal of Physical Chemistry Letters*, vol. 7, pp. 1083–1087, 2016.

[23] A. Walsh, "Principles of Chemical Bonding and Band Gap Engineering in Hybrid Organic-Inorganic Halide Perovskites," *Journal of Physical Chemistry C*, vol. 119, pp. 5755–5760, 2015.

[24] R. G. Niemann, A. G. Kontos, D. Palles, E. I. Kamitsos, A. Kaltzoglou, F. Brivio, P. Falaras, and P. J. Cameron, "Halogen Effects on Ordering and Bonding of CH3NH3+ in CH3NH3PbX3 (X = Cl, Br, I) Hybrid Perovskites: A vibrational spectroscopic study," *The Journal of Physical Chemistry C*, vol. 120, no. 5, pp. 2509–2519, 2016.

[25] W. Rehman, D. McMeekin, J. Patel, R. Milot, M. B. Johnston, H. Snaith, and L. M. Herz, "Photovoltaic mixed-cation lead mixed-halide perovskites: Links between crystallinity, photo-stability and electronic properties," *Energy Environ. Sci.*, vol. 10, pp. 361–369, 2017.

[26] A. Pockett, G. Eperon, N. Sakai, H. Snaith, L. M. Peter, and P. J. Cameron, "Microseconds, milliseconds and seconds: deconvoluting the dynamic behaviour of planar perovskite solar cells," *Phys. Chem. Chem. Phys.*, vol. 19, pp. 5959 – 5970, 2017.

[27] S. D. Stranks, V. M. Burlakov, T. Leijtens, J. M. Ball, A. Goriely, and H. J. Snaith, "Recombination Kinetics in Organic-Inorganic Perovskites: Excitons, Free Charge, and Subgap States," *Physical Review Applied*, vol. 2, no. 3, p. 034007, 2014.

[28] Y. Yamada, T. Nakamura, M. Endo, A. Wakamiya, and Y. Kanemitsu, "Photocarrier Recombination Dynamics in Photocarrier Recombination Dynamics in Perovskite CH3NH3PbI3 for Solar Cell Applications," *Journal of American Chemical Society*, vol. 136, pp. 11610–11613, 2014.

[29] a. Baumann, K. Tvingstedt, M. C. Heiber, S. Väth, C. Momblona, H. J. Bolink, and V. Dyakonov, "Persistent photovoltage in methylammonium lead iodide perovskite solar cells," *APL Materials*, vol. 2, no. 8, p. 081501, 2014.

[30] L. Bertoluzzi, R. S. Sanchez, L. Liu, J.-W. Lee, E. Mas-Marza, H. Han, N.-G. Park, I. Mora-Sero, and J. Bisquert, "Cooperative kinetics of depolarization in CH3NH3PbI3 perovskite solar cells," *Energy & Environmental Science*, vol. 8, pp. 910–915, 2015.

[31] G. Richardson, S. E. J. O'Kane, R. G. Niemann, T. A. Peltola, J. M. Foster, P. J. Cameron, and A. B.Walker, "Can slow-moving ions explain hysteresis in the current-voltage curves of perovskite solar cells?," *Energy & Environmental Science*, vol. 9, pp. 1476–1485, 2016.

[32] A. Zaban, M. Greenshtein, and J. Bisquert, "Determination of the Electron Lifetime in Nanocrystalline Dye Solar Cells by Open-Circuit Voltage Decay Measurements," *ChemPhysChem*, vol. 4, pp. 859–864, 2003.

[33] E. Mosconi and F. De Angelis, "Mobile Ions in Organohalide Perovskites: Interplay of Electronic Structure and Dynamics," *ACS Energy Letters*, vol. 1, no. 1, pp. 182–188, 2016.

[34] G. Niu, H. Yu, J. Li, D. Wang, and L. Wang, "Controlled orientation of perovskite films through mixed cations toward high performance perovskite solar cells," *Nano Energy*, vol. 27, pp. 87–94, 2016.

[35] D. Dong, H. Deng, C. Hu, H. Song, K. Qiao, X. Yang, J. Zhang, F. Cai, J. Tang, and H. Song, "Bandgap tunable Csx(CH3NH3)1-xPbI3 perovskite nanowires by aqueous solution synthesis for optoelectronic devices," *Nanoscale*, vol. 9, pp. 1567–1574, 2017.

[36] T. Zhang, M. Long, K. Yan, X. Zeng, F. Zhou, Z. Chen, X. Wan, K. Chen, P. Liu, F. Li, T. Yu, W. Xie, and J. Xu, "Facet-Dependent Property of Sequentially Deposited Perovskite Thin Films: Chemical Origin and Self-Annihilation," *ACS Applied Materials and Interfaces*, vol. 8, no. 47, pp. 32366–32375, 2016.

[37] Z. Chen, C. X. Kronawitter, and B. E. Koel, "Facet-dependent activity and stability of Co3O4 nanocrystals towards the oxygen evolution reaction," *Physical Chemistry Chemical Physics*, vol. 17, no. 43, pp. 29387–29393, 2015.

[38] A. F. Akbulatov, L. A. Frolova, D. A. Anokhin, K. L. Gerasimov, N. N. Dremova, and P. Troshin, "Hydrazinium-loaded perovskite solar cells with the enhanced performance and stability," *Journal of Materials Chemistry A*, vol. 4, pp. 18378–18382, 2016.

[39] X. Hou, Y. Hu, H. Liu, A. Mei, X. Li, M. Duan, G. Zhang, Y. Rong, and H. Han, "Effect of guanidinium on mesoscopic perovskite solar cells," *Journal of Materials Chemistry A*, vol. 5, pp. 73–78, 2017.

[40] W. Li, Z. Zhang, E. G. Bithell, A. S. Batsanov, P. T. Barton, P. J. Saines, P. Jain, C. J. Howard, M. A. Carpenter, and A. K. Cheetham, "Ferroelasticity in a metal-organic framework perovskite; Towards a new class of multiferroics," *Acta Materialia*, vol. 61, no. 13, pp. 4928–4938, 2013.

[41] M. Maczka, T. A. da Silva, W. Paraguassu, M. Ptak, and K. Hermanowicz, "Raman and IR Studies of Pressure-and Temperature-Induced Phase Transitions in [(CH2)3NH2][Zn(HCOO)3]," *Inorganic chemistry*, vol. 53, no. 23, pp. 12650–12657, 2014.

[42] T. Asaji, Y. Ito, J. Seliger, V. Žagar, A. Gradišek, and T. Apih, "Phase Transition and Ring-Puckering Motion in a Metal-Organic Perovskite [(CH2)3NH2][Zn(HCOO)3]," *The Journal of Physical Chemistry A*, vol. 116, no. 51, pp. 12422–12428, 2012.

[43] W. S. Yang, J. H. Noh, N. J. Jeon, Y. C. Kim, S. Ryu, J. Seo, and S. I. Seok, "High-performance photovoltaic perovskite layers fabricated through intramolecular exchange," *Science*, vol. 348, pp. 1234–1237, may 2015.

[44] M. Deepa, M. Salado, L. Caliob, S. Kazimb, S. M. Shivaprasadc, and S. Ahmad, "Cesium Power: Low Cs+ Levels Impart Stability to Perovskite Solar Cells," *Physical Chemistry Chemical Physics*, vol. 19, pp. 4069–4077, 2017.

[45] M. Saliba, T. Matsui, K. Domanski, J.-Y. Seo, A. Ummadisingu, S. M. Zakeeruddin, J.-P. Correa-Baena, W. R. Tress, A. Abate, A. Hagfeldt, and M. Grätzel, "Incorporation of rubidium cations into perovskite solar cells improves photovoltaic performance," *Science*, vol. 354, no. 6309, pp. 206–209, 2016.

Chapter 5

Spectroscopic analysis of structural dynamics

The interface is the device

Herbert Kroemer
Nobel Lecture, 2000 [1]

When Nobel laureate Herbert Kroemer coined the phrase *'The interface is the device'*, he was referring to heterogeneous semiconductor structures that give rise to astonishing properties on an increasingly smaller scale.[1] This statement still holds to be true nowadays; and electronic devices are continuously shrinking in size, which gives the interface dominance over the response of the whole system. Silicon is one of the cornerstones in the development of electronics and still forms the basis for most photovoltaic devices. New materials with higher molar absorption coefficients allow for even thinner devices and inorganic-organic perovskites form a good example of a high-performing semiconductor that could compete with silicon. Besides its decreased device thickness, other intriguing properties of PSC make it a fascinating subject of research. The movement of ion vacancies across the device and the resulting formation of Debye layers at the interface is only one example. Rotation of cations with a dipole moment that makes the whole device behave like a plastic crystal were suggested to give rise to a splitting of energy levels, hence suppressing recombination.[2] These structural dynamics are essential for a further understanding of this material. First of all they are key to understand many of the materials fundamental properties. Secondly, in order to achieve the ultimate goal of maximising the device performance, it is essential to interpret these nanoscopic phenomena to macroscopic processing parameters that eventually influence the performance (as described in chapter 3). This can only be

achieved with a fundamental and detailed knowledge of the underlying mechanisms that cause these phenomena. Many recent reports on structural dynamics suffer from measurement-induced changes, as described in the next paragraph. Appropriate and reliable tools are needed to overcome these limitations and fully evaluate the dynamics of HOIPs.

Structural dynamics can be dealt with using a bottom-up approach that simulates electronic properties with methods like DFT and from there on predicts material properties (*e.g.* energetic landscapes and vibrational dynamics). There are several DFT studies, most of them based on the *Vienna Ab Intio Simulation Package VASP* or *Quantum Espresso*.[3, 4, 5, 6, 7, 8] Despite their elegance in simulating properties from first principle, their downside is that small energetic offsets are relatively normal during their convergence which can result in large offsets in the simulation output. An offset of *e.g.* 10 meV is small for a DFT convergence but makes a significant difference in a vibronic spectrum (shifts a vibrational spectrum by 81 cm^{-1}). Therefore a peak assignment based solely on first-principle calculations can be ambiguous.[9] Secondly, a top-down approach can be used to predict structural properties from a measured spectrum. However, a measurement of the 'true spectrum' is difficult for hybrid inorganic-organic perovskites. Several effects make the spectrum acquisition ambiguous and need to be considered when interpreting the spectrum, *e.g.* phase-segregation,[10, 11] structural changes,[12] as well as optical changes,[13, 14] which can even be photo-induced during the measurement. Perovskites are more challenging as an intrinsic instability of the material makes it difficult to measure the material without causing degradation with the measurement laser.[15, 16, 17] This caused a variety of reported spectra for $MAPbI_3$, as laid out in chapter 1 (*e.g.* see fig. 1-4b). For the acquisition of a 'true' spectrum, it is necessary to consider these effects and take appropriate measure to avoid ambiguities.

The approach given in this work for the acquisition of a vibrational spectrum of the $MAPbI_3$ perovskite is to take a step back and not solely focus on a single aspect but rather see the material in the context of various parameters. This way, the true spectroscopic response can be differentiated from measurement artefacts. It also serves to better understand structural trends in the dynamic response of the system regarding these parameters: The influence of halide derivatives (Cl, Br, I) was studied at different excitation frequencies and temperatures *via* far-IR and Raman spectroscopy.

5.1 Experimental methods

The substrate cleaning was done in the same way as described in chapter 3. The synthesis of the methylammonium halide salts (MAI, MABr and MACl) was done by

neutralising methylamine with the corresponding hydrogen-halide. Details of the process can be found in the appendix.

For the spectroscopic study described in this chapter, we prepared a range of stoichiometric (1:1 ratio of lead(II) halide to methylammonium halide) single halide perovskite precursor solutions $MAPbI_3$, $MAPbBr_3$ and $MAPbCl_3$ at a 1 mol/L in DMSO. This is different from the 3:1 stoichiometry with chloride inclusion used in the last chapter. The mixed halide perovskite precursor solutions were prepared by mixing the respective ratios of single halide solutions and stirring the solutions for 1 h. Synthesis of the precursors was done in the fume hood, while the mixing, deposition and annealing of the perovskite precursor solutions was done in an argon-filled glovebox. For planar films the precursor solution was deposited on a microscopy glass slide. For meso-porous films a dispersion of Al_2O_3 nanoparticles was spin-coated onto glass slides (2000 rpm for 60 s) and annealed at 500 °C for 30 min. All solutions were spin-coated onto the flat or meso-structured substrates at 2000 rpm for 60 s and then annealed on a hotplate at 100 °C for 30 min.

Structural characterisation was performed on a Siemens D-500 diffractometer in Bragg-Brentano geometry with Cu $K_{\alpha 1}$ radiation ($\lambda = 1.5406$ Å) and Cu $K_{\alpha 2}$ radiation ($\lambda = 1.5444$ Å). Unit-cell refinements were performed with the GSAS package[18]. UV-Vis diffuse reflectance (R) spectra were acquired on a Hitachi 3010 spectrophotometer using an integrating sphere with 60 mm diameter and $BaSO_4$ as a reference. Far-IR spectra were collected in transmission mode at normal incidence on a Bruker Vertex 80v vacuum spectrometer. Raman measurements were performed with a Renishaw in *via* Reflex micro-Raman spectrometer equipped with solid-state lasers emitting at 514 and 785 nm Measurements were performed at different laser powers to assure the intensities used did not induce changes in the spectrum. Off-resonance Raman spectra were acquired with a Bruker RFS100 FT-Raman spectrometer probing with a Nd:YAG laser emitting at 1064 nm. Each spectrum was averaged over 100 scans or 200 scans with 4 cm^{-1} resolution. All FT Raman measurements were performed in air and at different laser powers to ensure that the intensities used did not induce changes in the spectral response. The spectra were analysed by fitting a mixed Lorenzian-Gaussian functions using the Wire software from Renishaw. Line widths were corrected for instrumental broadening.

5.2 Results and discussion

5.2.1 Structural influence of halide derivatives

Recent spectroscopic studies (in particular Raman studies) were specifically focusing on the $MAPbI_3$ and mostly the low-frequency region. This is useful because this region holds valuable information regarding the inorganic dynamics of the structure, while higher frequency modes are attributed to internal MA^+ modes. However, the just mentioned ambiguities often blurred a clear interpretation of this system. Therefore, our approach reported in this chapter, takes a step back to see the $MAPbI_3$ within its context while varying several parameters and thereby facilitating the assignment of spectroscopic features. Those parameters are two-fold: Firstly, the compounds were measured within their compositional range of halide derivatives. The reason is that the data acquisition for most of the $MAPbI_3$ halide derivatives is comparably easy and we expected many trends to change continuously, because Cl, Br, I show a continuous trend regarding size and electro negativity. Secondly, different excitation sources were employed; in order to exclude light-induced effects, the perovskite system was measured with 515, 785 and 1064 nm Raman lasers, therefore exciting in resonance as well as off-resonance conditions and circumventing the above-mentioned problems. Also a comparison to a far-IR spectra was done for the low-frequency Pb-X inorganic modes. Finally, measurements were taken between 100 K and RT to measure different phases of the perovskite system. The assignment of modes within the trends dictated by the parameters given above allowed for a sophisticated assignment of modes. In fact, our study is the first report that makes use of an off-resonance excitation and can be seen as the first unambiguous report of the 'true' $MAPbI_3$ Raman spectrum. The results allowed for an evaluation of bonding and ordering of the MA^+ within the PbX cage.

5.2.2 Related publications

RGN contributed to this study in several ways. This includes the synthesis of all $MAPbX_3$ materials (including MAX precursors) as well as their spectroscopic measurement (UV-Vis, far-IR, Raman on all instruments); composing of the manuscript, including graphs, was also done by RGN.

THE JOURNAL OF PHYSICAL CHEMISTRY C

Article

pubs.acs.org/JPCC

Halogen Effects on Ordering and Bonding of $CH_3NH_3^+$ in $CH_3NH_3PbX_3$ (X = Cl, Br, I) Hybrid Perovskites: A Vibrational Spectroscopic Study

Ralf G. Niemann,[†,⊥] Athanassios G. Kontos,[*,‡,⊥] Dimitrios Palles,[§] Efstratios I. Kamitsos,[§] Andreas Kaltzoglou,[‡] Federico Brivio,[†] Polycarpos Falaras,[‡] and Petra J. Cameron[†]

[†]Department of Chemistry, University of Bath, Bath BA2 7AY, United Kingdom

[‡]Institute of Nanoscience and Nanotechnology, NCSR Demokritos, 15310 Athens, Greece

[§]Theoretical and Physical Chemistry Institute, National Hellenic Research Foundation, 11635 Athens, Greece

Supporting Information

ABSTRACT: This study reports Raman and infrared spectra of hybrid organic−inorganic $MAPbX_3$ perovskites (MA = CH_3NH_3, X = Cl, Br, I) and their mixed-halide derivatives. Raman spectra were recorded at three laser wavelengths (514, 785, and 1064 nm) under on- and off-resonance conditions, as well as at room temperature and 100 K. The use of different excitation wavelengths allowed the unambiguous acquisition of "true" Raman spectra from the perovskites, without degradation or photoinduced structural changes. Low-frequency PbX vibrational modes were thoroughly identified by comparison of Raman and far-IR results. Red Raman frequency shifts for almost all MA vibrations from 200 to 3200 cm^{-1}, and particularly intense for the torsional mode, were observed toward heavy halide derivatives, indicative of strengthening the interaction between halides and the organic cation inside the inorganic cage. Different MA−X bonding schemes are evidenced by torsional mode pairs emerging in the orthorhombic phase. $MAPbBr_3$ was further characterized by variable temperature Raman measurements (100−295 K). Broadening of the MA rocking mode slightly above the tetragonal I to II phase transition is connected with disorder of the MA cation. Our results advance the understanding of perovksite materials properties (ferroelectric domain formation, anomalous hysteresis) and their use as efficient light absorbers in solar cells.

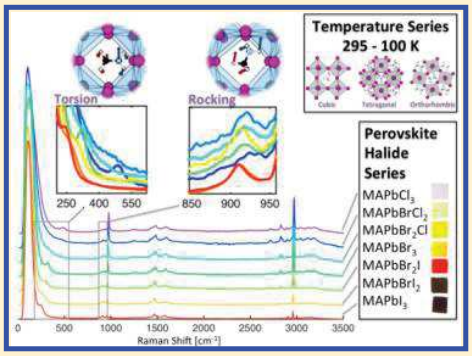

1. INTRODUCTION

Recently, there has been an increase in research on perovskite materials[1−6] leading to a steep rise in cell performances to a certified value of 21%[7] within a few years. Similar developments took decades for other photovoltaic technologies to achieve. Even though perovskites are a large family of compounds which all share the common stoichiometry ABX_3, most of the recent attention has been given to the hybrid organic−inorganic methylammonium lead halide perovskites ($MAPbX_3$, MA = methylammonium, Pb = lead, X = halide) and in particular the iodide derivative $MAPbI_3$. Structure and band gap in ABX_3 perovskites can be easily modified by changing the cation, the metal, or the halide. Partial substitution of the iodide in $MAPbI_3$ results in the isostructural $MAPbI_{3-x}Br_x$ with a blue-shifted band gap, which is favorable for multijunction devices and increases chemical stability.[8−11] However, the photo-instability of the excited state of $MAPbI_{3-x}Br_x$ results in segregation of the material into microdomains for $x > 0.6$.[12] Addition of chloride during perovskite crystallization has been shown to improve charge transport[13,14] even though its exact role remains unclear.[15,16] Besides the influences of chemical composition on optoelectronic performance and stability, temperature-dependent structural changes play a pivotal role as well. The low-temperature orthorhombic phase of $MAPbI_3$ is thermodynamically more stable compared to the tetragonal phase obtained at room temperature[10] and charge-carrier dynamics become more confined and show excitonic behavior in the orthorhombic phase.[17] This indicates that temperature-induced structural changes can tip the scales from an exothermic toward endothermic dissociation enthalpy and from free charge-carrier movement to excitonic confinement. Thus, tuning of the perovskite composition or structure can be used in order to enhance stability and performance of perovskite solar cells, both of which are investigated in this study.

X-ray diffraction has been widely used to determine the crystal structure of $MAPbX_3$ perovskite materials since their discovery in 1978.[18,19] However, it can be difficult to resolve the positions of lighter atoms like nitrogen and carbon in the presence of the heavier lead and iodine. The structural orientation of the MA cation within the inorganic framework has therefore been studied in more detail with NMR spectroscopy[20] and neutron scattering.[21,22] These studies were able to resolve the orientation of MA cations and show

Received: November 17, 2015
Revised: January 4, 2016
Published: January 7, 2016

DOI: 10.1021/acs.jpcc.5b11256
J. Phys. Chem. C 2016, 120, 2509−2519

an increasing disorder when moving from the orthorhombic phase toward higher temperature phases alongside a weakening of the bonding between the NH_3 in the MA and the halides.[21,22] Alignment of the MA cations can yield a net dipole that is energetically favorable in the tetragonal phase and is further stabilized in the orthorhombic perovskite phase. It has been suggested that this MA alignment can induce polar-ferroelectric characteristics in the material in low-symmetry phases.[23] Structural dynamics within the perovskite structure have important implications on the operation mechanism of perovskite solar cells. They are thought to assist charge separation,[24] tune the band gap,[25,26] improve open-circuit voltage,[27] and affect hysteresis during current−voltage measurements.[28] These versatile implications show the importance of a detailed study of MA dynamics with Raman and IR spectroscopies.

Perovskite halides have been examined before with mid-IR absorption experiments[29−32] which give valuable information about MA dynamics, hydrogen bonding, and water infiltration inside the perovskites, but they do not cover the important low-frequency range where vibrations of the inorganic lead halide network of corner sharing PbX_6 octahedra are mainly active. Despite the suitability of the infrared absorption technique for obtaining the vibrational modes in light sensitive systems, only limited far-IR data for single halide perovskite compounds have been reported up to now.[33,34] Besides, reports of Raman measurements on $MAPbI_3$ perovskites[23,35−40] have so far been limited to resonant or near resonant conditions with typical excitation wavelengths of 514, 532, or 785 nm. However, this may be problematic because of the high absorbance and photosensitivity of the material. Moreover, the Raman spectrum of $MAPbI_3$ at low frequencies resembles the PbI_2 precursor spectrum, which makes it difficult to distinguish between pristine and (partially) decomposed samples, as we pointed out recently.[41] Ledinsky et al. reported on photo-induced decomposition during resonant Raman measurements and emphasized the use of laser intensities far below the values that would usually be employed.[36] Apart from the photo-induced decomposition,[42] $MAPbI_3$ photoexcitation induces a range of other effects that can alter its structure and therefore the experimental outcome.[12,37,43] As mentioned earlier, mixed-halide perovskites have been shown to segregate into microdomains under illumination, presumably caused by an instability of the photoexcited state.[12] A recent study by Gottesman et al. showed reversible structural modifications of $MAPbI_3$ in the Raman spectrum by excitation under resonant conditions.[39] Experimental results are often backed by computational studies,[23,37,38] which give valuable information. Nevertheless, these calculations are based on several assumptions and produce complex spectra with many superimposed bands especially in the low-frequency range. Also, small uncertainties involved in calculations can result in very large offsets in the spectrum, making peak assignment ambiguous.[37]

The current work investigates $MAPbX_3$ structural dynamics for all halide derivatives by combining far-IR absorption and Raman scattering and addresses most of the critical issues raised in the literature up to now. For the first time we perform off-resonance Raman experiments and manage to obtain unambiguous Raman spectra avoiding decomposition or structural changes in the material. Measurements have also been carried out on the low-frequency Raman and IR active modes of the inorganic PbX_6 octahedra. Variable temperature Raman measurements show characteristic spectroscopic changes of the MA torsion and rocking vibrations which have implications on the ordering and bonding of MA inside the inorganic framework. Understanding the fundamental material properties is the key to the construction of perovskite solar cells with improved efficiency and stability.

2. EXPERIMENTAL METHODS

2.1. Materials and Depostion of Films. The methylammonium halide salts (MAI, MABr, and MACl) were synthesized by dropwise neutralization of an ice-bath cooled solution of 24 mL methylamine (Sigma-Aldrich) in 100 mL of ethanol with the corresponding hydrogen-halide (10 mL of 57 wt % HI in water; 14.6 mL of 48 wt % HBr in water; 15 mL of 37 wt % HCl in water; all Sigma-Aldrich). The solvent was removed in a rotary evaporator, and the powder was recrystallized from ethanol. Upon slow cooling of the ethanol solution white crystals were formed. Washing with diethyl ether and drying at 70 °C for 6 h was performed afterwards. The single halide perovskite ($MAPbI_3$, $MAPbBr_3$, and $MAPbCl_3$) precursor solutions were prepared by mixing a 1:1 stoichiometric ratio of lead(II) halide (PbI_2, 99%; $PbBr_2$, 99.99%; $PbCl_2$, 99.99%; all Sigma-Aldrich) with the corresponding methylammonium halide at a 1 mol/L concentration in DMSO (≥99.9%; Sigma-Aldrich) for 1 h at 60 °C. For the mixed halide perovskite precursor solutions, the respective ratios of single halide solutions were mixed and stirred for 1 h. Synthesis of the precursor salts was performed in the fume hood, while the mixing of the perovskite precursor solutions, films deposition, as well as annealing were done in an argon-filled glovebox (H_2O and O_2 concentration <1 ppm).

For the preparation of planar films the precursor solution was deposited on a microscope glass slide. For mesoporous films, a dispersion of Al_2O_3 nanoparticles (20 wt % in 2-propanol; Sigma-Aldrich) was spin-coated onto glass slides (2000 rpm for 60 s) and annealed at 500 °C for 30 min. All perovskite solutions were spin-coated onto the flat or mesostructured substrates at 2000 rpm for 60 s and then annealed on a hot plate at 100 °C for 30 min. Samples for far-IR characterization were prepared by depositing mesoporous perovskite films on a 0.8 mm thick high-density polyethylene (HDPE) to improve surface wettability. In order to enhance the perovskite Raman scattering volume, measurements were performed on powder samples taken by scratching the films.

2.2. Characterization. The perovskite films were structurally characterized using a Siemens D-500 diffractometer that operates in Bragg−Brentano geometry with Cu $K_{\alpha 1}$ radiation (λ = 1.5406 Å) and Cu $K_{\alpha 2}$ radiation (λ = 1.5444 Å). Data were collected over the angular range $5° \leq 2\theta \leq 100°$ counting for 1 s at each step of 0.05° in detector position. Unit-cell refinements were performed with the GSAS package.[44]

UV−vis diffuse reflectance (R) spectra were acquired on a Hitachi 3010 spectrophotometer using an integrating sphere with 60 mm diameter and $BaSO_4$ as a reference. The data were transformed into Kubelka−Munk absorbance $F(R) = (1 - R)^2/2R$.

The IR transmittance measurements were run at normal incidence on a Bruker Vertex 80v vacuum spectrometer using HDPE-alumina films as a reference. Each spectrum was averaged over 200 scans with a 4 cm^{-1} resolution. The far-infrared (FIR) beam splitter and detector offered a working range of ca. 60−680 cm^{-1}. The transmittance spectra were converted to absorbance and normalized to 1.

DOI: 10.1021/acs.jpcc.5b11256
J. Phys. Chem. C 2016, 120, 2509−2519

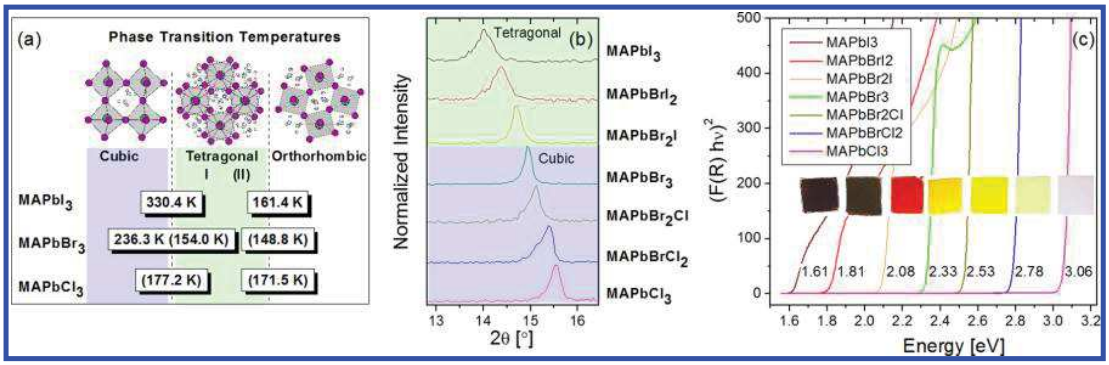

Figure 1. (a) Different phases of the $MAPbX_3$ perovskite, which transform upon changing temperature or halide composition: halides, large purple spheres, Pb, large gray spheres; MA, interstitial. Transition temperatures into tetragonal II $MAPbBr_3$ are in brackets. (b) Powder XRD patterns of the range of interest from all halide perovskites examined in this study. (c) UV−vis spectra (where $F(R)$ is the Kubelka−Munk function) of perovskite films which change in color (from dark brown to white) and show a shift in band gap energy (from 1.61 to 3.06 eV) as lighter halogens are introduced into the structure.

Raman measurements with excitation at 514 and 785 nm were performed with a Renishaw In-Via Reflex dispersive micro-Raman spectrometer with <2 cm^{-1} resolution. The laser beam was focused on a spot of 1 μm in diameter with a ×100 magnification lens. Rayleigh scattering was rejected with 50 or 110 cm^{-1} cutoff dielectric edge filters, and analysis of the scattered beam was performed on a 250 mm focal length spectrometer along with suitable diffraction gratings (1800 lines/mm for visible and 1200 lines/mm for NIR) and a high-sensitivity CCD detector. Cryostatic Raman measurements at low temperature (LT) were done under inert atmosphere in a THMS600PS Linkam cell by focusing the laser beam with a ×50 long focal distance lens. Raman spectra under off-resonance conditions for all samples were acquired with a Bruker RFS100 FT-Raman spectrometer equipped with a Nd:YAG laser emitting at 1064 nm. Each spectrum was averaged over 100 scans or 200 scans with 4 cm^{-1} resolution, while the effective working range was ca. 100−3500 cm^{-1}. All RT Raman measurements were performed in air and at different laser powers to ensure that the intensities used did not induce changes in the spectra. The measured Raman spectra present a strong elastic scattering background in the low-frequency (LF) spectral range. In order to enhance the Raman features at this LF range where very informative PbX and MA vibrations are active, and correctly determine spectral characteristics (frequency, line width, and line shape), the spectra were temperature-reduced using the expression of eq 1[45]

$$I_{red}(\omega) = I(\omega)\frac{1}{n(\omega, T) + 1}, \text{ with}$$
$$n(\omega, T) = (\exp^{\frac{hc\omega}{k_B T}} - 1)^{-1} \approx (\exp^{\frac{1.44\omega}{T}} - 1)^{-1} \quad (1)$$

where $I(\omega)$ and $I_{red}(\omega)$ are the measured and reduced Raman intensity, respectively. $n(\omega, T)$ is the Bose−Einstein statistic factor, h and k_B are the Planck and Boltzmann constants, respectively, c is the speed of light, ω is the Raman shift in cm^{-1}, and T is the temperature in K. The analysis of the reduced spectra was done by fitting them with mixed Lorenzian−Gaussian functions using the Wire software from Renishaw. Line widths were corrected for instrumental broadening.

3. RESULTS AND DISCUSSION

3.1. Structural and Optical Characterization. Schemes of the perovskites structure at the three different structural modifications (cubic, tetragonal, and orthorhombic) together with transition temperatures[46] are shown in Figure 1a. Powder-XRD patterns of the area of interest for the whole set of $MAPbX_{3-x}Y_x$ materials, shown in Figure 1b, confirm the presence of the perovskites as the main phase. In addition, certain amounts of admixtures were present, in particular PbI_2 for the I-containing samples (for the full patterns see Figure S1 in the Supporting Information). $MAPbCl_3$, $MAPbBrCl_2$, $MAPbBr_2Cl$, and $MAPbBr_3$ were indexed as cubic systems, whereas $MAPbBr_2I$, $MAPbBrI_2$, and $MAPbI_3$ were indexed as tetragonal systems, in accordance to ref 8. A regular trend in the unit-cell expansion with substitution of Cl by Br and I was observed. The determined lattice parameters of the tetragonal $MAPbI_3$ ($a = b = 8.861(2)$ Å, $c = 12.653(4)$ Å) are in agreement with the literature values of $a = b = 8.849(2)$ Å, $c = 12.642(2)$ Å,[47] within the 3σ estimated standard deviation. The lattice parameters are given in Table S1 of Supporting Information.

Substitution of heavy halogen atoms with lighter ones in $MAPbX_{3-x}Y_x$ results in films with tunable color from dark brown to white, as shown in the photographs of the prepared films inserted in Figure 1c. In order to analyze the light harvesting of the films over the solar spectrum, diffuse reflectance measurements were carried out. In Figure 1c, the absorption $F(R)$ data are plotted in terms of $(F(R)h\nu)^2$ vs $h\nu$, which is the standard analysis for materials having a direct band gap. Band gap values (E_g) were found by the intersections of the slope with the energy axis and are shown in the graphs, and further listed in Table S2 where they are compared with the Raman excitation energies. The values are slightly blue-shifted compared to literature values.[8] Blue-shifted absorption onsets were reported recently.[48,49] The shift can be caused by a ferroelectric domain wall-induced band gap reduction and has been observed for mesoporous scaffold architectures.[26,48] The influence of annealing temperature on band gap is another possible explanation for this observation.[49] In general, the reported band gaps for MA lead perovskites can vary significantly.[50] The excitonic peaks appearing in the spectra for lighter halide derivatives are presumably caused by an increase in the exciton binding energies.[51]

DOI: 10.1021/acs.jpcc.5b11256
J. Phys. Chem. C 2016, 120, 2509−2519

3.2. Low-Frequency Pb−X Vibrational Modes: Far-IR and Micro-Raman Results at Room Temperature. The PbX_6 octahedra of the perovskite halides belong to the O_h point group symmetry and have two IR active modes, ν_3 and ν_4, with T_{1u} symmetry and three Raman active modes ν_1, ν_2 and ν_5, with A_{1g}, E_g and T_{2g} symmetry, respectively.[37,52] Splitting of the doubly and triply degenerate modes is expected due to distortion of the octahedra, (a) by interaction between the methylammonium and certain halogen atoms and (b) by the occupation of the octahedral corners with different halide atoms in the complex halide derivatives. According to theoretical calculations,[37] the splitting is considerably larger for the Cl-based perovskites (Cl has the strongest electronegativity). In the present study, and for the first time in the literature, both the IR and Raman low-frequency Pb−X vibrational modes have been observed for all members of the $MAPbX_3$ family.

Far-IR spectra obtained for all $MAPbX_3$ derivatives are shown in the range of 50−300 cm^{-1} in Figure 2a, and analysis

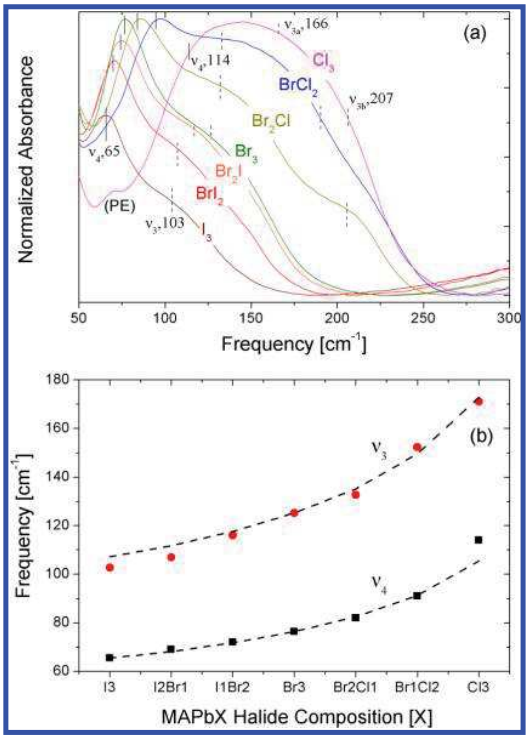

Figure 2. (a) Far-IR spectra for the various perovskite derivatives measured at RT. The band marked by PE is due to the polyethylene substrate. Peak frequencies of the ν_3 and ν_4 bands obtained by fitting the spectra (see Figure S2) are marked with dashed and solid lines, respectively. The values are noted for the end perovskite members, $MAPbI_3$ and $MAPbCl_3$. For Cl-based perovskites the ν_3 band is split into two component bands, ν_{3a} and ν_{3b}. (b) Frequency of ν_3 (average) and ν_4 modes vs halide composition. Dashed lines show predictions based on the harmonic oscillator model.

of spectral components is shown in Figure S2. HDPE-alumina substrate, taken as a reference, is also included in Figure S2 and has only minor influence in the results. Wide bands are observed in all far-IR spectra, which blue shift towards the lighter halides derivatives and present extensive broadening justified by the polycrystalline character of the materials. According to recent density functional perturbation theory calculations,[34] low-frequency IR-activity (below 120 cm^{-1} for $MAPbI_3$) is mainly due to internal PbI_3 vibrations. The spectra of the $MAPbI_{3-x}Br_x$ series are analyzed with two component bands, which thus are straightforwardly attributed to the ν_3 asymmetric stretching (103−125 cm^{-1}) and ν_4 asymmetric bending (66−76 cm^{-1}) vibrations of PbX_6 octahedra. For the Cl-containing samples, the higher frequency band is split into two component bands, which are well described by mixed Lorenzian−Gaussian character. For the pure Cl perovskite, a very broad band is observed which includes both the ν_4 band, as a low-frequency shoulder, as well as the split ν_3 band at higher frequencies. The peak positions of the deconvoluted ν_3 and ν_4 modes (two peaks for the Cl-containing perovskites) are marked in Figure 2a. In Figure 2b we plot the frequency of the two modes versus the halogen order. For the estimation of the ν_3 frequency for the mixed halides, a weight average of the two ν_3-related component bands was taken into account. First of all we should note that the ratio ν_4/ν_3 remains almost constant in the 0.60−0.64 range. The only exception is $MAPbCl_3$ for which it is slightly larger and equal to 0.67, presumably due to uncertainties in the fitting of the corresponding broad far-IR band. The fixed ν_4/ν_3 ratio verifies self-consistency of the analysis, and the ratio values match the corresponding ratios for several other compounds quite well (e.g., the ratio for the $[PbCl_6]^{2-}$ anion from ref S2 is 0.54).

Both ν_3 and ν_4 modes shift to higher frequencies upon introduction of lighter halogen atoms in the structure. The ν_3 and ν_4 frequencies depend strongly on the reduced mass μ of the Pb−X bond and follow the model for a harmonic oscillator $\nu = \left(\frac{1}{2\pi}\right)\sqrt{k/\mu}$, with the crude assumption of the same bond strength k for all halides. The reduced mass is $\mu^{-1} = m_{Pb}^{-1} + m_X^{-1}$ where m_X for the mixed halides was calculated by the weight average of the halogen atomic masses in their chemical formula. The model calculations have been done by weighting the ν_3 and ν_4 frequencies against those observed for $MAPbBr_3$ and are shown with dashed lines in Figure 2b. These results verify that the low-frequency IR active vibrations are of the inorganic Pb−X type and lack noticeable influence from the MA cation. A similar behavior which consolidates our argument is observed by analyzing the frequency shifts of the Sn−X modes in the analogous $[SnX_6]^{2-}$ octahedral system, irrespective of the vibration mode.[52]

Complementary to the far-IR spectra, low-frequency Raman spectra were obtained above 50 cm^{-1} with 785 nm laser line excitation. The spectra are presented in Figure 3a for all the perovskite compounds apart from the pure $MAPbI_3$ which showed only a strong photoluminescence (PL) response. The vibrational modes of the PbX_6 octahedra were observed below 250 cm^{-1}. At 270 cm^{-1} for $MAPbBrI_2$ and at higher frequencies for the rest of the compounds, a broad and well-formed band was observed. This band is due to the torsion of MA units and will be discussed in detail in the next section.

The Raman spectra below 230 cm^{-1} involve vibrations of Pb−X bonds consisting of heteropolar ionic/covalent interactions in the inorganic framework and show very broad multibands which are not easily resolved into components. The general trend is that all these measured bands increase in frequency by moving toward light halides following the corresponding behavior shown in the far-IR spectra. The multiband character of the Raman features is clearer for the mixed perovskite derivatives and is justified considering the lifting in degeneracy of modes. As already discussed, three

DOI: 10.1021/acs.jpcc.5b11256
J. Phys. Chem. C 2016, 120, 2509−2519

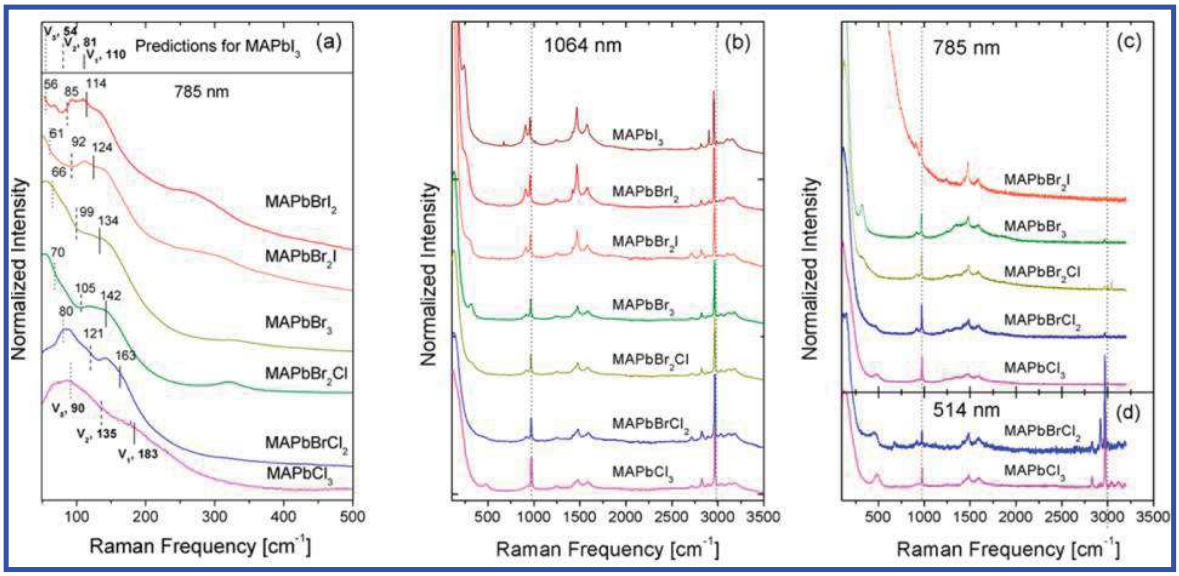

Figure 3. (a) Low-frequency Raman spectra obtained by excitation at 785 nm. Peak frequencies of ν_1 (solid line marks), ν_2 (dashed line marks), and ν_5 (dotted line marks) noted upon the graph are estimated from the experimentally recorded frequency of the ν_3 IR band and modes frequency ratios from the literature (for details see text). Raman spectra of the perovskite halide derivatives obtained by excitation at (b) 1064 nm, (c) 785 nm, and (d) 514 nm, at RT.

Table 1. Frequencies (in cm^{-1}) and Assignments of Vibrations Numbered in Series for MA Lead Derivatives MAPb[X], Where [X] Is the Halogen Composition[a]

mode/[X]	I3	I2Br	IBr2	Br3	Br2Cl	BrCl2	Cl3	assignment[b]
ν_1	(110)	114	124	134	142	163	183	ν_s (Pb−X)[this work]
ν_2	(81)	85	92	99	105	121	135	ν_s (X−Pb−X)[this work]
ν_3	103	107	116	125	133	152	171	ν_{as} (Pb−X)[this work]
ν_4	65	69	72	76	82	91	114	δ_{as} (X−Pb−X)[this work]
ν_5	(54)	56	61	66	70	80	90	δ_s (X−Pb−X)[this work]
ν_6	249	264	286	323	334	460	488	τ (MA)[54,55]
ν_7	911	913	914	917	919	919	923	ρ (MA)[54,55]
ν_8	960	962	965	968	971	974	977	ν (C−N)[55]
ν_9	1247	1246	1247	1248	1249	1248	1249	ρ (MA)[30]
ν_{10}	1424	1423	1425	1428	1427	1426	1430	δ_s (CH_3)[55]
ν_{11}	1444	1444	1451	1450	1451	1453	1454	δ_{as} (CH_3)[55]
ν_{12}	1469	1472	1475	1478	1480	1483	1483	δ_s (NH_3^+)[30]
ν_{13}	1580	1581	1584	1587	1588	1593	1592	δ_{as} (NH_3^+)[30]
–	2706	2712	2716	2714	2715	2717	2719	combination modes[30]
–	2821	2823	2824	2827	2827	2829	2830	combination modes[30]
–	2906	2906	2845	2846	2845	2847	2848	combination modes[30]
ν_{14}	2959	2961	2963	2966	2968	2969	2972	ν_{as} (CH_3)[30]
ν_{15}	2993	3026	3030	3035	3036	3036	3040	ν_s (NH_3^+)[55]

[a]Modes from ν_6 and above were obtained from Raman spectra with 1064 nm excitation and are due to MA vibrations. Modes ν_3 and ν_4 were obtained from far-IR spectra. ν_1, ν_2 and ν_5 records are estimated frequencies and match well with experimental Raman spectra at low frequencies. Corresponding values for $MAPbI_3$ are shown in parentheses to indicate that Raman experimental data are not available in this work. [b]ν: stretching; δ: bending; ρ: rocking; τ: torsion; s:symmetric; as: asymmetric.

Raman bands due to the Pb−X vibrations of the octahedral structure are expected in the LF range. Among them the symmetric stretching mode ν_1 is expected to be the highest in frequency, followed with the asymmetric stretching mode ν_2 and the asymmetric deformation ν_5.[52] Since it is difficult to fit the spectra, we attempt an analysis based on the ratios of the frequencies between the various inorganic vibrational modes from the literature. Thus, according to data in ref 52., the ratios ν_1/ν_3 = 1.07, ν_2/ν_1 = 0.74, and ν_5/ν_1 = 0.49 are observed for $[PbCl_6]^{2-}$ whereas similar values are found for other systems, too, such as for $[SnX_6]^{2-}$ and $[SbX_6]^{3-}$. Thus, based on our ν_3 values from our far-IR analysis we have predicted the mean frequencies of the corresponding Raman bands. The respective calculated values of the three Raman modes are reported in Figure 3a and qualitatively describe the shifts observed as a function of the halide change. By extending the calculations for $MAPbI_3$, the mean frequencies for the three Raman active modes are predicted to be at ν_1 = 110 cm^{-1}, ν_2 = 81 cm^{-1}, and ν_5 = 54 cm^{-1} (see also Figure 3a).

3.3. Variable Excitation Micro-Raman Spectra of All Perovskite Derivatives. Extensive Raman investigation with emphasis on MA vibrations was done by performing measure-

DOI: 10.1021/acs.jpcc.5b11256
J. Phys. Chem. C 2016, 120, 2509−2519

ments in a broad frequency range (100−3500 cm^{-1}) using three different excitation lines at 514, 785, and 1064 nm. This allowed data acquisition both at resonance (res) as well as off-resonance conditions (off-res). An overview of materials and excitation wavelengths is shown in the Supporting Information (Table S2). In general, the majority of resonance Raman measurements obtained from the $MAPbX_3$ perovskites carries limited information on the vibrational properties of the materials. The main reason is that the strong absorption of the perovskites, when excited within the band gap, can induce decomposition or phase transformations in the materials. This is an issue especially for $MAPbI_3$ with a phase transition from tetragonal to pseudo-cubic near room temperature, at 330 K. Despite keeping the laser power density very low, by working under resonance or near resonance conditions the Raman signals are frequently masked by the presence of a strong PL background signal. Furthermore, temporary PL signals which change with illumination time were observed here in Br−I mixed halide perovskites and are attributed to phase segregation, as previously reported by Hoke et al.[12] (see Figure S3).

Figures 3b−d show an overview of the Raman spectra for all the perovskite films obtained under different excitation wavelengths, 1064 nm (Figure 3b), 785 nm (Figure 3c), and 514 nm (Figure 3d). In the case where the Raman features are masked by strong PL signals, the corresponding spectra are not presented. Thus, for $MAPbI_3$, we include only the spectrum obtained at 1064 nm excitation in Figure 3b, and no spectra in Figure 3c and Figure 3d, because, under near band gap or resonance excitation, the Raman signal is either covered by a strong PL background or is affected by the quick degradation of the sample showing spectroscopic changes during the measurement. $MAPbCl_3$ on the other hand shows no apparent change in its Raman spectrum, for all the excitation sources used. Hence, excitation at 1064 nm (Figure 3b) ensures off-resonance conditions in all cases allowing a clear and unambiguous overview of the full MA spectrum for all halide perovskite derivatives, and no spectral changes were observed that could be related to humidity or light exposure of the material. Furthermore, the quality of the spectra is excellent mainly due to the fast acquisition in the FT technique and the materials tolerating high laser power densities at 1064 nm excitation, which compensate well for the inherently weaker scattering efficiency vs the increase of the excitation wavelength (inverse fourth power law applies).

The Raman spectra reported in Figures 3b−d show a large number of MA bands which present significant changes in their characteristics (shifts, widths, intensities) with halogen composition. An overview of the frequencies of the measured Raman bands and their mode assignments can be found in Table 1. Almost all MA vibrational modes present a blue shift from $MAPbI_3$ toward $MAPbCl_3$ (see Figure S4) in accordance with the IR data in ref 30, which indicates strong NH_3−X interaction. In particular, the mode that is most sensitive to the halide content is the high-frequency ν_{15}−ν_s (NH_3^+) mode which positively shifts abruptly from $MAPbI_3$ to $MAPbI_2Br$ by 33 cm^{-1} and then up to $MAPbCl_3$ by another 14 cm^{-1}. Significant positive shifts also occur in all other modes related to NH_3 vibrations. This is in line with recent NMR results,[53] which have shown that only the amine end of the MA group interacts strongly with the inorganic network. Nevertheless, the exact N−H bond lengths in $MAPbX_3$ cannot be accurately determined even with neutron diffraction methods due to the disorder in the MA group;[53] thus, the full understanding of the MA vibrational frequency shifts (e.g., the large ν_{15} shift for $MAPbI_3$ compared to the other perovskites) and the exact nature of the MA−halogen interaction is not possible.

Characteristic internal vibrational modes of MA appear at high frequencies, just below 1000 cm^{-1} (C−N stretching), at 1400−1600 cm^{-1} (CH_3 and NH_3 bending) and at around 3000 cm^{-1} (CH_3 and NH_3 stretching) and are well studied for methylammonium halides.[30,55] The most interesting vibrational modes are the rocking vibration, ν_7, and low-frequency torsion, ν_6, of MA around the C−N axis. The MA rocking mode, ν_7, appears in between 911 and 923 cm^{-1} and sharpens, increases in intensity, and red shifts when moving toward heavier halides Cl → Br → I (Figure 3b−d, Figure S4); the same trend was found for other modes (e.g., the ν_{12}, $\delta_s(NH_3^+)$ mode). This behavior can be attributed to orientational ordering of MA for which ν_7, having the E symmetry,[56] is a good indicator. The effect can be analyzed by the calculation of the correlation times (τ_c) from the peak Full Width at Half Maximum (FWHM),[29] which are shown in Figure 4a, according to eq 2

$$\tau_c = \frac{1}{2\pi c \mathrm{FWHM}} \tag{2}$$

where c is the velocity of light.

The results show correlation times below 0.15 ps for the ν_7 rocking vibration for all perovskite derivatives. τ_c gradually

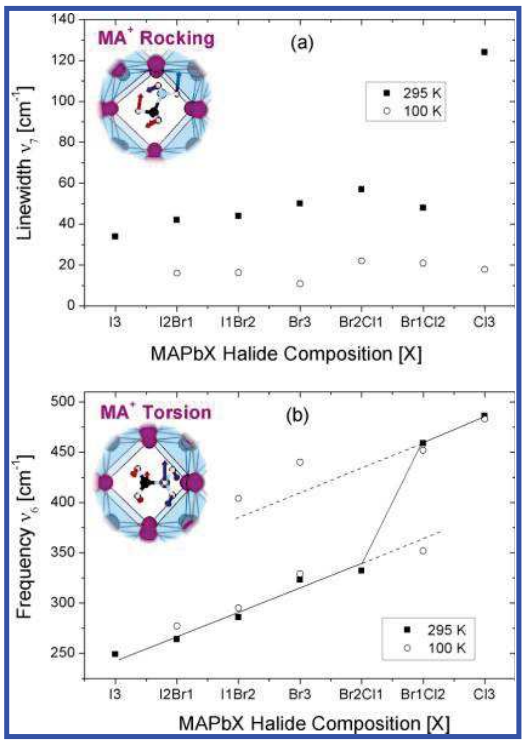

Figure 4. (a) FWHM of the ν_7 rocking mode averaged over measurements obtained at RT with different laser lines (solid squares—standard deviation <5 cm^{-1}) as well as at LT (100 K) obtained at 785 nm excitation (open circles). (b) Raman frequency of the torsional mode averaged over measurements obtained at RT with different laser lines (solid squares standard deviation <3 cm^{-1}) and corresponding results at LT (100 K) obtained at 785 nm (open circles). Solid line guides the eye for halogen dependence of the RT data and is extrapolated either sides with dashed lines.

DOI: 10.1021/acs.jpcc.5b11256
J. Phys. Chem. C 2016, 120, 2509−2519

decreases from 0.15 to 0.1 ps from $MAPbI_3$ up to $MAPbBrCl_2$ and drops to 0.05 ps for $MAPbCl_3$. Measurements of MA rocking vibration dynamics can be compared with early IR absorption data[29] obtained from large perovskite crystals, where the trend of correlation time decrease from heavy to light halides is also followed, as well as with recent results[34] on very high-quality thin films prepared with the dual source evaporation method. In both of these literature studies, the τ_c values for $MAPbI_3$ were substantially larger. Thus, the shorter correlation time in our samples is attributed to their polycrystalline character.

The ν_6 mode mainly consists of an NH_3 motion and has an A_2 symmetry which makes it forbidden in IR but permitted in Raman.[55] This mode is easily accessed in all Raman experiments and is analyzed in a straightforward way as it is not overlapping with other modes. For $MAPbCl_3$[54] the mode is observed at 488 cm^{-1} and presents an extremely large red frequency shift upon halide substitution, shifting down to 249 cm^{-1} for $MAPbI_3$ (see Figure 4b and Table 1). This large spread of resonance frequencies for MA is unusual for a torsional mode and indicates intense MA deformation and a strong interaction of MA with the inorganic cage. Fitting of ν_6 for different halide derivatives gives a continuous shift from $MAPbI_3$ to $MAPbBr_2Cl$, but jumps to higher wavenumbers for perovskites with large amounts of Cl, as shown in Figure 4b. According to recent theoretical studies,[23] different mechanisms like molecular deformation and dipolar orientational ordering of the MA as well as strength of the NH_3−X interaction are strongly affected by the nature of the halide in the perovskite and result in large shifts in the frequency of the MA torsion. Among them, changes in NH_3−X interaction upon halide substitution is the most prominent reason for the large frequency shift of the ν_6 mode, considering that it affects the frequencies of all other MA modes, too, in the same manner, even though to a much lesser extent. Preliminary calculations performed with the same methodology reported by Brivio at al.[38] confirm the observed increase of the torsional mode frequency for perovskites with Br and Cl with respect to iodine. This is due to a halogen specific NH_3−X interaction, and to a confinement effect. In fact, lighter halide results in a smaller cavity inside the inorganic cage that uplifts the frequencies of the molecular modes and reduces the distance between hydrogen and halide, amplifying the resulting shift. In Figure S5 we attempt a correlation of the torsional mode peak frequency at room temperature (RT) against the measured band gap for the various perovskite halides. Halide substitution results in vast changes of the materials optical properties, which can significantly affect their vibrational frequencies as also proposed before[30] by correlating the red shifts of MA vibrations in the Cl → Br → I order to the increase in the polarizability of the dielectric medium (Lorentz−Lorenz shift).

Interestingly, the signal intensity of ν_6 is much stronger for single halide perovskites (see Figure 3b−d), and its line width is not very broad, ranging from 40 to 60 cm^{-1}. In the mixed halide perovskites a big drop in the ν_6 intensity takes place which goes along with extensive line width broadening, reaching values up to 150 cm^{-1}. A general peak broadening can be caused in several ways. A decrease in long-range order and crystallinity typically yields broader peaks. Unresolved mode splitting also causes an increase of peak width and is connected to possible asymmetries of the mode. Such mode splitting can be enhanced by microstructural inhomogeneities due to an uneven distribution of a halide in the perovskite. This effect has been reported before for $MAPbI_{3-x}Br_x$, which forms microdomains upon crystallization that transform into a single phase within a few weeks[57] but also segregate again upon illumination.[12]

The informative torsional and rocking vibrations were further examined by comparative low-temperature Raman measurements in order to elucidate their behavior by lowering the symmetry of the perovskite structure.

3.4. Low-Temperature Raman Measurements. Another series of Raman experiments was performed for all perovskites at 100 K which is well below the phase transition of all materials into the orthorhombic phase.[46] Characteristic reduced spectra at low temperature are shown in Figure 5a obtained with excitation at 785 nm. The inset shows off-resonance spectra of $MAPbBrCl_2$ and $MAPbCl_3$ using 514 nm excitation. Peak frequencies of the strongest MA vibrations are given in Table S3. Mode splitting of the low-frequency modes was observed due to the lowering of the crystal symmetry. All materials transform from tetragonal to orthorhombic in the temperature range of 148.8−171.5 K.[58] Splitting was more evident for lighter halide derivatives, in accordance to early results for $MAPbCl_3$.[54] In the case of heavier derivatives, mode splitting was only partially observed due to the shifting of the majority of the modes below the experimentally accessed frequency range. Furthermore, apart from narrowing and blue shifting of the MA high-frequency bands above 950 cm^{-1}, no clear MA mode splitting was evidenced upon decrease of the temperature. A similar effect has been reported before for mid-IR data below the phase transition temperature[29] as well as for Raman in other perovskite systems[59] implying that the crystal deformation does not drastically affect the high-frequency vibrations of the MA units.

It is remarkable that at LT the rocking vibrations ν_7 and ν_9 at 920 and 1250 cm^{-1} present considerable line width narrowing. Thus, the ν_7 rocking mode width decreases to about 20 cm^{-1} for all perovskite derivatives (see Figure 4a) and the ν_7 correlation time increases from below 0.15 ps at RT to above 0.25 ps at 100 K, which implies MA dipolar ordering,[29] in accordance with quasi-elastic neutron-scattering results.[22]

Further insight into the behavior of the ν_6 torsion mode can be extracted from the low-temperature (LT) data. While the measurements at RT showed a jump to higher wavenumbers for the $MAPbBrCl_2$ and $MAPbCl_3$ perovskites, at LT pairs of peaks appeared (see spectra in Figure 5a and analysis in Figure 4b) that line up with modes on either side of the gap, suggesting that those peaks in fact represent two distinctive vibrational bands. The appearance of two torsional bands at low temperature is in line with early studies for $MAPCl_3$.[54] Doubling of the torsional modes for the low-symmetry orthorhombic phase and line width broadening might be due to different NH_3−X bonding schemes of the organic molecule within the hybrid.[60] On the other hand, the frequencies of the torsional modes at low temperature show small, mostly blue shifts relative to those at RT.

Another important aspect of the torsional mode is its significant broadening in the orthorhombic phase. The unit cell of this phase contains four different MA units and according to our preliminary calculations, the frequencies of respective modes are split in four due to slightly different local environments. This split is on the order of few cm^{-1} and therefore too small to be resolved but contributes to significant line width broadening. Moreover, as observed in molecules[61,62] or complex structures,[63] van der Waals forces that are enhanced at low temperature affect the stiffness of the bonds and

DOI: 10.1021/acs.jpcc.5b11256
J. Phys. Chem. C 2016, 120, 2509−2519

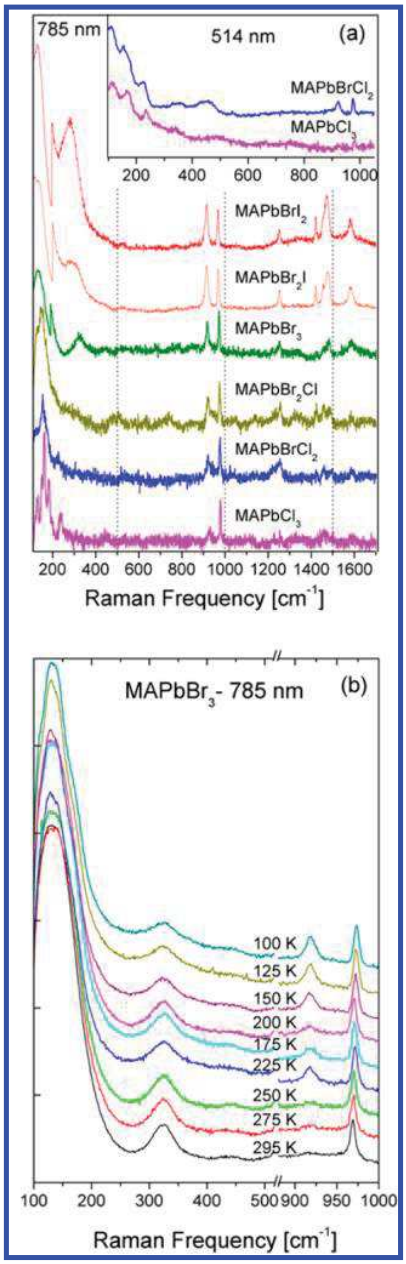

Figure 5. (a) Raman measurements of $MAPbX_{3-x}Y_x$ perovskites at 100 K obtained with 785 nm excitation. Intensity of the top three spectra below 200 cm^{-1} is scaled down by 3 for better vision of the spectra. Inset shows spectra obtained with 514 nm excitation. (b) Raman spectra of $MAPbBr_3$ (785 nm) vs temperature variation from 100 K (LT) to 295 K (RT).

influence the anharmonic terms of the vibration that lead to a larger broadening of the peak. This effect strongly depends and the geometry of the system and could justify the different behavior below the transition temperature. In previous work[64] an anomalous temperature behavior of a low-frequency Raman peak in NH_4Br around phase transition has been reported. This anomaly results in asymmetric peak shape and anomalous broadening of the signal. These effects are addressed and explained with a long-range order of the NH_4 cations. We can imagine that a similar mechanism, regarding the MA ordering, could influence the line widths at LT of the torsional mode in the hybrid MA perovskite halides, too.

In addition to fixed LT measurements at 100 K, variable temperature Raman measurements from 295 to 100 K have been carried out for $MAPbBr_3$. During this temperature ramp the material was transformed progressively from cubic to the tetragonal I phase (236.3 K), the tetragonal II phase at 154.0 K, and the orthorhombic phase at 148.8 K.[46] Recorded Raman spectra are shown in Figure 5b. $MAPbBr_3$ was chosen as the intermediate representative of our halide series and because of its high purity (see XRD in Figure S1), the fact that the full temperature dependence has not been reported before in the literature ($MAPbCl_3$ has been studied in ref 54 and $MAPbI_3$ Raman signal is covered by a strong PL background at 785 nm excitation), and its significance as light absorber for the preparation of very stable perovskite solar cells.[8−11,65]

All high-frequency MA modes above 950 cm^{-1} present a "normal" behavior with line narrowing and blue shift upon temperature decrease. Important observations are made by following the temperature dependence of the spectra below 950 cm^{-1} where peculiar behavior of the MA torsional and rocking modes at 320 and 925 cm^{-1} are observed upon moving from the cubic (295 K) to the orthorhombic phase (100 K).

Figure 6 plots the temperature dependence of the line widths for the "abnormal" torsional ν_6 and rocking ν_7 modes in

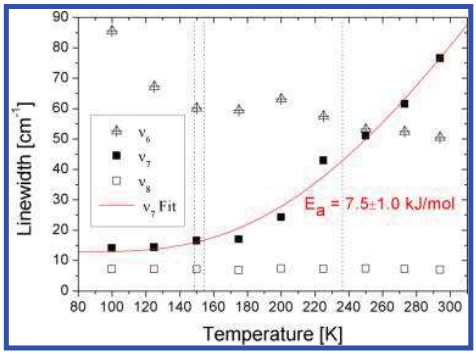

Figure 6. Temperature dependence of line widths for the torsional ν_6, rocking ν_7, and C−N stretching ν_8 vibrations of $MAPbBr_3$. Solid line represent fitting of ν_7 line widths by eq 3 with $b = 0$. Dotted lines mark the temperatures of phase transitions.

comparison to the CN stretching ν_8 mode which shows a "normal" behavior. The slope of line width against temperature shows a change for ν_7, at about 175 K, slightly above the tetragonal I−II phase transition at 154 K. This transition temperature is close to the temperature of a discontinuous decrease of the real part of the dielectric permittivity[58] as well as of significant changes in the H^1−NMR spectra and relaxation time.[66] According to this early H^1−NMR result, the tetragonal I to tetragonal II phase transition affects the alignment of MA by "freezing" of the C−N axis.

The temperature dependence of the line width of the ν_7 rocking mode in Figure 6 was used to calculate the activation energy (E_a) of the order−disorder process, according to eq 3[67−69]

$$\mathrm{FWHM}(T) = a + bT + c\exp(-E_a/RT) \quad (3)$$

where a, b, c are fitting parameters and R is the gas constant. The linear term describes the anharmonicity factor and the exponential term the increase of the line width due to the

DOI: 10.1021/acs.jpcc.5b11256
J. Phys. Chem. C 2016, 120, 2509−2519

thermal reorientational motions. We fitted the FWHM(T) data of ν_7 in Figure 6 with eq 3, neglecting the linear term which has a small contribution, and ended up with an estimation of the activation energy of E_a = 7.5 ± 1.0 kJ/mol which resembles the energy barrier in the disorder of the MA units. This value is very similar to that found for the rocking vibration of NH_3 in $[Mn(NH_3)_6](ClO_4)_2$.[69] As shown in Figure 6, the reorientational motions are not significantly disturbed near the phase transition temperature which is indicative that the order−disorder of the organic molecule does not contribute significantly to the phase transition mechanism.[69] Among different vibrational modes, the main torsional mode at about 320 cm^{-1} is the only one that shows line broadening instead of narrowing upon decreasing the temperature (see Figure 6). This broadening occurs progressively but shows a steep rise below the transition to the orthorhombic phase. This interesting behavior, which was also observed for other perovskite halides as discussed before, can be justified by the emergence of new unresolved torsional bands and long-range MA order in the low-symmetry phase.

4. CONCLUSIONS

In summary, our study gives a complete overview of the vibrational properties of single and mixed $MAPbX_3$ (X = Cl, Br, I) perovskites. Measurements in off-resonance conditions, at room- and low-temperatures, and a comparison of the Raman with far-IR spectra allow an unambiguous attribution of inorganic and organic modes and their shifts against halide constitution and temperature. Using three different excitation wavelengths for the Raman measurements, a significant influence of beam-induced degradation on the spectra of this material class can be ruled out for the first time in the literature. The low-frequency range is dominated by the modes of the inorganic anion, and the frequency shifts versus halide content is governed by the Pb−X reduced mass. Insight into structural dynamics of the MA cation has been given where specific vibrations such as the NH_3 rocking mode indicate ordering of MA at low temperatures. Among different modes, the MA torsion is particularly interesting since it spans a broad frequency range from 249 to 488 cm^{-1} by altering the halogen content. This behavior is attributed to changes in the interaction between the NH_3 head of MA and the halide. Furthermore, the MA torsional band shows broadening and splitting at 100 K in the orthorhombic phase, which indicates possible different MA−X bonding schemes. We hope that these findings encourage a broader usage of vibrational spectroscopy for inorganic−organic hybrid perovskites and aid a better understanding of their properties, which rank them among the most efficient solar cell active materials.

■ ASSOCIATED CONTENT

Supporting Information

The Supporting Information is available free of charge on the ACS Publications website at DOI: 10.1021/acs.jpcc.5b11256.

Lattice parameters from XRD data for $MAPbX_3$ perovskites (Table S1); band gaps and laser excitation energies for the Raman and PL investigation of perovskite materials (Table S2); overview of main MA Raman frequency peaks above 900 cm^{-1}, measured at 100 K (Table S3); full powder XRD patterns of all halide perovkites (Figure S1); fitting analysis of the far-IR absorption spectra (Figure S2); spectra showing shifting of PL during measuring $MAPbI_2Br$ under resonance (514 nm) excitation, indicating phase segregation (Figure S3); Raman frequency shifts of strongest MA modes above 900 cm^{-1} for various halogen contents in $MAPbX_3$ (Figure S4); frequency of the ν_6 torsional mode at RT against the band gaps for all measured $MAPbX_3$ derivatives (Figure S5) (PDF)

■ AUTHOR INFORMATION

Corresponding Author

*Tel.: +30 210 6503668. Fax: +30 210 6511766. E-mail: a.kontos@inn.demokritos.gr.

Author Contributions

⊥These authors contributed equally.

The manuscript was written through contributions of all authors. All authors have given approval to the final version of the manuscript.

Notes

The authors declare no competing financial interest.

■ ACKNOWLEDGMENTS

We acknowledge Dr. George Kordas for providing the 50 cm^{-1} NIR filter for the low-frequency Raman measurements and Dr. Eirini Siranidi for her assistance in Raman spectra acquisition. For enlightening and amicable conversations we thank Dr. Jarvist Frost and Harry Georgiou. The research is funded from the European Union Seventh Framework Programme [FP7/2007-2013] ('DESTINY' project) under grant agreement 316494.

■ REFERENCES

(1) Kojima, A.; Teshima, K.; Shirai, Y.; Miyasaka, T. Organometal Halide Perovskites as Visible-Light Sensitizers for Photovoltaic Cells. *J. Am. Chem. Soc.* **2009**, *131*, 6050−6051.

(2) Im, J.-H.; Lee, C.-R.; Lee, J.-W.; Park, S.-W.; Park, N.-G. 6.5% Efficient Perovskite Quantum-Dot-Sensitized Solar Cell. *Nanoscale* **2011**, *3*, 4088−4093.

(3) Kim, H.-S.; Lee, C.-R.; Im, J.-H.; Lee, K.-B.; Moehl, T.; Marchioro, A.; Moon, S.-J.; Humphry-Baker, R.; Yum, J.-H.; Moser, J. E.; Grätzel, M.; Park, N.-G.; et al. Lead Iodide Perovskite Sensitized All-Solid-State Submicron Thin Film Mesoscopic Solar Cell with Efficiency Exceeding 9%. *Sci. Rep.* **2012**, *2*, 591.

(4) Lee, M. M.; Teuscher, J.; Miyasaka, T.; Murakami, T. N.; Snaith, H. J. Efficient Hybrid Solar Cells Based on Meso-Superstructured Organometal Halide Perovskites. *Science* **2012**, *338*, 643−647.

(5) Zhang, W.; Saliba, M.; Moore, D. T.; Pathak, S. K.; Hörantner, M. T.; Stergiopoulos, T.; Stranks, S. D.; Eperon, G. E.; Alexander-Webber, J. A.; Abate, A.; Sadhanala, A.; Yao, S.; Chen, Y.; Friend, R. H.; Estroff, L. A.; Wiesner, U.; Snaith, H. J.; et al. Ultrasmooth Organic−Inorganic Perovskite Thin-Film Formation and Crystallization for Efficient Planar Heterojunction Solar Cells. *Nat. Commun.* **2015**, *6*, 6142.

(6) Park, B.; Philippe, B.; Jain, S. M.; Zhang, X.; Edvinsson, T.; Rensmo, H.; Zietz, B.; Boschloo, G. Chemical Engineering of Methylammonium Lead Iodide/Bromide Perovskites: Tuning of Optoelectronic Properties and Photovoltaic Performance. *J. Mater. Chem. A* **2015**, *3*, 21760−21771.

(7) http://www.solarserver.com/solar-magazine/solar-news/current/2015/kw50/epfl-achieves-21-world-record-efficiency-for-perovskite-solar-pv-cells.html (accessed December, 21, 2015).

(8) Noh, J. H.; Im, S. H.; Heo, J. H.; Mandal, T. N.; Seok, S. Il. Chemical Management for Colorful, Efficient, and Stable Inorganic−Organic Hybrid Nanostructured Solar Cells. *Nano Lett.* **2013**, *13*, 1764−1769.

(9) Conings, B.; Drijkoningen, J.; Gauquelin, N.; Babayigit, A.; D'Haen, J.; D'Olieslaeger, L.; Ethirajan, A.; Verbeeck, J.; Manca, J.;

DOI: 10.1021/acs.jpcc.5b11256
J. Phys. Chem. C 2016, 120, 2509−2519

Mosconi, E.; Angelis, F. D.; Boyen, H.-G.; et al. Intrinsic Thermal Instability of Methylammonium Lead Trihalide Perovskite. *Adv. Energy Mater.* **2015**, *5*, 1500477.
(10) Zhang, Y.-Y.; Chen, S.; Xu, P.; Xiang, H.; Gong, X.-G.; Walsh, A.; Wei, S.-H. Intrinsic Instability of the Hybrid Halide Perovskite Semiconductor $CH_3NH_3PbI_3$. *arXiv Prepr.* **2015**, arXiv:1506.01301.
(11) Buin, A.; Comin, R.; Xu, J.; Ip, A. H.; Sargent, E. H. Halide-Dependent Electronic Structure of Organolead Perovskite Materials. *Chem. Mater.* **2015**, *27*, 4405−4412.
(12) Hoke, E. T.; Slotcavage, D. J.; Dohner, E. R.; Bowring, A. R.; Karunadasa, H. I.; McGehee, M. D. Reversible Photo-Induced Trap Formation in Mixed-Halide Hybrid Perovskites for Photovoltaics. *Chem. Sci.* **2015**, *6*, 613−617.
(13) Stranks, S. D.; Eperon, G. E.; Grancini, G.; Menelaou, C.; Alcocer, M. J. P.; Leijtens, T.; Herz, L. M.; Petrozza, A.; Snaith, H. J. Electron-Hole Diffusion Lengths Exceeding 1 Micrometer in an Organometal Trihalide Perovskite Absorber. *Science* **2013**, *342*, 341−344.
(14) Colella, S.; Mosconi, E.; Fedeli, P.; Listorti, A.; Gazza, F.; Orlandi, F.; Ferro, P.; Besagni, T.; Rizzo, A.; Calestani, G.; et al. $MAPbI_{3-x}Cl_x$ Mixed Halide Perovskite for Hybrid Solar Cells: The Role of Chloride as Dopant on the Transport and Structural Properties. *Chem. Mater.* **2013**, *25*, 4613−4618.
(15) Colella, S.; Mosconi, E.; Pellegrino, G.; Alberti, A.; Guerra, V. L. P.; Masi, S.; Listorti, A.; Rizzo, A.; Condorelli, G. G.; De Angelis, F.; et al. Elusive Presence of Chloride in Mixed Halide Perovskite Solar Cells. *J. Phys. Chem. Lett.* **2014**, *5*, 3532−3538.
(16) Starr, D. E.; Sadoughi, G.; Handick, E.; Wilks, R. G.; Alsmeier, J. H.; Köhler, L.; Gorgoi, M.; Snaith, H. J.; Bär, M. Direct Observation of an Inhomogeneous Chlorine Distribution in $CH_3NH_3PbI_{3-x}Cl_x$ Layers: Surface Depletion and Interface Enrichment. *Energy Environ. Sci.* **2015**, *8*, 1609−1615.
(17) Milot, R. L.; Eperon, G. E.; Snaith, H. J.; Johnston, M. B.; Herz, L. M. Temperature-Dependent Charge-Carrier Dynamics in $CH_3NH_3PbI_3$ Perovskite Thin Films. *Adv. Funct. Mater.* **2015**, *25*, 6218−6227.
(18) Weber, D. $CH_3NH_3PbX_3$, a Pb(II)-System with Cubic Perovskite Structure. *Z. Naturforsch., B: J. Chem. Sci.* **1978**, *33b*, 1443−1445.
(19) Poglitsch, A.; Weber, D. Dynamic Disorder in Methylammoniumtrihalogenoplumbates(II) Observed by Millimeter-Wave Spectroscopy. *J. Chem. Phys.* **1987**, *87*, 6373−6378.
(20) Wasylishen, R. E.; Knop, O.; Macdonald, J. B. Cation Rotation in Methylammonium Lead Halides. *Solid State Commun.* **1985**, *56*, 581−582.
(21) Weller, M. T.; Weber, O. J.; Henry, P. F.; Di Pumpo, A. M.; Hansen, T. C. Complete Structure and Cation Orientation in the Perovskite Photovoltaic Methylammonium Lead Iodide between 100 and 352 K. *Chem. Commun.* **2015**, *51*, 4180−4183.
(22) Leguy, A. M. A.; Frost, J. M.; McMahon, A. P.; Sakai, V. G.; Kochelmann, W.; Law, C.; Li, X.; Foglia, F.; Walsh, A.; O'Regan, B. C.; et al. The Dynamics of Methylammonium Ions in Hybrid Organic−Inorganic Perovskite Solar Cells. *Nat. Commun.* **2015**, *6*, 7124.
(23) Quarti, C.; Grancini, G.; Mosconi, E.; Bruno, P.; Ball, J. M.; Lee, M. M.; Snaith, H. J.; Petrozza, A.; Angelis, F. D. The Raman Spectrum of the CH3NH3PbI3 Hybrid Perovskite: Interplay of Theory and Experiment. *J. Phys. Chem. Lett.* **2014**, *5*, 279−284.
(24) Frost, J.; Butler, K.; Brivio, F.; Hendon, C. H.; van Schilfgaarde, M.; Walsh, A. Atomistic Origins of High-Performance in Hybrid Halide Perovskite Solar Cells. *Nano Lett.* **2014**, *14*, 2584−2590.
(25) Liu, S.; Zheng, F.; Koocher, N. Z.; Takenaka, H.; Wang, F.; Rappe, A. M. Ferroelectric Domain Wall Induced Band Gap Reduction and Charge Separation in Organometal Halide Perovskites. *J. Phys. Chem. Lett.* **2015**, *6*, 693−699.
(26) Leguy, A.; Azarhoosh, P.; Alonso, M. I.; Campoy-Quiles, M.; Weber, O. J.; Yao, J.; Bryant, D.; Weller, M. T.; Nelson, J.; Walsh, A.; van Schilfgaarde, M.; Barnes, P. R. F.; et al. Experimental and Theoretical Optical Properties of Methylammonium Lead Halide Perovskites. *Nanoscale* **2015**, DOI: 10.1039/C5NR05435D.
(27) Quarti, C.; Mosconi, E.; De Angelis, F. Interplay of Orientational Order and Electronic Structure in Methylammonium Lead Iodide: Implications for Solar Cells Operation. *Chem. Mater.* **2014**, *26*, 6557−6569.
(28) Wu, B.; Fu, K.; Yantara, N.; Xing, G.; Sun, S.; Sum, T. C.; Mathews, N. Charge Accumulation and Hysteresis in Perovskite-Based Solar Cells: An Electro-Optical Analysis. *Adv. Energy Mater.* **2015**, *5*, 1500829.
(29) Onoda-Yamamuro, N.; Matsuo, T.; Suga, H. Calorimetric and IR Spectroscopic Studies of Phase Transitions in Methylammonium Trihalogenoplumbates. *J. Phys. Chem. Solids* **1990**, *51*, 1383−1395.
(30) Glaser, T.; Muller, C.; Sendner, M.; Krekeler, C.; Semonin, O. E.; Hull, T. D.; Yaffe, O.; Owen, J. S.; Kowalsky, W.; Pucci, A.; et al. Infrared Spectroscopic Study of Vibrational Modes in Methylammonium Lead Halide Perovskites. *J. Phys. Chem. Lett.* **2015**, *6*, 2913−2918.
(31) Bakulin, A. A.; Selig, O.; Bakker, H. J.; Rezus, Y. L. A.; Müller, C.; Glaser, T.; Lovrincic, R.; Sun, Z.; Chen, Z.; Walsh, A.; et al. Real-Time Observation of Organic Cation Reorientation in Methylammonium Lead Iodide Perovskites. *J. Phys. Chem. Lett.* **2015**, *6*, 3663−3669.
(32) Müller, C.; Glaser, T.; Plogmeyer, M.; Sendner, M.; Döring, S.; Bakulin, A. A.; Brzuska, C.; Scheer, R.; Pshenichnikov, M. S.; Kowalsky, W.; et al. Water Infiltration in Methylammonium Lead Iodide Perovskite: Fast and Inconspicuous. *Chem. Mater.* **2015**, *27*, 7835−7841.
(33) Mosconi, E.; Quarti, C.; Ivanovska, T.; Ruani, G.; De Angelis, F. Structural and Electronic Properties of Organo-Halide Lead Perovskites: A Combined IR-Spectroscopy and Ab Initio Molecular Dynamics Investigation. *Phys. Chem. Chem. Phys.* **2014**, *16*, 16137−16144.
(34) Perez-Osorio, M. A.; Milot, R. L.; Filip, M. R.; Patel, J. B.; Herz, L. M.; Johnston, M. B.; Giustino, F. Vibrational Properties of the Organic−Inorganic Halide Perovskite $CH_3NH_3PbI_3$ from Theory and Experiment: Factor Group Analysis, First-Principles Calculations, and Low-Temperature Infrared Spectra. *J. Phys. Chem. C* **2015**, *119*, 25703−25718.
(35) Grancini, G.; Marras, S.; Prato, M.; Giannini, C.; Quarti, C.; De Angelis, F.; De Bastiani, M.; Eperon, G. E.; Snaith, H. J.; Manna, L.; Petrozza, A.; et al. The Impact of the Crystallization Processes on the Structural and Optical Properties of Hybrid Perovskite Films for Photovoltaics. *J. Phys. Chem. Lett.* **2014**, *5*, 3836−3842.
(36) Ledinsky, M.; Löper, P.; Niesen, B.; Holovsky, J.; Moon, S. J.; Yum, J. H.; De Wolf, S.; Fejfar, A.; Ballif, C. Raman Spectroscopy of Organic−Inorganic Halide Perovskites. *J. Phys. Chem. Lett.* **2015**, *6*, 401−406.
(37) Park, B.; Jain, S. M.; Zhang, X.; Hagfeldt, A.; Boschloo, G.; Edvinsson, T. Resonance Raman and Excitation Energy Dependent Charge Transfer Mechanism in Halide-Substituted Hybrid Perovskite Solar Cells. *ACS Nano* **2015**, *9*, 2088−2101.
(38) Brivio, F.; Frost, J. M.; Skelton, J. M.; Jackson, A. J.; Weber, O. J.; Weller, M. T.; Walsh, A.; Goni, A. R.; Leguy, A. M. A.; Barnes, P. R. F.; et al. Lattice Dynamics and Vibrational Spectra of the Orthorhombic, Tetragonal, and Cubic Phases of Methylammonium Lead Iodide. *Phys. Rev. B: Condens. Matter Mater. Phys.* **2015**, *92*, 144308.
(39) Gottesman, R.; Gouda, L.; Kalanoor, B. S.; Haltzi, E.; Tirosh, S.; Rosh-Hodesh, E.; Tischler, Y.; Zaban, A.; Quarti, C.; Mosconi, E.; et al. Photoinduced Reversible Structural Transformations in Free-Standing $CH_3NH_3PbI_3$ Perovskite Films. *J. Phys. Chem. Lett.* **2015**, *6*, 2332−2338.
(40) Leijtens, T.; Hoke, E. T.; Grancini, G.; Slotcavage, D. J.; Eperon, G. E.; Ball, J. M.; De Bastiani, M.; Bowring, A. R.; Martino, N.; Wojciechowski, K.; McGehee, M. D.; Snaith, H. J.; Petrozza, A.; et al. Mapping Electric Field-Induced Switchable Poling and Structural Degradation in Hybrid Lead Halide Perovskite Thin Films. *Adv. Energy Mater.* **2015**, *5*, 1500962.
(41) Antoniadou, M.; Siranidi, E.; Vaenas, N.; Kontos, A. G.; Stathatos, E.; Falaras, P. Photovoltaic Performance and Stability of

DOI: 10.1021/acs.jpcc.5b11256
J. Phys. Chem. C 2016, 120, 2509−2519

$CH_3NH_3PbI_{3-x}Cl_x$ Perovskites. *J. Surfaces Interfaces Mater.* **2014**, *2*, 323−327.
(42) Misra, R. K.; Aharon, S.; Li, B.; Mogilyansky, D.; Visoly-Fisher, I.; Etgar, L.; Katz, E. A. Temperature- and Component-Dependent Degradation of Perovskite Photovoltaic Materials under Concentrated Sunlight. *J. Phys. Chem. Lett.* **2015**, *6*, 326−330.
(43) Kedem, N.; Brenner, T. M.; Kulbak, M.; Schaefer, N.; Levcenko, S.; Levine, I.; Abou-Ras, D.; Hodes, G.; Cahen, D. Light-Induced Increase of Electron Diffusion Length in a P-N Junction Type $CH_3NH_3PbBr_3$ Perovskite Solar Cell. *J. Phys. Chem. Lett.* **2015**, *6*, 2469−2476.
(44) Larson, A. C.; von Dreele, R. B. General Structure Analysis System; Rep. LAUR 85-748; Los Alamos Lab., 1994.
(45) Kamitsos, E. I.; Kapoutsis, J. A.; Jain, H.; Hsieh, C. H. Vibrational Study of the Role of Trivalent Ions in Sodium Trisilicate Glass. *J. Non-Cryst. Solids* **1994**, *171*, 31−45.
(46) Onoda-Yamamuro, N.; Yamamuro, O.; Matsuo, T.; Suga, H. *P*−*T* Phase Relations of $CH_3NH_3PbX_3$ (X = Cl, Br, I) Crystals. *J. Phys. Chem. Solids* **1992**, *53*, 277−281.
(47) Stoumpos, C. C.; Malliakas, C. D.; Kanatzidis, M. G. Semiconducting Tin and Lead Iodide Perovskites with Organic Cations: Phase Transitions, High Mobilities, and Near-Infrared Photoluminescent Properties. *Inorg. Chem.* **2013**, *52*, 9019−9038.
(48) Choi, J. J.; Yang, X.; Norman, Z. M.; Billinge, S. J. L.; Owen, J. S. Structure of Methylammonium Lead Iodide within Mesoporous Titanium Dioxide: Active Material in High Performance Perovskite Solar Cells. *Nano Lett.* **2014**, *14*, 127−133.
(49) Wei, M.; Chung, Y.-H.; Xiao, Y.; Chen, Z. Color Tunable Halide Perovskite $CH_3NH_3PbBr_{3-x}Cl_x$ Emission via Annealing. *Org. Electron.* **2015**, *26*, 260−264.
(50) Wehrenfennig, C. Ultrafast Spectroscopy of Charge Separation, Transport, and Recombination Processes in Functional Materials for Thin-Film Photovoltaics, Ph.D. Thesis, Oxford University, 2014.
(51) Kitazawa, N.; Watanabe, Y.; Nakamura, Y. Optical Properties of $CH_3NH_3PbX_3$ (X = Halogen) and Their Mixed-Halide Crystals. *J. Mater. Sci.* **2002**, *37*, 3585−3587.
(52) Nakamoto, K. in *Infrared and Raman Spectra of Inorganic and Coordination Compounds, Part A, Theory and Applications in Inorganic Chemistry*, 6th ed.; Wiley: New York, 2009.
(53) Baikie, T.; Barrow, N. S.; Fang, Y.; Keenan, P. J.; Slater, P. R.; Piltz, R. O.; Gutmann, M.; Mhaisalkar, S. G.; White, T. J. A Combined Single Crystal Neutron/X-Ray Diffraction and Solid-State Nuclear Magnetic Resonance Study of the Hybrid Perovskites $CH_3NH_3PbX_3$ (X = I, Br and Cl). *J. Mater. Chem. A* **2015**, *3*, 9298−9307.
(54) Maalej, A.; Abid, A.; Kallel, A.; Daoud, A.; Lautie, A.; Romain, F. Phase Transitions and Crystal Dynamics in the Cubic Perovskite $CH_3NH_3PbCl_3$. *Solid State Commun.* **1997**, *103*, 279−284.
(55) Theoret, A.; Sandorfy, C. The Infrared Spectra of Solid Methylammonium Halides. II. *Spectrochim. Acta* **1967**, *23A*, 519−542.
(56) Matsuo, T.; Ueda, M.; Suga, H. Calorimetric and Spectroscopic Studies of the Critical Phase Transition in $(CH_3NH_3)_2[SnCl_6]$. *Chem. Phys. Lett.* **1981**, *82*, 577−580.
(57) Sadhanala, A.; Deschler, F.; Thomas, T. H.; Dutton, E.; Goedel, K. C.; Hanusch, F. C.; Lai, M. L.; Steiner, U.; Bein, T.; Docampo, P.; et al. Preparation of Single-Phase Films of $CH_3NH_3Pb(I_{1-x}Br_x)_3$ with Sharp Optical Band Edges. *J. Phys. Chem. Lett.* **2014**, *5*, 2501−2505.
(58) Onoda-Yamamuro, N.; Matsuo, T.; Duga, H. Dielectric Study of $CH_3NH_3PbX_3$ (X = Cl, Br, I). *J. Phys. Chem. Solids* **1992**, *53*, 935−939.
(59) Popović, Z. V.; Kontos, A. G.; Raptis, Y. S.; Isobe, M.; Ueda, Y. Raman Scattering Study of β-$Sr_{0.33}V_2O_5$ in Charge Disordered and Ordered Phase. *J. Phys.: Condens. Matter* **2006**, *18*, 7779−7787.
(60) Mitzi, D. B. Templating and Structural Engineering in Organic−Inorganic Perovskites. *J. Chem. Soc. Dalt. Trans.* **2001**, *1*, 1−12.
(61) Michels, J. P. J.; Schouten, J. A. Broadening of Vibrational Raman Spectra by Concentration Fluctuations: A Molecular Dynamics Survey. *Int. J. Thermophys.* **2001**, *22*, 339−355.
(62) Das, A.; Kumar, K. Raman Anisotropic Linewidth Dependence on the Van Der Waals Volume of the Interacting Systems. *J. Raman Spectrosc.* **1999**, *30*, 547−549.
(63) Rao, A. M.; Chen, J.; Richter, E.; Schlecht, U.; Eklund, P. C.; Haddon, R. C.; Venkateswaran, U. D.; Kwon, Y. K.; Tománek, D. Effect of van Der Waals Interactions on the Raman Modes in Single Walled Carbon Nanotubes. *Phys. Rev. Lett.* **2001**, *86*, 3895−3898.
(64) Wang, C. H.; Wright, R. B. Nature of the λ Transition and the 56 cm^{-1} Anomalous Raman Mode in Ammonium Bromide. *J. Chem. Phys.* **1972**, *57*, 4401.
(65) Jeon, N. J.; Noh, J. H.; Yang, W. S.; Kim, Y. C.; Ryu, S.; Seo, J.; Seok, S. Il. Compositional Engineering of Perovskite Materials for High-Performance Solar Cells. *Nature* **2015**, *517*, 476−480.
(66) Knop, O.; Wasylishen, R. E.; White, M. A.; Cameron, T. S.; Van Oort, M. J. M. Alkylammonium Lead Halides. Part 2. $CH_3NH_3PbX_3$ (X = Cl, Br, I) Perovskites: Cuboctahedral Halide Cages with Isotropic Cation Reorientation. *Can. J. Chem.* **1990**, *68*, 412−422.
(67) Carabatos-Nedelec, C.; Becker, P. Order−Disorder and Structural Phase Transitions in Solid-State Materials by Raman Scattering Analysis. *J. Raman Spectrosc.* **1997**, *28*, 663−671.
(68) Hagemann, H.; Gomes, S.; Renaudin, G.; Yvon, K. Raman Studies of Reorientation Motions of $[BH_4]^-$ Anions in Alkali Borohydrides. *J. Alloys Compd.* **2004**, *363*, 126−129.
(69) Hetmanczyk, J.; Hetmanczyk, L.; Migdal-Mikuli, A.; Mikuli, E. Vibrations and Reorientations of NH_3 Molecules in $[Mn(NH_3)_6](ClO_4)_2$ Studied by Infrared Spectroscopy and Theoretical (DFT) Calculations. *Spectrochim. Acta, Part A* **2015**, *136*, 1515−1522.

NOTE ADDED AFTER ASAP PUBLICATION

An error was found in the last paragraph of section 3.2 in the version published to the Web on January 26, 2016. This is corrected in the version published to the Web on January 27, 2016.

DOI: 10.1021/acs.jpcc.5b11256
J. Phys. Chem. C 2016, 120, 2509−2519

Supporting Information

Halogen Effects on Ordering and Bonding of $CH_3NH_3^+$ in $CH_3NH_3PbX_3$ (X = Cl, Br, I) Hybrid Perovskites: A vibrational spectroscopic study

Ralf G. Niemann,[a‡] Athanassios G. Kontos,[b‡] Dimitrios Palles,[c] Efstratios I. Kamitsos,[c] Andreas Kaltzoglou,[b] Federico Brivio,[a] Polycarpos Falaras,[b] and Petra J. Cameron[a]*

[a] Department of Chemistry, University of Bath, Bath BA2 7AY, United Kingdom

[b] Institute of Nanoscience and Nanotechnology, NCSR Demokritos, 15310 Athens, Greece

[c] Theoretical and Physical Chemistry Institute, National Hellenic Research Foundation, 11635 Athens, Greece

[§] These authors contributed equally.

* To whom correspondence should be addressed.

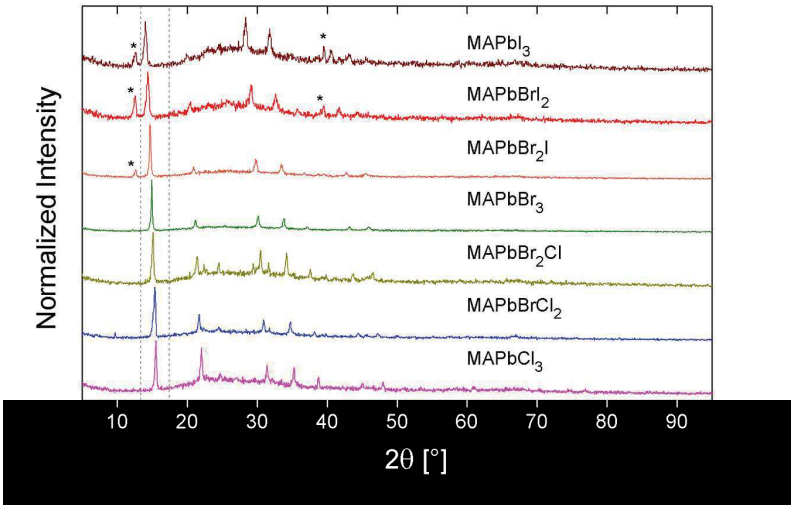

Figure S1: Full powder XRD patterns of all halide perovskites examined in this study. Reflections attributed to unconverted PbI_2 are denoted with asterisks.

Table S1: Lattice parameters from XRD data for $MAPbX_3$ perovskites

Composition	Crystal system	a = b (Å)	c (Å)
$MAPbCl_3$	Cubic	5.675(2)	5.675(2)
$MAPbBrCl_2$	Cubic	5.755(3)	5.755(3)
$MAPbBr_2Cl$	Cubic	5.849(3)	5.849(3)
$MAPbBr_3$	Cubic	5.954(2)	5.954(2)
$MAPbBr_2I$	Tetragonal	8.449(4)	11.997(4)
$MAPbBrI_2$	Tetragonal	8.682(6)	12.407(6)
$MAPbI_3$	Tetragonal	8.861(2)	12.653(2)

Table S2: Optical band gaps (E_g) and laser excitation energies for the Raman and PL investigation of perovskite materials. (Res) stands for Resonant, (Off-res) for off-resonance Raman excitation and (PL) for Photoluminescence which occurred upon excitation in the vicinity of E_g.

Perovskite	E_g (eV)	514 nm[t] *(2.41 eV)*	785 nm[t,w] *(1.58 eV)*	1064 nm *(1.17 eV)*
$MAPbCl_3$	3.06	Off-res	Off-res	Off-res
$MAPbBrCl_2$	2.78	Off-res	Off-res	Off-res
$MAPbBr_2Cl$	2.53	Off-res	Off-res	Off-res
$MAPbBr_3$	2.33	Res – PL	Off-res	Off-res
$MAPbBr_2I$	2.08	Res – PL	Off-res	Off-res
$MAPbBrI_2$	1.81	Res – PL	Off-res	Off-res
$MAPbI_3$	1.61	Res	PL	Off-res

[t] Extra Low-temperature measurements
[w] Extra Low-frequency range accessed

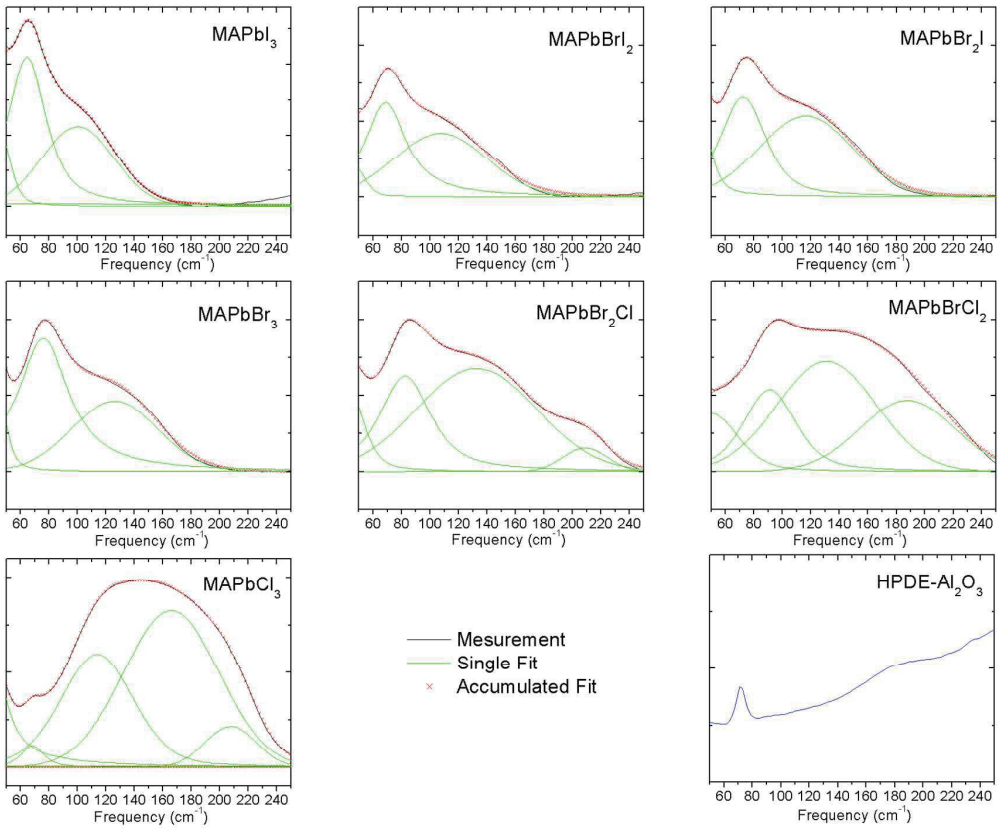

Figure S2: Fitting analysis of the far-IR absorption spectra (black lines). Fitting spectra are shown with red symbols and fitting components with green lines. Last graph shows spectrum of reference HPDE-Al_2O_3.

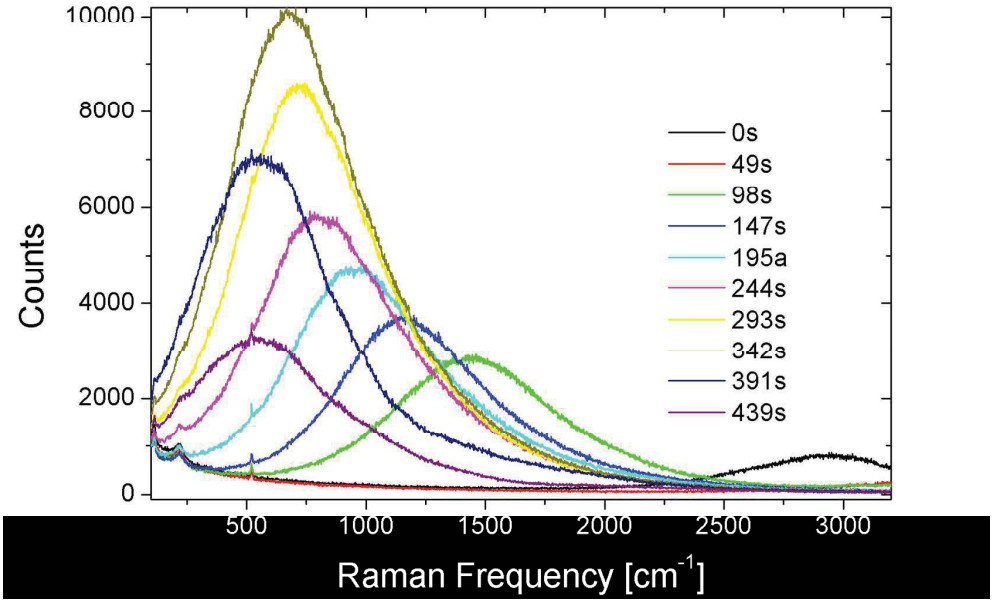

Figure S3: Spectra show shifting of PL during measuring $MAPbI_2Br$ under resonance (514 nm) conditions, indicating phase segregation.

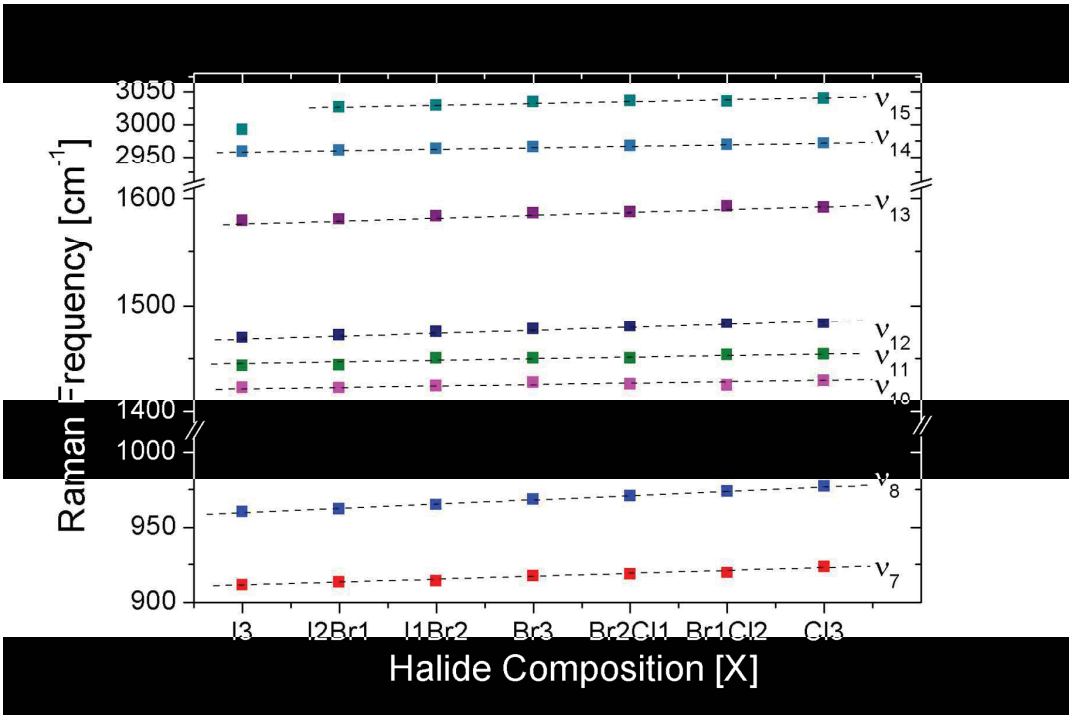

Figure S4: Raman frequency shifts of strongest MA modes above 900 cm^{-1} for various halogen contents in $MAPbX_3$.

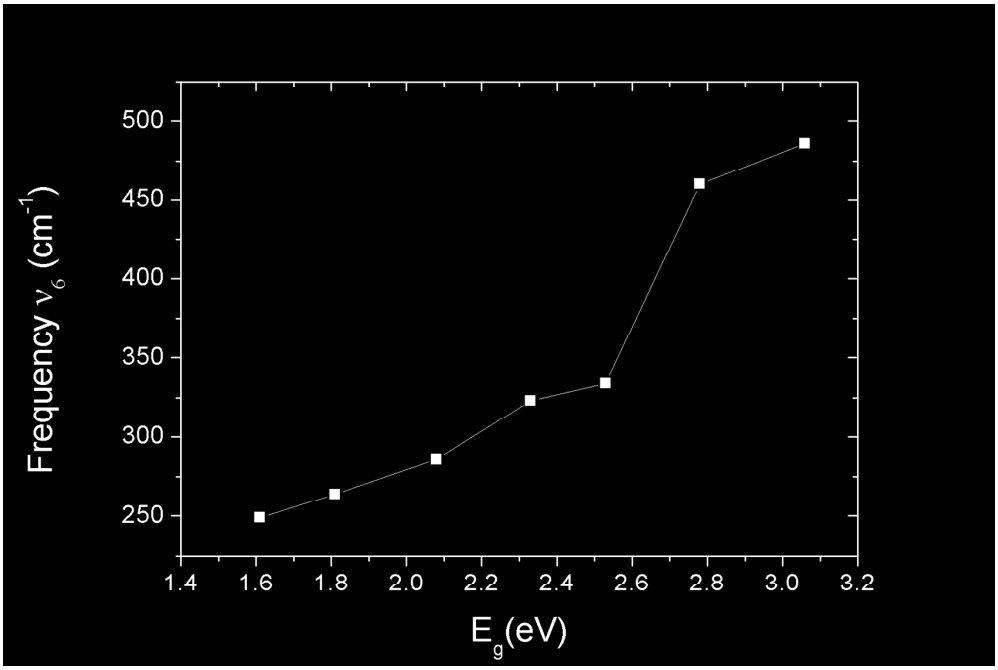

Figure S5: The frequency of the ν_6 torsional mode at RT against the band gaps for all measured $MAPbX_3$ derivatives.

Table S3: Overview of main MA Raman frequency peaks above 900 cm^{-1}, measured at 100 K by excitation at 785 nm, for MA lead derivatives MAPb[X].

Mode/[X]	I2Br	IBr2	Br3	Br2Cl	BrCl2	Cl3	Assignment
ν_7	912	915	918	923	925	927	ρ (MA)
ν_8	965	969	972	975	976	979	ν (CN)
ν_9	1250	1252	1253	1255	1255		ρ (MA)
ν_{10}	1420	1421	1428	1427	1426	1430	δ_s (CH_3)
ν_{11}	1454	1455	1463	1458	1458	1464	δ_a (CH_3)
ν_{12}	1472	1476	1483	1486	1488		δ_s (NH_3^+)

5.2.3 Contemporary assessment

After the publication of our study *Halogen Effects on Ordering and Bonding of $CH_3NH_3^+$ in $CH_3NH_3PbX_3$ (X = Cl, Br, I) Hybrid Perovskites: A Vibrational Spectroscopic Study*, several other studies were able to confirm its results in a similar fashion. For example, Xie *et al.* used a 1030 nm Raman line for an off-resonance study and confirmed a strong interaction between the cation and the cage that stems from the amine group *via* hydrogen bonding.[20] This is based upon a comparison of modes in the methylammonium halide salt and the caged perovskite.

Three consecutive studies by Brivio *et al.* and Ivanovska *et al.* and Leguy *et al.* used a similar combined approach by measuring the resonance and off-resonance Raman spectra of $MAPbX_3$ (X = Cl, Br, I) and comparing those to an ab-initio DFT phonon model.[6, 7, 8] These studies supported our assumptions about the increased ordering of the MA^+ below the orthorhombic phase transition temperature. Moreover, the phonon simulations confirm that in fact the MA^+ ordering is causing the torsional mode pairs at lower temperatures, which has also been predicted by our publication, based on a peak broadening at lower temperatures especially for the lighter halides.[7] The reason for the increase in MA-PbX_3 interaction is presumably the occurrence of medium-to-strong hydrogen bonding in the orthorhombic phase, caused by the increasing spacial restriction for smaller halides.[21, 8]

5.3 Conclusions

This chapter set out to investigate vibrational properties of the MA^+ cation by means of Raman and IR spectroscopy and to refine the mechanisms of bonding and ordering in the $MAPbX_3$ (X = Cl, Br, I) perovskite. Our study was placed in a background of multiple and conflicting spectra being reported for the $MAPbI_3$ perovskite, caused by numerous light-induced effects, that can occur during the measurement. Therefore, the most crucial result is the report of the 'true' vibrational spectrum, acquired with off-resonance Raman and far-IR spectroscopy. Furthermore, the results indicate specific bonding schemes for inorganic cage vibrations as well as the internal MA^+ modes at higher frequencies. The low-frequency Pb-X vibrations < 200 cm^{-1} fit well to the model of an harmonic oscillator and therefore show little contribution from the relatively light MA^+ cation. On the other hand, almost all internal MA^+ vibrations are progressively red-shifted for heavier halide derivatives $MAPbX_3$, indicating an increasing interaction for lighter halides with the inorganic cage. For the case of the $MAPbBr_3$, the order-disorder activation energy was quantified to be $E_a = 7.5 \pm 1.0$ kJ/mol (or 78 ± 10 meV). The low temperature study makes torsional mode pairs apparent, which shows the occurrence of new bonding schemes. These are proposed to arise below the transition temperature to the orthorhombic phase. This can be seen from the increase in line-width of the highly sensitive torsional mode. The orthorhombic phase transition might even induce long-range order between the MA^+ cation in the low-symmetry phase.

Several other groups confirmed our measurements and interpretation in consecutive studies, as outlined above. In the supplementary information of this paper, the development of a phase segregation is shown of Br-I perovskite systems under the Raman probe, which was the second report of this phenomenon after Hoke *et al.* [10] and was confirmed later by several other publications.[22, 23, 24, 11]

5.4 Bibliography

[1] "The interface is still the device," *Nature Materials*, vol. 11, no. 2, p. 91, 2012.

[2] J. Even, M. Carignano, and C. Katan, "Molecular disorder and translation/rotation coupling in the plastic crystal phase of hybrid perovskites," *Nanoscale*, vol. 8, pp. 6222–6236, 2016.

[3] F. Brivio, A. B. Walker, and A. Walsh, "Structural and electronic properties of hybrid perovskites for high-efficiency thin-film photovoltaics from first-principles," *APL Materials*, vol. 1, no. 4, p. 042111, 2013.

[4] C. Quarti, G. Grancini, E. Mosconi, P. Bruno, J. M. Ball, M. M. Lee, H. J. Snaith, A. Petrozza, and F. D. Angelis, "The Raman Spectrum of the CH3NH3PbI3 Hybrid Perovskite: Interplay of Theory and Experiment," *Journal of Physical Chemistry Letters*, vol. 5, pp. 279–284, 2014.

[5] C. Quarti, E. Mosconi, and F. De Angelis, "Interplay of Orientational Order and Electronic Structure in Methylammonium Lead Iodide: Implications for Solar Cells Operation," *Chemistry of Materials*, vol. 26, no. 22, pp. 6557–6569, 2014.

[6] F. Brivio, J. M. Frost, J. M. Skelton, A. J. Jackson, O. J. Weber, M. T. Weller, A. Walsh, A. R. Goni, A. M. A. Leguy, and P. R. Barnes, "Lattice dynamics and vibrational spectra of the orthorhombic, tetragonal and cubic phases of methylammonium lead iodide," *Physical Review B*, vol. 92, p. 144308, 2015.

[7] A. M. A. Leguy, A. R. Goni, J. M. Frost, J. Skelton, F. Brivio, X. Rodriguez-Martínez, O. J. Weber, A. Pallipurath, M. I. Alonso, M. Campoy-Quiles, M. T. Weller, J. Nelson, A. Walsh, and P. R. F. Barnes, "Dynamic disorder, phonon lifetimes, and the assignment of modes to the vibrational spectra of methylammonium lead halide perovskites," *Physical Chemistry Chemical Physics*, vol. 18, pp. 27051–27066, 2016.

[8] T. Ivanovska, C. Quarti, G. Grancini, A. Petrozza, F. De Angelis, A. Milani, and G. Ruani, "Vibrational Response of Methylammonium Lead Iodide: From Cation Dynamics to Phonon-Phonon Interactions," *ChemSusChem*, vol. 9, pp. 2994–3004, 2016.

[9] B.-W. Park, S. M. Jain, X. Zhang, A. Hagfeldt, G. Boschloo, and P. E. T. Al, "Resonance Raman and Excitation Energy Dependent Charge Transfer Mechanism in Halide-Substituted Hybrid Perovskite Solar Cells," *ACS Nano*, vol. 9, no. 2, pp. 2088–2101, 2015.

[10] E. T. Hoke, D. J. Slotcavage, E. R. Dohner, A. R. Bowring, H. I. Karunadasa, and M. D. McGehee, "Reversible photo-induced trap formation in mixed-halide hybrid perovskites for photovoltaics," *Chemical Science*, vol. 6, pp. 613–617, 2015.

[11] P. Gratia, G. Grancini, J.-N. Audinot, X. Jeanbourquin, E. Mosconi, I. Zimmermann, D. Dowsett, Y. Lee, M. Grätzel, F. De Angelis, K. Sivula, T. Wirtz, and

M. K. Nazeeruddin, "Intrinsic Halide Segregation at Nanometer Scale Determines the High-Efficiency of mixed cation/mixed halide Perovskite Solar Cells.," *Journal of the American Chemical Society*, vol. 138, no. 49, pp. 15821–15824, 2016.

[12] R. Gottesman, L. Gouda, B. S. Kalanoor, E. Haltzi, S. Tirosh, E. Rosh-Hodesh, Y. Tischler, A. Zaban, C. Quarti, E. Mosconi, and F. De Angelis, "Photoinduced Reversible Structural Transformations in Free-Standing CH3NH3PbI3 Perovskite Films," *Journal of Physical Chemistry Letters*, pp. 2332–2338, 2015.

[13] B. S. Kalanoor, L. Gouda, R. Gottesman, S. Tirosh, E. Haltzi, A. Zaban, and Y. R. Tischler, "Third order optical nonlinearities in organometallic methylammonium lead iodide perovskite thin films," *ACS Photonics*, vol. 3, pp. 361–370, 2016.

[14] J. C. Johnson, Z. Li, P. F. Ndione, and K. Zhu, "Third-Order Nonlinear Optical Properties of Methylammonium Lead Halide Perovskite Films," *Journal of Materials Chemistry C*, vol. 4, pp. 4847–4852, 2016.

[15] Y.-Y. Zhang, S. Chen, P. Xu, H. Xiang, X.-G. Gong, A. Walsh, and S.-H. Wei, "Intrinsic Instability of the Hybrid Halide Perovskite Semiconductor CH3NH3PbI3," *arXiv preprint*, p. 1506.01301, 2015.

[16] A. Walsh, "Principles of Chemical Bonding and Band Gap Engineering in Hybrid Organic-Inorganic Halide Perovskites," *Journal of Physical Chemistry C*, vol. 119, pp. 5755–5760, 2015.

[17] M. Ledinsky, P. Löper, B. Niesen, J. Holovsky, J.-h. Yum, S. D. Wolf, A. Fejfar, and C. Ballif, "Raman Spectroscopy of Organic-Inorganic Halide Perovskites," *Journal of Physical Chemistry Letters*, vol. 6, pp. 401–406, 2015.

[18] A. C. Larson and R. B. von Dreele, "General Structure Analysis System;," *Report LAUR 85-748; Los Alamos Laboratory: Los Alamos*, 1994.

[19] R. G. Niemann, A. G. Kontos, D. Palles, E. I. Kamitsos, A. Kaltzoglou, F. Brivio, P. Falaras, and P. J. Cameron, "Halogen Effects on Ordering and Bonding of CH3NH3+ in CH3NH3PbX3 (X = Cl, Br, I) Hybrid Perovskites: A vibrational spectroscopic study," *The Journal of Physical Chemistry C*, vol. 120, no. 5, pp. 2509–2519, 2016.

[20] L.-Q. Xie, T. Zhang, L. Chen, N. Guo, Y. Wang, G. Liu, J.-R. Wang, J.-Z. Zhou, J.-W. Yan, Y. Zhao, B. Mao, and Z.-q. Tian, "Organic-inorganic Interactions of Single Crystalline Organolead Halide Perovskites Studied by Raman Spectroscopy," *Physical Chemistry Chemical Physics*, vol. 18, pp. 18112–18118, 2016.

[21] M. T. Weller, O. J. Weber, P. F. Henry, A. M. D. Pumpo, and T. C. Hansen, "Complete structure and cation orientation in the perovskite photovoltaic methylammonium lead iodide between 100 and 352 K," *Chemical Communications*, vol. 51, pp. 4180–4183, 2015.

[22] F. Brivio, C. Caetano, and A. Walsh, "Thermodynamic Origin of Photoinstability in The CH3NH3Pb(I1-xBrx)3 Hybrid Halide Perovskite Alloy," *The Journal of Physical Chemistry Letters*, vol. 7, pp. 1083–1087, 2016.

[23] S. J. Yoon, S. Draguta, J. S. Manser, O. Sharia, W. F. Schneider, M. Kuno, and P. V. Kamat, "Tracking Iodide and Bromide Ion Movement in Mixed Halide Lead Perovskites during Photoirradiation," *ACS Energy Letters*, vol. 1, no. 1, pp. 290–296, 2016.

[24] B. A. Rosales, L. Men, S. D. Cady, M. P. Hanrahan, A. J. Rossini, and J. Vela, "Persistent Dopants and Phase Segregation in Organolead Mixed-Halide Perovskites," *Chemistry of Materials*, vol. 28, no. 19, pp. 6848–6859, 2016.

Chapter 6

Conclusions

Pierre Curie voluntarily exposed his arm to the action of radium for several hours. This resulted in damage resembling a burn that developed progressively and required several months to heal. Henri Becquerel had by accident a similar burn as a result of carrying in his vest pocket a glass tube containing radium salt. He came to tell us of this evil effect of radium, exclaiming in a manner at once delighted and annoyed: 'I love it, but I owe it a grudge.'

Marie Curie
1867 - 1934

The research that was conducted throughout this thesis fulfilled all of the three objectives that are listed in chapter 1: (a) Optimisation of processing parameters that influence the perovskite thin-film formation regarding the development of a solar cells fabrication routine. (b) Development of new perovskite materials with an enhanced stability, specifically against water-induced degradation. (c) Analysis of underlying structural motives of organic-inorganic hybrid perovskites regarding their macroscopic response and stability.

In particular, (a) the optimisation of processing parameters and development of a solar cell fabrication routine is shown in chapter 3: Firstly, the substrate treatment procedure was optimised regarding different cleaning treatments and their influence on the deposition of the compact TiO_2 layer and its electrochemical behaviour. Secondly, a solar cell fabrication routine was developed and optimised regarding an optimum layout that allows a fast measurement of several pixels at once and therefore makes it easier to deal with statistical variety that often underlies the fabrication process. Finally, two novel fabrication routines were presented as part of this thesis; a crystallisation of the $MAPbI_3$ layer at lower temperatures is presented (about 84 °C) through the usage of a high air-flow rate of a heat-gun. Also, an easy fabrication route that uses a vacuum assisted MAI vapour conversion of a PbI_2 layer allows for the perovskite conversion

independent of environmental factors, a condition that usually requires a glove box.

The development of new perovskite materials with an improved water resistance (b) is shown in chapter 4: Two chemical A-site derivatives of the standard $MAPbI_3$ system were analysed. Firstly, Cs^+ was employed, which does not form a stable perovskite RT structure but can be used as a mixed cation system $Cs_xMA_{1-x}PbI_3$. We show the structural limitations of this system with a substitution limit of $x > 0.13$, that is not solely caused by steric factors but indicates chemical bonding contributions. Secondly, the organic cation Az^+ was used, which likewise does not form a dark perovskite phase at RT. However, mixtures of $Az_xMA_{1-x}PbI_3$ showed to be stable for small Az-ratios of about $x \leq 0.05$, and improved the photovoltaic performance. Notably, both systems, Cs^+ and Az^+ solid state solutions, improved the water-resistance of the resulting perovskite. An initial assessment of the instability of the $AzPbI_3$ was undertaken with Raman spectroscopy; the results show a strong shift of the amine group, which indicates significant $\mathrm{N{-}H} \cdots X$ bonding, which could offer an alternative bonding scheme to the $[PbX_6]^{4-}$ octahedra and tear down the three-dimensional structure.

Finally, the structural motives and dynamics were analysed (c) with spectroscopic methods in chapter 5: First and foremost, the acquisition of an unambiguous spectrum was shown by measuring under various conditions (on- and off-resonance) and by comparing the spectral response of different halide derivatives of the $MAPbX_3$ system (X = Cl, Br, I). It showed that the low-frequency modes were caused by the $[PbX_6]^{4-}$ octahedra and matched the model of an harmonic oscillator, thus showing a negligible influence from the organic cation.[1] The internal MA^+ vibrations were progressively red-shifted, as expected, which shows an increasing interaction with the inorganic lattice. Temperature dependent measurements for the $MAPbBr_3$ between 100 K and RT revealed an order-disorder transition with an activation energy of about $E_a = 7.5 \pm 1.0$ kJ. Measurement of all $MAPbX_3$ species at 100 K revealed new bonding schemes that appear at low temperatures, possibly caused by long-range order between the MA^+ cations in the orthorhombic low-symmetry phase.

A graphical summary is given in figure 6-1.

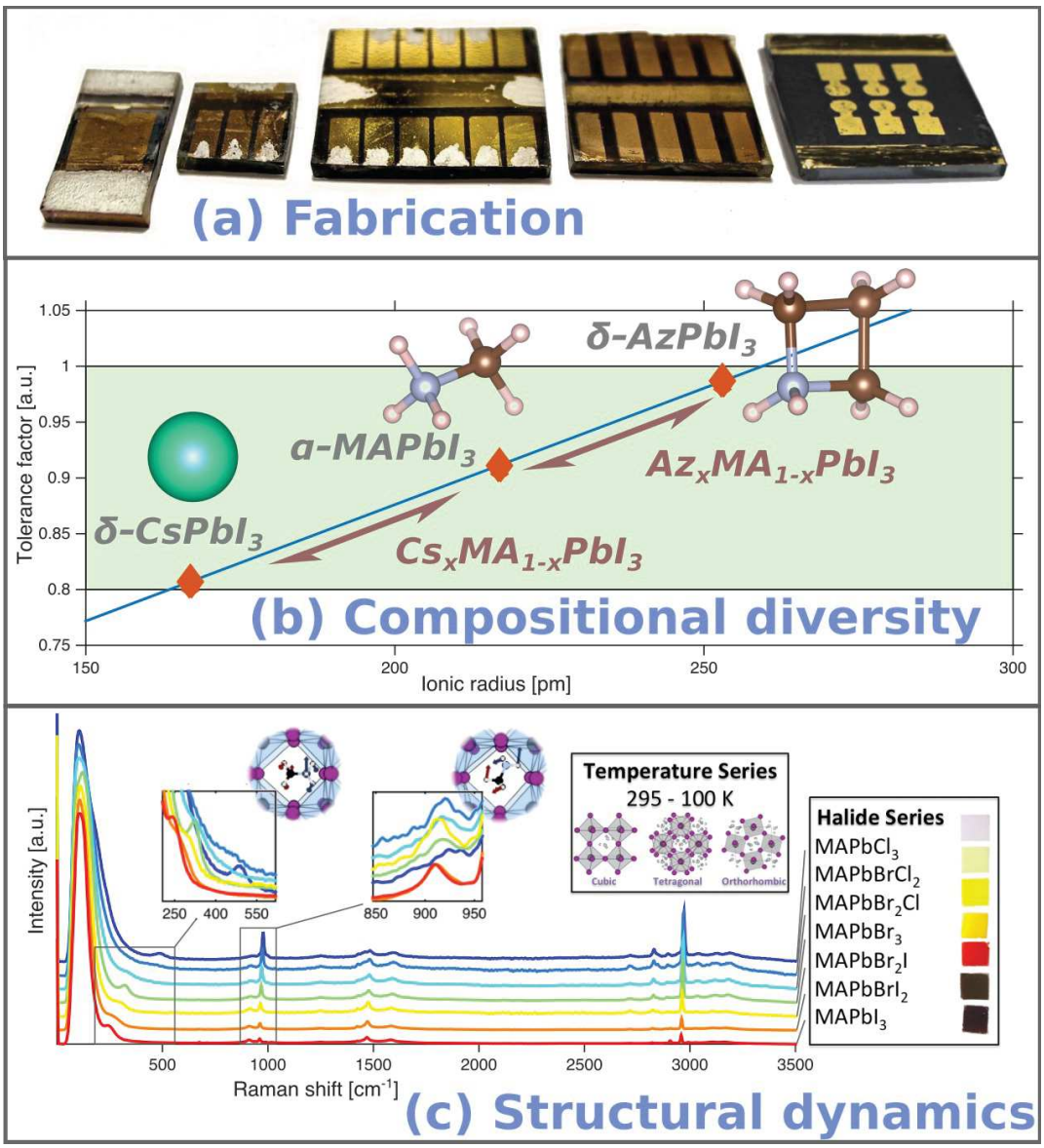

Figure 6-1: Summary of the results from this thesis: (a) Optimisation of fabrication parameters. (b) Exploration of the compositional diversity of A-site derivatives of the $MAPbI_3$ perovskite. (c) Structural dynamics, measured with spectroscopic methods (Reproduced in part with permission.[1] Copyright 2016 American Chemical Society.)

6.1 Impact of work

The work presented in this thesis has already led to several follow-up studies, that build upon the published parts of this work. The optimisation of perovskite fabrication routines (a) and developed V-VASP process[2] was further analysed regarding interfacial properties compared to other deposition methods and showed excellent contact properties and the formation of a compact film with a favourable morphology.[3] The process was also shown to be up-scalable to produce solar modules with an efficiency of 5.9 %.[4, 5] The modification of the V-VASP process to fabricate high hysteresis cells gave another strong indication that the vacancy-assisted movement of ions is responsible for the anomalous hysteresis in IV curves. This theory now seems to be broadly accepted in literature.[6, 7, 8, 9, 10] Notably, Tress *et al.* showed that the pile up of electric charges, which increases the electric field, can reduce extraction barriers and increase cell performance; this effect becomes apparent in an inverse hysteresis,[11] which typically occurs in mixed-cation, mixed-halide perovskites, that are commonly used for > 20 % PSC.[12]

The spectroscopic analysis (c) and acquisition of the Raman spectrum of $MAPbX_3$ (X = Cl, Br, I) in off-resonance conditions[1] was later on repeated by Xie *et al.* with a 1030 nm Raman line; the results confirm our data and show a strong interaction between the cation and the cage that stems from the amine group *via* hydrogen bonding.[13] Three other studies used a combined approach by measuring the Raman spectrum of $MAPbX_3$ in resonance and off-resonance conditions and compared the results to a DFT model.[14, 15, 16] These studies suggested new bonding schemes and long-range order of the MA^+ in the low-temperature phase, further supported by DFT modelling and in accordance with our findings. Low-temperature inelastic neutron scattering showed unexpected cation dynamics, that are presumably driven by zero-point-energy fluctuations and thermally activated cation motions and make an improved model of the low-temperature phase necessary.[17] Our study also includes the second report on photo-induced phase segregation for Br-I mixed halide perovskites after Hoke *et al.* [18] and the effect has since been confirmed by several other publications.[19, 20, 21]

In summary the published part of this thesis has received a considerable feedback and follow up studies within about a year since publishing. This goes for the V-VASP process development study, the hysteresis study and the $MAPbX_3$Raman analysis,[2, 22, 1] as outlined above. The investigated Cs-MA perovskite system was published only recently (October 2016) and has not been cited yet (stand 26^{th} of January 2016).[23] The work on Az-containing perovskites is still under review.[24]

6.2 Future work

The results presented in this work contributed towards the optimisation of new fabrication techniques, as well as the exploration of the perovskite's landscape regarding more stable materials and finally an analysis of structural dynamics, as explained in the previous sections. If the work in this thesis was to be extended, it could be done for certain studies in particular or by combining the methodology of several parts to gain a better understanding of the structure - property - performance relationship.

The V-VASP process gives an easily accessible route to well-performing cells that can be upscaled to give modules. If the process was to be further optimised, it would be desirable to have a vapour pressure control unit in order to increase reproducibility of the process. This is of importance because it was shown that the conversion parameters critically influence detrimental effects, such as hysteresis.

chap5 The analysis of different A-site cation mixtures in this thesis shows that the Cs-MA system and the Az-MA system have a miscibility gap, against the predictions given by the Goldschmidt tolerance factor. While this work quantifies the boundaries of this substitution limit, the underlying mechanism is yet unknown. A detailed and comprehensive exploration of other cation mixtures would give further insight into the material's compositional landscape, as opposed to a '*shake and bake*' synthesis of well-performing multi-cation solid-state solutions. Of special interest would be an analysis of the complete structure of such solid-state solutions with emphasis on the organic cation. The bonding motives between the organic cation and inorganic lattice seem critical for their stability, and structural similarity seems to favour the formation of well-performing solid-state solutions.[25] Employment of different types of organic cations could induce synergistic effects for the interaction with the octahedral network (*e.g.* for the Cs-FA-MA-Rb perovskite[12]) or induce spinodal phase segregation (*e.g.* for the Cs-MA perovskite[23]). A strong link between crystallinity, photo-stability and electronic performance has already been shown,[26] but the underlying mechanism remains inconclusive.

The spectroscopic analysis of the $MAPbX_3$ system gave valuable information, which, in combination with other studies such as XRD and neutron scattering,[27, 28] renders a complete pictures of the structure and its dynamics. However, other related structures such as the $FAPbI_3$ were solved in their higher temperature phases, but no satisfactory model exists for their low-temperature structure.[29, 25] A combined approach with a structural analysis combined with a vibrational analysis (similar to the one reported in this thesis) would facilitate the solving of the corresponding structure.

Overall, the recent development and research has already reduced the costs of

renewable energies to a level equal to carbon fuels and created an '*irreversible momentum of clean energy*'[30]. This momentum is to a considerable extent based on silicon-based PV systems, which are currently holding the largest market share; however they are approaching a practical limit in terms of efficiency.[31] In order to continue this trend new materials need to be established, where less is needed (higher absorption values) and the processing becomes cheaper (low processing temperature). The results presented in this thesis will hopefully contribute an infinitesimal step forward to keep this momentum going.

6.3 Bibliography

[1] R. G. Niemann, A. G. Kontos, D. Palles, E. I. Kamitsos, A. Kaltzoglou, F. Brivio, P. Falaras, and P. J. Cameron, "Halogen Effects on Ordering and Bonding of CH3NH3+ in CH3NH3PbX3 (X = Cl, Br, I) Hybrid Perovskites: A vibrational spectroscopic study," *The Journal of Physical Chemistry C*, vol. 120, no. 5, pp. 2509–2519, 2016.

[2] S. Casaluci, L. Cina, A. Pockett, P. S. Kubiak, R. G. Niemann, A. Reale, A. Di Carlo, and P. J. Cameron, "A Simple Approach for the Fabrication of Perovskite Solar Cells in Air," *Journal of Power Sources*, vol. 297, pp. 504–510, 2015.

[3] F. Matteocci, Y. Busby, J.-J. Pireaux, G. Divitini, S. Cacovich, C. Ducati, and A. Di Carlo, "Interface and Composition Analysis on Perovskite Solar Cells," *ACS Applied Materials and Interfaces*, vol. 7, no. 47, pp. 26176–26183, 2015.

[4] A. Fakharuddin, A. L. Palma, F. D. Giacomo, S. Casaluci, F. Matteocci, Q. Wali, M. Rauf, A. D. Carlo, T. M. Brown, and R. Jose, "Solid state perovskite solar modules by vacuum-vapor assisted sequential deposition on Nd:YVO 4 laser patterned rutile TiO 2 nanorods," *Nanotechnology*, vol. 26, no. 49, p. 494002, 2015.

[5] T. Gatti, S. Casaluci, M. Prato, M. Salerno, F. Di Stasio, A. Ansaldo, E. Menna, A. Di Carlo, and F. Bonaccorso, "Boosting Perovskite Solar Cells Performance and Stability through Doping a Poly-3(hexylthiophene) Hole Transporting Material with Organic Functionalized Carbon Nanostructures," *Advanced Functional Materials*, vol. 26, no. 41, pp. 7443–7453, 2016.

[6] A. Walsh, "Principles of Chemical Bonding and Band Gap Engineering in Hybrid Organic-Inorganic Halide Perovskites," *Journal of Physical Chemistry C*, vol. 119, pp. 5755–5760, 2015.

[7] J. Haruyama, K. Sodeyama, L. Han, and Y. Tateyama, "First-Principles Study of Ion Diffusion in Perovskite Solar Cell Sensitizers," *Journal of the American Chemical Society*, vol. 137, no. 32, pp. 10048–10051, 2015.

[8] D. Yang, W. Ming, H. Shi, L. Zhang, and M. Du, "Fast diffusion of native defects and impurities in perovskite solar cell material," *Chemistry of Materials*, vol. 28, no. 12, pp. 4349–4357, 2016.

[9] I. Levine, P. K. Nayak, J. Tse, W. Wang, N. Sakai, S. Van Reenen, T. M. Brenner, S. Mukhopadhyay, H. J. Snaith, G. Hodes, D. Cahen, and S. V. Reenen, "Interface-Dependent Ion Migration/Accumulation Controls Hysteresis in MAPbI 3 Solar Cells," *Journal of Physical Chemistry C*, vol. 120, no. 30, pp. 16399–16411, 2016.

[10] J. M. Frost and A. Walsh, "What Is Moving in Hybrid Halide Perovskite Solar Cells?," *Accounts of Chemical Research*, vol. 49, no. 3, pp. 528–535, 2016.

[11] W. Tress, J. P. Correa Baena, M. Saliba, A. Abate, and M. Graetzel, "Inverted Current-Voltage Hysteresis in Mixed Perovskite Solar Cells: Polarization, Energy

Barriers, and Defect Recombination," *Advanced Energy Materials*, p. 1600396, 2016.

[12] M. Saliba, T. Matsui, K. Domanski, J.-Y. Seo, A. Ummadisingu, S. M. Zakeeruddin, J.-P. Correa-Baena, W. R. Tress, A. Abate, A. Hagfeldt, and M. Grätzel, "Incorporation of rubidium cations into perovskite solar cells improves photovoltaic performance," *Science*, vol. 354, no. 6309, pp. 206–209, 2016.

[13] L.-Q. Xie, T. Zhang, L. Chen, N. Guo, Y. Wang, G. Liu, J.-R. Wang, J.-Z. Zhou, J.-W. Yan, Y. Zhao, B. Mao, and Z.-q. Tian, "Organic-inorganic Interactions of Single Crystalline Organolead Halide Perovskites Studied by Raman Spectroscopy," *Physical Chemistry Chemical Physics*, vol. 18, pp. 18112–18118, 2016.

[14] F. Brivio, J. M. Frost, J. M. Skelton, A. J. Jackson, O. J. Weber, M. T. Weller, A. Walsh, A. R. Goni, A. M. A. Leguy, and P. R. Barnes, "Lattice dynamics and vibrational spectra of the orthorhombic, tetragonal and cubic phases of methylammonium lead iodide," *Physical Review B*, vol. 92, p. 144308, 2015.

[15] A. M. A. Leguy, A. R. Goni, J. M. Frost, J. Skelton, F. Brivio, X. Rodriguez-Martínez, O. J. Weber, A. Pallipurath, M. I. Alonso, M. Campoy-Quiles, M. T. Weller, J. Nelson, A. Walsh, and P. R. F. Barnes, "Dynamic disorder, phonon lifetimes, and the assignment of modes to the vibrational spectra of methylammonium lead halide perovskites," *Physical Chemistry Chemical Physics*, vol. 18, pp. 27051–27066, 2016.

[16] T. Ivanovska, C. Quarti, G. Grancini, A. Petrozza, F. De Angelis, A. Milani, and G. Ruani, "Vibrational Response of Methylammonium Lead Iodide: From Cation Dynamics to Phonon-Phonon Interactions," *ChemSusChem*, vol. 9, pp. 2994–3004, 2016.

[17] K. Druzbicki, R. S. Pinna, S. Rudic, M. Jura, G. Gorini, and F. Fernandez-Alonso, "Unexpected Cation Dynamics in the Low-Temperature Phase of Methylammonium Lead Iodide: The Need for Improved Models," *Journal of Physical Chemistry Letters*, vol. 7, no. 22, pp. 4701–4709, 2016.

[18] E. T. Hoke, D. J. Slotcavage, E. R. Dohner, A. R. Bowring, H. I. Karunadasa, and M. D. McGehee, "Reversible photo-induced trap formation in mixed-halide hybrid perovskites for photovoltaics," *Chemical Science*, vol. 6, pp. 613–617, 2015.

[19] F. Brivio, C. Caetano, and A. Walsh, "Thermodynamic Origin of Photoinstability in The CH3NH3Pb(I1-xBrx)3 Hybrid Halide Perovskite Alloy," *The Journal of Physical Chemistry Letters*, vol. 7, pp. 1083–1087, 2016.

[20] S. J. Yoon, S. Draguta, J. S. Manser, O. Sharia, W. F. Schneider, M. Kuno, and P. V. Kamat, "Tracking Iodide and Bromide Ion Movement in Mixed Halide Lead Perovskites during Photoirradiation," *ACS Energy Letters*, vol. 1, no. 1, pp. 290–296, 2016.

[21] B. A. Rosales, L. Men, S. D. Cady, M. P. Hanrahan, A. J. Rossini, and J. Vela, "Persistent Dopants and Phase Segregation in Organolead Mixed-Halide Perovskites," *Chemistry of Materials*, vol. 28, no. 19, pp. 6848–6859, 2016.

[22] G. Richardson, S. E. J. O'Kane, R. G. Niemann, T. A. Peltola, J. M. Foster, P. J. Cameron, and A. B.Walker, "Can slow-moving ions explain hysteresis in the current-voltage curves of perovskite solar cells?," *Energy & Environmental Science*, vol. 9, pp. 1476–1485, 2016.

[23] R. G. Niemann, L. Gouda, J. Hu, S. Tirosh, R. Gottesman, P. J. Cameron, and A. Zaban, "Cs+ incorporation into CH3NH3PbI3 perovskite: Substitution limit and stability enhancement," *Journal of Materials Chemistry A*, vol. 4, pp. 17819–17827, 2016.

[24] S. R. Pering, W. Deng, J. R. Troughton, R. G. Niemann, F. Brivio, P. S. Kubiak, F. E. Jeffrey, T. M. Watson, P. R. Raithby, A. L. Johnson, S. E. Lewis, and P. J. Cameron, "Azetidinium as a Stable Organic Cation for Perovskite Solar Cells," *arXiv preprint*, vol. in press, 2017.

[25] M. T. Weller, O. J. Weber, J. M. Frost, and A. Walsh, "The Cubic Perovskite Structure of Black Formamidinium Lead Iodide, a-[HC(NH2)2]PbI3, at 298 K," *Journal of Physical Chemistry Letters*, vol. 6, pp. 3209–3212, 2015.

[26] W. Rehman, D. McMeekin, J. Patel, R. Milot, M. B. Johnston, H. Snaith, and L. M. Herz, "Photovoltaic mixed-cation lead mixed-halide perovskites: Links between crystallinity, photo-stability and electronic properties," *Energy Environ. Sci.*, vol. 10, pp. 361–369, 2017.

[27] D. Weber, "CH3NH3PbX3, a Pb(II)-System with Cubic Perovskite Structure," *Zeitschrift für Naturforschung*, vol. 33b, pp. 1443–1445, 1978.

[28] M. T. Weller, O. J. Weber, P. F. Henry, A. M. D. Pumpo, and T. C. Hansen, "Complete structure and cation orientation in the perovskite photovoltaic methylammonium lead iodide between 100 and 352 K," *Chemical Communications*, vol. 51, pp. 4180–4183, 2015.

[29] C. C. Stoumpos, C. D. Malliakas, and M. G. Kanatzidis, "Semiconducting tin and lead iodide perovskites with organic cations: phase transitions, high mobilities, and near-infrared photoluminescent properties.," *Inorganic Chemistry*, vol. 52, no. 15, pp. 9019–9038, 2013.

[30] B. Obama, "The irreversible momentum of clean energy," *Science*, vol. 355, no. 6321, pp. 126 – 129, 2017.

[31] D. D. Smith, P. Cousins, S. Westerberg, R. D. Jesus-Tabajonda, G. Aniero, and Y. C. Shen, "Toward the practical limits of silicon solar cells," *IEEE Journal of Photovoltaics*, vol. 4, no. 6, pp. 1465–1469, 2014.

Appendix A

Supporting figures and information

Several figures and supporting information is given here, that gives more detail than the main document, in particular for chapter 3. A more detailed description of the experimental summary is given, including the distributors of chemical, instrumental details, and other information. The supporting images show the morphology of all conversion temperatures (see fig. A-1), while only a selection was given in the main document. The temperature calibration is also shown, that correlates the set temperature of the heatgun to the measured temperature on the substrate (see fig. A-2a), as well as the conversion time that needed to be adjusted to each temperature (see fig. A-2b).

A.1 Experimental details

A.1.1 Chapter 3

FTO-covered glass (TEC7 with 7 Ω/sq sheet resistance, Pilkington) was scored for a final device size of 25×25 mm^2 and masked with Kapton tape (Polyimide Cleanroom Tape, 19 mm wide, Micronova). The uncovered FTO parts were etched with ZnO powder and 2 M HCl. The substrates were cleaned with Hellmanex (2 wt% Hellmanex® III solution in water), rinsed with deionised water, ethanol and finally 2-propanol (IPA for isopropyl alcohol). Organic residuals were removed *via* oxygen plasma treatment for 30 min.

Spin-coated blocking layers were deposited at a spinning speed of 2000 rpm for 60 s from a sightly acidic titanium isopropoxide (TTIP) solution (drop-wise adding a solution of 35 μL HCl in 2.53 mL IPA to 396 μL TTIP in 2.53 mL IPA). The layer was

dried at 150 °C for 30 min to form a layer of TiO_x and subsequently annealed at 500 °C for 30 min to form a compact blocking layer of TiO_2. Spray pyrolysis blocking layers were deposited from a hand-held atomiser (chromatography sprayer, Sigma-Aldrich) with a solution of titanium diisopropoxy bis(acetylacetonate) (0.2 M). The substrate was preheated to 450 °C and left to equilibrate for 30 min before spraying in intervals of 10 s for 2.5 min. The substrate was further annealed for 5 min and then allowed to cool down to room temperature.

The precursor methylammonium iodide (MAI) was synthesised by adding hydroiodic acid (57 wt% in water) drop-wise to a cooled methylamine solution (33 wt% in absolute ethanol) and removing the ethanol in the rotary evaporator (55 °C for 1 h). The white precipitate was dissolved in ethanol and recrystallised from Et_2O to obtain MAI as a white powder.

Perovskite thin-film deposition was carried out in three different ways. For the morphological study a precursor solution was spin-coated and the resulting thin-film annealed with a heat gun to evaporate the solvent and crystallise the perovskite. For the simple fabrication approach, PbI_2 thin-films were spin-coated and then converted into a perovskite layer by vacuum-vapour assisted solution processing (V-VASP). For the high hysteresis cell a modified V-VASP process was used with different parameters and cells deposited in a planar architecture, rather than onto a mp-TiO_2 scaffold. All deposition methods are described in detail further down in this paragraph. For the high air-flow processing of the perovskite, a 3:1 wt/wt ratio of MAI:$PbCl_2$ was dissolved in dimethylformamide (DMF). The precursor solution was spin-coated at 2000 rpm for 45 s and immediately afterwards taken onto a home-build stage, that fixed the substrate into its position and had the heat gun (Steinel HL 2020 E) above at a distance of 15 cm. The stage had a build-in window below the cell that allowed for an attachment of a reflection probe that was attached to an optical spectrometer (Ocean Optics USB2000+) and light source (DT-MINI-2-GS) to measure the reflectance signal during the perovskite formation. Different annealing temperatures were used for the annealing, which are described in the text below (for calibration see Appendix A, fig. A-2a). The annealing duration was dependent on temperature (see Appendix A, fig. A-2b). This was necessary because low temperatures required longer annealing times to fully evaporate the solvent and crystallise the perovskite. Using the same annealing time at higher temperatures would have decomposed the perovskite. For the simple fabrication approach, a mp-TiO_2 layer was first deposited from a paste (Dyesol 18NR-T) diluted 1:5 with ethanol and spin-coated at 1000 rpm for 60 s. The samples were then annealed in an over at 500 °C for 30 min. The PbI_2 layer was deposited by spin-coating (4000 rpm for 30 s) a hot solution of PbI_2 (Sigma-Aldrich, 99 %) in DMSO (400 mg/mL onto a hot substrate,

both at 70 °C. The thin-film was annealed at 120 °C for 60 min. The substrate was placed onto a hot plate, surrounded by MAI powder and the desiccator lid was placed on top with a rubber ring to seal the vacuum that was created with an attached rotary pump (Edwards 5 E2M5 Rotary Vane Dual Stage Mechanical Vacuum Pump). For the conversion process, the substrates and MAI powder were put under a low vacuum and the hotplate was heated to a temperature of 150 °C for the desired time (mentioned in context). For the high-hysteresis cells, the V-VASP fabrication was used as described above but in a planar architecture, rather than onto a mp-layer. The PbI_2 film was spun at a slower speed of 2000 rpm to compensate for the absence of the mp-scaffold and the PbI_2 annealing time a was shortened to 10 min. The perovskite conversion temperature was decreased from 150 °C to 120 °C and the time was set to 30 min, which is also shorter than the standard V-VASP process.

For the deposition of the hole transport material (HTM), 142.6 mg of Spiro-OMeTAD (spiro) were dissolved in 2 mL of chlorobenzene (Sigma-Aldrich, anhydrous 99.8 %). 4-tert butylpyridine (17.5 mL, 96 %, Sigma-Aldrich) and the previously prepared bis(trifluoromethane)sulfonimide lithium salt solution (37.5 mL of a 170 mg/mL Li-TFSI solution in acetonitrile) were added to the HTM solution and spin-coated at 4000 rpm for 45 s. The substrates were left in a desiccator filled with silica gel overnight for oxygen doping before the gold back contacts were evaporated with a thickness of about 80 nm and an active area of 0.1 cm^2.

For the sample analysis different characterisation techniques were used to measure the transparent conductive oxide (TCO) substrate, TiO_2 blocking layer, the $MAPbI_3$ thin-film and the complete solar device. For the TCO substrate analysis contact angle measurements were employed, according to the *Sessile drop technique*. Therefore an automatic dosing system (OCA-5, Dataphysics, Gerhard UK) dispersed a 2 μL drop of deionised water on the surface and contact angles were measured at five different points for each film. After depositing the bl-TiO_2 (as described above) the thin-film thickness was examined with a profilometer (Dektak 6M) and the blocking behaviour with cyclic voltammetry (AUTOLAB PGSTAT30). Cyclic voltammetry was carried out on a FTO substrate, covered with TiO_2. The area of the electrode was 1 cm^2 and was measured against a Ag/AgCl (3 M KCl) reference with a Pt wire as counter electrode. Scan speeds depend on the investigated system and are mentioned in the context. The electrodes were immersed into a 100 mM solution of Fe^{+II}/Fe^{+III} (equimolar amounts of $K_3Fe(CN)_6$ and $K_4Fe(CN)_6$) with background electrolyte (10 mM KCl). Scans went from -1 V to 1.2 V at different scan rates, which are mentioned in context. For the morphological analysis of the perovskite thin-films, an AFM (Nanosurf FlexAFM) was used in tapping mode (Budget Sensors AFM Probes TAP190-G). Powder X-ray diffraction (XRD) analysis

was performed with a BRUKER D8-Advance. Device performance was evaluated using a Class AAA solar simulator at AM1.5G and 100 mW/cm^2 connected to a source-meter (Keithley 2601A) that was driven by a home-built program written in LabView (see fig. 3-8). For the measurements, the samples were covered with a shadow mask with an opening area of 0.1 cm^2 to illuminate only one cell at a time. Measurements were performed by holding the cell at a voltage slightly above V_{OC} (1 - 1.2 V, depending on cell) for 5 s to equilibrate the cell. The measurement was then performed by sweeping the voltage to short-circuit and then back up to the equilibration potential. The sweeping speed was usually 100 mV/s, if not stated otherwise in the text. For the estimation of the size of the ferro-cyanide anion, an Assisted Model Building with Energy Refinement (AMBER) force field was used, as part of the Avogadro software package.[1]

A.1.2 Chapter 4

The FTO-covered glass (7.1×7.1 cm^2) was consecutively cleaned with soap solution, deionised water, ethanol and an argon plasma. A 100 nm TiO_2 blocking layer was deposited *via* spray pyrolysis. A 250 nm mp-TiO_2 was spin-coated (5000 rpm, 30 s) from a 1:10 diluted titania paste (18NR-T, Dyesol) in ethanol and annealed for 30 min. The perovskite layer was deposited from a solution of 460 mg/mL PbI_2 and 23 mg/mL $PbCl_2$ in DMSO by spin-coating at 4000 rpm for 60 s. The thin-film was annealed at 100 °C for 60 min. The lead halide film was dipped into a solution of methylammonium iodide (MAI) in 2-propanol (IPA) (32 mg/mL) for 2 min, which converted the film into the $MAPbI_3$ perovskite. The films were then washed in an IPA bath and annealed with MAI vapor at 140 °C for 60 min according to a previous report.[2] In order to sublime the excess MAI, the cells were annealed for another 60 min on the hotplate.

In order to obtain a $Cs_xMA_{1-x}PbI_3$ film, the cation exchange of the $MAPbI_3$ was done in analogy to recent reports.[3, 4] To facilitate the cation exchange, a supersaturated solution of CsI was prepared in IPA; therefore a saturated mixture with excess salt was heated and sonicated for 60 min. The solution was given time to cool down to 30 °C and was used straight away. A home-made dip coater was used to submerge the substrate into the supersaturated solution; the substrate was then partially lifted out of the solution at different conversion times of 1, 3, 10, 25 and 40 min for different conversion stages. After the conversion finished, the film was annealed at 100 °C for 10 min. The thin-film subtrates were directly used for elemental analysis. For the fabrication of solar cells and additional layer of spiro-MeOTAD (72 mg/mL in chlorobenzene doped with 34 μL Li-bis-(trifluoromethylsulfonyl)imide, 540 mg/mL in acetonitrile, and 58 μL 4-tert-Butylpyridine, 80 mM) was spin-coated at 4000 rpm for 30 s. To oxygen-dope the spiro-MeOTAD layer, the cells were kept in a dry atmosphere overnight. For the

top electrode, an array of 13 × 13 separate silver contacts (100 nm thickness) were thermally evaporated. Sonication soldering was used for the bottom contact, in order to strengthen the contact. For the stability testing, the solar cells were stored in clean dry air (about 0.6 % humidity) in darkness at room temperature. For the one-step deposited perovskite films, two equimolar precursor solutions were prepared from MAI with PbI_2 (each 1 mol/L in DMSO) and CsI with PbI_2 (each 1 mol/L in DMSO), by stirring at 60 °C over 6 h. The mixed cation solutions were prepared by mixing the $CsPbI_3$ and $MAPbI_3$ precursor solutions with the respective ratios x = 0.05, 0.1, 0.15, 0.2, 0.25, 0.3, 0.4, 0.5 and 0.75. Finally, the prepared precursor solutions were spin-coated at 2000 rpm for 60 s and then annealed at 100 °C for 10 min.

For the analysis, IV scans were performed with a home-build and automated scanner, using a Keithley 2400 source measurement unit at a scan rate of 50 mV/s and an active area of 0.026 cm^2 of each of the 169 cells, as defined by the size of the metal back contact and the shadow mask. Measurements were performed in forward and backward direction, details can be found in a recent study.[5] The in-situ absorption measurements were recorded on thin-films submerged in a cuvette with a CARY UV-Vis-NIR spectrophotometer. The thin-film absorbance mapping was measured on a home-build optical scanner, measuring total transmission, total reflection, and specular reflection with millimeter spatial resolution in a high-throughput fashion. Details of the optical scanning system can be found elsewhere.[6] The x-ray diffraction (XRD) was measured on a Bragg Brentano geometry diffractometer (CuKα1 with λ = 1.5406 Å and CuKα2 with λ = 1.5443 Å; intensity ratio of 2). All diffractograms were corrected against FTO as an internal standard. Baseline removal was performed with *fityk 0.9.8*.[7] For the time-resolved XRD measurements, the cation exchange setup was placed inside the diffractometer to be able to take measurements at different stages of the conversion process from the same position of the sample; therefore the native $MAPbI_3$ sample was loaded and 1 mL of CsI in IPA solution were placed on top. At a set of conversion times (0, 3, 8, 18, 28 and 38 min) the solution was removed and the sample blow-dried in order to measure a diffractogram, after which fresh solution was applied again. Peak fitting was done manually with CrystalDiffract 6.5 (CrystalMaker Software Ltd., Oxford, UK), using a Pseudo-Voigt peak profile. The geometrical broadening was 0.1 °. The occupancy fitting was done against single crystal data published by Stoumpos *et al.*,[8] comparing the dominant reflection peaks (002) and (110). For the used fitting model the Cs^+ was assumed to incorporate into the entire $MAPbI_3$ grains forming $Cs_xMA_{1-x}PbI_3$. Other options like two separate phases of $MAPbI_3$ and $Cs_xMA_{1-x}PbI_3$ with shared boundaries were tested. In this case the fitting converged to a complete domination of $Cs_xMA_{1-x}PbI_3$ upon $MAPbI_3$. We concluded that the two-phase model is not necessary.

Each fitting was done at least three times; the reported values are an average of those three fittings and their standard deviation as an error. SEM images were measured with a field-emission, FEI, Helios 600 high resolution scanning electron microscope. The energy-dispersive X-ray analysis (EDAX) was measured with a 80 mm^2 X-max, Oxford Instruments, scanning the entire substrate in analogy to the optical scanning system mentioned above. Raman measurements were performed with a Renishaw inVia Reflex micro-Raman spectrometer equipped with solid state lasers emitting at 514 and 785 nm with a resolution of < 2 cm^{-1}. The laser beam was focused with a x50 magnification lens, giving a laser spot size of about 1 μm in diameter. Rayleigh scattering was rejected with a 110 cm^{-1} cutoff dielectric edge filter. We measured the AzI sample with the 514 nm laser and the orange $AzPbI_3$ with the 785 nm laser in order to avoid resonant effects in the sample, which could change the spectroscopic response. All measurements were performed in air and with different laser powers to ensure that the laser probe did not induce damage or changes in the sample.

A.1.3 Chapter 5

The methylammonium halide salts (MAI, MABr and MACl) were synthesised by neutralising an ice-bath cooled solution of 24 mL methylamine (*Sigma-Aldrich*) in 100 mL of ethanol drop-by-drop with the corresponding hydrogen-halide (10 mL of 57 wt% HI in water; 14.6 mL of 48 wt% HBr in water; 15 mL of 37 wt% HCl in water). The solvent was removed in a rotary evaporator and the powder was recrystallised from ethanol. The ethanol solution was slowly cooled until the formation of white crystals was observed. The white product was washed with with diethylether and afterwards dried it at 70 °C for 6 h.

The single halide perovskite precursor solution ($MAPbI_3$, $MAPbBr_3$ and $MAPbCl_3$) was prepared by solving a 1:1 stoichiometric ratio of lead(II) halide (PbI_2, 99 %; $PbBr_2$, 99.99 %; $PbCl_2$, 99.99 %; all *Sigma-Aldrich*) with the corresponding methylammonium halide at a 1 mol/L concentration in DMSO ($\geq$ 99.9% *Sigma-Aldrich*) for 1 h at 60 °C. The mixed halide perovskite precursor solutions were prepared by mixing the respective ratios of single halide solutions and stirring the solution for 1 h. Synthesis of the precursors was done in the fume hood, while the mixing, deposition and annealing of the perovskite precursor solutions was done in an argon-filled glovebox (H_2O and O_2 concentrations $<$ 1 ppm). For planar films the precursor solution was deposited on a microscopy glass slide. For mesoporous films a dispersion of Al_2O_3 nanoparticles (20 wt% in 2-propanol, *Sigma-Aldrich*) was spin-coated onto glass slides (2000 rpm for 60 s) and annealed at 500 °C for 30 min. All solutions were spin-coated onto the flat or mesostructured substrates at 2000 rpm for 60 s and then annealed on a hotplate at

100 °C for 30 min.

Structural characterisation was performed on a Siemens D-500 diffractometer in Bragg-Brentano geometry with Cu $K_{\alpha 1}$ radiation ($\lambda = 1.5406$ Å) and Cu $K_{\alpha 2}$ radiation ($\lambda = 1.5444$ Å). Data was collected from $5 \leq 2\theta/^\circ \leq 100$ counting for 1 s at each step of 0.05 ° in detector position. Unit-cell refinements were performed with the GSAS package[9]. UV-Vis diffuse reflectance (R) spectra were acquired on a Hitachi 3010 spectrophotometer using an integrating sphere with 60 mm diameter and $BaSO_4$ as a reference. For the Kubelka-Munk spectrum the data was transformed with $F(R) = (1-R)^2/2R$. Far-IR spectra were collected in transmission mode at normal incidence on a Bruker Vertex 80v vacuum spectrometer. High-density polyethylene films were used as a reference. Spectra were averages over 200 scans with a 4 cm^{-1} resolution. The IR transmittance spectra were collected in the range of ca. $60-680$ cm^{-1}. The data was converted to absorbance and all spectra were normalised to 1. Raman measurements were performed with a Renishaw in *via* Reflex micro-Raman spectrometer equipped with solid-state lasers emitting at 514 and 785 nm with a resolution of < 2 cm^{-1}. The laser beam was focused on a spot of 1 μm in diameter with a x100 magnification lens. Rayleigh scattering was rejected with a 50 and a 110 cm^{-1} cutoff dielectric edge filter, and analysis of the scattered beam was performed on a 250 mm focal length spectrometer along with suitable diffraction gratings (1800 lines/mm for visible and 1200 lines/mm for NIR) and a high-sensitivity CCD detector. For the cryostatic measurements, the samples were placed in inert atmosphere in a *THMS600PS Linkam* cell and the laser beam was focused with a x50 long focal distance lens. Measurements were performed at different laser powers to assure the intensities used did not induce changes in the spectrum. Off-resonance Raman spectra were acquired with a Bruker RFS100 FT-Raman spectrometer probing with a Nd:YAG laser emitting at 1064 nm. Each spectrum was averaged over 100 scans or 200 scans with 4 cm^{-1} resolution. The effective working range was between about 100 and 3500 cm^{-1}. All FT Raman measurements were performed in air and at different laser powers to ensure that the intensities used did not induce changes in the spectra. All measured Raman spectra present a strong elastic scattering background in the low-frequency (LF) spectral range. In order to enhance the Raman features at this LF range, where very informative PbX and MA vibrations are active, and to correctly determine spectral characteristics (frequency, line width, and line shape), the spectra were temperature-reduced using the following expression:[10]

$$I_{red}(\omega) = I(\omega)\frac{1}{n(\omega,T)+1} \quad \text{with}$$

$$n(\omega,T) = (exp^{\frac{hc\omega}{k_BT}} - 1)^{-1} \approx (exp^{\frac{1.44\omega}{T}} - 1)^{-1}$$

where $I(\omega)$ and $I_{red}(\omega)$ are the measured and reduced Raman intensity, respectively. $n(\omega, T)$ is the Bose-Einstein statistic factor, h and k_B are the Planck and Boltzmann constants, respectively, c is the speed of light, ω is the Raman shift in cm^{-1}, and T is the temperature in K. The analysis of the reduced spectra was done by fitting them with mixed Lorenzian-Gaussian functions using the Wire software from Renishaw. Line widths were corrected for instrumental broadening.

A.2 Supporting figures

A summary of the photovoltaic performance of PSC, that were converted with the high flow-rate method (according to fig. 3-5) is given in figure A-3; the main document contains a typical IV curve of each conversion temperature. The summary shows that the open-circuit voltage does not vary significantly for most temperatures, exept for low temperatures (≤ 74 °C). Current density increases steadily with temperature. The fill-factor is unrealistically high, which indicates hysteretic contribution, which becomes most dominant at lower temperatures. ($77 - 110$ °C). We showed a full conversion at about 84 °C, which however, does not correspond to well-performing cells.

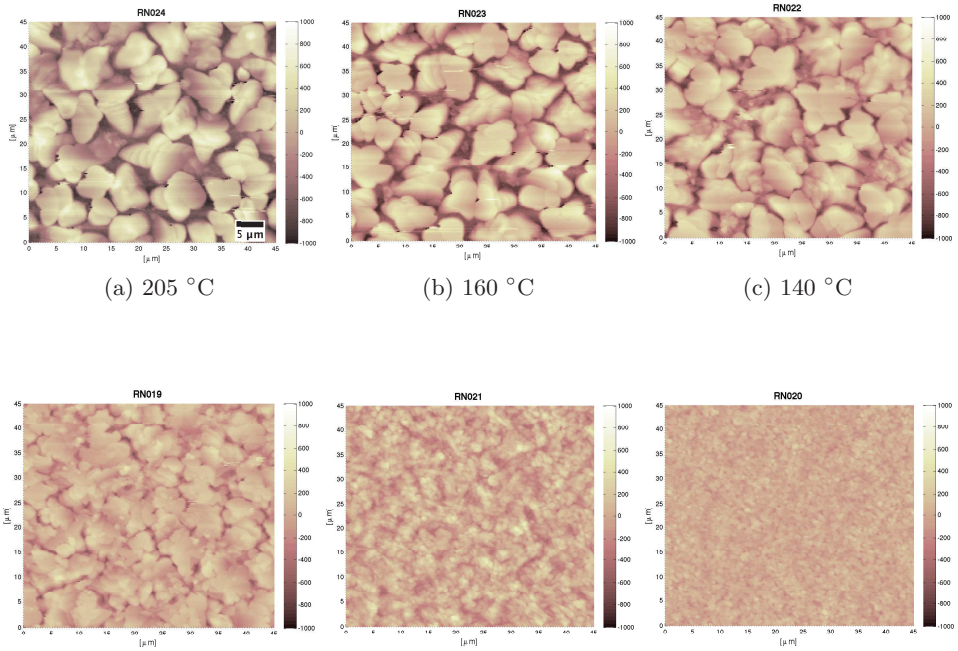

(a) 205 °C (b) 160 °C (c) 140 °C

(d) 120 °C (e) 105 °C (f) 84 °C

Figure A-1: AFM images of different perovskite annealing conditions. Variation of the temperature from 150 °C to 500 °C and flow rate at 300 l/min and 500 l/min.

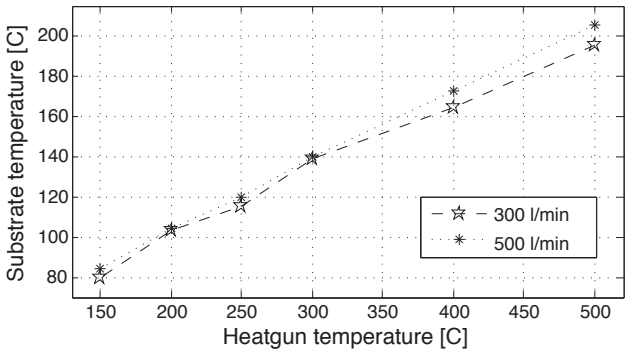

(a)

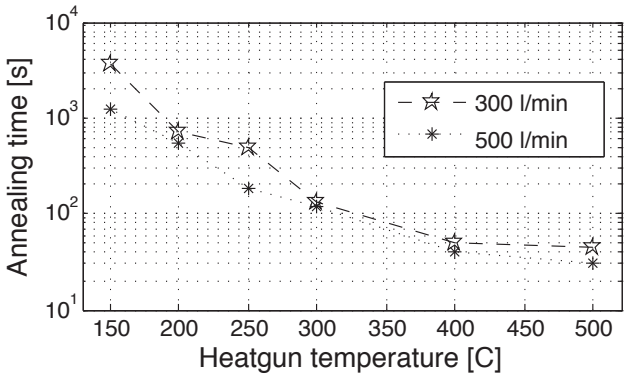

(b)

Figure A-2: *(a)* **Calibration of the temperature during the annealing for both flow rates.** *(b)* **Time of perovskite film formation over annealing temperature.**

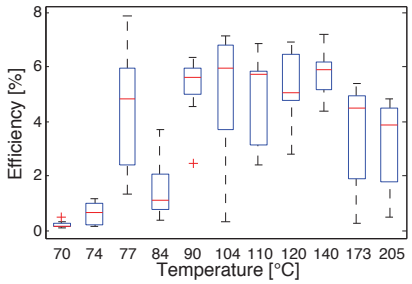

(a) Efficiency

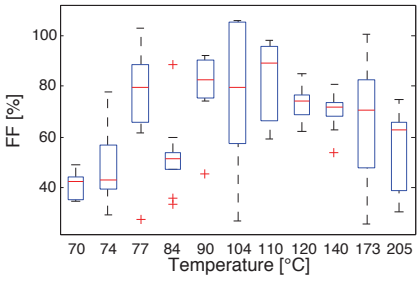

(b) Fill factor

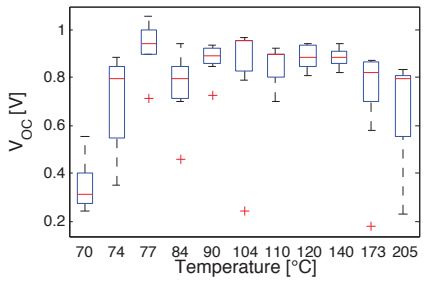

(c) Open-circuit voltage

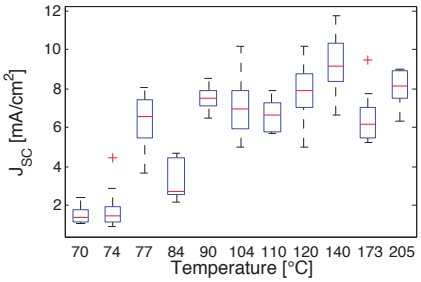

(d) Short-circuit current

Figure A-3: Cell performances of different annealing temperature conditions. Each column consists of ten measured devices, where the red line represents the median and, box indicates the 25 % confidence interval and the bar indicates the 75 % confidence interval. The fill factors are unrealistically high, with indicates a strong hysteretic contribution.

A.3 Bibliography

[1] P. Kollman, "Assisted Model Building with Energy Refinement." http://ambermd.org [Online; accessed: 5-Aug-2014], 2014.

[2] L. Gouda, R. Gottesman, S. Tirosh, E. Haltzi, J. Hu, A. Ginsburg, D. A. Keller, Y. Bouhadana, and A. Zaban, "Vapor and Healing Treatment for CH3NH3PbI3-xClx Films toward Large-Area Perovskite Solar cells," *Nanoscale*, vol. 8, pp. 6386–6392, 2016.

[3] G. Nedelcu, L. Protesescu, S. Yakunin, M. I. Bodnarchuk, M. J. Grotevent, and M. V. Kovalenko, "Fast Anion-Exchange in Highly Luminescent Nanocrystals of Cesium Lead Halide Perovskites (CsPbX3, X = Cl, Br, I)," *Nano Letters*, vol. 15, no. 8, pp. 5635–5640, 2015.

[4] G. E. Eperon, C. E. Beck, and H. J. Snaith, "Cation exchange for thin film lead iodide perovskite interconversion," *Materials Horizons*, vol. 3, pp. 63–71, 2016.

[5] S. Ruhle, H. N. Barad, Y. Bouhadana, D. Keller, A. Ginsburg, K. Shimanovich, K. Majhi, R. Lovrincic, Y. Anderson, and A. Zaban, "Combinatorial solar cell libraries for the investigation of different metal back contacts for TiO2-Cu2O hetero-junction solar cells.," *Physical Chemistry Chemical Physics*, vol. 16, no. 15, pp. 7066–7073, 2014.

[6] A. Y. Anderson, Y. Bouhadana, H. N. Barad, B. Kupfer, E. Rosh-Hodesh, H. Aviv, Y. R. Tischler, S. Ruhle, and A. Zaban, "Quantum efficiency and bandgap analysis for combinatorial photovoltaics: Sorting activity of Cu-O compounds in all-oxide device libraries," *ACS Combinatorial Science*, vol. 16, no. 2, pp. 53–65, 2014.

[7] M. Wojdyr, "Fityk: A general-purpose peak fitting program," *Journal of Applied Crystallography*, vol. 43, no. 5, pp. 1126–1128, 2010.

[8] C. C. Stoumpos, C. D. Malliakas, and M. G. Kanatzidis, "Semiconducting tin and lead iodide perovskites with organic cations: phase transitions, high mobilities, and near-infrared photoluminescent properties.," *Inorganic Chemistry*, vol. 52, no. 15, pp. 9019–9038, 2013.

[9] A. C. Larson and R. B. von Dreele, "General Structure Analysis System;," *Report LAUR 85-748; Los Alamos Laboratory: Los Alamos*, 1994.

[10] E. I. Kamitsos, J. A. Kapoutsis, H. Jain, and C. H. Hsieh, "Vibrational study of the role of trivalent ions in sodium trisilicate glass," *Journal of Non-Crystalline Solids*, vol. 171, no. 1, pp. 31–45, 1994.